UNIVERSIDAD COMPLUTENSE DE MADRID

FACULTAD DE CIENCIAS FÍSICAS

PROGRAMA DE DOCTORADO EN FÍSICA

TESIS DOCTORAL

Low-cost and versatile optical biometer scanning components and binocular afocal projection system for use in cataract and presbyopia treatment planning.

Componentes de escaneo versátiles y de bajo coste para biometría óptica, y sistema de proyección afocal para la planificación de tratamientos de cataratas y presbicia

MEMORIA PARA OPTAR AL GRADO DE DOCTORA

PRESENTADA POR

MARÍA PILAR URIZAR URSUA

DIRECTORES

ANDREA CURATOLO

ENRIQUE GAMBRA URRALBURU

ALBERTO DE CASTRO ARRIBAS

VioBio Lab.
Instituto de Óptica
CSIC

2EyesVision S.L.

Departamento de Óptica
Facultad de Ciencias Físicas
UCM

UNIVERSIDAD COMPLUTENSE MADRID

DECLARACIÓN DE AUTORÍA Y ORIGINALIDAD DE LA TESIS PRESENTADA PARA OBTENER EL TÍTULO DE DOCTOR

D./Dña. **María Pilar Urizar Ursua**, estudiante en el Programa de Doctorado en Física, de la Facultad de Ciencias Físicas de la Universidad Complutense de Madrid, como autor/a de la tesis presentada para la obtención del título de Doctor y titulada:

Componentes de escaneo versátiles y de bajo coste para biometría óptica, y sistema de proyección afocal para la planificación de tratamientos de cataratas y presbicia

Y dirigida por: Dr. **Andrea Curatolo,** Dr. **Enrique Gambra** y Dr. **Alberto De Castro**.

DECLARO QUE:

La tesis es una obra original que no infringe los derechos de propiedad intelectual ni los derechos de propiedad industrial u otros, de acuerdo con el ordenamiento jurídico vigente, en particular, la Ley de Propiedad Intelectual (R.D. legislativo 1/1996, de 12 de abril, por el que se aprueba el texto refundido de la Ley de Propiedad Intelectual, modificado por la Ley 2/2019, de 1 de marzo, regularizando, aclarando y armonizando las disposiciones legales vigentes sobre la materia), en particular, las disposiciones referidas al derecho de cita.

Del mismo modo, asumo frente a la Universidad cualquier responsabilidad que pudiera derivarse de la autoría o falta de originalidad del contenido de la tesis presentada de conformidad con el ordenamiento jurídico vigente.

En Madrid, a 4 de Septiembre de 2023

Fdo. URIZAR URSUA MARIA PILAR - 73126406E

Firmado digitalmente por URIZAR URSUA MARIA PILAR - 73126406E
Fecha: 2023.09.04 18:31:59 +02'00'

Esta DECLARACIÓN DE AUTORÍA Y ORIGINALIDAD debe ser insertada en la primera página de la tesis presentada para la obtención del título de Doctor.

"Lo que con mucho trabajo se adquiere, más se ama."

Aristóteles

"En la vida no existe nada que temer, solo cosas que aprender."

Marie Curie

O incluso una pandemia…

Agradecimientos

Por fin llega el momento de completar este trabajo de tesis agradeciendo a todos los que me habéis acompañado en esta aventura. ¡Sois tantos que espero no dejarme a nadie!

Empiezo por mis directores de tesis, ¡que no son pocos! A los que se fueron, pero sobre todo a los que están. Ha sido un lujo haber podido trabajar con vosotros durante este tiempo. Gracias a los tres, Andrea, Enrique y Alberto, por vuestro conocimiento y dejarme aprender de vosotros. Gracias por la confianza depositada durante el proyecto de esta tesis.

A Andrea por estar siempre, y siempre cerca. Independientemente de la distancia física siempre has estado disponible para una llamada o un mensaje en cualquier momento. Gracias por las sesiones infinitas de laboratorio (¡incluso remoto!) y las discusiones sobre óptica, por la paciencia, por los empujones a seguir aprendiendo y avanzar, y por la enseñanza de constancia y esfuerzo. Gracias por la pasión que pones en tu trabajo.

A Enrique por tus consejos y tu tiempo, aunque no sé de dónde lo sacabas. Gracias por escucharme, ayudarme a organizarme, y por pensar en mí cuando aparecían nuevos proyectos y ayudarme a conseguirlos. Trabajar contigo y conocerte durante los 'SanFermiting' ha sido un gran placer. ¡Espero continuar siguiendo tus pasos!

Y por supuesto también a Alberto. Desde que te incorporaste al proyecto has sido un apoyo siempre que me atascaba. Gracias por tu tranquilidad, tus consejos y hacer siempre las cosas más fáciles. Gracias por tener la puerta de tu despacho siempre abierta.

No puedo dejar de agradecer también a Susana y a Carlos por brindarme la oportunidad de trabajar en dos grandes equipos, VioBio y 2EyesVision. La dedicación que invertís en ellos es realmente asombrosa y se transmite desde el primer instante. Las discusiones en las OCT meetings o en las ventanas/pizarras de Tres Cantos han sido un aprendizaje continuo. Gracias por tener siempre un comentario, un consejo o nuevos puntos de vista.

Xoana, ¡quien nos iba a decir que acabaríamos viviendo juntas! Gracias por tus consejos y por las interminables charlas durante tantas noches hablando e intentando solucionar el mundo. Gracias por escucharme siempre y ser tan buena compañera y amiga.

Alejandra y Lupe, ¡mis incansables compañeras de despacho! ¿Qué deciros que no nos hayamos dicho ya a las tantas en el laboratorio, en el despacho o en las cañas de después? Solo nos ha faltado ponernos la 'sleeping' en el despacho para hacer las tertulias más cómodas. Gracias por todas las risas compartidas y todo el apoyo que me habéis dado. Aquí entra también Fernando, que siempre venías atraído por los chocolates al despacho. Llegaste pisando fuerte y revolucionándonos a todos. En poco tiempo te convertiste en fundamental. Gracias por toda la energía y el positivismo que contagias.

Carmen, compañera incansable de charlas 11F y de largas horas al otro lado de la pared del laboratorio. Gracias por los descansos entre experimentos para ver un poco la luz del sol. Sara, ¡qué vacío dejaste cuando te fuiste! Pero, aún así, no he dejado nunca de notar tu apoyo siempre ¡gracias! Edu, gracias por todas las conversaciones, las quedadas en patines y el grupo del Sí. ¡Vosotros sí que habéis sido un descubrimiento!

Gracias, a todo el equipo VioBio. A Álvaro, por aceptar trabajar conmigo y sacar adelante todo lo que necesitábamos a pesar de mí. Gracias por toda la ayuda este último año ¡que no ha sido poca! A Elena por siempre estar disponible y por toda la ayuda con las compras y las gestiones ¡qué paciencia tienes! A Dani por todas las ‘chapucillas’ para ayudar a que todos los sistemas funcionaran. A Judith, Rocío, Clara, James, Victor, Nohelia, Edu, Mar, Paula, Amal, Andrés…

Gracias al equipo 2EyesVision. En especial a Diana, por aguantarme tantas mañanas durante el último sprint de la tesis. A Gonzalo, por ayudarme con algún que otro problema informático. Y a todos los demás (Cris, Irene, Yassine, Joshua, Juan, Jose Ramón, Álvaro, Petros…).

Qué decir de todos los amigos que me habéis acompañado en el cambio hasta aquí, desde la carrera hasta ahora, aunque lejos siempre cerca. En especial a Jorge y David que, aunque ya no compartimos apuntes sí seguimos sumando experiencias. Y, por supuesto, gracias a Quique. Gracias por acompañarme siempre, entenderme y quedarte a mi lado siempre. Gracias por aguantarme y quererme.

Y cómo no, muchas muchas muchas gracias a toda mi familia. Tengo mucho que agradeceros, papás y tatita, por ser siempre un ejemplo de trabajo y esfuerzo constante, pero también por enseñarnos a disfrutar de ello. Gracias por ser siempre un apoyo seguro e incansable. Gracias por creer siempre en mí. Yo, de mayor, quiero parecerme un poquito a vosotros.

¡Gracias a todos por enseñarme tanto!

Funding

The research developed during this thesis would have not been possible without the funding received from the following public and private institutions:

- Madrid Regional Government (CAM). Industrial PhD Grant IND2019/BMD-17262 to María Pilar Urizar.

- Spanish Government Grant PID2020-115191RB ‘Nuevos paradigmas de diseño, selección y evaluación de lentes intraoculares’ to Alberto de Castro and Susana Marcos

- Spanish Government Grant FIS2017-8453 ‘Nuevas tecnologías ópticas para entender y tratar la miopia’ to Susana Marcos and Carlos Dorronsoro

- Foundation for Polish Science MAB/2019/12 to Andrea Curatolo.

Summary of the thesis in English

The aging of the eye can lead to the appearance of several ocular diseases due to different mechanisms (the loss of the accommodation ability in the case of presbyopia, the cloudiness of the crystalline lens in the case of cataract and the presence of inadequate eye dimension to focus distant objects in the case of myopia), making the use of optical aids necessary to correct them. In recent years, age related ocular diseases have become of increasing concern due to their rising global prevalence, in part related with the global aging of the population. Many efforts have been addressed to correct them and mitigate patient's visual impairment. Nevertheless, the development of strategies for individualized and optimal treatment planning still remains in progress and barriers to access eye care are still present in remote and low-resource settings, where the prevalence is higher.

Optical coherence tomography (OCT) is a non-invasive biomedical imaging technique based on low coherence interferometry used in optical biometers to measure the intraocular distances of an eye, among other uses. Eye biometry is an indispensable step in cataract surgery planning as it allows to select the power of the intraocular lens to implant. Since the first use of light interferometry for ocular biometry, optical biometers have made their way into the ophthalmology market becoming the gold standard in the clinical practice due the higher accuracy and increased patient's comfort compared to ultrasound-based biometers. However, either due to the use of high-cost components in Fourier Domain (FD)-OCT biometers and the limited transportability of Time Domain (TD)-OCT biometers, there is still reduced accessibility to this technology in remote and low-resource settings. Several attempts have been made to develop low-cost and portable OCT systems. However, the majority of such devices has targeted applications not requiring long axial scan ranges, and only recently attempts with thermally tuned vertical cavity surface emitting laser (VCSEL) swept sources have been directed to low-cost biometry.

On the other hand, before undergoing a surgical procedure, presbyopia correction with spectacles is a commonly chosen option. Progressive addition lenses (PALs) have a high added value as they provide users good vision at different distances when looking through different regions of the lens. Nowadays, a significant effort is being made by manufacturers to improve their properties and quality, especially in personalizing the lenses design. However, the selection of the most adequate optical design with respect to each user's preferences is still a challenge. Many patients face problems with their adaptation to PALs, leading to discarding the lenses and needing to manufacture new ones, affecting the whole value chain (the manufacturer that has to produce new spectacles, the optometrist that needs to spend more chair time with each patient, the experience of the patient and the environment since the discarded glasses cannot be reused). Attempts have been made with virtual reality simulators to simulate the vision through different progressive addition lenses design before

manufacturing the spectacles. However, providing an unnatural vision limits the application of such systems.

In this thesis we propose the development of a low-cost optical biometer to increase patients' access to optical biometry before undergoing cataract surgery. We propose the low-cost development of two of the main components of an OCT-based optical biometer. On one side, we propose a novel, long-range frequency domain optical delay line (FD-ODL), by changing its design such that a more cost-effective actuation method, i.e., a stepper motor spinning a tilted mirror, can be used to induce a group delay scan, for axial ranges and speed suitable to eye axial length scans. We have integrated the proposed optical delay line into a low-cost time domain biometer, and we have performed 1-D axial scans of a model eye. The novel low-cost optical biometer enables to independently select the scan range and frequency by changing the mirror tilt angle and motor speed respectively, unlike in standard galvanometer mirror-based FD-ODLs.

On the other hand, we also propose a low-cost whole-eye optical beam scanner as 2-D cross-sectional scans are also of high interest in ocular biometry as they allow to obtain structural information of the eye as well as checking proper subject's fixation for improved measurement repeatability. In this work, we propose the implementation of a versatile beam scanner based on three electro-tunable lenses (ETLs) capable of non-mechanically switching between anterior and posterior segment imaging configurations, i.e., performing dynamic focusing and control of the beam direction. We experimentally validated both scanning components when integrated into an OCT system to image various ocular samples in both imaging configurations.

Additionally, we also present the concept and custom design of a wide field of view afocal projection system to allow presbyopic patients to test different progressive lenses before buying them. We performed a detailed analysis of the system requirements and built a proof-of-concept prototype to validate the working principle of the proposed system.

In summary, we present the design and experimental validation of different low-cost and versatile systems to be used in the cataract and presbyopia treatment planning.

Resumen de la tesis en castellano

El envejecimiento del ojo puede dar lugar a la aparición de varias condiciones oculares como, entre otras, la pérdida de acomodación en el caso de la presbicia, la opacidad del cristalino en el caso de la catarata y la presencia de propiedades ópticas inadecuadas para enfocar objetos lejanos en el caso de la miopía; haciendo necesario el uso de correcciones ópticas. En los últimos años, la preocupación por estas condiciones oculares asociadas a la edad ha aumentado debido a su creciente prevalencia a nivel mundial, relacionada con el envejecimiento global de la población. Aunque se han realizado muchos esfuerzos para corregir y mitigar la discapacidad visual de las personas, aún es necesario continuar trabajando en el desarrollo de estrategias para la planificación y optimización del tratamiento personalizado de cada paciente, así como en su accesibilidad en entornos remotos y vías de desarrollo, donde la prevalencia es mayor.

La tomografía de coherencia óptica (OCT) es una técnica de imagen no invasiva, basada en la interferometría de baja coherencia, con aplicación en biometría óptica para medir las distancias intraoculares del ojo entre otras aplicaciones. La biometría ocular es un paso crucial en la planificación de la cirugía de cataratas, ya que permite seleccionar la potencia óptica de la lente intraocular a implantar. Los biómetros ópticos ofrecen, frente a los biómetros de ultrasonidos, una mayor precisión y comodidad para el paciente. Esto es lo que ha facilitado su penetración en el mercado y su uso diario en la práctica clínica. Sin embargo, debido al uso de componentes de alto coste en biómetros OCT de dominio frecuencial y a la limitada portabilidad de biómetros OCT de dominio temporal, la accesibilidad a esta tecnología sigue siendo reducida en entornos remotos o en vías de desarrollo. Aunque se han realizado varios intentos para desarrollar sistemas OCT portátiles y de bajo coste, estos dispositivos solo se han demostrado para aplicaciones donde no es necesario escanear largas distancias, y sólo recientemente los intentos con fuentes de barrido láser de emisión superficial de cavidad vertical (VCSEL) sintonizadas térmicamente se han dirigido a la biometría de bajo coste.

Por otro lado, la corrección de la presbicia con gafas es una opción frecuentemente elegida frente a la cirugía refractiva. Las lentes de adición progresivas tienen un alto valor añadido, ya que proporcionan a los usuarios una buena visión a diferentes distancias al mirar a través de distintas regiones de la lente. En la actualidad, los fabricantes y diseñadores realizan un importante esfuerzo para mejorar su calidad, buscando una personalización de los parámetros del diseño de las lentes. Sin embargo, la selección del diseño óptico más adecuado según las necesidades de cada usuario sigue siendo un reto. Muchos pacientes tienen problemas de adaptación a las gafas progresivas, lo que lleva a desecharlas y a tener que fabricar otras nuevas. Esto perjudica a toda la cadena de valor: al fabricante que tiene que producir unas nuevas gafas, al optometrista que tiene que dedicar más tiempo de consulta a cada paciente, a la experiencia del paciente y al medio ambiente, ya que las gafas desechadas no se reutilizan. En los últimos años se ha intentado simular la visión con distintos

diseños de lentes progresivas con simuladores de realidad virtual antes de la fabricación de las gafas para ayudar a optimizar su selección. Sin embargo, el hecho de no proporcionar una visión natural limita la aplicación de estos sistemas.

En esta tesis proponemos el desarrollo de un biómetro óptico de bajo coste para aumentar el acceso de los pacientes a la biometría óptica cuando se someten a cirugía refractiva de cataratas, a través del desarrollo económico de dos de los componentes principales de un biómetro óptico basado en OCT. Por un lado, proponemos una novedosa línea de retardo óptico en el dominio frecuencial (FD-ODL) de largo recorrido, modificando su diseño de forma que pueda utilizarse un método de actuación más rentable, es decir un motor paso a paso que hace girar un espejo inclinado, para generar escaneos de rangos axiales y velocidad adecuados para los escaneos de longitud axial del ojo. Hemos integrado la línea de retardo óptica propuesta en un biómetro de dominio temporal de bajo coste y hemos realizado escaneos axiales 1-D de un ojo modelo. El nuevo biómetro óptico de bajo coste permite seleccionar de forma independiente el rango y la frecuencia de escaneado cambiando el ángulo de inclinación del espejo y la velocidad del motor respectivamente, a diferencia de las líneas de retardos FD-ODL estándar basadas en espejos galvanométricos.

Por otro lado, también proponemos la reducción de costes de un escáner óptico, ya que la adquisición de imágenes 2-D del ojo completo también son de gran interés en biometría ocular al permitir obtener tanto información estructural del ojo como comprobar la fijación de mirada del paciente para mejorar la repetibilidad de las medidas. El versátil escáner óptico propuesto en esta tesis se basa en la combinación de tres lentes optoajustables y es capaz de cambiar sin modificaciones mecánicas entre las configuraciones de imagen del segmento anterior y posterior del ojo. Hemos validado experimentalmente el escáner óptico propuesto integrándolo en un sistema OCT y obteniendo imágenes de diversas muestras oculares en ambas configuraciones de escaneo.

Presentamos también el concepto y el diseño personalizado de un sistema de proyección afocal de campo de visión amplio para permitir a los pacientes présbitas probar diferentes lentes progresivas antes de comprarlas. Realizamos un análisis detallado de los requisitos del sistema, así como una prueba de concepto del principio de funcionamiento del mismo.

En resumen, presentamos el diseño y la validación experimental de diferentes sistemas versátiles y de bajo coste para su uso en la planificación del tratamiento de presbicia y catarata.

Keywords

Afocal

Axial scan

Cataract

Custom design

Electro-tunable lenses

Frequency domain

Intraocular lenses

Laboratory

Low-cost

Matlab

Optical Coherence Tomography

OCT

Optical delay line

Optical design

Optical beam scanner

Optics

OpticStudio

Ophthalmology

Presbyopia

Projection system

Progressive addition spectacle

Prototype

Relay

Scanner

Spectacles

Time domain

Whole-eye

Wide field

Zemax

List of most used abbreviations

A
ACD: Anterior chamber depth
AL: Axial length
ASP: Analog signal processing
B
C
CA: clear aperture
CCT: central corneal thickness
D
D: Diopters
DC: Direct current (when used for a motor)
DC: Digital counts (when used for the PWM duty cycle)
DG: Diffraction grating
DU: Detour unit
E
E: Eyepiece
EP: Entrance pupil
ETL: Electro-tunable lens
F
FD: Fourier Domain
FFC: Flexible flat cable
FFT-MTF: Fast Fourier transform of the modulation transfer function
FoV: Field of view
FT: Fourier transform
FWHM: Full width at half maximum
FZ: Far zone of the PAL
G
H
HRM: Hollow-roof-mirror
Hz: Hertz
I
IOL: Intraocular lens
J
K
K: Keratometry

L

LCI: Low coherence interferometry
LT: Lens thickness

M

M: Mirror
MEMS: Micro-electron-mechanical system
MMLD: Multi-mode laser diode
MTF: Modulation transfer function

N

NIR: Near-infrared
NZ: Near zone of the PAL

O

OCT: Optical Coherence Tomography
ODL: Optical delay line
OLCR: Optical low-coherence reflectometry
OPL: Optical pathlength

P

P: Periscope
PAL: Progressive addition lens
PCI: Partial coherence interferometry
PD: Photodetector
PDM: Perforated double pass mirror
PS: Projection system
PSB: Polarization beam splitter
PWM: Pulse width modulation

Q

R

RMS: Root mean square
RSOD: Rapid scanning optical delay line
RT: Retinal thickness
RU: Relay unit

S

SD: Spectral domain
SLED: Superluminiscent light emitting diode
SS: Swept Source
STM: Spinning tilted mirror

T

TD: Time Domain
TL: Trial lens

U

US: Ultrasound

V

VCSEL: Vertical cavity surface emitting laser

W

WHO: World health organization

X

Y

Z

Table of contents

Agradecimientos **7**
Funding **9**
Summary of the thesis in English **11**
Resumen de la tesis en castellano **13**
Keywords **15**
List of most used abbreviations **17**
Chapter 1 Introduction **25**
1.1 – Ocular biometry of the eye 25
1.1.1 – The optics of the eye 25
1.1.2 – Ocular biometry 27
1.1.3 – Importance of ocular biometry on diagnosis and treatment of ocular conditions. 29
1.2 – Techniques for ocular biometry measurement 33
1.2.1 – Ultrasound vs optical biometers 33
1.2.2 – Low coherence interferometry (LCI) 35
1.2.3 – Commercial optical biometers 43
1.3 – Ocular condition prevalence in low resource and remote settings 45
1.4 – Towards low-cost and portable ocular biometry 46
1.5 – Motivation 48
1.6 – Open questions 49
1.7 – Goals of the thesis 50
1.8 – Hypothesis 51
Chapter 2 Methods **53**
2.1 – Software 54
2.2.1 –OpticStudio Software 54
2.2.2 – MATLAB 55
2.2.3 – LabVIEW 55
2.2 - Hardware 56
2.2.1 – Laboratory set-ups 56
2.2.2 – Ocular samples 61
2.2.3 – Commercial biometers 61
2.3 – Summary of the methodology applied in this thesis 66
Chapter 3 Optical delay line selection **67**
3.1 – Introduction 68
3.2 – Layout of two types of FD-ODL 69
3.3 – Scanning performance two types of FD-ODL 70
3.3.1 – Scanning power 70
3.3.2 – Axial resolution (Δz) 72
3.3.3 – Overall scanning performance 75

3.4 – Next steps 76
3.5 – Discussion 76
3.6 – Conclusion 77
Chapter 4 Low-cost FD-ODL 79
4.1 – Introduction 80
4.2 – Working principle of the proposed FD-ODL 80
4.2.1 – Schematic and analytical description 81
4.2.2 – Proposed FD-ODL system components and specifications 86
4.2.3 – Proposed FD-ODL simulation: axial performance analysis 87
4.3 – Experimental setup 89
4.3.1 – Tilted mirror (TM) control system 89
4.3.2 – OLCR experimental setup 90
4.3.2 – OLCR signal processing system 92
4.4 – Experimental measurements 94
4.4.1 – System characterization 94
4.4.2 – Comparison to a gold standard FD-ODL 96
4.4.3 – Experimental axial biometry results 97
4.5 – Future work 99
4.6 – Discussion 100
4.7 – Conclusion 103
Chapter 5 ETL based optical beam scanner for whole eye OCT scanning 105
5.1 – Introduction 106
5.2 – Working principle 108
5.2.1 – Schematic and analytical description 109
5.2.2 – System parameters space: dependencies and limitation 113
5.3 – Simulation of the optimized designed optical beam scanner 117
5.3.1 – System components and specifications 117
5.3.2 – Optical performance simulation of the optimized beam scanner 118
5.4 – Experimental implementation of the optical beam scanner 121
5.4.1 – Beam scanner control system 121
5.4.2 – Calibration of the ETLs 122
5.4.3 – Experimental setup and characterization 124
5.5 – Whole-eye OCT scans 128
5.5.1 – SS-OCT experimental setup 128
5.5.2 – Ocular samples imaged 129
5.6 – Alternative implementations 132
5.6 – Discussion 133
5.7 – Conclusion 137
Chapter 6 Ophthalmic progressive lens demonstrator 139
6.1 – Introduction 140
6.2 – Working principle description 143
6.2.1 – Schematic description 143
6.2.2 – System optical requirements 145

6.3 – Experimental proof-of-concept ... 147
6.3.1 – Setup components ... 147
6.3.2 – Experimental validation ... 149
6.4 – Projection system design ... 151
6.4.1 – Optical design description ... 151
6.4.2 – Optical performance analysis on model retina ... 153
6.4.3 – Requirements evaluation ... 157
6.5 – Future work ... 158
6.6 – Discussion ... 159
6.7 – Conclusions ... 161
Chapter 7 Conclusions ... 163
List of scientific activities ... 167
Bibliography ... 171

Chapter 1

Introduction

1.1 – Ocular biometry of the eye

1.1.1 – The optics of the eye

The eye is a very important optical system, as it is fundamental for the vision process, involving the projection of an image of the outside world on the retina, and part of the neural processing of the received information received. Despite the ability of the eye to form images over a large field of view of objects placed at different distances, the optical system of the eye is rather simple as it only involves two optical components, the cornea and the crystalline lens. In comparison, manmade optical systems often require the combination of several optical elements to achieve a good image quality [1].

The main optical elements of a human eye are shown in Figure 1.1. An adult human eye can be approximated by a sphere of around 24 mm diameter, with a transparent aperture through which light is refracted by two positive lenses. In the first place, the light propagates through the cornea, which is a transparent meniscus. The cornea can be approximated by two spherical sections separated by about 0.55 mm with an approximate refractive index of 1.377, and contributes with about two thirds (around 42 D) of the total power of the eye (around 60 D) [1-3].

The light is also refracted by the crystalline lens, which is a biconvex lens that provides the remaining third of the optical power of the eye. Due to its layered structure, the crystalline lens presents a gradient index of refraction that peaks in the center. An approximation of this gradient refractive index is the equivalent homogeneous refractive index that is defined as the refractive index of a lens with the same external geometry and dioptric power and has a value of around 1.42 [4]. The crystalline lens also presents the capability of changing its external shape and thickness thanks to the action of the ciliary muscle, process known as accommodation, so that the optical power of the lens is changed and objects at different distances can be focused on the retina [5].

Another important component of the visual system is the iris, placed in front of the anterior surface of the crystalline lens. The iris or pupil is formed by a set of muscles with a central hole that works as a diaphragm or aperture stop of the optical system of the eye. The iris is capable of controlling the amount of light entering the eye as it changes its diameter as a function of the illumination conditions. Thus, the image of the iris through the cornea and the lens correspond to the entrance and exit pupil of the optical system of the eye respectively. The pupil diameter can range between 2 mm and 8 mm when changing from bright to dark illumination, with an average size in daily light conditions of 4 mm [1, 6].

Lastly, the image of the outside world is formed in the retina. The ideal situation where the optics of the eye enables to image distant and close objects in focus is called emmetropia. However, often the eye does not have the adequate optical properties or dimensions to focus the image on the right plane and is affected by an optical refractive error that results in a blurred image in the retina.

The retina consists of a layer structure that comprises the photoreceptors, which are the cells that detect light. There are two types of photoreceptors in the retina: rods with high sensitivity to light that allow vision in low luminance conditions, and cones with lower sensitivity that are responsible for daytime and color vision [1]. The central area of the retina is known as macula. Its diameter is about 5.5 mm and contains the foveal pit, its central smaller area of about 350 μm, that is the region with the highest resolution as it contains the highest density of cones and no rods [7]. The eye moves continuously to fixate the desired details onto the fovea. Due to both the reduced optical quality and the lower density of cones at the periphery of the retina, the visual acuity is reduced. However, this area is highly important for movement detection. The retina also contains the optical disc, where the optic nerve is connected. This area lacks cones and rods, thus represents a blind spot in the subject's visual field [8]. From an optical perspective, the retina can be understood as the screen on which the images are formed. It covers the posterior part of the ocular globe, and its radius of curvature is approximately -12 mm. This curvature approximates the ideal optical conditions for peripheral vision where the off-axis rays are focused on the retina.

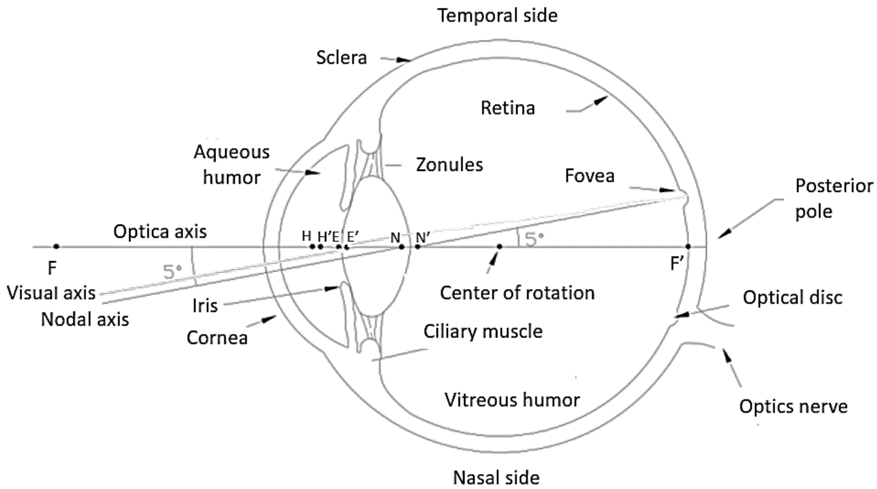

***Figure 1.1** – Schematic representation of the main optical components of the optical system of the eye. The six cardinal points are shown: F and F' are the focal points in the object and image space, H and H' are the principal points in the object and image space, and N and N' are the nodal points in the object and image space. The position of the entrance pupil E and the exit pupil E' are also shown (figure adapted from [8]).*

The optical system of the eye also presents a significant difference with respect to other manmade optical systems, which is that the eye is mostly formed by aspherical surfaces that are not aligned with each other. Several studies have shown that the cornea and lens present asphericities [2, 4]. Additionally, the fovea is decentered 5 deg temporally with respect to the optical axis of the eye, and the lens is often tilted (around 2.8 deg) and decentered (between -0.22 mm and 0.45 mm respectively) with respect to the cornea [1, 9]. Two axes are commonly defined when studying the optical properties of the human eye: the optical axis and the visual axis (also shown in Figure 1.1). The optical axis passes through the center of the entrance pupil (E) and the center of rotation of the eye. The definition of the visual axis can slightly vary between authors, although the most standard is to define it as the ray connecting the fovea with the fixation point [8]. This discrepancy is shown in Figure 1.1 with the nodal and visual axis respectively. The angle deviation between the visual and optical axis is called κ angle.

1.1.2 – Ocular biometry

The measurement of the dimension and the shape of the refractive components of the eye and the distances among them and the retina is known as ocular biometry. Historically, the main application of ocular biometry has been the selection of the intraocular lens (IOL) to be implanted in cataract surgery, where the axial length of the eye is the bare minimum required data [10]. Ocular biometry plays an important role in the diagnosis, monitoring and treatment of various ocular diseases, and it is also a research tool for understanding the ocular growth and ageing processes and the associated development of pathologies such as myopia and presbyopia, among others [11]. The main ocular parameters measured during an ocular biometry test are shown in Figure 1.2. Each of the biometric parameters is explained below.

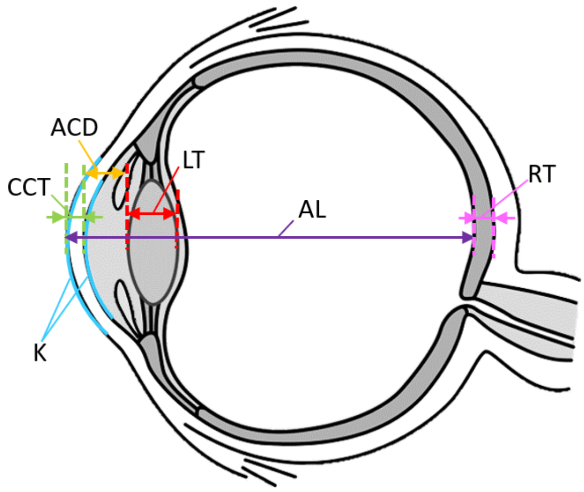

Figure 1.2 *- Schematic representation of the ocular parameters measured during an ocular biometry test: central corneal thickness (CCT), anterior chamber depth (ACD), lens thickness (LT), axial length (AL), retinal thickness (RT), and keratometry (K) [12].*

- **Axial length (AL):**

The axial length of the eye (AL) is the distance between the anterior surface of the cornea and the retina, and it is usually measured along the visual axis of the eye [13]. The axial length of the eye is determined by various factors including age and refractive error. The average axial length of an emmetropic eye is typically around 23 mm in the adulthood. Eyes that are larger than 23 mm are classified as long eyes and usually correspond to myopic eyes where far-away objects are focused in front of the retina, while those with an axial length below 23 mm are classified as short eyes and normally correspond to hyperopic eyes which form the image of far-away objects behind the retina [14-17].

Peripheral AL measurement or off-axis AL is also important in several clinical applications. This measurement is usually performed with the same instrument by rotating the patient's head or the light incidence, or by using 2-D or 3-D whole-eye imaging techniques [13, 18, 19].

- **Cornea: central corneal thickness (CCT) and keratometry (K)**

There are two main biometric parameters of interest in the cornea. On one side, the central corneal thickness (CCT), which is also measured along the visual axis of the eye and has an average value of 0.55 mm, although it has been shown to vary with gender, age and pigmentation phenotypes [20, 21]. On the other side, the spherical curvature of the anterior and posterior surfaces of the cornea, known as keratometry (K), which have an average central radius of curvature 7.8 mm and 6.5 mm respectively [2]. The conical shape of the cornea is also clinically relevant [22].

- **Crystalline lens: anterior chamber depth (ACD) and lens thickness (LT)**

Regarding the crystalline lens, the main parameter is the anterior chamber depth (ACD), which is defined as the distance from the posterior surface of the cornea to the anterior surface of the lens. The anterior chamber is filled with the aqueous humor, a transparent compound with a 98% water content. The ACD is on average around 3.1 mm in emmetropic eyes but it can also vary and it is generally shorter for myopic eyes and larger for hyperopic eyes [15].

The lens central thickness (LT) is also a parameter of interest that ranges between 3.2 mm and 4 mm when it is relaxed, *i.e.,* when focusing a far stimulus at 0 D, and that changes on average less than 0.1 mm per diopter of accommodative demand [23, 24] .

Moreover, the ACD and LT variation during the aging of the eye are related as the ACD tends to decrease as a consequence of the lens thickness increment with age [11, 25].

- **Retinal thickness (RT):**

The retinal thickness (RT) measured at the central macula region is also of interest in retinal diseases. The retina thickness is on average 294 µm and estimated to vary in the periphery of the posterior pole of the eye [7, 26].

1.1.3 – Importance of ocular biometry on diagnosis and treatment of ocular conditions.

The use of ocular biometry for diagnostics and treatment planning requires the measurement of different ocular parameters depending on the ocular condition. In this section we present some of the main ocular conditions that benefit from a precise ocular biometry test: cataract, presbyopia and myopia.

A – Cataract

Cataract is the clouding of the crystalline lens of the eye, generally taking place after the age of 65. Cataract causes severe vision loss affecting daily routines and quality of life due to blurred vision, glare and halos. The World Health Organization (WHO) considers cataract as a priority eye disease as is one of the main causes of blindness worldwide. The treatment for cataract correction is a surgical process where the natural lens of the eye is replaced by an artificial intraocular lens (IOL) to restore the transparency of the lens for a clear vision. Due to the exchange of the crystalline lens, cataract surgery is also a refractive surgery procedure as through the implantation of an IOL with the proper optical power, the patients' refractive error is also corrected. Additionally, the new designs of multifocal IOL produce multiple foci providing vision at multiple distances to prevent the need of glasses for close vision. Cataract surgery is the most frequently performed ophthalmic surgical procedure. There are around 20 million cataract surgeries performed every year worldwide, although they vary among countries because of differences in accessibility to diagnosis, referral, healthcare systems and surgical care [27, 28].

Accurate ocular biometry is essential in the preoperative planning of cataract surgery. It allows to precisely calculate the optical power of the IOL to be implanted, and thus to achieve the desired refractive outcome, *i.e.,* to ensure a focused retinal image. Ideally, if ocular biometry measurements, IOL power calculation, and surgical IOL implantations were perfect, the remaining refractive error after surgery would always be zero.

A precise measurement of the axial length AL of the patient is important for the accuracy of the IOL power formulas, as an error of 1 mm is estimated to induce, on average, a refractive error of 2.7 D [29]. Aside from the axial length, the anterior corneal radius of curvature is among the most important parameters to determine the refractive error, as an error of 1 mm is estimated to induce a refractive error of 5.7 D. Inaccuracies in the measurement of the axial length and keratometry are a significant source of error as they account for 17.0% and 10.1% of the postoperative refractive error, respectively [30]. However, the biggest source of error comes from the inaccuracy of the IOL formulas to predict the postoperative position of the IOL, which contributes to around 35% of the postoperative refractive error. Moreover, choosing the appropriate formula to calculate the optical power of the IOL to be implanted is key especially for eyes that underwent previous corneal surgery or very short/long eyes [12, 28].

During the last decades, new generations of formulas for the calculation of the optical power of the IOL have been developed based on the patients' ocular biometry measurement and the outcome of the performed surgeries. The first generation of formulas used paraxial optics for the IOL power estimation using the power of the anterior surface of the cornea and the axial length of the eye. A second generation of theoretical formulas incorporated a scaling factor depending on the axial length of the patient for the estimation of the effective post-operative lens position [27]. The newer third generation (Holladay, SRK/T, Hoffer Q, Olsen) and forth generation (Barrett, Holladay II and Haigis) of formulas provide considerably more accurate results at the expense of incorporating additional variables. On top of the measurement of the axial length and corneal power of the eye, some of them also include the measurement of the anterior chamber depth and lens thickness, as well as the white-to-white diameter, age, and preoperative refraction of the patient. Each of these third and fourth generation formulas also rely on several constant parameters that can either be provided by the lens manufacturers or adjusted by the surgeon experience depending on the outcome of previous surgeries [27]. Several clinical studies [28, 30-32] have recommended the use of SRK/T and Barrett for long eyes above 26 mm, Holladay for eyes between 22 mm and 26 mm long, and Hoffer Q and Haigis L for very short eye below 22 mm. This difference of formula application as a function of eye length is important due the significant population in each group (up to around 10% according to some studies [33]).

Table 1.1 summarizes the parameters used by the new generation of IOL-power calculation formulas, as well as their preferred case of use as a function of the axial length of the patients.

Table 1.1 – *Number of variables used in each formula together with their best use case (if reported) and their refractive error main biometric correlation [10, 30, 33-35]. AL, CCT, K, ACD and W-W correspond to axial length, keratometry, anterior chamber depth and white-to-white parameter. An X is shown when the IOL power formula uses that variable.*

	Ocular parameter						Num. constants	Best case of use	Refractive error (RE) correlation
IOL formula	CCT	AL	K	ACD	LT	Others: W-W, Age			
Hoffer Q Holladay I (3^{rd} gen.)		X	X				1	Short eyes	AL and ACD
SRK II, SRK/T and T2 (3^{rd} gen.)		X	X				1	Long eyes	AL and K
Haigis (4^{th} gen.)		X	X	X			3	Short eyes	AL and ACD
Olsen (4^{th} gen.)	X	X	X	X	X		1	Long eyes	ACD
Holladay II Barret Universal II (4^{th} gen.)		X	X	X	X	X	1	Long eyes	AL and LT

In summary, optical biometry is considered a fundamental diagnostic tool in the ophthalmic practice for cataract surgery planning, as its measurement is essential for reliable IOL-power calculation and thus IOL selection [12].

B – Presbyopia

Presbyopia is another age-related process that occurs in the crystalline lens. With age there is an increase in lens stiffness preventing the required change in the optical power of the lens to focus on the retina objects at both far and near distances. This loss of the amplitude of accommodation is a process that affects 100% of the population and that becomes noticeable from the age of around 40 or 50, when the amplitude of accommodation of the subject falls below 3 D, affecting people productivity and life quality [36, 37]. With an aging population worldwide, the correction of visual impairment due to presbyopia is becoming of increasing importance. The estimations of presbyopia prevalence show an increment to 1.8 billion people in 2050 from the 1.4 billion in 2020, being predominantly uncorrected in developing areas [38].

The treatment for presbyopia correction aims to restore, at least partially, the functionality of near vision. Different options are available for presbyopia correction, involving both surgical and non-surgical methods which are summarized in Figure 1.3.

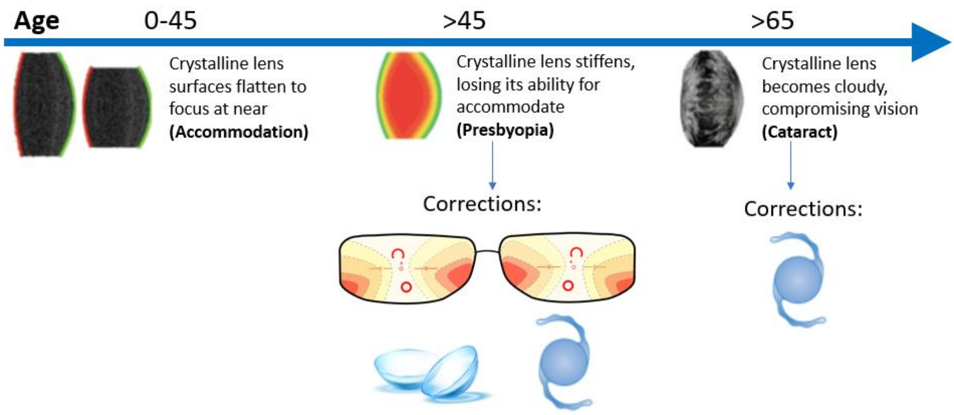

Figure 1.3 *– Timeline representation of the changes occurring to the crystalline lens with aging and the corresponding methods of correction (representation based on the reference [27]). Before the age of 45, the crystalline lens can dynamically change its shape to focus at near and at far distances: accommodation (images on the left are cross section of the lens of an eye viewing far objects (left) and near objects (right)). At around the age of 45, the crystalline lens stiffens and its accommodation ability is significantly reduced: presbyopia (middle image). The corrections for presbyopia to improve near vision are: spectacles (either progressive or monofocal), multifocal contact lenses and the implantation of IOLs. At approximately the age of 65, the crystalline lens is opacified: cataract (right image is an image of a cataractous crystalline lens). The correction for cataract is only the implantation of an IOL to restore clear vision.*

On one side, within the non-surgical options, different near vision aids such as reading glasses, bifocal, progressive addition lenses and multifocal contact lenses can be prescribed. On the other hand, the surgical options include the bilateral implantation of multifocal IOLs, monovision (the correction of each eye for near vision and far vision respectively [39]) or corneal refractive surgery (the use of an excimer laser to compensate the ocular refractive error [40]). The implantation of IOL before cataract development, *i.e.*, when the crystalline lens is still transparent, has become popular to treat presbyopia symptoms although the patient's preference on the presbyopia correction may change with time [41].

C – Myopia

Many eyes have neither the adequate optical properties nor the right dimensions to achieve perfect focus and are affected by refractive errors. When the eye is too long for the combined optical power of the cornea and the crystalline lens, the image of distant objects is formed before the retina. This condition is termed myopia, and results in blurred vision of distant objects. The increase of myopia prevalence in the last few decades has contributed to raising the status of myopia as a major health issue, especially in urban areas in regions such as east Asia, North America and Europe, where around 80-90% of the children at high school level are myopic and 10-20% of them are even high myopes with refractive errors over 6 D. Changes in lifestyle such as the reduction of time that children spend outside seems to be associated with this higher prevalence. Even though myopia is a benign disorder considering that far distance vision can be restored with spectacles, contact lenses and even refractive surgery, the World Health Organization (WHO) has recognized that myopia, if not fully corrected, represents a major cause of visual impairment. In addition, people with high myopia are at a substantially increased risk of potentially blinding myopic pathologies which cannot be prevented by spectacle correction [42].

During childhood, the eye grows considerably, and its optical components grow accordingly to eventually produce a focused image onto the retina while the axial length increases, starting with a hyperopic vision at birth to, ideally, emmetropic vision in adulthood. This process is known as emmetropization. Eye length has been shown to increase from 18 mm at birth to 23 mm by the age of 3 approximately. Several studies have described that during approximately the first year of age, the adjustment is achieved by reshaping the cornea, the most refractive component of the eye, which changes from a radius of curvature of around 5 mm and 4 mm in the anterior and posterior surface of the cornea to 10 mm and 6 mm, respectively. Later, the adjustment is achieved by the change of the power of the crystalline lens. The emmetropic condition is usually stable around 7 years of age, although ocular globe growth may continue until the age of 20. Therefore, the most stable period of the refractive state of the eye is between 20 and 40 years, after growth has ceased and before the aging of lens starts to become clinically relevant [8]. In such a way, the period when myopia is generally developed is the years of early-middle childhood, although significant myopia can also be developed later in the early stages of adulthood [42].

The measurement of ocular biometry parameters is needed to estimate their relative importance on the patient's refractive error. Corneal radius of curvature and vitreous chamber depth (distance between the posterior surface of the lens and the retina) are the parameters contributing the most to the refractive error, while the lens thickness and the anterior chamber depth have shown to have a lower impact. The vitreous chamber depth has been observed to be larger in myopic eyes and shorter in hyperopic subjects, while the corneal radius of curvature has been observed to be, on average, smaller in myopic eyes than in hyperopic eyes [43]. It has been shown that, during a regular growth in the infancy and early childhood period, the axial length increases at a slightly slower rate than the equatorial diameter, but when myopia starts to develop, the axial length increases more rapidly instead. Thus, myopic eyes are larger than emmetropic eyes [44].

As the axial length AL is the biometric parameter that changes the most during myopia development and it is also the parameter with the highest correlation to the refractive status, its control is crucial for achieving normal vision. Therefore, AL is one of the main factors to monitor when studying the arising and control of the refractive error [42]. The goal of myopia control treatments is to reduce the myopia development for avoiding high myopia which, as already stated, entails a risk of developing secondary ocular complications such as degenerative changes in the sclera, choroid and retinal pigment epithelium, cataracts and glaucoma [45]. In order to slow the myopia progression orthokeratology and soft bifocal contact lenses have shown a similar evidence of myopia control slowing the growth of the eye of around 43% and 46% respectively, while under-correction. Progressive or bifocal spectacles have not shown a clinically meaningful reduction of the eye length of children [46].

The mechanisms driving the evolution of myopia are still uncertain and there is a huge interest in the scientific community in determining the causes for such a prevalent refractive error. Ocular biometry is one of the most informative measurements to this end and has been used to understand the myopia development, both on- and off-axis [47, 48].

1.2 – Techniques for ocular biometry measurement

The most common method to measure ocular biometry is the use of ultrasonography or optical interferometry to determine the distance between intraocular structures. The measurement is generally performed at the corneal apex along the visual axis of the eye of a fixating subject. In the last few decades, significant advances in ultrasound and optics-based technology have improved the measurement of the intraocular distances. In this section we aim to present a comparison between these techniques and to describe their presence in the market.

1.2.1 – Ultrasound vs optical biometers

The first technique applied to the measurement of the intraocular distances was the ultrasound (US) A-scan biometry in 1965 [49]. In this technique, a small probe is placed against the eye emitting sound waves in the ultrasound regime. The sound waves propagate through the eye and reflect at each ocular surface due to the elasticity and density change in the media. By knowing the propagation speed and measuring the travel time, the distance travelled by the soundwave is calculated. The precision in the first human tests was not better than 2 mm [50], however, the technique allowed to detect abnormalities, such as tumors, in the scanned eyes through the analysis of the size of the reflected signals.

Ultrasound biometry can be divided in two main modalities: applanation US biometry where the probe is in direct contact with the cornea, and immersion US biometry where a saline solution is placed between the cornea and the probe. These two modalities lead to a systematic difference among them achieving shorter values for all distances measured with applanation US due to the indentation of the cornea when direct contact is applied [17, 51, 52].

In the last decades of the 20th century, laser interferometry was found as a suitable tool to perform biometry measurements equivalent to the US-based A-scan biometry. In 1986, Fercher and Roth proposed for the first time the use of partial coherence interferometry (PCI) for ocular biometry [53]. They performed the first in vivo AL measurement with laser techniques and provided the tools to advance from US biometry to optical biometry [12]. Optical biometers use a similar working principle to US biometer but use light instead of sound waves, since part of the incident light is also reflected at each ocular surface due to the differences in refractive index. Hitzenberger reported the use of PCI for human in vivo axial length measurement with an accuracy of 30 μm in the AL measurements, which compared to the 200 μm achieved with US biometry represents a significant improvement, mostly due to the change in the size of the wave used in the measurement [54]. The use of a shorter wavelength in optical biometry has allowed a more precise measurement of the ocular AL with a precision of 0.012 mm for optical biometers and 0.1 mm for US biometers [55]. The AL measurements on pseudophakic eyes, i.e. with an IOL implanted replacing the crystalline lens, is also more precise with optical biometry since the IOL material has less impact on the AL measurement in optical measurements [12].

Many studies have compared the accuracy and repeatability of US and optical biometry techniques as well as their influence in IOL power calculations [30]. All of them show that the optical measurements are comparable to the US measurements in terms of the accuracy and reproducibility of the IOL power calculation. In general, within the US techniques, immersion US has been found to be the more similar to the optical methods [30]. Moreover, a subtle improvement in the prediction of the patient refractive error has been demonstrated with optical biometry [56]. The change in the operating principle between US and optical biometry also leads to additional differences between both techniques.

The main differences have been summarized in Table 1.2 [57, 58], where a list of their advantages and disadvantages is shown. Different values of ocular axial length can be the result of the different technologies used to measure it as, while US biometry measures the AL along the optical axes of the eye, optical biometry measures AL along the visual axis of the eye. In addition, the layer of the retina that reflects the signal is also different. While ultrasound biometers measure the axial length from the cornea to the internal limiting membrane, optical biometers measure the back reflection from the retinal pigment epithelium, i.e. a deeper position in the retina. Thus, optical biometers are expected to measure a longer axial length than the acoustic based ones. Importantly, the photoreceptor plane lays in between the two measured layers [12, 59].

***Table 1.2** - Comparison of US and optical biometry techniques: advantages and disadvantages [57, 58].*

	Ultrasound Biometry	Optical biometry
Wave type	Sound	Light
Ocular measuring axis	Optical axis of the eye.	Visual axis of eye during subject's fixation.
Last surface reflected	Inner limiting membrane	Retinal pigment epithelium
Measurement procedure	Contact for applanation technique. Non-contact for immersion technique.	Non-contact
Advantages	• Well established method • Can perform in cases of opaque media.	• Higher precision. • Non-invasive and more comfortable • Faster measurement.
Disadvantages	• Time consuming exam. • More skilled examiner required. • Depressing the cornea when the applanation technique is used. • Risk of infection.	• Inability to measure through dense cataracts, and serious corneal pathologies. • Higher cost of the equipment.

In summary, optical biometry technique has several advantages over ultrasound biometry: being non-contact, acquiring more precise measurements and relying less on the clinician's experience [32]. Optical biometers have become the gold standard for eye care due to their advantages, shifting in the early 2000s the standard of care in biometry from US to optical biometry (see Figure 1.4) [49, 58]. However, the main limitation of optical methods are: 1) the inability to measure the axial length in approximately 10% of eyes, typically those with dense opacities such as highly cataractous eyes, where US-biometry is required instead, and 2) the fact that they are more expensive and less portable than ultrasound ones [30, 32].

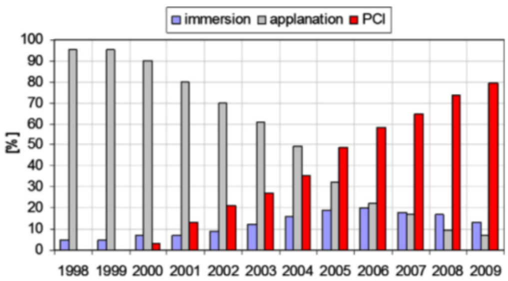

***Figure 1.4** - Use of immersion ultrasound (purple), applanation ultrasound (grey) and optical biometry technique based on partial coherence interferometry (PCI) (red) in the USA since 1998 until 2009 [49].*

1.2.2 – Low coherence interferometry (LCI)

Optical biometers are based on the principle of low coherence interferometry (LCI). A Michelson interferometer, schematically drawn in Figure 1.5, splits a light beam from a broadband light source with a central wavelength λ_c into two components with a beam splitter. We will call one of the beams the reference beam E_r, and the other the sample beam E_s. Each of them is reflected either at a mirror in the reference arm E_r', or at the sample surfaces with the specific reflectivity factor of the sample tissue E_s', and the back-reflected light from both beams is recombined at the beam splitter and directed towards the photodetector.

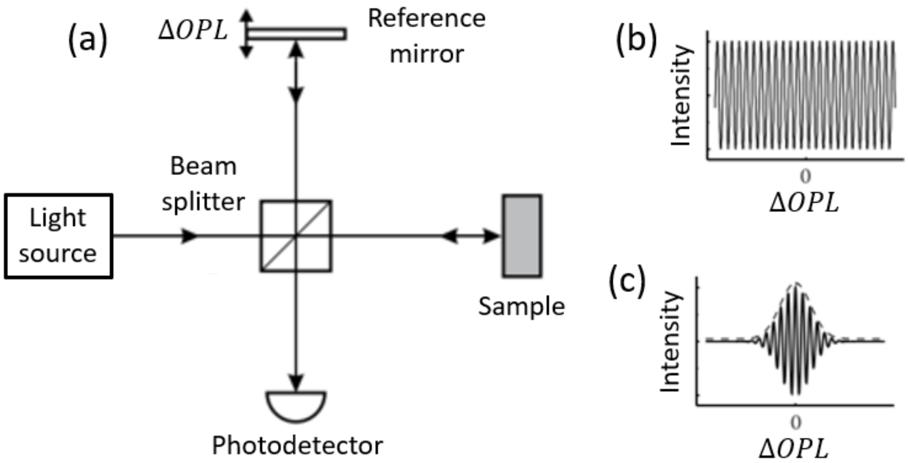

Figure 1.5 – *Representation of the working principle of LCI from [60]. (a) Drawing of a simple Michelson interferometer. (b) Example of an interferogram of the first sample surface at the photodetector if a high-coherence light source is used. (c) Example of an interferogram of the first sample surface at the photodetector if a low-coherence light source is used.*

The light intensity recorded at the photodetector I_D can be described by the interferometer equation, see Equation (1), where I_r' and I_s' are the mean DC intensities returning from the reference and sample arms of the interferometer, and τ sets the optical time delay between the reference light beam and the sample beam. Thus, the interferometric signal presents two terms: 1) a DC term which can be interpreted as a background of constant intensity and 2) a carrier oscillating term which is the interferogram that carries the information about the sample structure. The distance "gating" ability, i.e., the spread of the envelope of the interferogram term depends on the temporal coherence characteristics and the Fourier Transform of the power spectral density $G(\tau)$ of the light source, which acts as the envelope of the interferogram.

$$\begin{aligned} I_D(\tau) = \langle |E_d|^2 \rangle &= \frac{1}{2}(I_r' + I_s') + \mathrm{Re}\{\langle E_r'^{*}(t+\tau)E_s'(t)\rangle\} \\ &= \frac{1}{2}(I_r' + I_s') + |G(\tau)| \cos\left(\frac{2\pi c}{\lambda_c}\tau + \phi(\tau)\right) \\ &= \frac{1}{2}(I_r' + I_s') + |G(\tau)| \cos\left(\frac{2\pi}{\lambda_c}\Delta OPL + \phi(\tau)\right) \end{aligned} \tag{1}$$

If the reference mirror is axially moved, the time delay $\tau(t)$ between both arms varies, and so does the optical pathlength difference ΔOPL. Thus, an optical axial scan or A-scan can be generated by moving the reference mirror over time while the light intensity is recorded in the detection arm by a photodetector [60, 61].

If a high spatial and temporal coherence source is used, the envelope of the interferogram $G(\tau)$ tends to 1 and the interferogram presents a constant fringe amplitude as shown in Figure 1.5(b), leaving ambiguity in the position of the sample features with respect to the reference arm length, i.e., no temporal "gating" effect. However, if a low temporal coherence source is used, the interferogram fringe amplitude is modulated by the complex degree of coherence of the light field and thus the ambiguity is eliminated, generating the coherence gate as shown in the interferogram at Figure 1.5(c). If a Gaussian power spectral density distribution $G(\tau)$ of the light source is assumed, the coherence gate and thus the full width half maximum (FWHM) of the Gaussian signal envelope l_c follows Equation (2) as a function of the central wavelength λ_c and bandwidth $\Delta\lambda$ of the spectrum of the light source. From Equation (2) we can conclude that sources with a broader spectrum are desirable as they produce interference patterns with shorter temporal and, hence, spatial extent, thus providing a higher axial resolution [60, 61]. Near-infrared (NIR) light sources are often used for LCI. Among them, superluminiscent diodes (SLEDs) are preferrable to multimode laser diodes MMLDs, as they present a broader bandwidth.

$$\mathrm{l_c} = \frac{2\ln 2}{\pi}\frac{\lambda_c^2}{\Delta\lambda} \tag{2}$$

The analysis of the spectrum of a bandlimited light source based on a first-order Taylor expansion around the center frequency, allows to obtain the phase delay $\Delta\tau_p$ and the group delay mismatch $\Delta\tau_g$ as shown in Equation (3) and Equation (4) where v_p is the phase velocity of the center frequency of the light source and v_g is the group velocity. From Equation (3), one can convert the measurement over time at the detector to an optical pathlength variation between the two arms of the interferometer.

$$\Delta\mathrm{\tau_p} = \frac{2\Delta OPL}{v_p} \tag{3}$$

$$\Delta\mathrm{\tau_g} = \frac{2\Delta OPL}{v_g} \tag{4}$$

While for deeper tissue penetration into the retina past the photoreceptor layer, NIR sources are preferable to visible light sources, the main limiting factor when using NIR light in ocular tissue is the absorption of it on the way to the retina, as it has a very similar curve to the water absorption curve. Local minimums of the absorption curve, located at 850 nm and 1050 nm, are used to avoid the loss of signal due to absorption since the beam passes twice through the media [62]. Figure 1.6 shows the transmittance of each ocular media components, showing in this case, the maximum peaks at 850 nm and 1050 nm. Assuming the vitreous contains approximately 90% of water and the average human eye length is approximately 25 mm, one can estimate the losses for an OCT signal at the wavelengths of 800 nm and 1060 nm where the absorption coefficients of the water are 0.0023 mm^{-1} and 0.015 mm^{-1} respectively. This results in a reduction of the detectable light signal from the retina about 88 % and 25 % respectively [63]. On the other hand, emission in the near infrared is desirable because of the low visibility of the measurement beam facilitates the measurements in subjects.

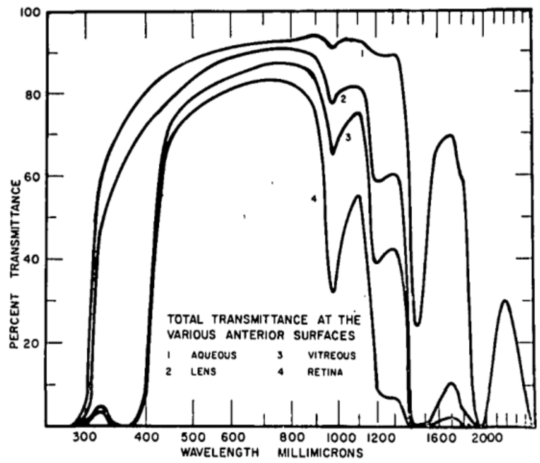

Figure 1.6 *– Transmittance through each of the ocular media of the eye as a function of the illumination wavelength (figure 7 from [62]).*

In order to use LCI for in vivo imaging, it is especially important to follow laser safety regulations to avoid unreversible damage of the retina or other ocular media as the wavelength bands typically used are either barely visible for a human eye for the 800 nm regime or totally imperceptible for the 1050 nm band. For OCT imaging, the American National Standards for Safe Use of Lasers (ANSI) widely used as a reference, defines the maximum permissible exposure (MPE) as 10 times lower than the radiant energies that would damage the retina, being the last expressed as the 50% of the probability of generating a minimum visible lesion. The MPE calculated for typical LCI wavelength illumination are calculated assuming: a collimated light beam covering a 7 mm entrance pupil diameter, an illumination time larger than 10 s and a beam spot diameter on the retina of around 20-30 μm. Under this assumption, the MPE as a function of the most commonly used wavelength bands is 0.56 mW for a 780 nm wavelength, 0.73 mW for an 840 nm wavelength and 1.93 mW for 1050 nm wavelength. Thus, with longer wavelength illumination, the MPE increases, in part due to the increase in the absorption coefficient of the ocular media [63-65].

The measurement of several consecutive A-scans by transversally displacing the sample beam over the sample allows to obtain an optical B-scan or OCT cross sectional image [60].

<u>A – TD-OCT: OLCR and PCI systems</u>

The interferometer system to obtain axial scans of the eye described so far is known as time-domain (TD)-OCT, with an axial resolution of approximately l_c and an axial scan range equal (in optical pathlength) to the range that the reference mirror has been axially displaced. In such a case, it is enough to obtain the envelope of the interferometric signal with time, as the position of the signal peaks already provides the location of the sample surfaces. If the eye is scanned with a TD-OCT system, each of the interfaces of the eye would generate a peak, allowing then a measurement of the intraocular distance between the eye components [60].

TD-OCT biometry systems can be classified in two main categories depending on the LCI configuration: optical low coherence reflectometry (OLCR) [18, 66, 67] schematically represented in Figure 1.7(a), and partial coherence interferometry (PCI) [68-70] schematically represented in Figure 1.7 (b).

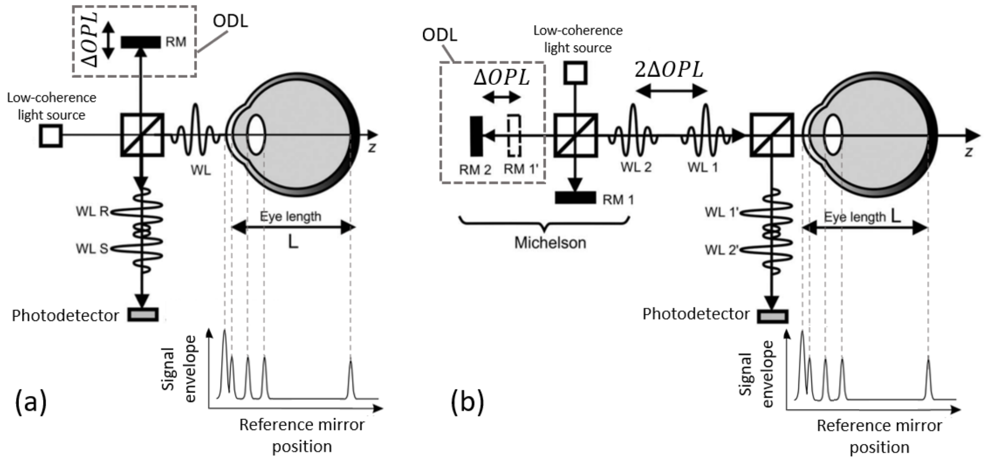

Figure 1.7 *– Schematic of two TD-OCT implementation (modified figure from [54]). (a) An optical low coherence reflectometry OLCR system where a single sample beam propagates through the eye and interferes at the photodetector with the reference beam. (b) A partial coherence interferometry PCI system were a dual-beam, WL1 and WL2, delayed between each other, propagate through the eye and get detected at the photodetector after being reflected by the cornea and the retina.*

While OLCR is a similar implementation to the Michelson interferometer presented in Figure 1.5 [71], a PCI system involves the propagation through the eye of two light beams with a variable delay between them in a common-path interferometer configuration. In such a case, the two beams are reflected at the cornea and the retina generating a constructive interference in the photodetector when the optical pathlength difference ΔOPL between both beams is equal to the axial length of the eye; i.e. when the corneal reflection of one of the beam has travelled the same optical pathlength as the retinal reflection of the other beam, thus having the cornea acting as a reference [54]. Hence, the PCI implementation presents the advantage of eliminating any influence of longitudinal eye motions during measurement as the axial length is directly measured through the interference between a reflection from the cornea and another from the retina. However, it also presents the disadvantage of a more complex interferometer setup requiring two beam splitters.

In any of these cases, the optical pathlength (OPL) of either the reference arm in an OLCR system or of one of the dual beams in a PCI system has to be varied with respect to the remaining interferometric beam in order to measure all the intraocular distances of interest. The component that allows this optical pathlength variation is known as optical delay line (ODL) and it is the component determining the axial range of scan achievable in any TD-OCT system. The scanning speed of the ODL, also has an effect on frequency of the interferometric signal recorded by the photodetector, thus defining the requirements of the photodetector and digitizer to be used.

The variation of the OPL by the ODL generates a Doppler shift of the interferometric signal. The center frequency f_o and the bandwidth Δf of the interferometric signal of the detector can be expressed, as shown in Equations (5) and (6), as a function of the scan speed phase delay V_ϕ and of the scanning group delay V_g respectively. Thus, the phase delay scan speed and the scanning group delay are defined by the derivative over time of the previously presented phase delay $\Delta\tau_p$ and group delay $\Delta\tau_g$ (see Equations (3) and (4)) [72].

$$\mathrm{f}_0 = \frac{V_\phi}{\lambda_0} \; where \; V_\phi = \frac{d\,\Delta\tau_p(t)}{dt} \tag{5}$$

$$\Delta f = \frac{\Delta\lambda \mathrm{V_g}}{\lambda_0^2} \; where \; V_g = \frac{d\Delta\tau_g(t)}{dt} \tag{6}$$

Different methods and devices to induce an optical pathlength difference for biometry measurements have been proposed. They can be classified in four main categories: 1) methods based on the linear translation of retroreflective elements, 2) methods based on rotating an optical element, 3) methods based on optical fiber stretchers and 4) methods based on generating a group delay using Fourier domain optical pulse shaping technology, or Fourier-Domain Optical Delay Lines (FD-ODL) [72]. A further explanation of different types of optical delay lines will be presented in the introduction of Chapter 3.

The main advantage of TD-OCT biometry systems is the easy scalability to scan large axial ranges they present, allowing to achieve a whole axial scan of the eye, without the signal roll-off with distance issues that many faster and more sensitive Fourier Domain (FD)-OCT systems have. The main drawback is that they usually involve mechanical movements of some of the components of the ODL limiting the scan velocity up to a few kHz. Thus, while a TD-OCT system is enough to perform a 1-D axial scan, in vivo 2-D cross-sectional OCT images with this technique are highly limited due to eye movements.

B – FD-OCT: SD-OCT and SS-OCT systems

The scan speed limitation of TD-OCT systems is largely overcome by FD-OCT systems. FD-OCT systems take advantage of the Fourier relationship between ΔOPL and the light amplitude as a function of the wavelength $E(\lambda)$. By detecting the spectral intensity distribution of the interferometric signal and performing the inverse Fourier transform of the spectral amplitude, a depth profile of the sample interfaces can be obtained without requiring the axial displacement of a reference mirror [60]. Within this technique, two different approaches have been developed: spectral domain (SD)-OCT and swept source (SS)-OCT. A schematic representation of a SD-OCT and a SS-OCT system is presented in Figure 1.8(a) and (b), respectively.

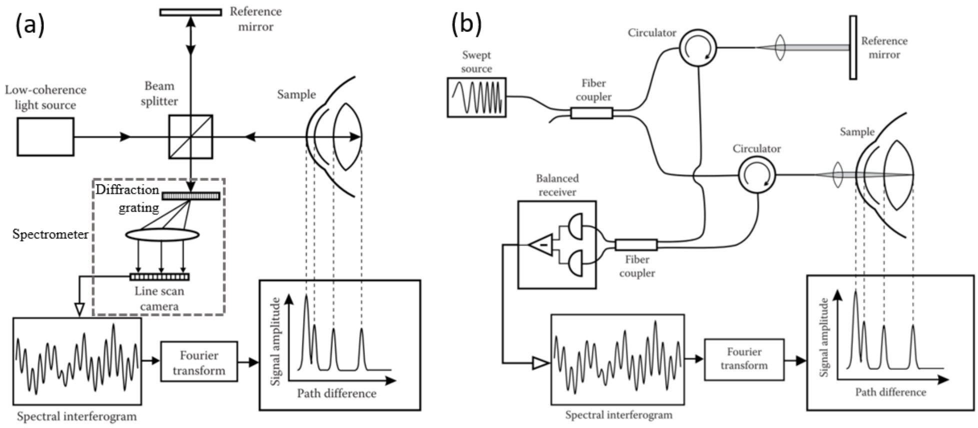

Figure 1.8 - *Schematic of two FD-OCT implementations (modified figure from [60]). (a) A SD-OCT system where a spectrometer is used instead of a photodetector for the spectral interferometric signal acquisition. (b) A SS-OCT system where a swept source laser is used instead of a superluminiscent light emitting diode SLED to acquire the spectral information in time at the photodetector.*

The light source and the interferometer setup between a TD-OCT and a SD-OCT remain the same. However, in the case of a SD-OCT system the ODL used in the TD-OCT system is substituted by a static mirror and the single photodetector by a spectrometer comprising a diffraction grating, that spatially disperses the interfering light beam, and a lens to focus each spectral component onto a line camera. The frequency of the spectral fringes of the recorded interferogram corresponds to the measured ΔOPL . Simultaneously detecting all depths allows a faster acquisition rate than the TD-OCT systems, which ranges between 20 and 40 kA-scans/s for actual commercial systems [60]. In SD-OCT systems, the axial scanning range is determined by the resolution of the spectrometer, hence it is directly proportional to the number of pixels of the line camera and inversely proportional to the light source bandwidth $\Delta\lambda$. The axial resolution is also inversely proportional to $\Delta\lambda$ (see previous Equation (2)), however, a smaller value of the axial resolution means a higher resolving power. Thus, there is a trade-off between the axial resolution and the scan range as increasing the light source bandwidth $\Delta\lambda$ is beneficial to improving the axial resolution but it also implies the disadvantage of a reduced scan range (for the same line camera) [73]. The signal roll-off with depth of these systems is determined by the spectrometer pixel size, the spot size for each wavelength component, and the spectrometer spectral resolution itself and, while the axial scan range is usually limited to the range of 5-6 mm, the signal roll-off with depth becoming important even before the full range. To achieve whole-eye imaging of the eye to perform a complete biometry test, a movable stage or the combination of several reference arms are needed to axially adjust the zero-delay scan position [74, 75].

In a SS-OCT biometers, the spectrometer is substituted by a point detector and the superluminiscent light emitting diode (SLED) by a swept source laser (SS) which is a tunable wavelength source with a narrow instantaneous linewidth and a center wavelength that changes rapidly. In this case, the point photodetector is used to detect the interference created by each wavelength of the swept source in time. A Mach-Zehnder interferometer and a dual balanced detector is usually preferred in these systems to avoid coupling of noise from the light source. The axial scan range is determined by the digitizer sampling frequency, and it is possibly limited by the signal roll-off with depth caused by the finite instantaneous linewidth of the swept source and the bandwidth of the detector [60]. While SS-OCT system can provide A-scan rates up to a few MHz [76], the majority of commercial SS-OCT biometers use A-scan rates only up to 3 kHz, as A-scan rate is also inversely related to the axial scan range (all else in the system being equal).

Table 1.3 summarizes the advantages and disadvantages of each of the three main OCT imaging techniques presented so far.

Table 1.3 *– Advantages and disadvantages of the three main OCT imaging techniques: TD-OCT, SD-OCT and SS-OCT.*

<table>
<tr><th rowspan="2"></th><th rowspan="2">TD-OCT</th><th colspan="2">FD-OCT</th></tr>
<tr><th>SD-OCT</th><th>SS-OCT</th></tr>
<tr><td>Advantages</td><td>• Allowing larger scan ranges without signal roll-off.
• Avoiding duality between FT conjugate images.
• Lower cost than FD-OCT.</td><td>• Fast A-scan rates.
• 2-D cross sectional image.
• Low-cost designs have been shown [77].
• Higher sensitivity than TD-OCT.</td><td>• Long axial scan range.
• Fast A-scan rates.
• 2-D cross sectional image.
• Higher sensitivity than TD-OCT.</td></tr>
<tr><td>Disadvantages</td><td>• Low A-scan rates (< 1kHz).
• 1-D axial scan.
• Lower sensitivity than FD-OCT.</td><td>• Short axial scan range.
• Strong signal-roll off with depth.
• Ambiguity of dual FT conjugate images.</td><td>• Mostly high-cost.
• Ambiguity of dual FT conjugate images.</td></tr>
</table>

Both FD-OCT techniques, SD-OCT and SS-OCT present a clear advantage of faster scan speeds than TD-OCT systems, making them suitable for acquiring cross-sectional images of the anterior or the posterior segment of the eye when a scanner system is incorporated in the sample arm. However, they are either limited to short axial ranges in the case of SD-OCT or must use high-cost components in the case of SS-OCT, especially when long coherence lengths (i.e., low signal roll-offs with depth) are required, while TD-OCT systems can be implemented at a lower cost and can be scaled to achieve a long axial scan range. An exception has been recently proposed [78], with the use of inexpensive thermal tuning instead of the standard expensive MEMS-based cavity tuning of vertical cavity surface emitting lasers (VCSELs). However, at the time of the writing of this thesis, this option was still under development and the authors were unaware of its potential use for low-cost ocular biometry.

1.2.3 – Commercial optical biometers

Since the first demonstration of low coherence interferometry for ocular biometry, OCT-based optical biometers have made their way into the ophthalmology market using different implementations of the OCT alternatives described above. Many studies have reported the reproducibility and accuracy of different optical biometers as well as the comparison between the results with devices from different manufacturers when measuring the main ocular biometric parameters: axial length (AL), corneal radius of curvature (K), anterior chamber depth (ACD) and lens thickness (LT) [55].

Table 1.4 summarizes the optical techniques used in the main commercial optical biometers, together with the ocular parameters they measure and the measurement resolution if available. While the intraocular distances of the eye (CCT, AL, ACD, LT) are measured with different OCT techniques, optical biometers often exploit other techniques to acquire the radius of curvature of the cornea. The different technologies used to measure the curvature of the corneal surfaces are reflection-based methods, such as Placido-ring topography or keratometry to obtain the topography of the anterior surface of the cornea (indicated in Table 1.4 as Placido disc and automated, video and dual-zone keratometry), Scheimpflug imaging, used to study the shape of the cornea [79, 80], and anterior segment 2-D OCT for accurate measurement of the radius of curvature of the posterior surface of the cornea. However, patient's motion artifacts during the data acquisition affect all of those techniques [34, 55].

As can be observed in Table 1.4, the two main categories used in optical biometers are either TD-OCT in its two possible implementations (partial coherence interferometry PCI and optical low coherence reflectometry OLCR) and SS-OCT systems. [81]. The two main TD-OCT biometer are IOL Master 500 (Carl Zeiss), the first optical biometer in the market, and the Lenstar LS 900 (Hagg-Streit). When comparing them, three main differences are found. In the first place the optical delay lines (ODLs) used are different. While IOL Master 500 uses a system to axially displace a reflective component actuated by a stepper motor with leadscrews [69, 82, 83], Lenstar LS 900 rotates a transparent cube with reflective corners [13, 84, 85]. In terms of axial speeds and scan ranges, the speed of the leadscrew mechanism can reach up to 70 mm/s, resulting in full eye biometry scan at frequencies below 2 Hz, while with a cube rotation the frequency increases to 3.2 Hz resulting in 12.8 A-scans per second as multiple A-scan are performed at each cube rotation [18]. The axial scan range in the latter case is approximately 10 mm. However, a detour unit [13] based on two polarizing beam splitters, allows to replicate the 10 mm scan window at a distance of roughly 23 mm from each other to cover both the anterior and posterior segments (for a more detailed explanation of it go to Chapter 2). The corresponding axial scanning speed is therefore approximately 420 mm/s. This speed is ultimately limited by the size of the rotating cube and the rotational frequency it can be imparted to it. Higher speeds are required to minimize patient's motion artifacts, affecting the measurement precision, especially in OLCR. Secondly, the type of the light source of the two biometers employ is different. The IOL Master 500 biometer uses a multimode laser diode (MMLD) with a spectrum with discrete spikes centered at 780 nm and a 3 nm bandwidth for each spike, while the Lenstar LS 900 uses a superluminescent light emitting diode (SLED) centered at 820 nm with a 25 nm bandwidth. As mentioned before, the MMLD presents the disadvantage of secondary peaks in the interferometric detection, not present in the SLED. Lastly, the interferometer setup is also different, with a common path PCI for the IOL Master 500 and an OLCR interferometer for the Lenstar LS 900 [31, 86, 87].

Table 1.4 – *Comparison of the optical techniques and ocular biometric parameters measured by commonly used commercial optical biometers. Data obtained from literature [34, 88, 89] and manufacturer brochures, when available. AL, CCT, K, ACD and W-W correspond to axial length, keratometry, anterior chamber depth and white-to-white parameter. An X is shown when the instrument provides that variable. The axial technologies PCI, OLCR, SD-OCT and SS-OCT correspond to partial coherence tomography, optical low coherence tomography, spectral domain OCT and swept source OCT respectively.*

Device (Company)	Optical technique		Ocular biometrical parameter					
	Axial technology	Keratometry technology	AL	CCT	K	ACD	LT	W-W
IOL Master 500 (Zeiss)	PCI	Automated keratometry	X 10 μm	-	X 10 μm	X 10 μm	-	X 0.1 mm
AL-Scan (Nidek)	PCI	Automated Keratometry	X 10 μm	X 1 μm	X 10 μm	X 10 μm	-	X 0.1 mm
Pentacam AXL (Oculus)	PCI	Scheimpflug imaging	X	X	X	X	X	X
Lenstar 900 (Haag-Streit)	OLCR	Automated Keratometry	X 10 μm	X 1 μm	X 10 μm	X 10 μm	X 10 μm	X 10 μm
Galilei G6 ColorZ (Ziemer)	OLCR	Scheimpflug imaging and Placido disc	X 25 μm	X 2 μm	X 0.1 D	X 34 μm	X 34 μm	X
Aladdin (Topcon)	OLCR	Placido-disc	X	X	X	X	X	X
Mirricon (Clearsight)	OLCR	Purkinje imaging	X	X	X	X	X	-
REVO NX (Optocol)	SD-OCT	Topography OCT	X 5 μm	X	X	X	X	X
HP-OCT (Cylite)	SD-OCT	SD-OCT	X	X	X	X	X	X
IOL Master 700 (Zeiss)	SS-OCT	Telecentric keratometry	X 10 μm	X 1 μm	X 10 μm	X 10 μm	X 10 μm	X 0.1 mm
OA-2000 (Tomey)	SS-OCT	Placido-disc	X	X	X	X	X	X
Argos (ALCON Movu)	SS-OCT	Video keratometry	X 10 μm	X <10 μm	X 0.13 D	X 10 μm	X 20 μm	X 60 μm
Anterion (Heidelberg)	SS-OCT	SS-OCT	X	X	X	X	X	X
EyeStar 900 (Haag-Streit)	SS-OCT	Dual zone keratometry	X 10 μm	X 1 μm	X 0.01 D	X 10 μm	X 10 μm	X 10 μm

The newest biometer from Carl Zeiss is the IOL Master 700, which is a SS-OCT biometer with a central wavelength of 1050 nm. The higher wavelength enabled to reduce measurement failures from 6.4% for the IOL Master 500 to 0.6% for the IOL Master 700, as the latter's higher wavelength penetrates deeper in dense cataracts [90]. A similar advantage in dense cataract has also been observed when comparing the IOL Master 700 with the REVO NX SD-OCT system, as the REVO NX also uses a SLED centered at 830 nm with a 25 nm bandwidth [34, 88].

The different LCI technique applied at each case also implies the fact that different assumptions in the refractive index are required between parameters and systems. While IOL Master 500 uses an average group refractive index of 1.3549 as is not able to measure all intraocular distances, the Lenstar LS 900 uses different refractive indices for each ocular media estimated to be 1.340, 1.341, 1.415 and 1.354 for the cornea, humor vitreous, crystalline lens and average overall eye respectively [87].

1.3 – Ocular conditions prevalence in low resource and remote settings

Despite the significant progress in ocular biometry during the last decades, ocular diseases such as cataract and myopia remain the main cause of blindness worldwide with reported inequality between high-income and low-income countries. Cataracts account for about 50% of all cases of blindness worldwide, although the number of blind people due to cataract has substantially decreased by 11.4% from 1990 to 2010, due to the rise in the number of surgeries performed worldwide [91]. However, differences between countries have been reported as, while cataract is responsible for over 50% of blindness in low-income countries, it is only responsible for 5% in developed countries [28].

Regarding cataract surgery and presbyopia treatment, the lack to facilities, equipment and expertise, together with financial barriers, are reported as the major barriers to access surgical care in developing areas [92]. For example, in rural areas of China, a cataract surgery costs twice the average annual income [28]. Inaccessibility to healthcare facilities and the need to travel to a hospital or eye care center is also a great impediment as most of cataract-blind people live in rural areas, while ophthalmologists and hospitals are in urban areas [93].

Attempts to reduce the cost of cataract surgery have been made. According to India's National Program for Control of Blindness, cataracts account for 62% of avoidable blindness cases. Cataract surgery has a high cost in Western countries (2000 €/eye in Spain; 3540 USD/eye in the USA on average), but in some underdeveloped countries, local companies (such as Aurolab in India) manufacture low-cost intraocular lenses and medical supplies, which has allowed the cost of these surgeries to decrease to 49-124 USD/surgery [94, 95].

Another important barrier are cultural aspects, beliefs and attitudes such as family and gender roles and fear [96, 97]; as well as the lack of community services to support the families and the misunderstanding of the need for the surgery are also relevant for cataract prevalence in low-resource settings even though cost of cataract surgery has decreased [98].

The use of optical biometer in established healthcare centers or eye departments with uninterrupted power supply is clearly advantageous. However, the use of optical biometers is still a limited resource in settings without a reliable supply of electricity, where instead systems operated with portable batteries are used and thus ultrasound biometry and keratometry devices have been used [32, 93, 96, 98]. In addition, the availability of portable equipment would also allow surgeries or preoperative evaluations to be performed even in remote locations.

Therefore, cost and transportability are important factors in remote and low-resource settings, where the prevalence of cataracts is higher [99] and accessibility to ocular biometry, especially the more accurate optical biometry, is currently limited [92, 100]. However, FD-OCT biometers remain a lot more expensive than TD biometers, with sale prices exceeding 40 kUSD [81, 101, 102]. The high-cost components in FD-OCT biometers and the limited transportability of TD-OCT biometers, results in reduced accessibility to optical biometers in remote and low-recourse setting [103-105] where the visual impairment due to cataract is higher [106].

1.4 – Towards low-cost and portable ocular biometry

In the last years there have been several attempts to develop low-cost and portable OCT systems [107, 108]. SD-OCT systems presented a good opportunity for cost reduction as the SLED light source can be relatively cheap, and the spectrometer is amenable to redesign for lower cost. Customization of the spectrometer indeed enabled low-cost SD-OCT systems for either anterior or retinal imaging applications [77, 109]. A self-imaging SD-OCT system for retinal imaging was developed for remote home monitoring and validated in clinical trials to determine the progression of age-related macular degeneration [110]. All-in-one SD-OCT devices have also been developed by customizing both the spectrometer and the SLED drive to prevent optical performance degradation when transporting the system [111]. However, such devices have only been shown in applications were either the anterior or the posterior segment of the eye is imaged but not for ocular biometry, probably because the limited axial scan range prevents the measurement of the axial length of the eye [16]. On the other hand, the development of low-cost swept source lasers has also been recently investigated [112, 113]. Even though efforts have been made to reduce their cost [77, 109, 113, 114], FD-OCT biometers (and their components) remain a lot more expensive than TD biometers.

In terms of miniaturization and portability of OCT systems, several efforts have also been made in the implementation of compact handheld device that attempt to avoid the need of a chin rest components and allow bedside use of the devices [115, 116].

Thus, TD-OCT biometers have the opportunity to make optical biometry more accessible. There have been attempts to develop a 10 USD ultra low-cost TD-OCT system by using the voice coil present in a typical CD-ROM pickup unit and when integrating it in a multi-reference arm configuration to perform fast axial scans [117]. This approach has also been combined with a smartphone-based detection system to allow further cost reduction [118]. However, such system only allowed to performed axial scans up to 2 mm, thus preventing its use in ocular biometry. Nevertheless, other strategies to make low-cost TD-OCT biometers through careful design of a long-range ODL, and to increase the measurement precision (repeatability), via fast scans and motion artifact control (e.g., corneal centration and visual fixation checks), are still possible, and will be part of the aim of this thesis.

1.5 – Motivation

Age related ocular diseases such as presbyopia, cataract and myopia, have become a matter of increasing concern in the last several years due to their rising global prevalence. Many strategies have been developed to correct these ocular conditions and to reduce the patient's visual impairment. However, strategies to allow the selection of the most adequate and customized solution for treatment planning are still under development.

OCT technology has emerged as the gold standard in a wide range of applications involving ocular biometry and whole-eye imaging, substituting in many cases ultrasound technology. A variety of OCT systems have been developed and numerous studies have demonstrated the advantages of OCT technology. In fact, the use of OCT-based biometers is now widely prevalent in the clinical practice due to its high precision measurements and the improvement in patient's comfort. OCT has also facilitated the comprehensive visualization of the entire eye. The ability of OCT to provide high-resolution cross-sectional images of ocular structures has revolutionized ophthalmology, enabling clinicians to accurately measure and assess various ocular parameters, diagnose diseases, and monitor treatment outcomes. The widespread acceptance and integration of OCT into clinical settings highlights its transformative impact on ocular imaging and its crucial role in improving the quality of eye care.

Despite the significant advancements, access to OCT technology remains limited in low-resource and remote settings, as the available systems are expensive, and in some cases non-compact and heavy to transport. Various attempts have been made to develop portable and affordable OCT systems to enhance accessibility in specific applications such as anterior segment or retina imaging, independently. However, none of these systems have yet been capable of performing comprehensive ocular biometry. The challenges lie in achieving a balance between portability, cost-effectiveness, and the ability to provide a complete assessment of the eye. Further research and innovations are needed to overcome these limitations and enable comprehensive ocular biometry using portable OCT systems.

This thesis is devoted to such research and innovations. The setting for these scientific and technology breakthroughs is the Visual Optics and Biophotonics (VioBio) laboratory of the Instituto de Óptica – CSIC and the company 2EyesVision, S.L. The significant knowledge accumulated over time in the VioBio laboratory of the Instituto de Óptica – CSIC allows for a comprehensive examination of OCT from different perspectives. Additional know-how in OCT for ophthalmic applications and scanning technology was also brought by the International Centre for Translational Eye Research (ICTER) in Warsaw, Poland. The incorporation of complementary technologies such as the use of electro-tunable lenses, with which both the VioBio research group and 2EyesVision have excelled in the last few years, have the potential to reduce costs and simplify processes, providing additional functionality that is not present in current commercial biometers. Moreover, both VioBio and 2EyesVision gathered broad knowledge on optical design and expertise on developing disruptive technology for presbyopia and cataract treatment planning.

1.6 – Open questions

In this thesis, we have conceptualized and designed optical systems, as well as implemented and validated computationally and experimentally different solutions to answer the following open questions:

1. **Is it possible to develop a low-cost axial scan system to precisely perform ocular biometry measurements? How can the cost of a frequency domain optical delay line be reduced?** Currently**,** optical delay lines used in optical biometers typically involve the displacement or rotation of bulky components. Frequency domain optical delay lines do allow to perform axial scans without displacing any component but, until now, only by using expensive galvanometric mirror scanners.

2. **Is it possible to implement a versatile system to image both the anterior and the posterior segment of the eye, avoiding the use of different components for each ocular segment, at a reduced cost? Can tunable lenses be used to eliminate the need of galvanometric scanners and to determine the focusing properties and the direction of the OCT beam?** Electro-tunable lenses have been widely used in Viobio Lab and 2EyesVision to simulate different profiles of intraocular lenses based on the temporal multiplexing principle, taking advantage of their fast ability to change power. They have also been used to steer a beam and are becoming a relatively inexpensive and versatile optical element.

3. **Is it possible to develop an optical see-through system to experience vision through different ophthalmic progressive corrections for presbyopia before the personalized spectacles are manufactured? Which are the optical elements and the requirements of such a system?** An afocal projection system was used in SimVis technology to project on the patient's pupil the simulation of the through focus performance of an intraocular lens. However, the projection of progressive addition lenses will require a different approach due to the much higher field of view, which has many implications on the viability of such a system.

1.7 – Goals of the thesis

The main purpose of the thesis is to develop novel technologies to be used in cataract and presbyopia treatment planning. For cataract surgery planning the goal of the thesis is to develop low-cost and versatile scanning components to implement in an optical biometer to overcome the high-cost and low portability of current systems. For presbyopia treatment planning we intend to develop a system to test different commercial designs of progressive corrections.

The specific goals are:

1. To determine which type of frequency-domain optical delay line is best to use for a TD-OCT biometer, by comparing two different designs found in the literature.

2. To develop a frequency domain optical delay line suitable for rapid scanning with enough axial range to scan the full eye and to reduce its cost by using a stepper motor spinning a tilted mirror to replace the generally used galvanometric scanner.

3. To develop a non-mechanical beam scanner system with tunable lenses to obtain whole-eye cross sectional images of the eye.

4. To design a see-through system with no magnification and wide field of view to allow the experience of vision through different ophthalmic progressive addition lenses before manufacturing personalized spectacles.

1.8 – Hypothesis

The hypotheses of this thesis are:

- The substitution of the galvanometer scanner generally used in the most standard design of frequency domain optical delay lines by a stepper motor spinning a tilted mirror attached to its shaft, lowers the cost of the optical delay line system and provides enough speed and axial scan range for ocular biometry.

- The combination of tunable lenses allows to non-mechanically displace a laser light beam and to independently select its direction and vergence. With this technology, such beam scanner can be combined with an OCT system to acquire whole-eye cross-sectional images while containing the cost of the optical components and beam control system. Thus, allowing to non-mechanically switch between anterior and posterior eye segment imaging, and proving useful for improving biometric measurement repeatability, via both corneal centration 2-D scans and quasi simultaneous 2-D foveal fixation checks.

- An afocal projection system based on two equal mirror eyepieces with a relay unit in between can be used for the development of a progressive addition lens demonstrator, to allow patients to experience vision through different progressive lens design before manufacturing their spectacles.

Chapter 2

Methods

This chapter presents the instruments, the developed experimental set-ups and the software used during this thesis. The working methodology adopted in the different projects of this study involved the following steps:

1. Theoretical analysis: an in depth-examination of the theoretical foundations was conducted to understand the basic operating principles of the developed systems.
2. Simulations-based optimization: to optimize the optical performance of the systems developed based on off-the-shelf components. By using computational tools, various parameters and configurations were explored to identify the most efficient designs.
3. Experimental validation: a proof-of-concept stage was carried out. This involved the experimental implementation of a prototype and its characterization, as well as the validation of its functionality to acquire OCT measurements.

In the next sections, the main tools used during each of these steps are presented. The first section describes the software platforms utilized in this thesis to solve equations, perform simulations, control systems and process data. The second section describes the hardware systems used including the experimental setups already available in the laboratory as well as the ones developed during the thesis. There is also a description of the commercial optical biometers employed to validate the results obtained.

I have been a main contributor in most of the experimental setups implemented (custom 1-D OCT set-up and the custom SS-OCT 3-D biometer) and have become familiar with all the commercial systems presented. I have also learned to develop custom codes to automatize data acquisition and data processing or to run and control the developed systems. The commercial devices and the license for the software were provided by the Visual Optics and Biophotonics Group at the Institute of Optics 'Daza de Valdes'.

2.1 – Software

Throughout the thesis, various software tools were employed for the purpose of: designing the optical systems, simulating and analyzing their optical performance, and acquiring and processing data.

2.2.1 –OpticStudio Software

OpticStudio (Zemax Ansys Inc., Canonsburg, PA) is an optical design software widely used for modeling optical systems. The comprehensive set of features and tools for designing and analyzing optical systems with a user-friendly interface, together with the possibility to optimize the design parameters of the system and to define different metrics, make it a powerful software suitable to explore various design alternatives. During this thesis, Zemax software was used for the optimization of the optical performance of the designed systems before their experimental implementation using mainly the raytracing algorithms it incorporates.

To simulate an optical system, the first step is to specify the geometry and optical properties of each optical element (curvature, thickness, refractive index, and diameter) arranged in a sequential order in the 'Lens Editor' tab. The software is capable of simulating a wide range of optical components such as lenses, mirrors, diffraction gratings and detectors among others using different options for the surface definition. For this thesis, the most common surface type (Standard Surface type), which defines a conical surface, was used. The two parameters of this surface are the curvature (c) and the conic constant (k) following the

$$z = \frac{cr^2}{1 + \sqrt{1 - (1 + k)\, c^2 r^2}} \tag{7}$$

The second step is to define the characteristics of the light source. In the sequential simulation mode of OpticStudio, the features of the light source that can be defined includes the type of light source (for instance a point source or a collimated beam), its position, direction, wavelength spectral components, and intensity. OpticStudio allows to generate a large number of rays from the defined light source according to the user-specified settings, and to trace each of them through the optical system by sequentially interacting with each optical surface. At each of the interactions, the parameters of the rays (position, direction, and optical path) are calculated based on the properties of the elements applying the laws of geometrical and physical optics of refraction, reflection, absorption or diffraction. By analyzing the rays, OpticStudio obtains valuable information such as the spot diagram in a surface, an analysis of the wavefront aberrations and the modulation transfer functions (MTFs).

Within the tools available in OpticStudio software, three of them were used repeatedly during the work of this thesis. (1) The multiconfiguration tool, used to define and analyze multiple configurations of the same optical system. This tool is useful to study the influence of some of the parameters such as the position of a component, the curvature of a surface or the properties of one of the materials in the system. It allows an efficient comparison between different design options, and thus permits to optimize the performance across multiple configurations. (2) The macro programming capability (based on Zemax Programming Language, ZPL), that was used to automate tasks of analysis while switching between configurations. (3) The Merit Function editor that was used to define the optimization metric to improve the custom designs. The merit function is a user-defined mathematical expression that quantifies the performance of an optical system based on a specific design criterion.

2.2.2 - MATLAB

MATLAB (MathWorks, Natik, MA) is a high-level programming language and development environment well known for its use in scientific and engineering works. It provides a comprehensive set of tools and libraries for numerical computation, data analysis and visualization, and algorithm development. MATLAB's built-in functions and libraries allowed to perform complex mathematical calculations, implement numerical algorithms for scientific computations and perform data manipulation and visualization. It also includes simulation tools for creating and simulating dynamic control and communications systems.

MATLAB also offers the option to program a Graphical User Interface (GUI) that allows to generate interactive interfaces for custom applications. The program includes a drag-and-dop interface for designing GUIs, where users can add components like buttons, sliders, menus, and plots to simulate dynamic systems. During this thesis the control of some of the external components and part of the data processing were done through GUI interfaces, allowing a friendlier use of the developed code.

2.2.3 - LabVIEW

LabVIEW (National Instruments, Austin, TX), which stands for Laboratory Virtual Instrument Engineering Workbench, is a graphical programming language and development environment designed to create measurement and control systems. LabVIEW allows to develop programs called virtual instruments (VIs) using a visual programming approach. Instead of writing lines of code, LabVIEW uses a graphical programming language where graphical elements known as nodes are dragged and dropped on a block diagram to define the flow of data and to control structures and algorithms. Nodes can represent mathematical functions, data types, structures like loops and conditional, and other subVIs which are reusable sections of code that encapsulate specific functionalities. The nodes are connected through wires, representing the flow of data. LabVIEW also contains a front panel, which serves as the user interface and consists of controls and indicators (buttons, slides, text boxes knobs, and graphs) which allow to interact with the program and display data or results. LabVIEW follows a dataflow programming model, where nodes execute when data is available at their inputs. This parallel execution allows for efficient use of system resources and facilitates the handling of real time and parallel processing tasks.

LabVIEW provides a wide range of built-in libraries and tools that allow to integrate different hardware instruments into LabVIEW applications. During the work of this thesis, National Instrument and LabJack (LabJack Corportation, Lakewood, CO) data acquisition devices were used and interfaced with LabVIEW, to acquire data from sensors, control external devices and perform automated tasks. Both companies already offer software solution based on LabVIEW programming software.

2.2 - Hardware

The hardware systems used during this thesis are grouped into two categories: laboratory setups and commercial biometers. The laboratory systems were used for the characterization of the systems developed during the thesis as well as for their validation when combined with an OCT system; the commercial biometers were used for the comparison of the ocular biometric measurements results obtained with the developed systems of the thesis.

2.2.1– Laboratory set-ups

This section aims to describe the main laboratory systems utilized during this thesis.

A – Custom 1-D OCT-biometer set-up with exchangeable components

The first experimental set-up developed during this thesis was a customized and flexible OCT system that allowed to easily switch between an SD-OCT to a TD-OCT system. Figure 2.1 shows a schematic representation of the system. Its main characteristic is its flexible implementation, which facilitated adapting the system to different needs depending on the tests to perform.

The custom 1-D OCT set-up is a fiber-based Michelson interferometer where different fiber couplers were implemented to achieve different optical power ratios in each arm of the interferometer, to find the right balance between the contribution of each arm intensity at the detector. The use of a fiber-based interferometer also allowed an easy exchange of several of the components, permitting a wide flexibility on the performance to the system. On one side, the interferometer could easily be coupled to different implementations of optical delay lines (ODLs), all designed to have an optical path length equivalent to the one of the sample arm, enabling to axially scan any sample with various methods without the need to change the sample arm or realign the sample between them. In such a way, the optical delay line developed during this thesis could be easily compared to a standard implementation. On the other side, the detection system was also interchangeable. Both a photodetector and a spectrometer could be coupled, enabling the system to be used as an SD-OCT when the reference arm remained static and connected to the spectrometer, or as a TD-OCT when the delay line was moved and connected to the photodetector. In addition, a polarization controller was incorporated to the fiber of each of the arms of the interferometer to allow a fine adjustment optimization of the interferometric signal in each situation.

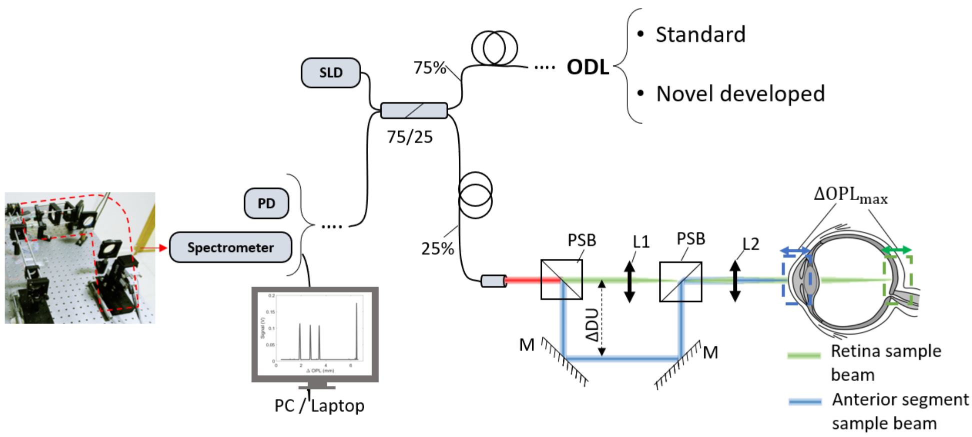

***Figure 2.1** – Schematic representation of the flexible 1-D OCT biometer system implemented. The light source is a superluminiscent diode (SELD) and a light splitter was used to direct part of the light to an optical delay line (ODL), and to the sample arm that included two polarizing beam splitters (PBS) and two mirrors (M) to introduce an additional optical path difference (ΔDU) and two lenses (L1 and L2). The interference between both arms was detected with a photodetector (PD) or with a spectrometer, which allowed to easily switch between a SD-OCT system and a TD-OCT system while the rest of the components remained unchanged. The capability of coupling different ODLs also allowed an easy switch between different axially scanning methods.*

The SD-OCT working mode was often used during the alignment of the optical delay line set-ups, especially when they included diffraction gratings, as it allowed to ensure that the whole spectrum from the light is back-coupled into the interferometer. Moreover, it was also useful for the alignment of the samples as it presented faster scanning speed than the TD-OCT working mode. The spectrometer employed was previously developed by the VioBio research group as part of a SD-OCT system used for the development of an accommodative intraocular lens prototype [119]. The main components of the spectrometer to record the spectral interference fringes were a holographic transmission grating (HD 1800 l/mm @ 840 nm, Wasatch Photonics) and a line CCD camera (spL4096-140km Basler Sprint, Basler). The spectrometer was controlled with a custom developed LabVIEW program that also performed the Fourier transform of the interferometric signal to show the temporal profile of the signal in real time. The acquisition rate of the spectrometer was 50 kA-scans/s, with an axial range of approximately 5 mm and a pixel resolution of 5.2 μm.

The characterization of the interferometric signal was done using a photodetector (Model 2007, Nirvana) and recording the interferometric fringes with an oscilloscope (DSOX2002A, Keysight Technologies). When the envelope of the interferometric PSF was required for the measurement of the distances between the surfaces of the samples, the photodetector was used in combination with a custom low-cost analogue filtering system and a DAQ card (T4, LabJack). This last detection system was controlled using a custom LabVIEW program, which will be explained in Chapter 4.

As can also be observed in Figure 2.1, the components that remained constant were the sample arm and the light source. The light source used was a SLED (SLD-371, Superlum) with a central wavelength of 840 nm and a bandwidth of 56.2 nm. The optical power of the SELD was controllable by a driver. This feature allowed to increase the optical power of the SELD when diffraction components were included in the reference arm, and a fraction of the intensity was lost in the non-used diffraction modes. The sample arm of the system contained a detour unit (DU) based on polarization beam splitters (PSB) which allowed to duplicate the sample light beam. In such a way, the anterior and posterior segment of an ocular sample could be scanned simultaneously. This feature will be explained in more detail in Chapter 4.

B – Custom SS-OCT 3-D biometer

A 3-D biometer system was developed mimicking an existing SS-OCT system already implemented in the group in the framework of an H2020 project. The existing SS-OCT system was a multi-meridional corneal imaging system capable of imaging the mechanical deformation induced in the cornea by different stimulus such an air-puff or a loudspeaker [120, 121], and was dedicated for the early detection of corneal biomechanical abnormalities such as keratoconus. However, this system prevented from achieving a complete ocular biometry as the retina was not observable due to the high absorption of water at 1300 nm [63]. Thus, a new system was needed in order to acquire full 3-D ocular biometric measurements. A schematic representation of the system is shown in Figure 2.2.

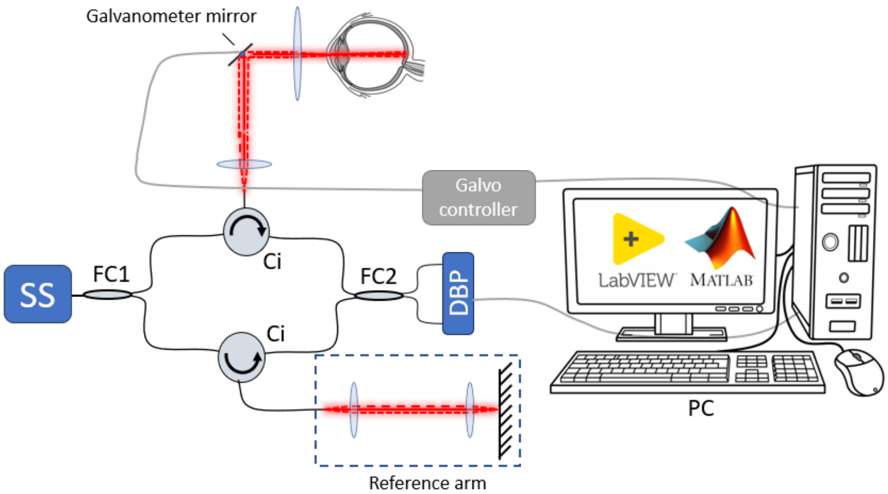

Figure 2.2 – *Schematic representation of the 3-D biometer developed. A fiber-based Match-Zehnder interferometer was used in combination with a swept source laser (SS) and a dual balanced photodetector (DBP). The galvanometer mirror and the digitization of the photodetector signal were synchronized with LabVIEW and the OCT image processing was performed adapting the existing MATLAB codes.*

As the SS-OCT system available in the laboratory, the custom SS-OCT 3-D biometer was also based on a similar Mach-Zehnder interferometric configuration. In this case the selected VCSEL swept source laser was centered at 1060 nm (SL100060, Thorlabs, USA), with a spectral bandwidth of 100 nm and a swept rate of 60 kHz. In such a way water absorption when propagating through the vitreous humor was avoided and the retina could be visualized. This system allowed for a FWHM axial resolution of 11 μm. Due to the change of light source, the balanced photodetector was also changed. The new balanced photodetector used

(PDB481C-AC, Thorlabs, USA) had a 3dB bandwidth from 3 kHz to 1 GHz allowed an axial scan range up to 27 mm in air when the interferometric signal was recorded with a 12-bit 8-lane PCI Express card (ATS 9360, Alazartech, Canada) at a sampling frequency of 1 GHz. The specifications of the developed 3-D biometer are listed in Table 2.1.

The sample arm was compound of a fast galvanometric scanner with 3 mm aperture (Saturn 1B, ScannerMAX, Pangolin, USA) combined with a 2" aperture f-theta telecentric objective lens (LSM05, Thorlabs, USA), with a 93.8 mm working distance length. This implementation allowed the use of different scanning patterns (meridional, crosshair, raster…) through a field of view of 15 mm and a depth of field of 5.15 mm at a frequency of 1 kHz, being enough to image the white-to-white range of an adult eye and maintain a focused beam through the full anterior chamber depth. A data acquisition DAQ card (PCI-6731, National Instrument, USA) was used to synchronize the A- and B- scan triggers and the scanner's voltage signal.

***Table 2.1** – List of the specifications of the developed 3-D ocular biometer.*

SS-OCT system specification	
Central wavelength	1060 nm
A-scan rate	60 kHz
Axial resolution (FWHM)	11 μm
Depth of field	5.15 mm
Axial depth range (maximum)	27 mm
Transverse field of view (FoV)	15 mm

The digitization of the interferometric signal was synchronized with the galvanometric scanner adapting the already existing LabVIEW codes from the SS-OCT system available in the VioBio laboratory. Similarly, the OCT image processing was easily obtained adapting the code used with the previous SS-OCT system. To do so, a K-linearization curve of the new 3-D biometer was obtained by performing the proper spectral re-shaping of the new swept source laser used.

C– High-speed tunable lens driver and high-speed focimeter

For the initial characterization of the electro-tunable lenses (ETLs) used in the proof-of-concept of the systems developed in the thesis, a high-speed focimeter developed in the company 2EyesVision was used. During the last years the company 2EyesVision has achieved significant knowledge on the characterization and control of electro-tunable lenses as they are the main component of their product, SimVis Gekko™. The company has developed customized systems for the control and characterization of electro-tunable lenses, specifically those of the company Optotune (Dietikon, Switzerland).

On one side, at 2EyesVision they have developed customized hardware and firmware to implement a high-speed driver for the electro-tunable lenses and to be able to achieve accurate temporal foci profiles while compensating the dynamic effects of the lenses. The hardware is based on an Arduino Nano board (Arduino, Italy) and a DRV8833 Dual Motor Driver (Texas Instruments, TX). The electro-tunable lenses were driven with a pulse width modulation signal (PWHM) at 32 kHz although is configurable [122].

On the other side, the characterization of the electro-tunable lenses at 2EyesVision is performed by a custom developed high-speed focimeter capable of measuring the optical power of the ETLs as presents high temporal sampling rates [122]. During the work of this thesis, the high-focimeter was used to perform an initial characterization of the electro-tunable lenses (ETLs) before their alignment into the optical systems. In Figure 2.3 a schematic of the working principle of the focimeter is shown (see Figure 2.3 (a)) together with a picture of the optical set-up (see Figure 2.3 (b)).

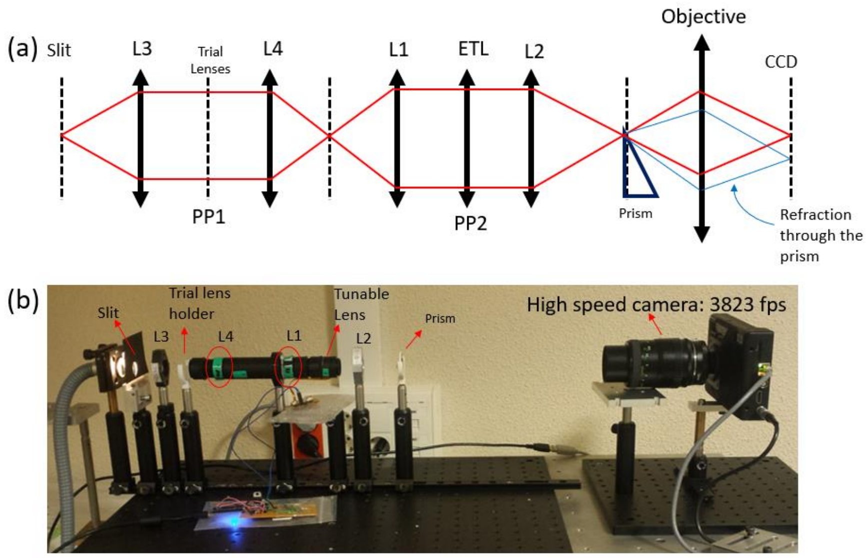

Figure 2.3 – *(a) Schematic representation of the working principle of the high-speed focimeter developed in 2EyesVision. (b) Image of the experimental set-up of the high-speed focimeter implemented.*

The high-speed focimeter transforms the axial displacement of an image along the optical axis when the optical power of the ETL is changed into a transversal displacement using the refraction when light is propagated through a prism placed at a conjugated image plane as shown in Figure 2.3(a). The object used for this work was a thin tilted slit and the prism was set to affect only half of the image. In this way, the region of the slit affected by the prism would be displaced when the optical power of the ETL was changed while the other half would only be defocused but maintained at a static position and was used as the reference. Both sides of the slit were recorded with a high-speed camera permitting to measure the optical power of the ETL at each single shot. In such a way, through the measurement of the distance between the displaced and the reference slit images, the instrument is capable of providing a robust characterizion of the transient optical power response of the ETL.

The slit image propagates through two projection systems with a 4f configuration (lenses L1-L4, f = 50 mm), that form two conjugated image planes and pupil planes (PP). These two planes were used to place the ETL under characterization and additional trial lenses to partially compensate for the refraction of the ETL to allow a larger optical power range characterization of the ETLs.

2.2.2 – Ocular samples

The main ocular sample used during the thesis was a model eye designed specifically for OCT systems (Modell-Auge Manufaktur, Rondeshagen, Germany) that mimics a human eye by incorporating a plastic cornea, a glass lens and a laminar structured retina resembling the structure of a human eye including the optic nerve and macula. Figure 2.4 shows a schematic representation of the model eye, a picture of the anterior and posterior segments and an OCT cross-sectional image of each segment. The dimensions of the model eye were modified from the average size of a human adult eye to compensate for the change in refractive index that commercial biometers would face between the refractive index they assume for a real human eye and the one of the model eye materials. When possible, human participants or eyes from animal models were also imaged with the developed systems. Specifically, in vivo human volunteers and ex-vivo rabbit eyes obtained from a local facility were imaged.

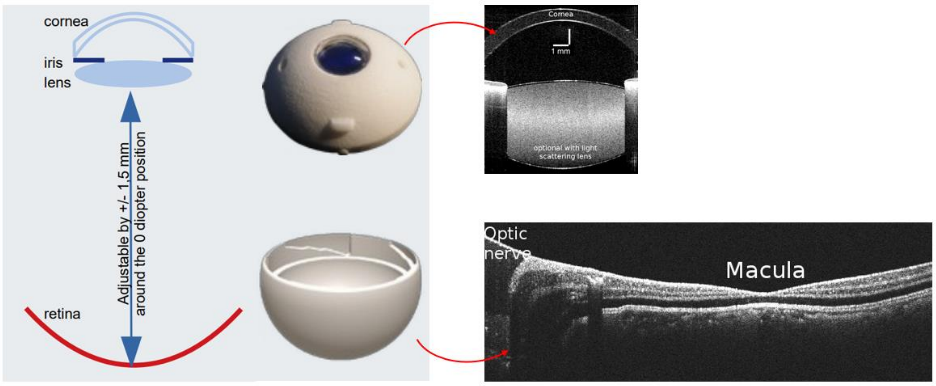

Figure 2.4 *– OCT model eye used for the biometric measurements during the thesis. This model eye mimics an adult human eye biometry and contains the main ocular components: cornea, iris, lens and retina. The retina presents a layered structure showing the main retinal surfaces as well as the macula and optic nerve. The model eye also presents an adjustable axial length as the anterior and the posterior segments could be detached [123].*

2.2.3 – Commercial biometers

Different commercial optical biometers available in the laboratory were used to compare the biometry measurements performed on different samples with the systems developed during the thesis. It was not possible to use a single biometer since the choice of system depended on the specific ocular parameter to be measured. In this section, the working principle of the two commercial optical biometers used is presented.

A – Lenstar LS 900

As briefly presented in Chapter 1, the Lenstar LS 900 (Haag-Streit Group, Rondeshagen, Germany) is an optical biometer widely used in ophthalmology that is based on the working principle of an optical low coherence reflectometry (OLCR) system. The system provides precise high-resolution measurements of the axial length, cornea curvature, central corneal thickness, anterior chamber depth, and lens thickness of the subject [124].

Figure 2.5 shows the components of the Lenstar LS 900 as reported in a patent of the instrument [125]. The Lenstar LS 900 is based on a Michelson interferometer with a movable reference arm (see component 56, marked in orange in Figure 2.5(a)). According to the patent, the component responsible for the optical pathlength variation in the reference arm was a transparent glass cube of 30-40 mm with 4 reflective corners (see component 15, marked in blue in Figure 2.5(a)) rotating around its center (37). Figure 2.5(b-c) shows a detailed representation of the rotating glass cube at two different rotation positions.

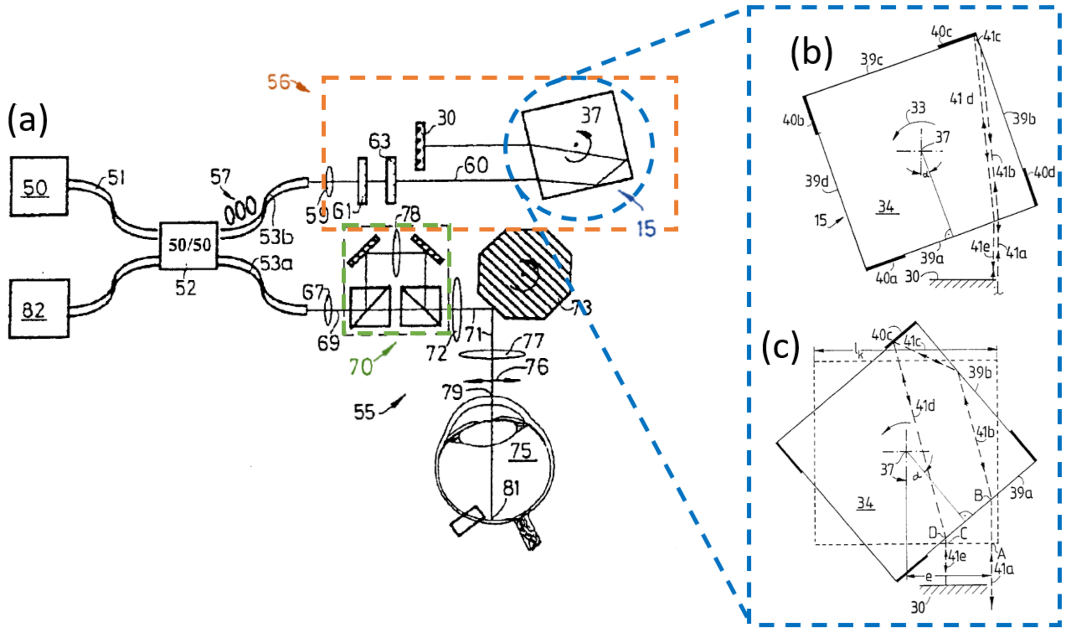

Figure 2.5 – *(a) Schematic of the OLCR interferometer system of the Lenstar LS 900 with a rotating cube in the reference arm to vary the optical pathlength, and a detour unit in the sample arm to allow a reduction on the axial scan range. (c) and (d) show two different rotation positions of the glass cube showing the difference of pathlength followed by the reference light beam at each rotation position of the cube (figure based on Fig. 3-4 from [125] and Fig. 2 from [126]).*

Each of the surfaces of the cube was partially coated (40a to 40d at Figure 2.5(b)) at one edge to make it reflective. Combining the reflection of the light beam at these areas and the effect of total internal reflection when the incident angle was large enough, the reference light beam was reflected twice inside the cube before exiting the cube displaced from its initial incident position(41a) (see Figure 2.5(b)-(c))). In such a way, the optical pathlength of the reference arm was changed while rotating the cube. At the end of the optical delay line, a mirror is placed (see component 30 in Figure 2.5(a)-(c)) in order to allow the light beam to be back coupled into the interferometer and reach the photodetector (82) (see Figure 2.5(a)).

In the sample arm of the interferometer, a detour unit similar to the one presented previously in the 1-D laboratory OCT set-up in Figure 2.1 can also be observed (see 70, marked in green in Figure 2.5(a)). The detour unit was based on two polarization beam splitters where the sample beam was duplicated, introducing an additional pathlength difference between them. In such a way, one sample beam was focused on the cornea or the anterior segment of the eye, while the other one was focused on the retina. This reduced the pathlength variation needed to be introduced to the reference light beam by the optical delay line, as the vitreous length was compensated with the detour unit. In this case, the detour introduced a difference in optical path of 34 mm and the cube was designed to scan an axial range of 8 mm [126]. The cube face length was 40 mm and rotated an angular range of ± 50 deg, leaving a gap of 4-10 mm where no measurement was registered that corresponded to the vitreous humor [127].

To ensure accurate and precise measurements, the Lenstar LS 900 incorporated algorithms that analyze the interference pattern generated by the reflected light waves. By processing the interference pattern, the device calculates the time delay between the reference and sample beams. The system performed up to 16 A-scans at a ‘shot’ without the need of realignment, lasting for roughly 20 s [128-130]. Figure 2.6 shows an example of the report generated after the measurement of an eye. In this case, the axial measurement corresponds to a myopic volunteer and the data was acquired during a training session. A train of peaks that corresponds to the axial position through the visual axis of each of the ocular surfaces was obtained. With this data, the intraocular distances were calculated and the central corneal thickness (CCT), anterior chamber depth (AD), lens thickness (LT) and axial length (AL) were reported in the table below the graph. The sign next to the reported parameters remarks the recommendation from the system to perform more than one measurement in order to have enough data for statistical analysis. Each of this physical distances were obtained assuming the different refractive indices for each ocular medium [87]. The system also reported the retinal thickness (RT) although this was a constant value and not a measured parameter.

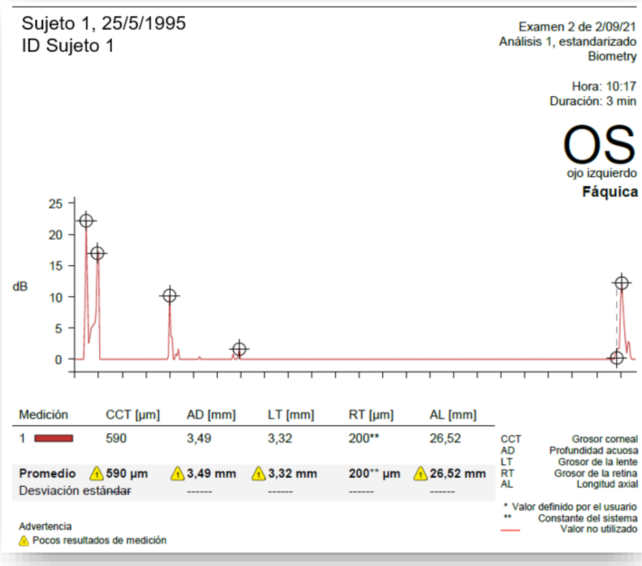

Figure 2.6 ***–*** *Example of the reports generated by the Lenstar LS 900 of the intraocular distances measured on an eye (the report is in Spanish due to the language configuration of the system). Except the retinal thickness, the rest of the intraocular distances were measured. The report indicates with exclamation marks the recommendation to acquire more measurements to perform a statistical analysis.*

<u>B – ANTERION</u>

ANTERION (Heidelberg Engineering Inc. Franklin, MA) is a multi-platform imaging system that comprises four in-built applications (Imaging, Cornea, Cataract and Metrics Apps) and provide a wide flexibility of use [131].

The main difference between Lenstar LS 900 and ANTERION, is that the latter is a SS-OCT system optimized for anterior segment imaging. ANTERION uses a longer central wavelength of 1300 nm and a faster acquisition speed, 50kHz A-scans/s [132]. The system's scan range is 14 mm and the lateral field of view 16.05 mm. All measurements were stabilized with eye-tracking technology for ocular movements control. ANTERION uses different refractive index for each of the anterior segment components (1.376 for the cornea and 1.336 for the aqueous humor) and a mean group refractive index for the axial length calculation similar to the one used by the IOL Master 500 [133].

During this thesis the Metric Apps was used. Metric App allowed to export the raw data of the measurement, that we used to obtain the optical distances rather than the physical distances. Optical distances were then converted to physical distances of the sample with the desired refractive index. Figure 2.7 shows an image exported from the Metric App when measuring the anterior segment of the model eye previously explained. This image is the one used in for the validation of the anterior segment intraocular distances in Chapter 4.

Figure 2.7 *– Image exported from the Metric App after a measurement of the presented model eye on the ANTERION system. A meridional scan with 7 angularly equi-spaced meridians was performed (schematically shown on the white figure on the right).*

2.3 – Summary of the methodology applied in this thesis

In summary, the hardware and software tools presented in this chapter were used as follows:

- MATLAB: to plot the results of the analytical equations derived to describe the performance of the new optical delay lines presented (Chapter 3-4) and the novel optical beam scanner (Chapter 5); to optimize the design parameters; to develop an easy-to-use graphical user interface that facilitated the control of the novel optical beam scanner (Chapter 5).
- OpticStudio Ansys-Zemax: to simulate the performance of the optimized device as concluded from the previous analytical study using nonparaxial optics; to test whether the descriptive equations of each system were correct (Chapter 3-6).
- LabVIEW: to develop a control system for the optical set-ups implemented during the thesis, to automate the data acquisition processing of the measurements performed (Chapter 3-5).
- 1-D OCT optical set-up: in the SD-OCT mode the system was used to guide the alignment of the optical components during the implementation of the diffraction gratings; in the TD-OCT mode the system was used to acquire the intraocular distances of a model eye to validate the performance of the proposed optical delay line (Chapter 3-4).
- Custom SS-OCT 3-D biometer: to validate the biometric data obtained with the optical devices developed (Chapter 4); to show the scanning capabilities of the novel optical beam scanner proposed (Chapter 5).
- Lenstar LS 900 and ANTERION: to compare and validate the measurements performed with the developed components (Chapter 4-5).

Chapter 3
Optical delay line selection

In this chapter, I describe a comparison of two implementations of a frequency domain optical delay line with the aim of identifying the most appropriate for a compact, accurate, low-cost optical biometer. An analytical characterization of their optical specifications was performed to validate their ability to measure the main intraocular distances.

The author of this thesis (1) performed the literature search, and (2) developed the analytical analysis and implemented the optical systems in the simulation program and (3) interpreted the results of both the analytical analysis and the simulation (supervised by Dr. Andrea Curatolo and collaborating with Dr. Enrique Gambra and Dr. Alberto de Castro)

This work was presented in an oral contribution at the “International Optica Network of Students (IONS)” Conference in Dublin (Ireland) (2021/11/09-11), and at the Optica Vision and Color Summer Data Blast with a virtual talk (2022/08/03).

3.1 – Introduction

As already mentioned in Chapter 1, the high-cost components used in FD-OCT based optical biometers reduces their accessibility in remote and low-resource settings making TD-OCT based systems preferable [92]. However, accurate readings are linked to good axial resolution and to fast measurement speeds, which are not easily attainable with TD-systems. A fundamental part of the interferometer configuration of any TD-biometer, be it a partial coherence interferometry (PCI) [68-70] or an optical low-coherence reflectometer (OLCR) [18, 66, 67], is an optical delay line (ODL). The ODL is needed to vary the optical pathlength difference (ΔOPL) between two beams to axially scan the sample under inspection. As such, the design of the ODL used affects the scanning speed and to some extent also the axial resolution.

Commercial and research TD optical biometers include various types of ODLs generally within two categories: bulky mechanically scanning components, such as retroreflectors mounted on a linear translation stage [69, 83] as in the Zeiss IOL Master 500 [82], or rotating cube [13, 85] as in the Haag-Streit Lenstar LS 900 [84]. These optical delay line implementations present scan speed limited by the size of their mechanical components. Alternatively, voice coil-based ODLs have been proposed as a compact and lower cost alternative that can provide fast axial scanning, either through a multipass geometry [134], or multi-reference OCT [135] for scan ranges up to 3.1 mm, and, for biometry, in combination with methods to reference and compensate eye axial motion during acquisitions [89].

Diffraction grating-based frequency domain optical delay lines (FD-ODL), also known as rapid scanning optical delay (RSOD) lines [72, 136, 137] have been used in TD-OCT mainly for rapid axial scanning up to a few kHz as, to generate an axial scan, they only involve a tilt of a small mirror back and forth over a short angular range. Other uses include hardware-based dispersion imbalance compensation in OCT [138-140], fast depth tracking and adaptive ranging [141-144], and complex conjugate artifact removal in FD-OCT [145-149]. This feature makes FD-ODL also suited for rapid long-range scanning. We propose the integration of a long-range FD-ODL into a TD-OCT biometer for an accurate and cost/effective optical biometer.

This chapter presents the analysis of the optical performance of two different FD-ODL designs found in the literature, and the analysis of their potential implementation in a TD optical biometer.

3.2– Layout of two types of FD-ODL

We considered two frequency domain configurations based on either a single [136] or a pair of diffraction gratings [150] presented in peer-reviewed publications in Optics Letters and Applied Optics, respectively. Figure 3.1 shows the optical schematics of the two FD-ODLs.

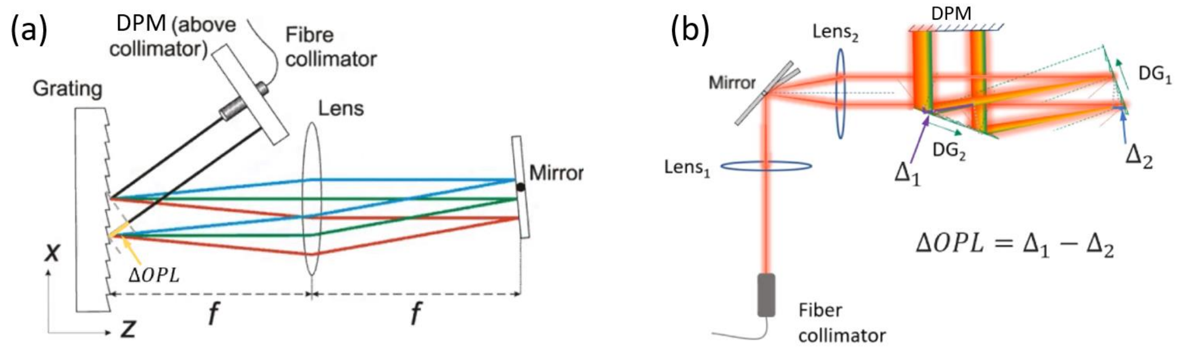

***Figure 3.1** – Schematic representation of the two FD-ODL designs under consideration: (a) a design based on a single diffraction grating (modified from [136]), and (b) a design based on a two diffraction grating (based on [151]).*

Figure 3.1(a) shows the schematic of the most popular implementation of a FD-ODL in the literature, called from here on as 1DG design. It comprises a collimator, a diffraction grating, a lens, a galvanometric mirror and a double pass mirror. The working principle of a FD-ODL is similar to the one used for stretching ultrafast laser pulses and is based on the fact that a linear ramp in the frequency domain is related with a time shift via the Fourier transform [137]. In the first instance, the light source is dispersed by a grating into its spectral components and focused by a decentered lens on a galvanometric scanning mirror. After the light is reflected and recombined into a broadband beam, it returns towards the fiber collimator but displaced by a distance dependent on the tilt angle of the mirror. Finally, a double pass mirror (DPM), placed above the collimator, enables the light beam to propagate again through the optical delay line and back-couple into the fiber collimator duplicating the ΔOPL.

Figure 3.1(b) shows an alternative FD-ODL, proposed in [151] and based on the combination of non-parallel diffraction grating (DG_1 and DG_2), called from here on as 2DG design. Similarly, to the 1DG design, the beam is also incident on the optical delay line through a fiber collimator and uses a galvanometer scanner (or possibly a MEMS mirror) to transversally displace the light beam on a pair of non-parallel diffraction gratings. However, in this case, the galvanometer scanners are placed before the broadband light beam is diffracted. In the 2DG design, the light beam is first propagated through the scanning mirror placed at the focal plane of a lens, so that the change of the tilt angle is transformed into a lateral displacement of the light beam. The light beam then interacts with the pair of diffraction grating at an angle between them, and, finally, a retroreflecting mirror allows the light beam to back propagate through the optical delay line in a double pass configuration. The variation of optical pathlength ΔOPL is, as before, dependent on the tilt angle of the scanning mirror as different optical path lengths can be induced for different transverse displacements on the first grating.

3.3– Scanning performance two types of FD-ODL

In this section we compare the performance of the two optical designs of a FD-ODL through the analysis of two different parameters:

1. Scanning power: which is the ΔOPL corresponding to a scan of a mechanical tilt angle α of 1 deg of the galvanometric mirror (see Figure 3.2).
2. Axial resolution: which is the FWHM of the envelope of the interferometric signal of a single reflector when the optical delay lines are integrated in an OCT system.

These parameters were theoretically analyzed through ray tracing simulations using OpticStudio software as well as through an analytical analysis implemented in MATLAB. To ensure a more direct comparison between the two designs we assumed equal components in both cases. We assumed a light source with a 840 nm central wavelength and a 50 nm bandwidth, a diffraction grating with a 600 lines/mm grove density and a 75 mm focal length lens. In the 1DG design, the distance set between the diffraction grating and the lens as well as between the lens and the scanning mirrors was equal to the focal length of the lens f, 75 mm. In the 2DG design, the distance *D* between the two diffraction gratings measured at the normal of the first diffraction grating and from the point of incidence of the central wavelength on it was set to 85 mm, and the distance *P* between the second diffraction grating and the double pass mirror defined as D was set to 100 mm. Additional parameters, such as the duty cycle, the scan range, the linearity of the scan, the insertion losses and the polarization and dispersion effects will be studied more in detail for the chosen design in Chapter 4.

3.3.1– Scanning power

We analyzed the scanning power by calculating the difference of optical pathlength ΔOPL of the light beam at different angular positions of the galvanometric mirror in OpticStudio. In both cases the angle of incidence β_{in}, between the incident light beam and the normal direction to the first diffraction grating, was 30.3 deg (see Figure 3.2). In such a way, the diffracted angle of the central wavelength of the light source is zero and the corresponding components propagate parallel to the normal to the diffraction grating.

Figure 3.2 shows the optical pathlength of the light beam, for either FD-ODL designs, at two positions of the galvanometer scanner: 1) at the starting position of the scan, namely at $\alpha = 0\ deg$ where the central wavelength component of the light beam propagates along the normal to the first grating and 2) at a scanning position $\alpha \neq 0\ deg$ where the light beam is laterally displaced. Notice that in the 2DG design the case labelled as $\alpha\ =\ 0\ deg$ required the scanning mirror to be set at 45 deg to the optical axis of the first lens. The optical path of the chief ray of the central wavelength component is represented for both scanner positions in red in Figure 3.2(a) and in green in Figure 3.2(b) for the 1DG and the 2DG designs, respectively.

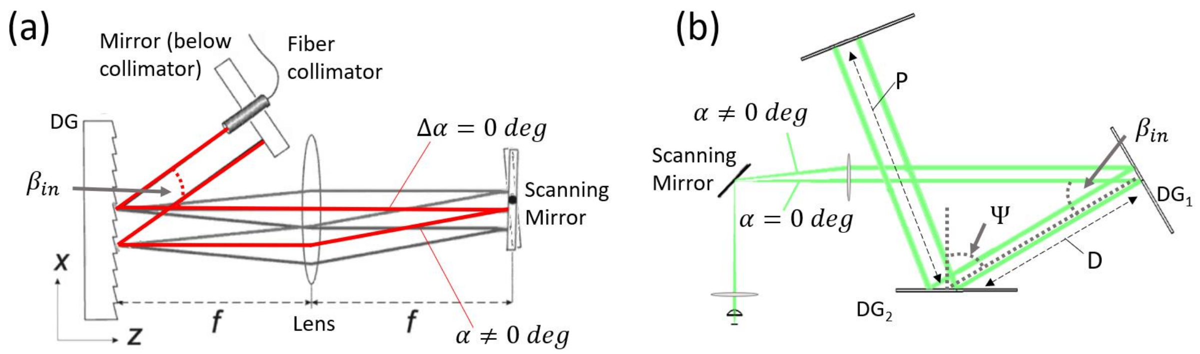

***Figure 3.2** – Optical path in the FD-ODL for two galvanometer angles, for the case of (a) a single diffraction grating, and (b) the two-diffraction grating system.*

For the case employing two diffraction gratings, we also analyzed the effect of varying the angle Ψ between the normal directions of the two diffraction gratings. Three different example angles Ψ are represented in Figure 3.3, showing the layout and raytracing of the each of them.

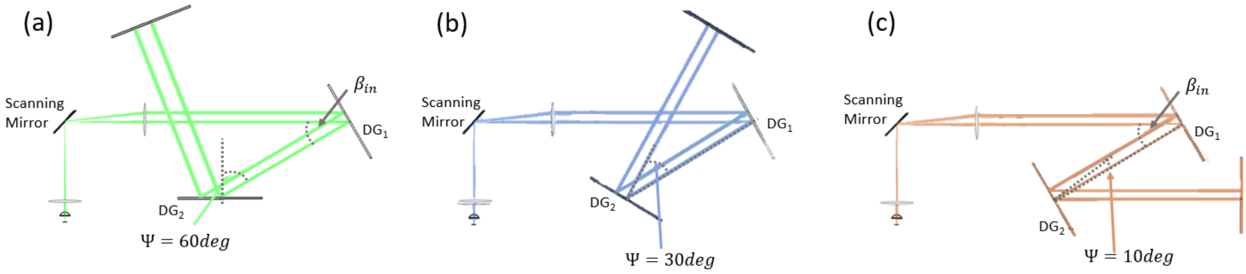

***Figure 3.3** – Three angular configurations of the 2DG FD-ODL implementation, varying the angle Ψ between the two diffraction gratings: (a) $\Psi = 60\ deg$, (b) $\Psi = 30\ deg$ and (c) $\Psi = 10\ deg$.*

Figure 3.4(a) shows the ΔOPL obtained for the three angular configurations, Ψ, between the two diffraction gratings in the 2DG design as a function of the tilt angle α of the galvanometric scanner. The starting point for ΔOPL is when α is equal to 0 deg as explained before. As Figure 3.4(a) shows, the optical pathlength is larger when the angle Ψ is greater. Figure 3.4(b) shows with black dots the results for the scanning power as a function of the angle Ψ for the 2DG design and a red line superimposed shows the scanning power of the 1DG design. For the 1DG design the scanning power, represented as a constant red solid line in Figure 3.4(b), was 5.19 deg/mm. For the 2DG design, the scanning power increased as the angle Ψ between the two diffraction gratings increased. Thus, improving the scanning power of the optical delay line with smaller angles Ψ would be required to scan the same axial length. The 2DG system showed a better scanning power than the single diffraction grating system when the angle Ψ was above 50 deg.

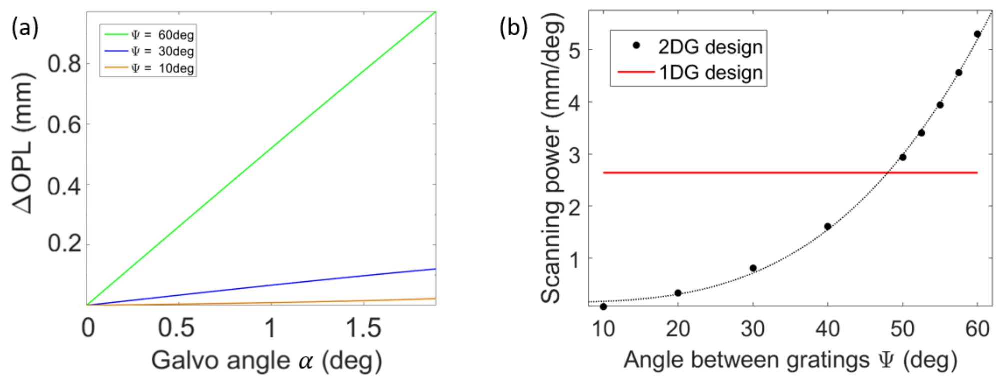

Figure 3.4 – *(a) ΔOPL obtained from the OpticStudio simulation model of the 2DG design as a function of the tilt angle of the scanning mirror for three cases of the angle Ψ between the pair of diffraction grating. (b) Scanning power as a function of the angle Ψ between the pair of diffraction grating. The black dots represent the simulation results for the 2DG design, while the colored lines represent the three angles displayed in Figure 3.3. The dotted line shows the best fit to the simulated results for the 2DG design. The red line represents the scanning power of the 1DG system for comparison.*

3.3.2– Axial resolution (Δz)

To analyze the axial resolution Δz, two effects were considered: the spectral filtering, due to wavelength-selective light back-coupling after the double pass through the FD-ODL, and the group delay dispersion (GDD). In this work we analyzed them separately and then we simulated the combination of the two effects.

A) Spectral filtering

In the 2DG design, for different Ψ, the spectral components of the light source are diffracted at different angles and thus, the light returning to the collimator does not always recombine into a broadband collimated light in Figure 3.5.

We calculated the spectral filtering by analyzing the spectral coupling efficiency of the 2DG design in the OpticStudio simulation. Figure 3.5 shows the steps for this calculation. Firstly, the spectrum of the light source was simulated with a Gaussian profile (see Figure 3.5(a)). Next, through a ray tracing analysis, we obtained the power of each wavelength components back coupled into the fiber after the propagation through the pair of diffraction gratings at different angular configuration using the fiber coupling tool in OpticStudio. Figure 3.5(b) shows the ray tracing for the highest angle Ψ in our analysis, evidencing that several wavelength components (marked with rays of different colors) were not back coupled on the collimator lens. For the sake of clarity the 1:1 lens telescope with the scanning mirror was omitted as it does not affect the back-coupling efficiency of the various wavelength components into the collimator.

Figure 3.5(c) shows the back-coupling efficiency into the input fiber through the collimator lens for the angles Ψ equal to 10, 30 and 60 deg in orange, blue and green respectively.

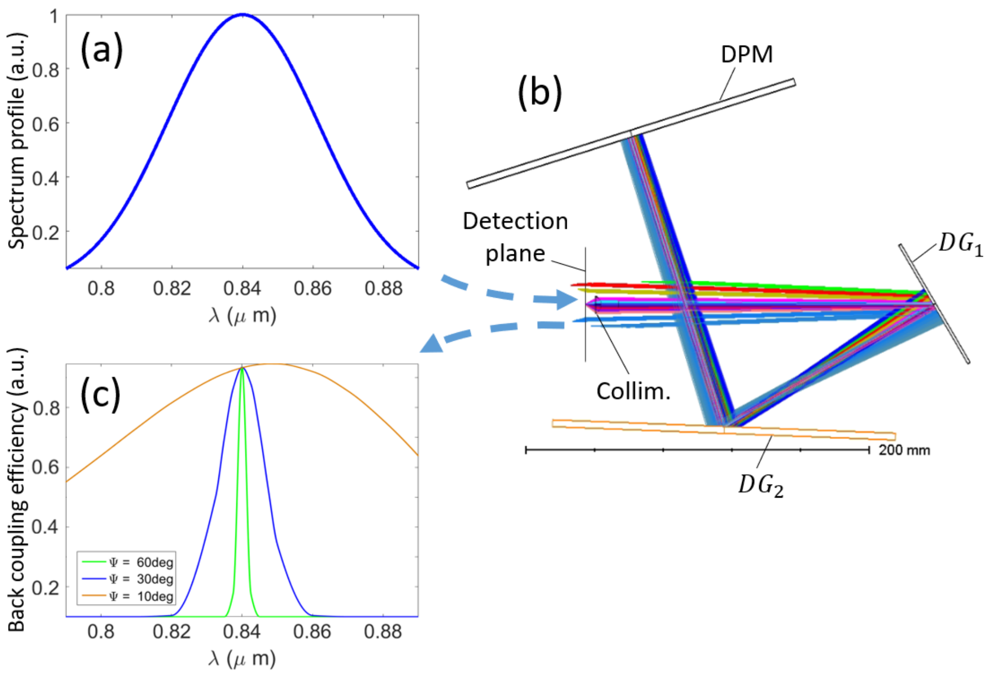

Figure 3.5 *– (a) Gaussian spectrum profile of the simulated light source. (b) Ray tracing through the OpticStudio model of the 2DG optical design at the configuration of $\Psi = 60\ deg$ where DG_1 and DG_2 are the two diffraction gratings of the non-parallel pair of diffraction gratings, and DPM is the double pass mirror. (c) Normalized optical power back-coupling efficiency into the input fiber for the three angles Ψ equal to 10 deg, 30 deg and 60 deg in orange, blue and green respectively.*

Finally, we calculated the back-coupled spectrum by multiplying the Gaussian input spectrum profile and the spectral back-coupling efficiency. Figure 3.6(a) shows the resulting back-coupled spectrum for the three angles Ψ. The FHWM bandwidth obtained for the cases where Ψ is equal to 10, 30 and 60 deg was 45.81 nm, 14.86 nm and 2.73 nm respectively. Thus, the larger we set the angle Ψ between the pair of diffraction gratings, the larger the spectral spread of the beam at the input fiber and, therefore, less wavelength components get back-coupled.

Following Equation (2), we calculated the axial resolution of the corresponding low coherence interferometry system as a function of the back-coupled FWHM for the different angles Ψ. This is shown in Figure 3.6(b) with black dots. The colored dots represent the specific cases shown in Figure 3.6(a). The solid red line in Figure 3.6(b) represents the expected axial resolution assuming that the whole 50 nm bandwidth of the light source is completely back-coupled without presenting any spectral filtering, thus giving a theoretical axial resolution of 6.38 μm (from Equation (2)). This is the case for the 1DG design. For the 2DG design, the reduction in the back-coupled bandwidth into the interferometer when increasing the angle Ψ results in a reduction of the axial resolution, and, hence, biometric measurement accuracy. Similar axial resolution as the optimal value for the 1DG design was achieved for a small Ψ angle of around 10 deg ($\Delta z\left(\Psi_{10\ deg}\right) = 6.79\ \mu m$).

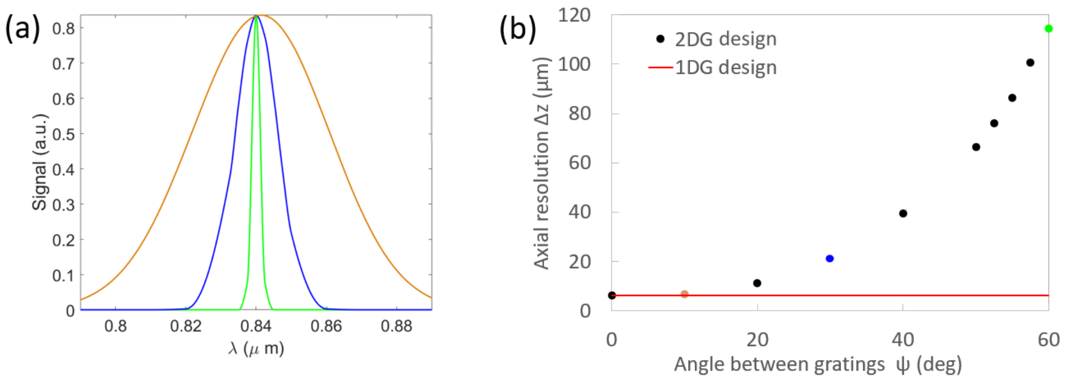

Figure 3.6 *– (a) Back-coupled spectrum for the three analyzed angles Ψ of the 2DG design: 10 deg in orange, 30 deg in blue and 60 deg in green. (b) Axial resolution as a function of the angle Ψ for the 2DG design (dots) and the optimal axial resolution without any spectral filtering for the 1DG design (red solid line).*

B) Dispersion

We also analyzed the dispersion induced by propagation through the FD-ODL in the 2DG design, by calculating the group delay dispersion (GDD) of the optical delay line. The GDD represents the variation of the optical pathlength with respect to the optical wavelength and is calculated as the second derivative of the phase of the light beam φ with respect to optical frequency ω: $GDD(\omega) = \frac{\partial^2 \varphi}{\partial \omega^2}$ where $\varphi(\omega) = \omega \frac{\Delta OPL(\omega)}{c}$ [152]. For this purpose, we computed the optical pathlength of each wavelength component of the light source for different angular configurations of the two diffraction gratings using the geometrical analysis of the optical pathlength though the 2DG design. Then, we obtained the GDD in the simulated optical delay line by performing the second derivate of the optical phase of the optical signal. Figure 3.7(a) shows the GDD obtained for the three Ψ angular configurations shown so far.

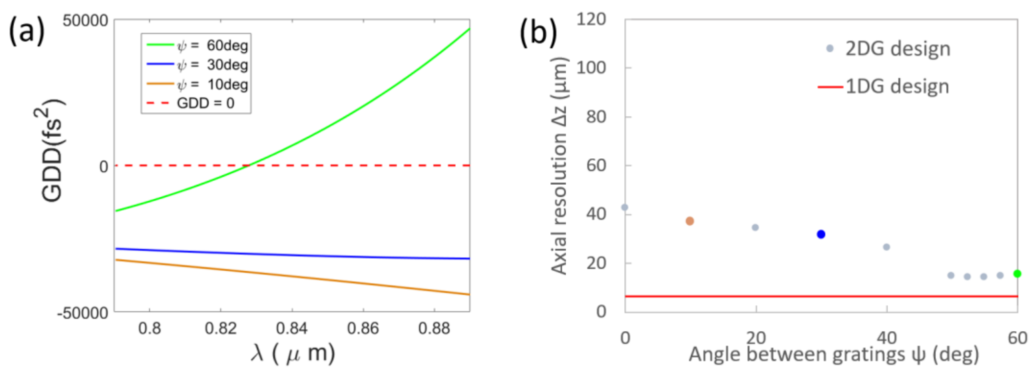

Figure 3.7 *– (a) Dispersion as a function of wavelength obtained for the three values of Ψ between the pair of diffraction grating: 10 deg in orange, 30 deg in blue and 60 deg in green. (b) Axial resolution variation as a function of Ψ influenced by the dispersion for the 2DG design (dots) and optimal (i.e., with balanced dispersion) axial resolution for the 1DG design.*

The influence of the GDD in the axial resolution was computed by applying, in the frequency domain, the dispersion coefficient to the optical phase as the second order of the Taylor series, and then performing the Fourier transformation of the signal to obtain its time dependence $\left(G(\tau) = e^{i\left(\omega_c \frac{\Delta OPL}{c} + GD(\omega-\omega_c)+\frac{1}{2}GDD\,(\omega-\omega_c)^2\,\right)}\right)$. Thus, the FWHM of the simulated envelope could be measured. In this case, the whole bandwidth of 50 nm of the simulated light source was considered. Figure 3.7(b) shows the axial resolution under the influence of the dispersion induced by the 2DG design with gray dots for different angle Ψ. As before, the red solid line represents the optimal axial resolution value of 6.38 μm for the 1DG designed, for a balanced (or no-) dispersion propagation. For the 2DG design case, the minimum axial resolution was 14.10 μm for an angle Ψ of 55 deg, as for this angle the GDD curve is closest to zero.

C) Combined influence on the axial resolution

Figure 3. 8 shows the axial resolution (blue line) as a function of the angle Ψ, considering the combined effect of both spectral filtering and dispersion on the axial resolution of the 2DG design. In this case, we performed a similar calculation as in the previous dispersion analysis but this time considering the FWHM of the back-coupled spectrum after the propagation through the simulated optical delay line. As can be observed, the dominant factor between the spectral filtering and dispersion changes at Ψ equal to 30 deg. While for Ψ angles below 30 deg, dispersion is the dominant effect in the broadening of the envelope of the interferometric signal, for angles above 30 deg the dominant effect is the high spectral filtering. From this combined and more complete analysis, the minimum axial resolution for the 2DG design was 22.7 μm for Ψ equal to 30 deg, which is 3.7 times bigger than the axial resolution of the 1DG design.

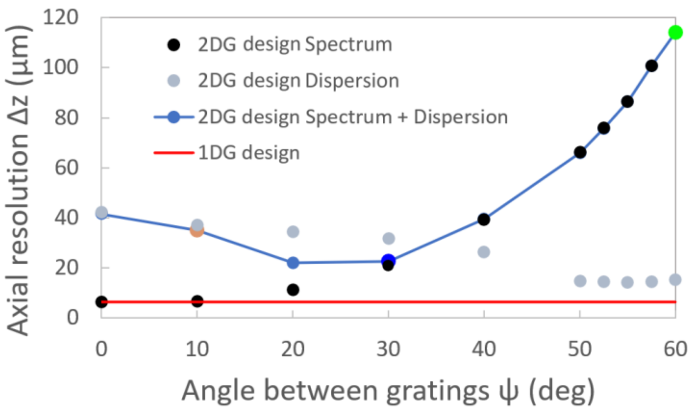

***Figure 3. 8** – Axial resolution for the 2DG design (blue line) affected by both the dispersion (in grey) and the spectral filtering (in black). Colors orange, blue and green show the three configurations with different Ψ angle studied. The axial resolution for the 1DG design superimposed (red line) for comparison purposes.*

3.3.3– Overall scanning performance

If we consider the scanning power and the axial resolution dependence with the angle Ψ for the 2DG design, we observe that the cases of best performance are for different angles Ψ. While the best scanning power monotonically increases with the angle Ψ, the best axial resolution was obtained at an angle of 30 deg. When benchmarking the 1DG design against the 2DG design, we see that the scanning power of the 2DG design outperforms that of the

1DG design, for angles Ψ larger than 50 deg. However, the axial resolution, and hence the biometric accuracy, of the 2DG design is always worse than the one of the 1DG design, by at least 3.7 times.

Considering the best axial resolution case for the 2DG system, i.e., 22.7 μm, the corresponding scanning power was 0.82 mm/deg, while the axial resolution for the 1DG design was 6.4 μm, and the corresponding scanning power was 2.64 mm/deg. Thus, the 1DG design is superior to the 2DG design in the two parameters that we considered, and therefore it is a more appropriate design for a rapid, long-range FD-ODL.

3.4 – Next steps

After settling on the FD-ODL design based on a single diffraction grating, for rapid, long-range axial scanning suitable for ocular biometry, we will focus on tackling the cost issue. Therefore Chapter 4 will be devoted to finding a solution that reduces the cost of a standard galvanometer-based FD-ODL. We will demonstrate that by changing the actuator and rotation axis that displaces the light beam on the diffraction grating of the optical delay line, we will achieve a lower-cost FD-ODL for TD biometry.

3.5 – Discussion

In this chapter, we presented a comparison of two optical designs of a FD-ODL. The goal was to determine which design provided better scanning performance when integrated in a TD biometer. We characterized their scanning performance by analyzing their scanning power and axial resolution, i.e., biometric accuracy.

In terms of scanning power, i.e., optical pathlength of axial scan corresponding to 1 deg of mechanical tilt angle of the scanning mirror, we observed that the 1DG design of the FD-ODL presents a higher scanning power than the 2DG designs for configurations where the angle between the normal direction of the two diffraction gratings is smaller than 50 deg. A higher scanning power is important as it means that a specific axial scanning speed could be achieved with a lower A-scan rate, and therefore a less stringent requirement on the actuator scanning the angle α.

The smaller scanning power achieved in our simulation compared to the case reported in [151] for the 2DG design is due to the different wavelength used. While in the previously reported case [151], a longer central wavelength of 1310 nm with a broader bandwidth of 80 nm was used, we considered a central wavelength of 840 nm and a bandwidth of 50 nm in order to take the advantage of transmission through the eye in the 840 nm wavelength band with respect to the 1300 nm band, which presents a higher absorption [63].

We also compared the axial resolution achievable with the two FD-ODL designs. For the 1DG design, previous studies reported that the axial resolution was not affected by dispersion or spectral filtering [152]. For the 2DG the best axial resolution was 22.7 μm, nearly four times bigger than the one obtained for the 1DG design ($6.38\ \mu m$). This factor plus the additional cost of two lenses and two diffraction gratings for the 2DG design, made the choice of the 1DG design the most natural. However, the most expensive component remains the galvanometric scanner, which can cost more than 2000 USD. Therefore, in the next chapter, we focused our effort in finding an alternative design that substitutes this component for one with a lower cost, and do not trade off other scan parameters in doing so.

3.6 – Conclusion

We performed a comparison of two optical designs of a FD-ODL presented in the literature. We simulated both ODL designs in OpticStudio using the same components to allow a direct comparison between them. We performed a theoretical analysis and ray tracing simulations to compare the scan performance in terms of scanning power and axial resolution, taking into account the spectral filtering and dispersion effects. The study of the different configurations of the 2DG design have shown a case of best axial resolution equal to 22.7 μm, and corresponding scanning power of 0.82 mm/deg. The analysis of the 1DG design showed an axial resolution of 6.38 μm and a scanning power of 2.64 mm/deg thus outperforming the 2DG design in both parameters. Therefore, from here onwards, we will use the 1DG design for a FD-ODL as part of a TD-biometer and try to avoid the use of a galvanometer mirror to lower its cost.

Chapter 4

Low-cost FD-ODL

In this chapter, I describe the development of a novel low-cost optical delay line. I present the working principle as well as the implementation of an experimental prototype. A characterization of the proposed optical delay line was performed when combined with a custom TD-biometer, in order to validate its capability to measure the thickness of the main ocular components.

This chapter is based on the paper by M.P. Urizar et al., “Long-range frequency-domain optical delay line based on a spinning tilted mirror for low-cost ocular biometry” submitted to Biomedical Optics Express (2023). The authors of the work are María Pilar Urizar, Alberto de Castro, Enrique Gambra, Álvaro de la Peña, Daniel Pascual, Onur Cetinkaya, Susana Marcos and Andrea Curatolo.

The author of this thesis (1) performed the literature search, (2) developed the analytical and simulation analysis of the system performance, (3) implemented and characterized an experimental prototype of the system, (4) validated the system by experimentally measuring the intraocular distances in a model eye and (5) contributed to prepare the manuscript (supervised by Dr. Andrea Curatolo and collaborating with Dr. Alberto de Castro and Dr. Enrique Gambra).

The intellectual property behind the operating principle of this low-cost device is protected by the patent [M2201P007EP] owned by 2EyesVision. The author of the thesis contributed to the patent preparation and is a co-inventor.

This work was presented as a poster contribution at the SPIE Photonic West Conference in San Francisco (USA) (28/01/2023– 02/02/2023) where it won the second place in the 3-min poster competition, and at the Biophotonics for Eye Research Conference in Jaca (Spain) (01/06/2023 – 04/06/2023).

4.1 - Introduction

As seen in Chapter 3, diffraction grating-based frequency domain optical delay lines (FD-ODL) or rapid scanning optical delay (RSOD) lines have been used with different purposes in TD-OCT systems as they allow rapid axial scanning by tilting a small mirror back and forth over a short angular range [72, 136, 137]. In FD-ODL the mirror counter-rotation is typically actuated by a galvanometric scanner, for which the operation of a PID servo controller and associated electronics including a power supply capable of supplying high currents are needed. Alternative actuators include the use of a polygon scanner in place of the galvanometer [153], and for the optical components, all-reflective [154], transmissive [155], and double grating [151, 156] optical designs.

FD-ODLs have also been used for long range scanning [157] in anatomical OCT (aOCT), scanning up to 26 mm for +/- 3.6° galvanometer tilt at 100 Hz (subsequently upgraded to 500 Hz), for measuring with an endoscopic probe the size and shape of the lumen of the human upper [158] and lower airways [159] with an endoscopic probe. Thus, a FD-ODL would also be suited for robust long-range scanning in ocular biometry. In Chapter 3, we determined that the standard single-grating FD-ODL is the most suitable for biometric accuracy. However, the high cost of a galvanometric mirror scanner [160] makes its use impractical for low-cost applications.

This chapter presents the working principle, design and experimental implementation of a novel low-cost FD-ODL employing a small mirror and an inexpensive stepper motor instead of a galvanometric scanner. In this case, the direction normal to the small mirror surface is set at a constant tilt angle to the stepper motor shaft axis so that the angle projection on the X axis (see Figure 4.1) varies similarly to the variable tilt angle of a mirror in a galvanometric scanner. This way, the proposed novel low-cost FD-ODL consists of effectively spinning a slightly tilted mirror that allows to independently set the scan range and frequency by the mirror tilt angle and motor speed respectively, unlike in leadscrew-based linear mirror translation ODLs or galvanometer mirror-based FD-ODLs. We validated the use of the proposed FD-ODL in a novel optical low-coherence reflectometry (OLCR) TD optical biometer prototype, capable of scanning long depth ranges, and compare its biometry readings for a model eye with those of commercial and custom built biometers.

4.2 – Working principle of the proposed FD-ODL

The goal of this section is to provide a detailed explanation of the working principle of the proposed optical delay line. In the first instance, we present an analytical description. We study the optical performance of the proposed FD-ODL, employing commercial components available on the market and using the derived analytical equations to study the dependency from the main mechanical parameters. The analytical equations that describe the tilted mirror-based FD-ODL are also validated through a simulation of the proposed system in the optical design software OpticStudio.

The proposed optical delay line is based on the working principle of a standard FD-ODL [136] with a novel actuator to induce the displacement of the light beam on the diffraction grating. While in a standard FD-ODL a galvanometric mirror scanner is used to linearly displace the reference light beam on the diffraction grating, in the novel FD-ODL we propose to circularly displace the reference light beam by using a tilted mirror (TM). The variation of the optical pathlength due to the circular displacement of the reference beam reflected by the TM allows to perform long axial scans with low-cost components, as well as to independently set the axial scan range and the scan frequency.

4.2.1 - Schematic and analytical description

A schematic representation of the proposed optical delay line with a schematic raytracing is presented in Figure 4.1. The main optical components are a fiber collimator, a diffraction grating (DG), an achromatic doublet lens (L), a tilted mirror (TM) attached to the shaft of a stepper motor (SM) and a perforated double pass mirror (PDM). In such a way, the optical pathlength and thus the group delay of the light beam propagating through the proposed optical delay line is varied during the rotation of the TM. A full TM rotation corresponds to a full forward and backward group delay scan.

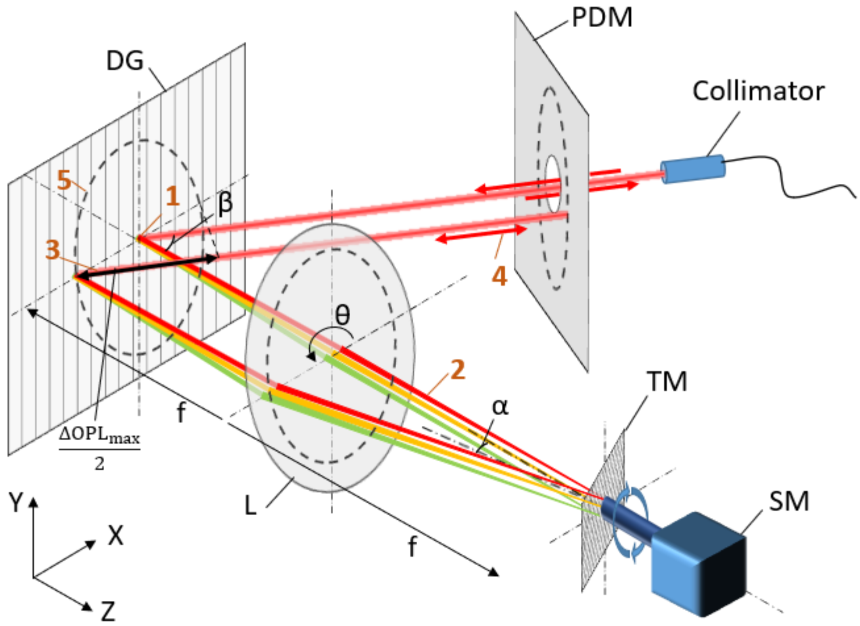

Figure 4.1- *Schematic representation of the proposed FD-ODL showing the optical path and circular displacement of the light beam resulting in a group delay scan. (DG: diffraction grating, L: achromatic doublet lens, TM: spinning tilted mirror, SM: stepper motor, and PDM perforated double pass mirror).*

The designed tilted mirror-based FD-ODL works in a double pass configuration that can be described in the following five steps:

1. A collimated broadband input light beam from a fiber collimator propagates through the central hole of the perforated double pass mirror (PDM) and is incident on the diffraction grating at an angle β to the normal of the diffraction grating (see step 1 in Figure 4.1). The angle β was chosen so that the angle γ between the normal to the diffraction grating and the central wavelength component of the light beam is zero (following the diffraction equation $dsin\beta = m\lambda$ where *d* is the groove density of the diffraction grating and m is the diffraction order). Hence, the diffracted beam at the central wavelength propagates on-axis with the optical axis of the FD-ODL (see orange beamlet after step 1 in Figure 4.1).
2. A lens L was placed at a focal length *f* distance from the diffraction grating (DG) on one side, and from the spinning tilted mirror (TM) on the other side. Unlike in the standard FD-ODL [158], the achromatic doublet lens L was centered on-axis with the optical axis of the FD-ODL. This way, the lens L both focused each wavelength component of the diffracted beam on the tilted mirror TM and redirected the chief rays of each wavelength component parallel among themselves, creating a horizontally oblong spot on the TM (see step 2 in Figure 4.1).
3. The light beam is back reflected by the TM towards the diffraction grating. The TM was tilted such that the normal to the mirror surface forms an angle α with the stepper motor shaft axis, which, in turn, it was aligned with the optical axis of the delay line. Therefore, the light impinging on the TM was reflected at an angle 2α from the optical axis. The reflected light passes again, this time off-axis, through the lens L, which collimated all wavelength components and redirected them to the same spot on the diffraction grating at a distance $f\tan(2\alpha)$ from the original spot. Thus, light gets diffracted again into a collimated broadband beam parallel to the input light beam (see step 3 in Figure 4.1).
4. The beam propagates until the perforated double pass mirror PDM, where it is reflected on its path (see step 4 in Figure 4.1), and back-traces all previous steps until it couples back into the collimator.
5. As the tilted mirror TM was rotated by the stepper motor about the FD-ODL optical axis (Z-axis in Figure 4.1), the tilt angle α was maintained constant. This results in the reflected light tracing a circle on the lens L and on the diffraction grating plane during the rotation of the TM (see step 5 in Figure 4.1). The circle radius is $f\tan(2\alpha)$. However, after diffraction at an angle β in step 3 of Figure 4.1, the circle becomes an ellipse on the perforated double pass mirror PDM, with the major axis (equal to the circle diameter) on the vertical direction, and the minor axis on the horizontal direction.

The optical path length (OPL) inside the FD-ODL varies as the TM is rotated. Interestingly, the only direction of the light beam displacement that induces a difference in OPL is the one orthogonal to the diffraction grating grooves orientation, hence the horizontal direction, i.e., the X-axis in Figure 4.1. The variation of the optical pathlength (ΔOPL) after the double pass as a function of the rotational angle θ of the stepper motor shaft follows the projection of the beam position on the X-axis at the diffraction grating, i.e., $\left[1-\cos\left(\theta(t)\right)\right]$. Equation (8) puts it all together, by expressing ΔOPL as a function of time and all the aforementioned angles:

$$\Delta OPL(t) = 2\,f\tan(2\alpha)\sin(\beta)\left[1-\cos\left(\theta(t)\right)\right] \tag{8}$$

From Equation (8), we can notice that the maximum ΔOPL that can be induced is proportional to the diameter of the circle traced by the beam at the diffraction grating and that a complete rotation of the stepper motor shaft performs two scans of the group delay (over the full axial range), in opposite directions. The double pass configuration allows to double the ΔOPL of the reference light beam when back-coupled into the collimator (see factor 2 in Equation (8)). Equation (9) develops Equation (8) by expressing the incidence angle β on the diffraction grating as a function of the grating pitch p and the central wavelength λ_o, as:

$$\Delta OPL\left(f,p,\lambda_0,\alpha,\theta(t)\right) = 2f\tan(2\alpha)\frac{\lambda_0}{p}\left[1-\cos\left(\theta(t)\right)\right] \tag{9}$$

From Equation (9) we can observe that ΔOPL increases with longer central wavelengths λ_o, shorter grating pitches p, longer focal lengths f, and larger tilt angle α of the spinning titled mirror. To maintain a small footprint, it is advisable to keep the focal length below 100 mm. Increasing the tilt angle α increase the radius of the circle traced on the lens L surface, therefore, the clear aperture of the lens L was ultimately a constraint to the maximum axial scan range of the proposed FD-ODL. Therefore, a larger focal length enables to achieve a larger scan range for a set tilt angle, but the clear aperture of the lens would be filled at a smaller tilt angle.

As for a standard FD-ODL, the heterodyne modulation frequency f_{FD-ODL}, i.e., the fringe carrier frequency, can be induced by using an off-pivot configuration, where x_0 is the offset between the rotation axis of the spinning TM, i.e., the stepper motor shaft axis, and optical axis of the FD-ODL. The heterodyne modulation frequency, in the double pass, was determined by the temporal rate of change of the phase delay $\phi(\lambda_0,t)$ [136], i.e.,

$$f_{FD-ODL}(t) = \frac{1}{2\pi}\left|\frac{\partial\phi(\lambda_0,t)}{\partial t}\right| = 4\frac{x_0}{\lambda_0}\left|\Gamma_Z{}'(t)\right|, \tag{10}$$

where $\Gamma_Z{}'(t) = 2\alpha\cdot\partial\left[1-\cos\left(\theta(t)\right)\right]/\partial t$, is the angular velocity about the Z axis of the projection of the optical angle 2α of the tilted mirror on the X-Z plane, which, unlike in the standard FD-ODL, it is not constant in time. Considering that the stepper motor rotation angle $\theta(t)$ varies as $\theta(t) = 2\pi f_{SM}t$, where f_{SM} is the rotational frequency of the stepper motor, $\Gamma_Z{}'(t) = 4\pi\alpha f_{SM}\cdot sin(2\pi f_{SM}t)$. Hence,

$$f_{FD-ODL}(t) = 16\pi\alpha f_{SM}\frac{x_0}{\lambda_0}\,|sin(2\pi f_{SM}t)|. \tag{11}$$

Therefore, by increasing the offset x_0, as in the off-pivot configuration in a standard FD-ODL [137], one increases the maximum fringe frequency. However, the projection on the X-Z plane of the variable angular velocity of the spinning tilted implies that the fringe carrier frequency varies sinusoidally across the axial scan range.

Moreover, as for a standard FD-ODL, the group velocity dispersion can be controlled by modifying the distance between the diffraction grating and the lens L to compensate the potential dispersion imbalance with the sample arm and improve the axial resolution [139].

Figure 4.2 shows a side-by-side comparison between a standard FD-ODL in the left column and the proposed FD-ODL based on a tilted mirror spun by an inexpensive stepper motor in the right column. Three positions of the beam generating equal ΔOPL at each step are shown. Figure 4.2(a),(d) show the reference beam at a position close to the start of the scan so close to $\Delta OPL = 0$; Figure 4.2(b),(e) show an intermediate position close to the half of the scan so at $\Delta OPL_{max}/\ 2$; and Figure 4.2(c),(f) show the reference beam close the position of maximum axil scan ΔOPL_{max}.

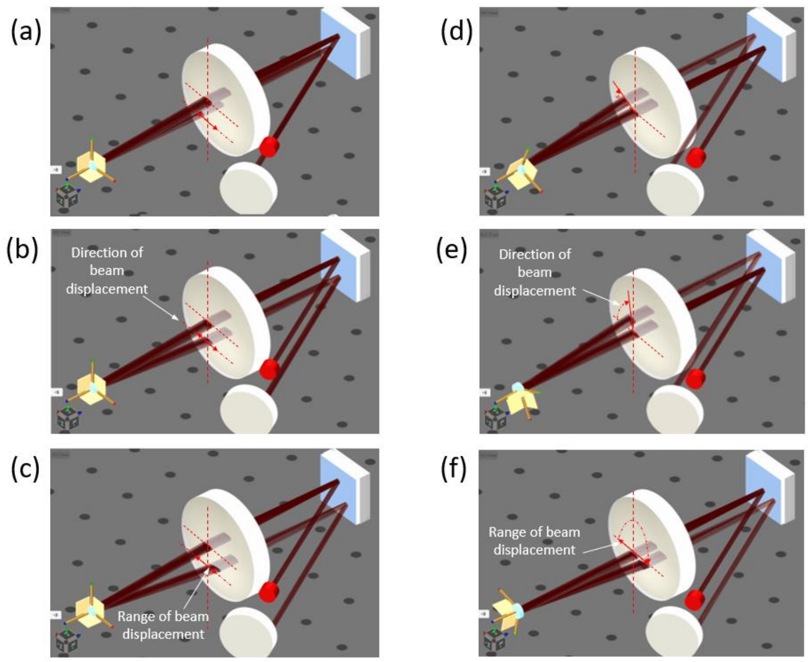

***Figure 4.2 –** 3-D representation of a standard galvanometer-based FD-ODL (left column) and the proposed FD-ODL (right column), showing three corresponding positions of the reference beam when performing an axial scan: (a) and (d) close to the beginning to the scan, (b) and (e) at the middle position, and (c) and (f) close to the maximum scan range.*

In both optical delay lines, the range of displacement of the beam, i.e., a proxy for the axial scan range, is shown as a red solid arrow, while the direction of the displacement of the beam is shown with a red dot-dash line. We can clearly appreciate the differences between the two designs, leading nonetheless to the generation of equal optical delays at the same frequency.

The most striking difference is the need for alternating rotation in the galvanometer-based mirror rotation around the Y-axis for the standard FD-ODL versus the continuous rotation in the stepper motor-based titled mirror rotation around the Z-axis. As continuously rotating the proposed FD-ODL, it does not require the complex electronics control of a servo system nor the high currents needed for the start-stop motion, and thus, a much cheaper mirror actuator can be used in the proposed FD-ODL: a simple low-cost stepper motor.

This is represented also in Figure 4.3, where Figure 4.3(a) and (c) show the variation of the angles θ and α with time for the standard galvanometer-based and the proposed spinning tilted mirror-based FD-ODL, respectively, and Figure 4.3(b) and (d) show their respective actuator speed with time, where the standard FD-ODL requires regular abrupt changes of direction and speed, while the proposed FD-ODL simply requires a constant rotation to provide the same duty cycle and axial scan range as that generated by the standard FD-ODL, if the TM is titled by the corresponding peak α.

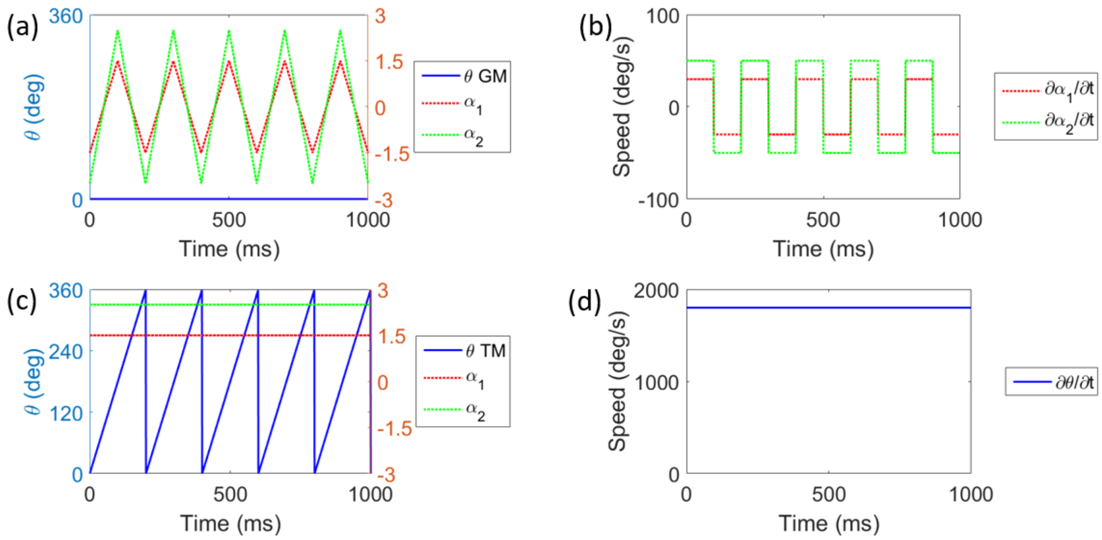

Figure 4.3 - *Representation of the variation with time of the angles of interest $\alpha(t)$ and $\theta(t)$, as defined in Figure 4.1 and Figure 4.2, driven by the actuator responsible for delay generation in (a) a galvanometer-based FD-ODL and (c) the proposed stepper motor-based FD-ODL. Variation with time of the corresponding angular velocities for (b) the galvanometer-based FD-ODL, where the repeated abrupt change of speed and direction is evident, and (d) the proposed stepper motor-based FD-ODL, where the continuously rotating nature of the actuator guarantees its low-cost implementation, regardless of the mirror tilt angle α.*

The advantage of the proposed design of the optical delay line resides in the circular displacement of the light beam during the TM rotation, as this can be implemented with a low-cost stepper motor or DC motor. Additionally, this design is highly versatile, as it enables to independently select the scan range without affecting the scan frequency, as the axial scan range can be changed by modifying the tilt angle α of the TM, whilst maintaining the rotation speed.

4.2.2 – Proposed FD-ODL system components and specifications

We selected off-the-shelf components for the proposed FD-ODL to allow a quick implementation of an experimental prototype. The specifications of the selected optical components are summarized on the left side of Table 4.1.

Table 4.1 *- List of the proposed FD-ODL main optical and mechanical design parameters (left column) and corresponding system specifications (right column).*

Optical and mechanical system design		Expected system specification	
Parameter	Value	Parameter	Value
Central wavelength and bandwidth	850 nm +/- 25 nm	Axial resolution	6 μm
Angle of incidence	30.2 deg	Axial range	7.89 mm / 13.22 mm
DG groove density	600 lines/mm	Axial scan rate	10 Hz
Focal length of L	75 mm	Duty cycle	~100%
Off-pivot offset x_0	3.5 mm	Fringe frequency root-mean-square (RMS)	19.2 kHz
Mechanical tilt semi-angle of TM	1.5 deg / 2.5 deg	FD-ODL cost	<750 USD

We designed the FD-ODL for use with light from a Superluminescent Light Emitting Diode (SLED) centered at 840 nm with 50 nm of bandwidth (SLD-371, Superlum), leading to a theoretical axial resolution of ~6 μm. The light was delivered to the FD-ODL by optical fiber to a collimator (F220APC-850, Thorlabs), producing a beam with $1/e^2$ diameter of 2.41 mm. The beam impinged on a reflective diffractive grating (DG) (GR50-0608, Thorlabs) with a groove density of 600 lines/mm. For the diffracted angle γ to the normal of the DG at the central wavelength to be zero, the incident angle β was set to 30.2 deg. The subsequent lens was an achromatic doublet (AC508-075-B-ML, Thorlabs) with a focal length of 75 mm and a 2" aperture. The focal length was selected to maintain a small FD-ODL footprint and to keep the reference arm optical path length contained, as it adds up to more than 4 times the lens focal length and it needs to be compensated in the sample arm. A shorter focal length was also favored because it implies a smaller spread of the beam on the TM, allowing to use a smaller TM. The diameter of the lens was selected to allow a large axial scan. The spinning titled mirror TM was a 12.5 mm diameter mirror (PF05-03-P01, Thorlabs) and we tested the FD-ODL with the mechanical tilt semi-angle α set to either 1.5 deg or 2.5 deg. The constant tilt to the rotation axis was provided by a 3-D printed collar mount to the shaft of a stepper motor SM which houses the TM already at the set angle by design. The SM (12V Bipolar NEMA 17, Longruner) rotated the TM at a chosen revolution speed. For the sake of demonstration, we programmed a rotation speed of about 5 Hz. The double pass mirror (ME2-P01, Thorlabs) was a 2" circular mirror that had been machined cut to produce a central hole of approximately 5 mm diameter.

The right column of Table 4.1 summarizes the expected system specifications for the proposed FD-ODL with the chosen components. The axial range of the FD-ODL, calculated from Equation (8), was 7.89 mm for α = 1.5 deg, and 13.22 mm for α = 2.5 deg. The axial scan (A-scan) frequency of the ODL corresponds to twice the revolution speed of the SM, as both a forward and backward scan take place during a complete rotation of the TM. Thus, the A-scan rate is ~10 Hz. Moreover, due to the continuous rotation of the TM, the duty cycle of the proposed FD-ODL could approach ~100%. Considering that the root-mean-square (RMS) of a sine wave is $1/\sqrt{2}$ of its peak amplitude, the expected RMS fringe frequency was 19.2 kHz, as per Equation (11).

4.2.3 – Proposed FD-ODL simulation: axial performance analysis

An analysis of the dependency of the optical pathlength variation ΔOPL on the system parameters was conducted using Equation (9) for the components and values shown in Table 4.1. The aim of the analysis was to study the effect of varying the tilt angle α of the TM on the axial scan range using MATLAB to solve the analytical equations and OpticStudio to validate the analytical results. Figure 4.4 shows a 3-D layout of the simulated optical delay line showing the raytracing of several angular configurations of the simulation of the proposed FD-ODL (each of them shown with different colors). We only simulated the optical components: PDM in yellow, DG in pink, lens in gray and TM in blue. The collimator was not simulated. Instead, a collimated input light beam was defined with a uniform apodization. The OpticStudio multi-configuration tool was used to analyze various systems simultaneously with different rotation angle θ of the TM and to study simultaneously the optical pathlength variation ΔOPL in each of them.

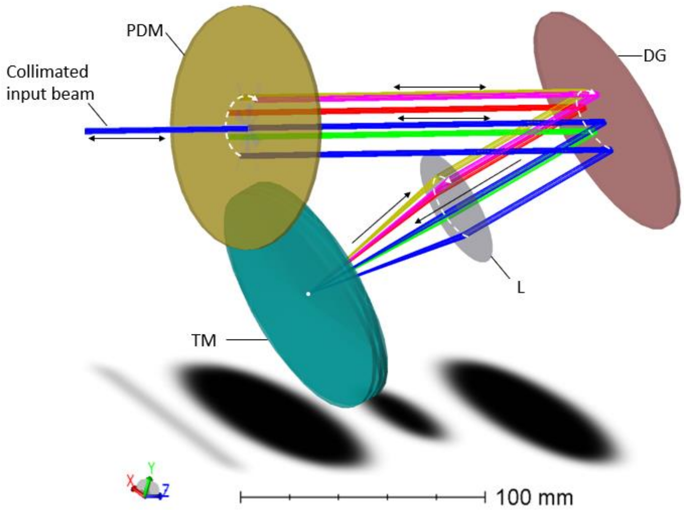

Figure 4.4 – *3-D layout of the simulated FD-ODL showing the raytracing of the angular configurations simulated to vary the angular position θ of the TM (shown with the different colors). Only the optical components of the TM-based FD-ODL are simulated. A white dashed arrow is used to indicate the light beam position variation when rotating the TM.*

The independent variables considered for the analysis of the axial scan range were the stepper motor rotation angle θ and the tilt angle α of the TM. The rest of the parameters were maintained constant.

Figure 4. 5(a) shows in solid lines the ΔOPL induced during a complete rotation of the TM for different tilt angles α. The corresponding axial scan range, *i.e.*, the maximum ΔOPL calculated form the peak-to-peak amplitude, is shown in Figure 4. 5(b) with a solid line as a function of the tilt angle α. ΔOPL follows a sinusoid as a function of θ with a period equal to that of a full rotation of the TM and an amplitude set by the tilt angle α of the TM. Figure 4. 5(b) shows that the axial scan range of the proposed FD-ODL increases linearly with the tilt angle α, as expected from Equation (9). With a tilt angle $\alpha = 5.5$ deg, the axial scan range would be 29.74 mm. Larger tilt angles would redirect the beam outside the clear aperture of the lens L, and therefore cannot be considered with the chosen components. The results from the simulation of the FD-ODL in OpticStudio are also shown in Figure 4. 5(a) and Figure 4. 5(b) with a dotted line and dots, respectively. We can notice that the results of the simulation are in good agreement with the analytical results.

While the maximum axial scan range is nearly 10 times larger than that reported in [136], it is not sufficiently large to cover the variability in AL from different human eyes, considering also that for an average human eye with AL = 24 mm [1], the corresponding OPL is 32.5 mm, assuming an average refractive index of 1.354 for the whole eye [87]. Nevertheless, we solved this issue by employing a dual sample arm, as described in the next section 4.3.2.

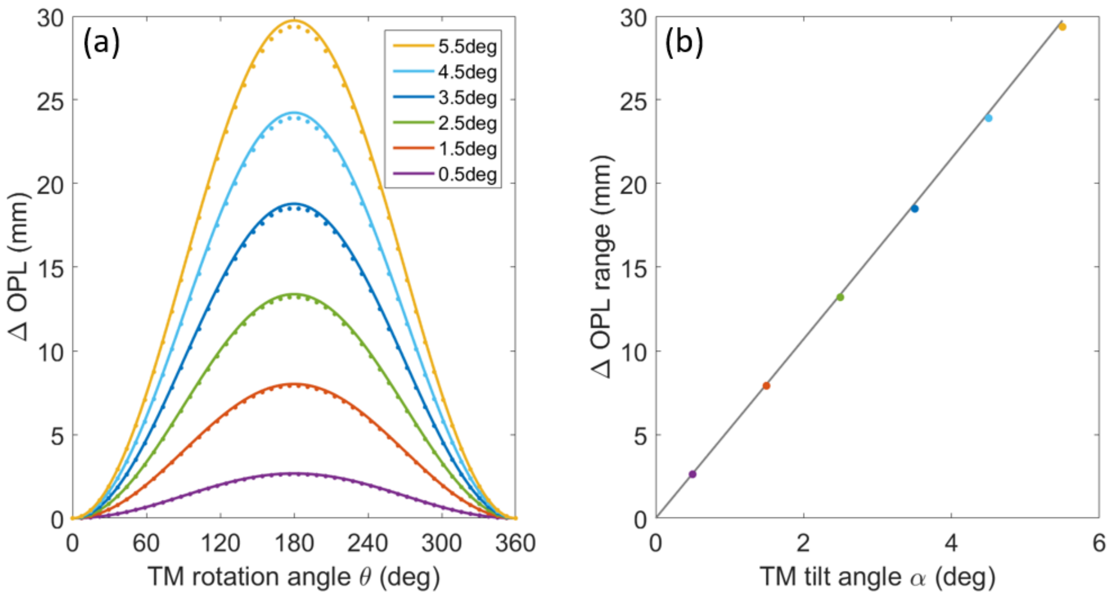

Figure 4. 5 *– (a) ΔOPL variation as a function of the TM rotation angle θ for different tilt angles α. Solid lines represent the analytical plot while dotted lines represent OpticStudio simulations. (b) Axial scan range as a function of the tilt angle α of the TM. The solid lines represent the analytical result while the dots represent the simulations in OpticStudio.*

4.3 – Experimental setup

To demonstrate the axial scan capability of the proposed low-cost FD-ODL in measuring the intraocular distances of a model eye, we built an experimental prototype. In this section, we present the different components of a low-cost 1-D TD-biometer employing the TM-based FD-ODL as the reference arm. In the first place, the spinning tilted mirror TM control system is presented. Then, the OLCR experimental set-up together with the signal processing unit is also explained.

4.3.1 –Tilted mirror (TM) control system

The TM was attached to the shaft of a stepper motor (NEMA 17, Longruner) and controlled through a computer using the combination of a programable Arduino UNO microcontroller (Arduino, Italy) and a T4 DAQ card (LabJack) through a custom interface developed in LabVIEW. Both the Arduino board and the DAQ card used USB connections for communication with the host PC. A schematic representation of the control system with the main electrical connections is shown in Figure 4.6. We designed a TM holder (shown in orange in Figure 4.6) with a hole in the back were to introduce the shaft of the stepper motor and a base with the defined tilt angle α where the mirror was positioned. It also contained an arm extension to be used in combination with a piston to define the starting position of the scan. The designed base mount (shown in gray in Figure 4.6) allowed to hold the stepper motor in place such that the TM holder was aligned with the piston. We also implemented the piston (shown in green in Figure 4.6) such that it passes through the base mount at the proper height to block the rotation of the TM holder before starting the scan. All these components, the base mount, TM holder and piston, were 3-D printed.

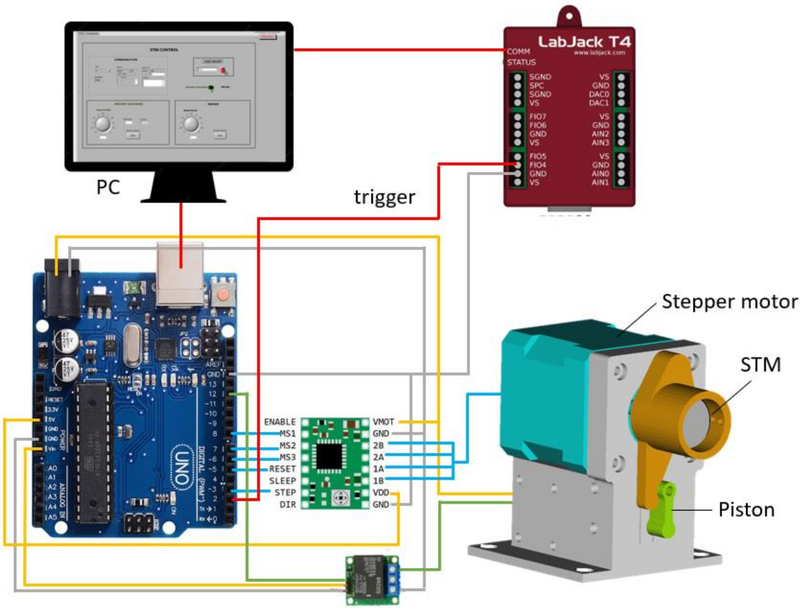

***Figure 4.6 -** Schematic representation of the electronic control system of the TM. A programmable Arduino UNO board sets the specified motor speed for the A-scan, controls a piston to start the A-scan at $\theta = 0$, and generates a trigger signal to synchronize the interferogram acquisition.*

Before starting the axial scan, through a custom developed LabVIEW interface we: 1) started the communication with the Arduino and the T4 DAQ card, 2) switched on the light source, and 3) selected the scan parameters setting the number of A-scans to be acquired and the acquisition frequency. The Arduino board was programmed to drive the stepper motion through a bipolar driver (A4988, Pololu) using a sixteenth micro-step resolution. When connected to the power supply and initialized, the Arduino board activated the piston and rotated the TM until its external arm collides with the piston, defining that position as the starting point of the axial scan, as $\theta = 0$. Then, the piston was retracted back, and the scan started. The Arduino board also generated a square pulse trigger signal every time the rotation of the TM was completed. The trigger signal was received by the T4 DAQ card for the synchronization of the A-scan interferometric signal acquisition. It was also used to characterize the speed of the motor during the experimental measurements.

4.3.2 – OLCR experimental setup

We integrated the proposed FD-ODL in the reference arm of a Michelson-based TD-biometer based on an OLCR configuration, as shown in Figure 4.7 to demonstrate the possibility to measure intraocular distances in a model eye. Light from the SLED was coupled into an optical fiber and split by a fiber coupler with a 75:25 ratio to the reference and sample arms, respectively. The measured optical power from the light source was 12.74 mW, thus an optical power of 7.73 mW and 2.82 mW were split in the reference and sample arm, respectively. This power distribution was implemented to compensate the intensity reduction at the diffraction grating in the reference arm, as the light beam incised 4 times on it. Thus, even if the optimal slitting configuration for a Michelson interferometer is 50/50 [161], in our case we prefer to boost the heterodyne gain by feeding more power in the reference arm. Additionally, for maximum permissible exposure (MPE) concerns, we had to limit the power incident on the eye to fall below the ANSI standards [65] (more details in the Discussion Section). Light returning from the sample and reference arm was coupled in the detection arm and interferes at the photodetector (Nirvana Model 2007, Newport). This photodetector was available in the laboratory and provided dual balanced detection but we used it with a single input to emulate a low-cost photodetector. An analog signal processing (ASP) electronic circuit was also designed to extract the envelope of the interferometric signal (see next section 4.3.3) and thus allowed the digitization of A-scans with the low-cost DAQ card (T4, LabJack) synchronized with the TM movement with the trigger signal generated by the low-cost microcontroller board (UNO, Arduino).

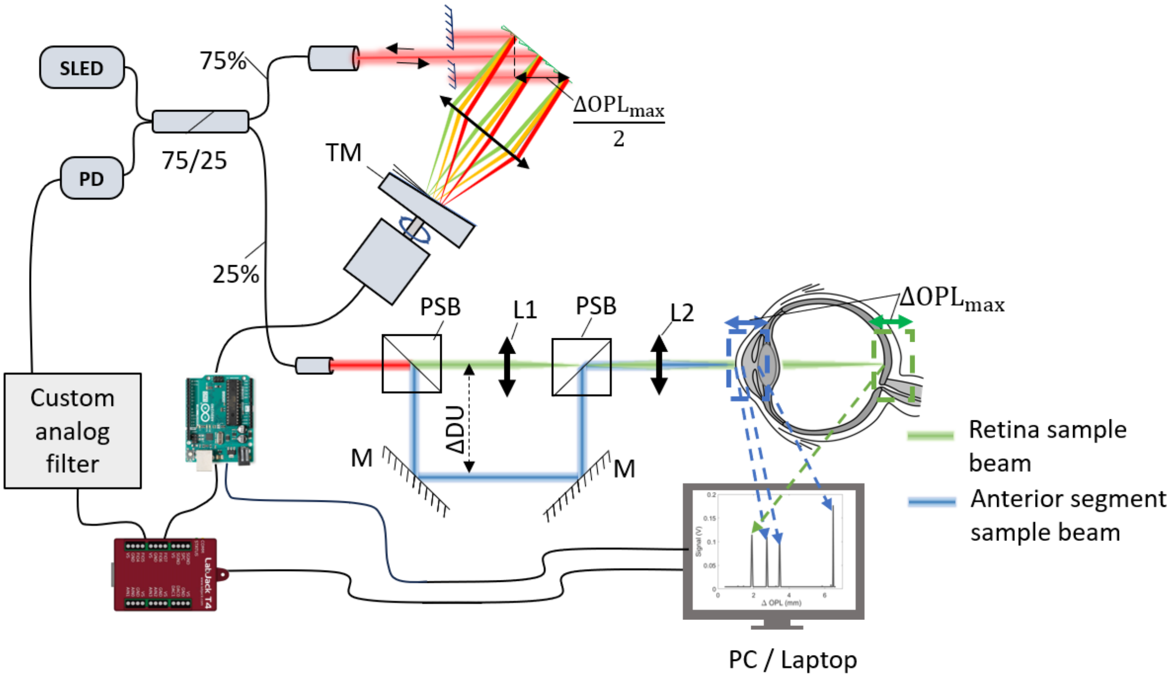

Figure 4.7 ***–*** *Schematic representation of the OLCR-based TD biometer including the proposed TM-based FD-ODL in the refrence arm and a dual sample beam in the sample arm. (SLED: superluminiscent laser emitting diode, PD: photodiode, TM: spinning tilted mirror, M: mirror, PSB: polarization beam splitter, L: lens, DU: detour unit).*

To measure the axial length AL, considering the large portion of humor vitreous without biometric features of interest, we implemented a dual sample arm system [13], as commonly employed in several TD biometers. A fixed delay detour unit (DU) based on two polarization beam splitters (PBSs) was used: 1) to originate two orthogonally polarized beams focusing on the anterior segment and the retina, respectively, thus improving the signal to noise ratio with better backscattered light collection; and 2) to generate two "measurement windows" with a range equal to the axial scan range of the FD-ODL at a set optical pathlength from each other, centered around the anterior segment and retina, respectively. Light in the sample arm was delivered by an optical fiber and a collimator (F220APC-850, Thorlabs). Collimated light splits in two orthogonally polarized components at the first of two PBSs (PBS052, Thorlabs). The beam focusing on the retina (green in Figure 4.7) passed through a 1:1 magnification two-lens telescope, with the first lens L1 (AC127-075-B, Thorlabs) located between the two PBSs, and the second lens L2 (AC508-075-B, Thorlabs) located after the second PBS. The beam focusing on the anterior segment (blue in Figure 4.7) instead, only passed through L2, and therefore it was focused on the cornea. Moreover, the beam focusing on the retina travelled a shorter optical pathlength through the polarization beam splitters than the one focusing on the anterior segment. The sample beams have a power of 1.582 mW and 0.61 mW at the focal plane of the anterior segment sample beam, for the one focusing on the anterior segment and the collimated beam for the retina, respectively. This way, the light backscattered by the anterior segment, and the retina can be simultaneously detected, and the axial length recovered by accounting for the fixed delay between the two sample beams.

4.3.2 – OLCR signal processing system

To reduce the burden of digitizing the full fringe signal at frequencies over 100 kHz (twice the Nyquist limit for the maximum heterodyne modulation frequency), and associated cost of the digitizer, we designed and implemented an analog signal processing (ASP) electronic circuit for signal envelope detection.

The ASP circuit input was the interferometric signal from the photodetector and its output was its one-sided envelope for slower digitization. It comprised 3 stages: high-pass filtering, rectification with amplification, and low-pass filtering. Figure 4.8 shows each of the stages of the ASP circuit. The output at each stage is shown as an example for the signal acquired from the model cornea and recorded at each step with an oscilloscope (DSOX2002A, Keysight Technologies). The output of the ASP circuit, *i.e.*, the A-scan envelope signal, is then digitized by the low-cost LabJack T4 DAQ card with a sampling rate of 15 kS/s. Lastly, the signal peak positions are digitally detected and the signal envelope at each sample surface is then fitted to a Gaussian curve.

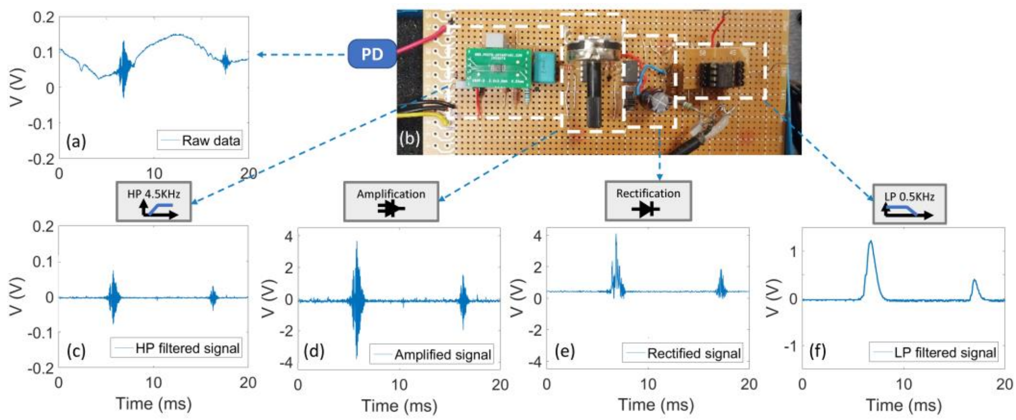

Figure 4.8 *–Representation of the optical low-coherence reflectometry (OLCR) signal processing steps. (a) An example of the raw data of a segment of an A-scan, including anterior and posterior corneal reflections, obtained with the proposed FD-ODL at the photodetector (PD) stage. (b) A photograph of the electronics of the ASP system with white boxes around the components of its main stages. (c)-(f) The corresponding signal at each stage of the APS fed with the raw data displayed in (a).*

The first stage of the ASP circuit included a high-pass filter to suppress the DC and low-frequency components present in the interferogram. Unlike in previous ASP designs for linearly driven galvanometric scanner-based FD-ODL, where a band-pass filter was centered around the set heterodyne modulation frequency [72, 162], here the fringe frequency varied along the scan, so we implemented a high-pass filter instead. This helped to remove the low-frequency modulation due to slight light back-coupling variations throughout the A-scan. The second stage comprised signal rectification and amplification of the high-passed signal as only the positive side of the interferometric signal was needed for the surface detection. The high-passed signal was amplified with a gain of ~10 dB. The rectification stage used a diode-based full wave rectifier to convert the negative component of the signal into positive duplicating the frequency of the signal. To ensure no DC level limits the dynamic range of the subsequent digitizer, an additional capacitor-based DC suppressing stage was implemented. The last stage included a low-pass filter to remove the rectified fringes (with doubled frequency) and leave the envelope signal.

Both high-pass and low-pass filters were low-order Butterworth filters to allow the use of low-cost components in their implementation. Based on the analysis of the fringe frequency variation during the axial scan (see experimental results in the following section 4.4.1), the high-pass filter was designed with a 3 dB-cut-off frequency of 4.5 kHz and a stopband at 1 kHz of 50 dB to filter the low frequencies avoiding the attenuation of the interferometric fringes, and the low-pass filter was designed with a 3 dB-cut-off frequency of 0.5 kHz and a stopband at 30 kHz of 50 dB to allow the envelope extraction of the interferometric signal. A filter design software (Filter Design Tool, Texas Instruments) was used to design the filter based on off-the-shelf active components. From the filter design software, the high-pass filter was implemented as a 4th order Butterworth filter with a measured 3 dB-cut-off frequency of 4.5 kHz and a stopband at 1 kHz of 52.3 dB, and the low-pass filter as a 2nd order Butterworth filter with a 3 dB-cut-off frequency of 0.5 kHz and a stopband at 30 kHz of 71.1 dB. We experimentally characterized both filters by using a function generator to insert a sinusoidal wave with a variable frequency. Figure 4.9(a) and (b) show the theoretical and experimental performance of the high-pass and low-pass respectively. In solid lines the theoretical performance of the designed filters is shown simulated with MATLAB, and in dots their experimental characterization, which is in good agreement with the theoretical results.

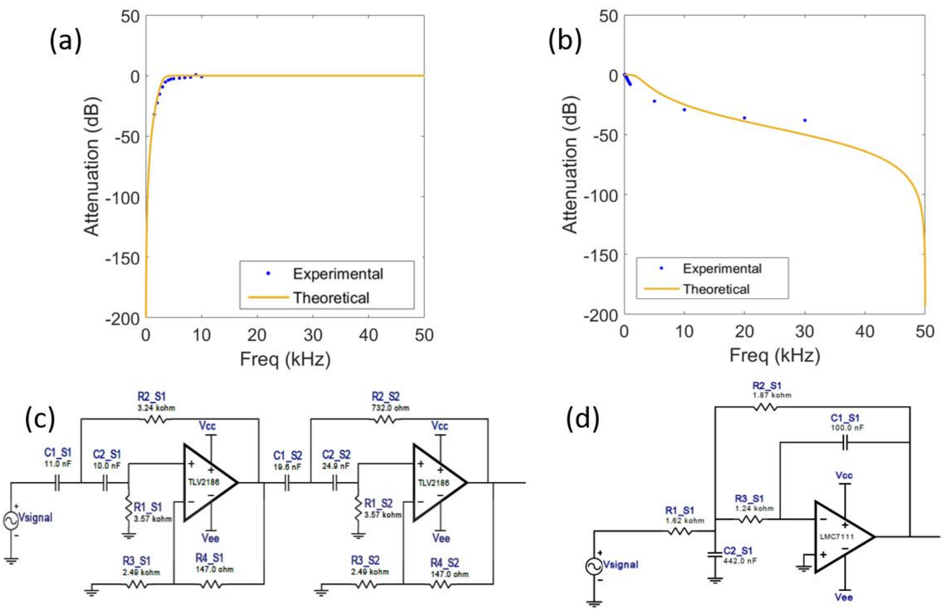

Figure 4.9 – *Frequency performance of the high-pass (a) and low-pass (b) filters, showing their theoretical (solid line) and experimental (dots) performance. Circuit diagram of the designed filters based on off-the-shelf active elements for (c) the high-pass filter and (d) the low-pass filter.*

4.4 – Experimental measurements

The proposed FD-ODL was experimentally implemented and validated in combination with the presented OLCR-based TD-biometer. In this section we present the different experimental results obtained during: 1) the characterization of the proposed FD-ODL and the implemented OLCR TD-biometer, 2) the comparison of the proposed FD-ODL with a standard galvanometer-based FD-ODL, and 3) the measurement of the biometric parameters of a model eye. The TM-based FD-ODL biometric measurements of the model eye were compared to those obtained with a research custom SS-OCT system and two commercial biometers, namely the Lenstar and ANTERION devices.

4.4.1 – System characterization

The variation in optical pathlength ΔOPL with the TM rotation angle θ, the axial scan range and the fixed delay between the two sample beams have been experimentally characterized by a calibration procedure consisting of axially displacing a flat mirror in the sample arm by equally spaced distances and recording the corresponding interferograms with the oscilloscope (DSOX2002A, Keysight Technologies). From the interferograms, the envelope peak positions, the envelope Full-Width at Half Maximum (FWHM), i.e., the axial resolution, and the heterodyne modulation frequency f_{FD-ODL} were extracted. The resulting calibration curve fitting the sequence of the envelope peak positions was then used to linearize the TD-biometer A-scans, varying sinusoidally with time.

Figure 4.10(a) and (b) show an overlay of the interferograms recorded at different axial positions of the sample mirror, each one displaced by 0.5 mm from the previous, for the anterior and posterior segment sample beams respectively. In this case the TM was titled by an angle α = 1.5 deg and the A-scan frequency was 9.5 Hz. Due to the sinusoidal dependence of ΔOPL with the tilted mirror rotation angle θ, the axial positions of the mirror are not equally spaced in time, as θ varies linearly with time. By fitting a sinusoid to the timepoints at which the equidistant peak positions were found, we obtained an experimental distance calibration curve for the axial scan of the FD-ODL (see Figure 4.10(c) and (d) for the anterior and posterior segment sample beams calibration respectively).

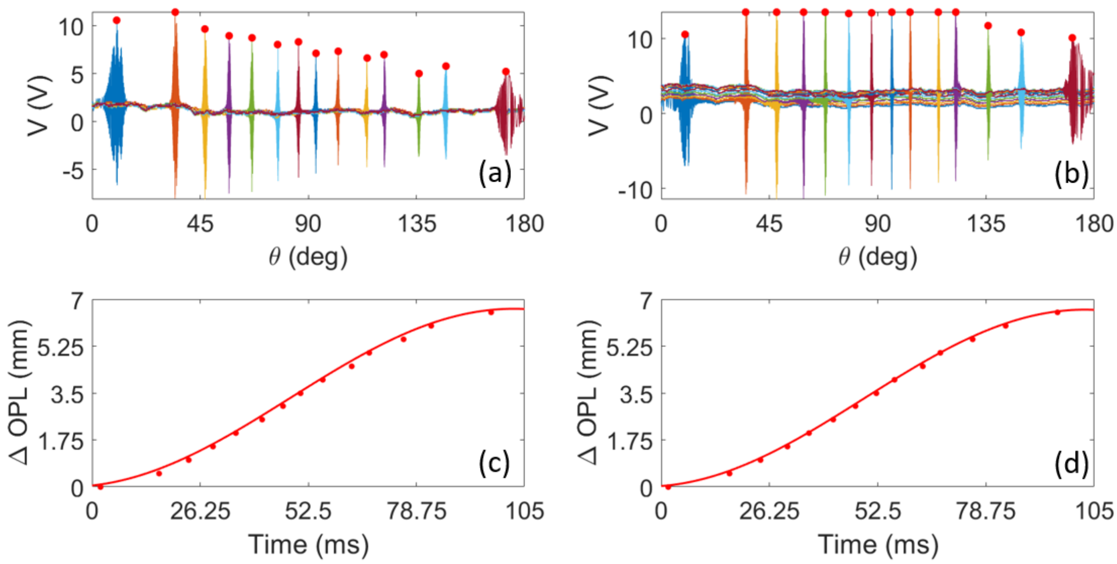

Figure 4.10 *- Scan performance and distance calibration of the proposed FD-ODL. (a) Overlay of 14 interferograms recorded at different axial positions of the sample mirror, each one displaced by 0.5 mm from the previous using (a) the anterior and (b) the posterior sample beams. Calibration curve of ΔOPL versus time of (c) the anterior and (d) the posterior sample beams. Solid lines represent fits. Points represent experimental data.*

As we can observe, there is a noticeable difference in the peak intensity during the axial scan of each sample beam. While in the posterior sample beam the peak intensity is maintained highly constant over time for θ between 35 and 120 degrees and decreased outside that range (Figure 4.10(b)), in the case of the anterior sample beam the peak amplitude is reduced after 45 deg of rotation (Figure 4.10(a)). This effect was expected as, while the posterior segment sample beam is collimated, the anterior segment sample beam is focused at the sample plane, thus the axial peak profile follows its confocal function. Moreover, the experimental duty cycle, calculated from the distance calibration as the angular range where the interferometric signal is measurable, was at least ~90%. The measured axial scan range for the proposed FD-ODL with the TM at an angle α = 1.5 deg, was 6.64 mm and 6.61 mm for the anterior and the posterior segment sample beam, respectively, in agreement but slightly smaller than the expected 7.89 mm from theory.

The axial resolution of the OLCR biometer was experimentally measured by analyzing the FWHM of the envelope of the interferometric signals after applying the distance calibration. Figure 4.11(a) shows, as an example, the interferogram for $\Delta OPL \cong 5$ mm from the previously presented distance calibration of the posterior segment sample beam in the case of α = 1.5 deg, with a FWHM of the signal envelope equal to 31.1 µm. The full characterization throughout the axial scan is presented in Figure 4.11(b) for the anterior and posterior sample beams in red and blue, respectively. In this representation the first and last point measurements are omitted because the full envelope was not visualized. The average axial resolution was 44.15 $\pm$ 7.79 µm and 38.17 $\pm$ 3.62 µm for the anterior and the posterior sample beams respectively, roughly constant throughout the axial scan, especially in the case of the posterior sample beam. We also characterized the heterodyne modulation frequency f_{FD-ODL} as a function of the axial scan distance. The expected sinusoidal trend was observed, with an RMS value of 22.62 kHz and 22.57 kHz for both sample beams, not far from the theoretical value of 19.2 kHz.

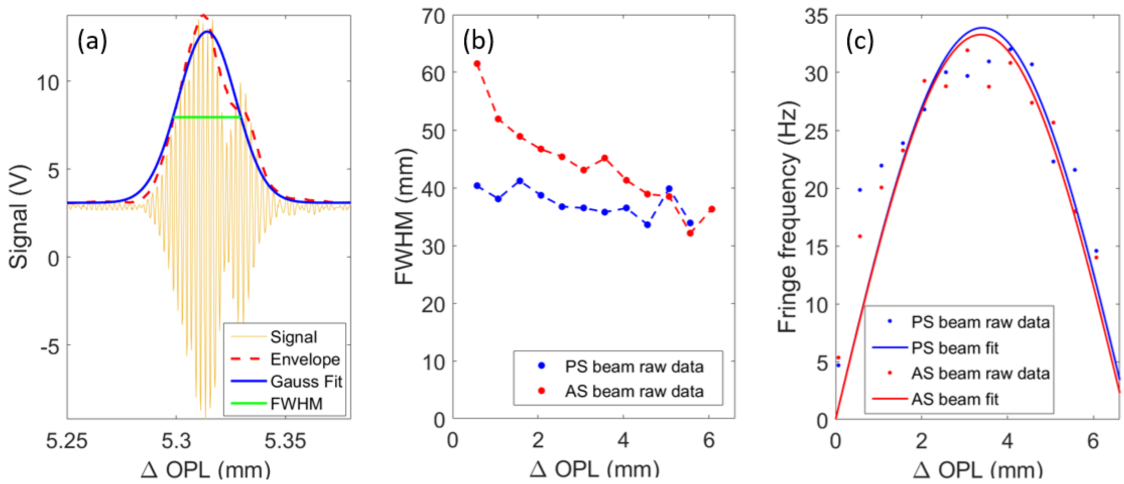

***Figure 4.11** - Characterization of the axial resolution and heterodyne modulation frequency. (a) Interferogram close-up on a reflector point-spread-function for the case of α = 1.5 deg. (b) Axial resolution characterization throughout the axial scan for the anterior and posterior segment sample beams. (c) Heterodyne modulation frequency f_{FD-ODL} as a function of the axial scan distance for both sample beams.*

Lastly, we characterized the fixed delay of the detour unit DU between anterior and posterior beams in the sample arm, which was set at an optical pathlength difference of 33.3 mm.

4.4.2 – Comparison to a gold standard FD-ODL

For benchmarking purposes, we compared the axial scanning performance of the proposed low-cost FD-ODL with that of a standard FD-ODL based on a galvanometric scanner (> 2000 USD), where we exchanged the stepper motor and tilted mirror with a galvanometer scanner (GVS012, Thorlabs). We ran the calibration procedure for both FD-ODLs for two axial scan ranges each, with similar A-scan rate. For the standard FD-ODL, the galvanometer mirror was driven with a triangular wave. Figure 4.12 shows the experimental distance calibration obtained for both FD-ODLs for their two scan ranges.

The measured axial scan ranges for the proposed FD-ODL (see Figure 4.12(b)) was 6.61 mm and 11.08 mm for the cases where the TM was tilted at an angle α = 1.5 deg and α = 2.5 deg, respectively. Thus, the expected trend with the increasing tilt angle was observed, although in both cases the measured axial scan range was smaller than the expected 7.89 mm and 13.22 mm, respectively, from theory. For the standard FD-ODL (see Figure 4.12(a)), where α was varied between -1.6 deg and 1.6 deg, the corresponding axial scan range was 8.16 mm, while when α was varied between -2.8 deg and 2.8 deg, the corresponding axial scan range was 12.83 mm. Figure 4.12(c) and (d) show the ΔOPL plotted against the actuator angle of interest, i.e., α and θ, for the standard and proposed FD-ODL, respectively. These results demonstrate that the angle α determines the axial scan range, as expected from theory, and that a continuous rotation of θ allows to complete both a forward and backward scan without the need of counter rotation, as required for the standard FD-ODL (compare to Figure 4.2).

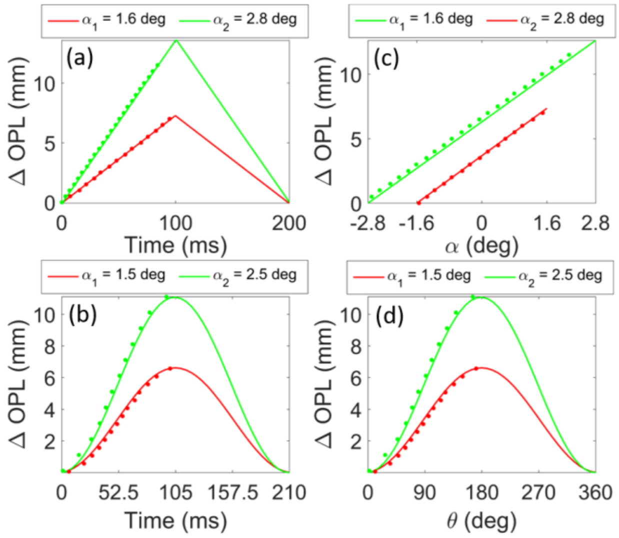

Figure 4.12 *- Full forward and backward variation of ΔOPL with time for two axial scan ranges for (a) the standard FD-ODL and (b) the proposed FD-ODL. Experimental datapoints are shown as dots. Solid lines represent fits. Corresponding experimental fits to the variation of ΔOPL with the actuator angle of interest, i.e., α for (c) the standard FD-ODL, and θ for (d) the proposed FD-ODL.*

4.4.3 – Experimental axial biometry results

To demonstrate the ability of the proposed TD-biometer to record ocular biometry measurements, we employed a model eye (OCT model eye, Modell-Augen Manufaktur) comprising air-spaced cornea, crystalline lens, and layered retina, which were designed to mimick the human eye biometric features. We acquired measurements of the CCT, ACD and AL of the model eye with the proposed FD-ODL-based OLCR-biometer (at the case of α = 1.5 deg) and compared the obtained results with those obtained with a custom research SS-OCT system [120], Lenstar LS 900 (Haag-Streit), a prime example of OLCR TD 1-D biometer, and with those obtained with ANTERION (Heidelberg Engineering), an example of 3-D SS-OCT biometer. When possible, we obtained the optical distances and then converted them into physical distances by dividing them by the refractive indices provided by the model eye manufacturer. The experimental measurement of the model eye is shown in Figure 4.13.

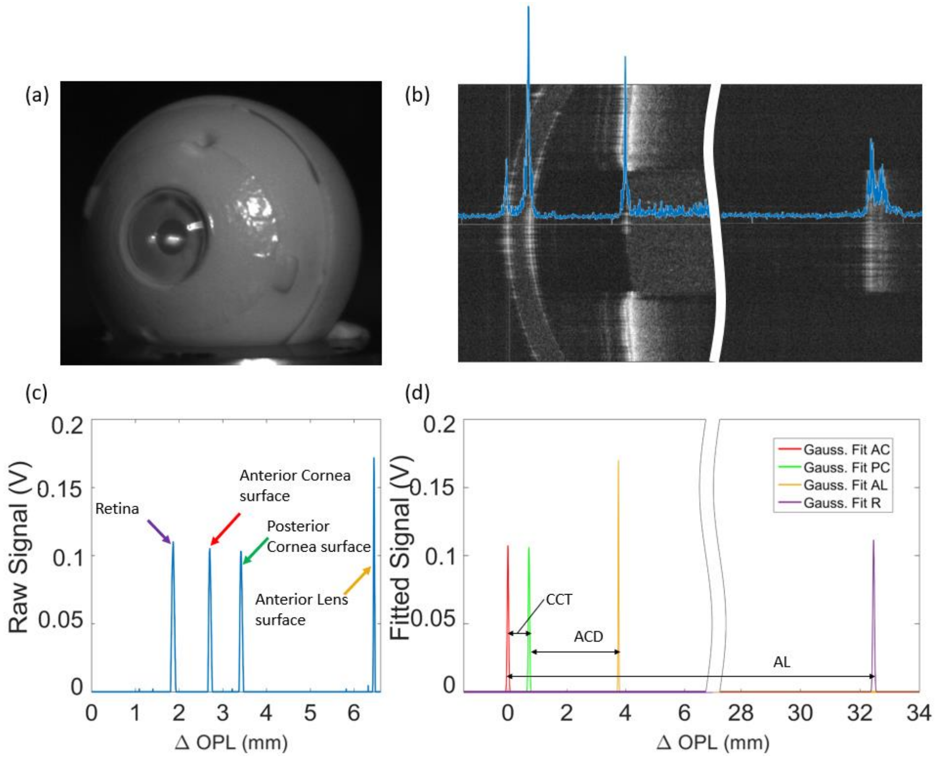

Figure 4.13- – *Model eye biometry. (a) Photograph of the model eye. (b) B-scan of the model eye acquired with a custom laboratory SS-OCT system and the central scan overlaid in blue. (c) Detected A-scan with the proposed OLCR TD-biometer after the ASP processing and optical pathlength calibration. (d) Reconstructed A-scan with Gaussian fitted peaks accounting for the fixed delay between the anterior and the posterior sample beams.*

Figure 4.13(a) shows a photograph of the model eye during a biometry measurement with the proposed OLCR biometer. Infrared light scattered by the various surfaces of the anterior segment highlights a trace of the axis where the biometry measurement takes place. Figure 4.13(b) shows the custom laboratory SS-OCT system B-scan of the full-length of the eye (edited to skip the posterior lens and most of the humor vitreous), and the corresponding central axis A-scan (in linear units) with the cornea, anterior lens, and retinal reflections clearly visible. Figure 4.13(c) presents the detected A-scan with the proposed OLCR TD-biometer along the optical axis of the model eye, after the ASP processing, low-cost DAQ digitization, and optical pathlength calibration. Peaks from both the anterior and posterior segment appear in the A-scan. These correspond, in order from left to right, to the retina, anterior corneal surface, posterior corneal surface, and anterior crystalline lens surface. Each ocular surface signal envelope was fitted with a Gaussian function. Figure 4.13(d) shows the fitted peaks accounting for the fixed delay between the two sample beams induced by the detour unit. Therefore, it shows a full-length A-scan in optical pathlength units, where zero pathlength has been assigned to the anterior corneal surface. To measure the physical axial biometric distances of the model eye, we worked out the peak positions of the aforementioned ocular surfaces and divided the corresponding distances by the associated refractive indices provided by the manufacturer. We repeated these measurements several times after realigning the model eye to simulate different measurement sessions.

The measured ocular biometric parameters for the model eye are summarized in Table 4.2, and compared to those measured with the custom laboratory SS-OCT system and the Lenstar and ANTERION biometers. The measured CCT was 0.478 mm $\pm$0.039 mm, in good agreement with the values from all other instruments with a maximum mean error of $23\ \mu\mathrm{m}$. The measured ACD was $2.968\ \mathrm{mm} \pm 0.101$ mm versus a value of $3.114\ \mathrm{mm}$ by the ANTERION, and a value of $3.222\ \mathrm{mm}$ by the custom SS-OCT system. The differences can be possibly due to slightly different alignments of the corneal apex among measurements and across systems. The Lenstar software did not identify the crystalline lens in the scan, probably due to the difference in back reflection compared to an average human eye. For the AL measurement, a good agreement between our TD biometer and the custom SS-OCT system was obtained at 24.004 mm $\pm$0.027 mm and 23.959 mm, respectively. Lenstar returned a value of 22.95 mm, and ANTERION was not used to measure AL. The discrepancy with the measurement from the Lenstar can be explained by the difference in the refractive indices used by default for human eye measurements, versus those required for an eye phantom where both the spaces for the aqueous humor and vitreous humor are filled with air.

Table 4.2 *– Benchmark of average biometer readings from different devices*

Ocular distance	Proposed TD-OCT biometer	Custom SS-OCT biometer	ANTERION	Lenstar
CCT (physical)	0.478 mm	0.501 mm	0.489 mm	0.492 mm
ACD (physical)	2.968 mm	3.222 mm	3.114 mm	-
AL (physical)*	23.985 mm	23.959 mm	-	22.95 mm

*Assuming eye model full of humor-mimicking fluid

For the conversion of the CCT optical pathlength to the CCT physical pathlength, we used a refractive index of 1.416, as indicated by the manufacturer. For the conversion of the AL optical pathlength to the AL physical pathlength, assuming the eye model was full of humor-mimicking fluid, as the Lenstar system did by default, we used a refractive index of 1.354 as the human eye average [87]. However, this might not be the exact value used by the Lenstar system itself.

4.5 – Future work

In order to achieve *in vivo* biometric measurements, the following modifications to the current system are required:

- Reduction of the optical power in the sample arm to below the MPE to allow eye-safe *in vivo* measurements.
- Implementation of a pupil camera to allow the visualization of the patient's eye with respect to the OLCR sample beam and thus allow an easy alignment of the patient.

- Implementation of a fixation channel and fixation checks, to reduce ocular movements of the patient's eye during the measurement.

Moreover, to convert the developed proof-of-concept into a portable device, the fiber interferometer together with the free-space reference arm and the detection system could be designed to fit in a sturdy but compact case. Additionally, the sample arm could also be designed to fit within a handheld probe to allow to hold the sample beam in front of the patient's eye. In such a case, some mechanical stabilization of the patient's head could be achieved by a simple forehead support. To also allow *in vivo* measurements, larger tilt angles and greater motor speeds should be possible.

Lastly, an upgrade of the detour unit could be achieved by motorizing it. In such a way, the detour unit could be adapted to allow the use of the device with a wider range of patients. This could be especially beneficial to cover very long or short eyes.

4.6 - Discussion

We presented a novel, low-cost FD-ODL enabled by converting the alternate counter-rotating motion needed for the standard galvanometer-based FD-ODL into a continuously spinning motion of a tilted mirror, driven by an inexpensive stepper motor. We characterized its performance and compared it to that of a standard FD-ODL. We then employed it into an OLCR biometer to provide the intraocular distances of a model eye, and we benchmarked the system against the results produced by a custom SS-OCT biometer and two commercial biometers.

In terms of cost, we evaluated that even with off-the-shelf components, the cost of the proposed FD-ODL optics and mechanical actuator did not exceed 750 USD, with the stepper motor itself only contributing to less than 50 USD, compared to an average of ~2000 USD for a 1-axis galvanometer mirror scanner. This could be very advantageous for remote and low-resource settings. In terms of transportability, the FD-ODL fits within a relatively small footprint of a 25 x 15 cm breadboard, with the remaining parts of the OLCR biometer prototype being amenable to a compact design. In terms of hand-held operability, and more in general, reduction of motion-artifacts during acquisition, the single most important factor is the A-scan rate and the axial scanning speed. Even though the A-scan rate used in this demonstration was only 10 Hz, the OLCR biometer exhibited an effective axial scanning speed of 222 mm/s, considering the scan window duplication via the detour unit in the sample arm. These values are still too low for hand-held artifact-free axial biometry, but they compare well with those from the standard of care in OLCR TD-biometers, i.e., the Lenstar, with an A-scan rate of 12.8 Hz and an effective axial scanning speed of 420 mm/s.

Moreover, the stepper motor frequency could be reasonably increased to 15-20 Hz, leading to an A-scan rate of 30-40 Hz. Alternatively, for a slightly higher cost, but still below 100 USD, the stepper motor could be substituted by a DC motor which could lead to A-scan rates up to 100 Hz. The effect of vibrations or small precession angles would need to be thoroughly evaluated in such a case.

In terms of scan range, we derived the analytical equations describing the relationship between the desired axial scan range of the proposed optical delay line and the tilt angle α of the TM. The experimental characterization of the scan range for different α showed that the axial scan range increased with α. Although angles up to 5.5 deg could be accepted by the proposed experimental FD-ODL, the alignment tolerances for proper light back-coupling become more stringent with larger angles α. Therefore, in the developed prototype, only angles up to 2.5 deg were tested, leading to a measured maximum scan range of 11.08 mm. The measured axial range was shorter than expected from theory by 15%. This could be attributed to a combination of the low manufacturing tolerances of the 3-D printed collar mount to the shaft of a stepper motor SM which houses the TM, and the TM not sitting exactly at the set angle inside the mount. A custom machined mount would be beneficial in reducing this discrepancy.

The short axial scan range compared to the full axial length of a human eye is not considered a particularly limiting factor of the experimental implementation as can be easily extended with the use of the detour unit in the sample arm to separately cover anterior and posterior segments, a common practice for most commercial biometers. Flawless identification and separation of the retinal signal from the anterior segment is utterly important in such a configuration. Signal processing strategies can help with it, by simply contrasting the characteristic prolonged scattered signal with depth from the retina versus the signal from the anterior segment surfaces, or, if needed, with the addition of hardware methods to encode a discriminating factor between the two segments. Such hardware methods could include either a phase modulator in one of the two sample beam paths, or simply a beam chopper to block periodically one beam and discern the corresponding signal. Nevertheless, the current implementation can already find good use in low-cost biometer by providing the intraocular distances of an eye.

We also compared the axial scan range performance of the proposed FD-ODL with that of a standard galvanometer-based FD-ODL, by substituting the spinning tilted mirror with a galvanometer mirror and changing the rotation axis from along the Z-axis back to the Y-axis. The experimental characterization of both FD-ODL implementations showed similar scan ranges for a given α (maximum). Small differences are due to the fact that the galvanometer voltage to angle conversion was fully calibrated only after the measurements, resulting in slightly larger maximum α than desired. A significant difference we expected and observed was in the effect that changes in the axial scan range have on the FD-ODL actuator for a set A-scan rate. To increase the axial scan range at a given A-scan rate, in the standard FD-ODL the galvanometer scanner is required to scan faster a larger angular range, increasing its power consumption, especially if driven with a triangular waveform. In the proposed FD-ODL instead, the axial scan range and scan rate are decoupled from one another. The stepper motor rotation only determines the axial scan rate, while the set tilt angle α determines the scan range, making our solution not only cheaper, but more versatile than the standard one. Nonetheless, a drawback of the proposed FD-ODL is the sinusoidal variation of the optical pathlength in time. Thus, a distance calibration throughout the axial scan range is required to linearize the depth reflectance profile of the measured samples.

The sinusoidal variation in optical pathlength also implied a sinusoidal variation of the interferometric fringe frequency, thus a high-pass filter in the first stage of the ASP was implemented instead of a standard band-pass filter centered at a set fringe frequency. Because of this, the proposed FD-ODL provided a 89% duty cycle, instead of the theorized 100%.

In terms of biometric accuracy, two factors are important: the system axial resolution and the corneal centration for measurement repeatability. Although sub-resolution accuracies can be obtained for distances between strongly reflecting surfaces as those in the anterior segment, the axial resolution is a good measure of the standard ceiling for axial biometry accuracy. In the proposed OLCR biometer, the measured axial resolution was significantly broader than expected from the theory, despite being roughly constant throughout the scan range. This discrepancy could be explained in part by the residual dispersion imbalance between the sample and reference arm, and possibly by some spectral vignetting at the TM, due to an offset, for the heterodyne frequency generation, as large as 3.5 mm, with a mirror radius of only 6.25 mm. This could have caused a spectral bandwidth reduction, leading to a worse axial resolution. If so, the choice of a slightly larger mirror and careful dispersion imbalance compensation should restore the theoretical resolution of 6 μm.

Nevertheless, corneal centration is far more critical to measurement repeatability and likely the more limiting factor for the detected discrepancy in the ACD measurement. For eye alignment, our system only used a single pupil camera (see Figure 4. 14(a)) not fully integrated in the sample arm of our OLCR biometer. The pupil camera could be integrated collinearly with the OLCR sample arm or in a stereoscopic setup and Purkinje reflection detection [9, 89] could be detected to ensure repeatable eye alignment.

For the sake of demonstrating the capability of an OLCR biometer based on the proposed FD-ODL, we measured the intraocular distances of a model eye and compared them to the ones obtained with a SS-OCT laboratory system and commercial optical biometers. The relatively high intra-system standard deviation of 141 mm for the ACD of the model eye considering repeated measurements after model eye realignment can be attributed to the absence of the corneal centration setup in our OLCR biometer. Similarly, the difference in the ACD measurement with that by the custom SS-OCT laboratory system and the ANTERION system points to the fact that, for example, for the scan shown in Figure 4.13(d), the measurement axis of the proposed OLCR biometer was likely slightly off the corneal apex, therefore resulting in a slightly smaller ACD measurement, while the CCT measurement was essentially the same for all systems. Differences in the intraocular distance measurements from the commercial biometers can also stem from the different refractive indexes used by each instrument. While the Lenstar uses refractive indices compatible with those of an adult eye [87], they are hidden from the user and their exact value kept proprietary and the intraocular distances are only reported in their physical units. However, as the model eye was made of different materials such as glass, polymers and air, it would be beneficial to compare the optical distances first. As the exact refractive indices used in the Lenstar were unknown, we use the approximations reported in [87] to reconvert the measurement back to optical distances for further processing. In the ANTERION system instead, the optical distances were available, so we converted them into physical distances by dividing them by the model eye manufacturer's refractive indexes. An error in the used approximation could be to blame for the difference in the AL measurement for the Lenstar system.

Lastly, the biometer could be tested on a human eye exchanging the 75:25 fiber couple with a 90:10 fiber coupler, to ensure that the sample beam collective power is well below the ANSI laser safety standards for maximum permissible eye exposure [64, 65]. This system modification should not affect the ability to detect the ocular surfaces, as the reference power will receive 20% more power, boosting the heterodyne gain.

4.7 - Conclusion

We presented a novel low-cost FD-ODL employing a spinning mirror tilted by a fixed angle to the shaft of an inexpensive stepper motor, with the rotation axis parallel to the optical axis of the beam incident on the tilted mirror. We derived the analytical equation for the variation of the optical pathlength and the heterodyne modulation frequency as a function of the stepper motor rotation angle and the angle of the tilted mirror. We experimentally characterized the former throughout the scan range for two tilt angles and compared it with the variation of optical pathlength over time for a standard FD-ODL with the galvanometer scanning up to the same angles, both at a nominal frequency of 5 Hz, resulting in an A-scan rate of 10 Hz. The measured scan ranges for the proposed FD-ODL were 6.61 mm and 11.08 mm, for a nominal tilt angle of 1.5 deg and 2.5 deg, respectively. They were in good agreement (up to a 15% difference) with both the theory and the equivalent scan range for the standard FD-ODL. We then characterized the heterodyne modulation frequency, the axial resolution and the time-to-optical pathlength calibration curve for the smaller tilt angle in the proposed FD-ODL, obtaining an RMS fringe frequency of 22.62 kHz, an average axial resolution of 38.2 μm, and an evident sinusoidal calibration curve. We integrated the proposed FD-ODL in a dual beam OLCR system with the central wavelength at 840 nm, delivering a power of 1.582 mW and 0.61 mW on the cornea, for the beams focusing on the anterior segment and retina, respectively. We built a custom ASP circuit board to extract the interferometric signal envelope and ease the digitizing task for low-cost integration. Finally, we acquired repeated biometry measurement of a model eye, showing readings of the central cornea thickness, anterior chamber depth and axial length, and compared those to the ones acquired with a custom SS-OCT laboratory system, and two commercial biometers, showing good agreement among each other.

In summary, the proposed optical delay line reduces the cost of the standard galvanometer-based FD-ODL. Additionally, it allows to independently select the A-scan rate, by changing the stepper motor speed, and the axial scan range, by simply changing the set tilt angle of the rotating mirror. Sourcing a faster motor will enable to overcome the current limitations on the A-scan rate and expand its use to diagnostic and scientific applications. Integration of the proposed FD-ODL in an OLCR biometer design with a compact form factor with a more conservative coupler splitting ratio for eye safety and a corneal centration setup shall provide a robust portable device for biometry testing in remote areas.

Chapter 5
ETL based optical beam scanner for whole eye OCT scanning

In this chapter, I describe the development of a novel optical beam scanner that employs electro-tunable lenses (ETL) to scan the beam and to control its vergence. I present the working principle as well as the implementation of a prototype with which a complete experimental characterization of the technique was performed combining the beam scanner with a custom SS-OCT system to validate its capability of performing whole eye OCT scans.

This chapter is based on the paper by M.P. Urizar et al. “Optical beam scanner with reconfigurable non-mechanical control of beam position, angle and focus for low-cost whole-eye OCT imaging” published in Biomedical Optics Express (2023). The authors of the work are María Pilar Urizar, Enrique Gambra, Alberto de Castro, Álvaro De la Peña, Onur Cetinkaya, Susana Marcos and Andrea Curatolo.

The author of this thesis (1) performed the literature search, (2) developed the analytical and simulation analysis of the system, (3) implemented and characterized the experimental prototype of the system, (4) developed and acquired whole eye data with the SS-OCT system and (5) contributed to prepare the manuscript (supervised by Dr. Andrea Curatolo and collaborating with Dr. Enrique Gambra and Dr. Alberto de Castro).

This work is protected by the patent [EP22382246] owned by the Institute of Optics “Daza de Valdés” and presented at the EPO, for which the author of the thesis contributed and is a co-inventor.

This work was presented as an oral contribution at “Optica Biophotonics Congress: Biomedical Optics” in the 24th-27th of April 2022 in Fort Lauderdale (USA) and “Optica Biophotonics congress: optics in the life sciences” in the 21st-24th of April 2023 in Vancouver (Canada). Part of this work was also presented as a poster contribution at the PhDay of the University Complutense of Madrid in 11th – 14th of October 2022 in Madrid (Spain), being chosen as finalist.

5.1 - Introduction

As presented in Chapter 1, although the indispensable measurement in ocular biometry for cataract surgery planning is the axial length and the intraocular distances of an eye, obtaining structural information from the eye as a whole is also of great interest. Also, more accurate and repeatable measurements can be obtained when imaging the posterior segment of the eye in a region around the retinal foveal pit to ensure the patient fixation was maintained during the measurement of the axial length [163-165]. Additionally, there are other clinical and vision science applications such as narrow-angle glaucoma and myopia progression studies that require obtaining both anterior and posterior segment OCT images and would benefit from whole-eye biometry measurements performed by a single device [13, 166]. In narrow-angle glaucoma, an anterior segment OCT scan provides information about the irido-corneal angle [167] but a posterior segment OCT scan is usually performed to measure the retinal nerve fiber layer thickness. In myopia progression studies a biometric measurement of the axial length is important to evaluate the associated risk of myopia progression, but also peripheral eye length measurements and lens biometry data are of interest to evaluate peripheral defocus and to understand its role as driver of myopia development [168, 169]. Additionally, imaging the retina in myopic subjects can be clinically relevant as the OCT scan can inform on potential myopic maculopathy and pathologic myopia [170].

However, whole-eye OCT scanners are not very common probably because of the technical difficulties to change the focus and the scanning configurations to image each ocular segment. The optical power of the anterior segment of the eye imposes the need of different scanning configurations for each ocular segment. While for imaging the anterior segment of an eye the typical scanning configuration involves a parallel or telecentric displacement of a focused beam perpendicular to the OCT imaging axis (see Figure 5.1(a)), to image the posterior segment of the eye, the scanning configuration implies an angular displacement of a collimated beam that ideally pivots at the pupil plane of the eye so that the light beam is focused on to the retina by the cornea and crystalline lens without affecting the beam direction (see Figure 5.1(b)) [171]. Conventional OCT systems are set up to perform either anterior or posterior segment scans and cannot switch between the two modes unless some optical components of the system are exchanged or added to account for the refraction of the optics of the eye.

It is also important to notice that this differentiation between OCT scanning systems, either devoted to image the anterior or the posterior system of the eye, also have consequences in cost, as clinicians have to separately procure an anterior and posterior segment OCT systems additionally to OCT biometers, which cost can be in excess of 40 kUSD [105]. This is particularly taxing for practices in low-resource settings and emerging economies, where, for example, the prevalence of cataract is higher than in developed countries [99].

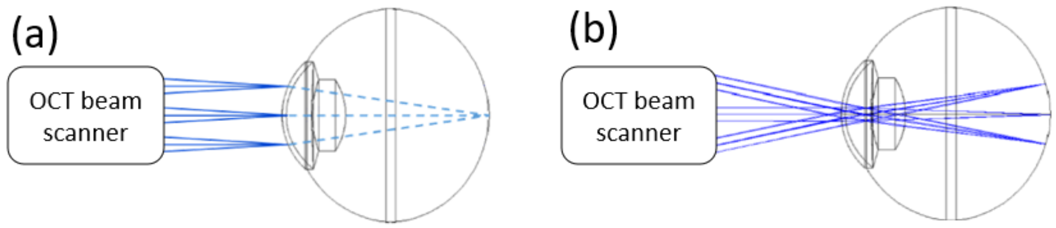

Figure 5.1 – *Schematic representation of the different scanning configurations in OCT for each ocular segment: (a) for anterior segment imaging, (b) posterior segment imaging [171].*

Different approaches have been proposed to overcome this physical limitation by imaging, sequentially or simultaneously, both ocular segments of the eye of the subject within the same acquisition. Sequentially imaging each ocular segment by using mechanical actuators (e.g., a bi-stable rotary solenoid [172], or a fold mirror [173]) have been proposed to switch between two sample arms where each of them is configured for each ocular segment scanning configuration. Alternatively, simultaneously imaging both ocular segments was achieved by Kim et al. [174] using two-sample arm configuration based on a polarization-encoding approach to separate the sample light beam into two different beams to propagate through the anterior and posterior segment scan paths. In this case, the same polarization-based optical split of the light beam was also implemented to achieve a two-reference arm configuration to match each of the sample arms, a necessary step due to the short axial range of spectrometer-based OCT system. Additionally, an optical switch was needed to interlace the acquisition of each interferometric A-scan signal at the detector [174]. Also for simultaneous imaging, Fan et al. [175] used dichroic mirrors to combine two wavelength bands that were devoted for the two ocular segments. However, this approach requires two sources and two detectors. Kim et al., relaxed this requirement with the previously proposed polarization-encoding dual-sample beam approach in combination with two synchronized photodetectors in a SS-OCT system [176]. McNabb et al. [177] demonstrated a polarization- and pathlength-encoding approach with only one source and one detector to scan a wide field of view of both anterior and posterior segments taking advantage of the longer coherence length of MEMS-swept VCSEL sources and the coherence revival effect.

On the other hand, to dynamically control the optical beam divergence, the system of McNabb et al. [177] also included a lens mounted on a motorized translation stage at the posterior segment sample beam. This allowed to correct the patient defocus without adjusting any optics of the anterior segment sample arm. Beam divergence control for focus tuning has also been used in an dynamic whole-eye scanner via an electro-tunable lens (ETL) by Grulkowski et al. [178]. However, in this case, only a static scanning configuration was present, which was a trade-off between the two typical scanning configurations for either segment.

Having the same flexibility afforded by focus tuning in switching between two or more scanning configurations, without the need for duplicating or requiring expensive components, would result in improved image quality at a reduced cost. Moreover, a dynamically reconfigurable scan configuration would also allow customization for specific applications even beyond whole-eye imaging. In order to incorporate an additional degree of versatility in the selection of the scan configuration, i.e., the control of beam axis displacement and deflection, several non-mechanical components for beam steering could be used [179]. Among them, ETLs are the most promising for lower-cost applications, and they have already been used in devices such as an adjustable beam expander [180] where two ETLs were arranged on axis in a telescope configuration, as well as in a wide-angle beam steering system [179, 181] where two or more ETLs were arranged at an offset from their respective axes.

This chapter presents the working principle, design and experimental implementation of a novel low-cost optical beam scanner based on the combination of three ETLs that allow to sequentially switch between the anterior and posterior segment scanning configurations by performing both dynamic focusing and changes in the scanning configuration without requiring any exchange in the optics or mechanical displacement of the OCT system [182]. We characterized the scanning performance of the assembled prototype by measuring the beam profiles for each scan configuration at different planes. We also connected the novel beam scanner to the sample arm of a SS-OCT system and obtained whole-eye OCT images first in a human phantom eye and then in an *ex vivo* rabbit eye and in human subjects. We show experimental data to prove the capabilities of the novel beam scanner to image the whole-eye and to acquire precise biometric measurements when combined with any OCT system, while maintaining the cost constrained.

5.2 - Working principle

The goal of this section is to provide a detailed explanation of the working principle of the low-cost whole-eye optical beam scanner that has been designed. First, an analytical description of the scanner optics is presented. Then the analytical equations are used to study the dependencies between the design variables to provide a comprehensive understanding of how the various components of the system are combined to achieve its intended purpose.

The whole-eye optical beam scanner developed is mainly based on the combination of three ETLs and several common optical components: a fiber collimator, a hollow-roof mirror (HRM), a silver mirror (M), a periscope system(P) and a DC or stepper motor. The two commonly used scanning configurations are:

- Telecentric and focused scan configuration: when the output light beam is displaced in a telecentric or parallel manner and a constant focal plane is maintained at a selected distance from the optical beam scanner, as would be required to scan the anterior segment of an eye.
- Angular and collimated scan configuration: when a collimated output light beam is displaced changing its angle pivoting at a constant point at a selected distance from the optical beam scanner, as would be required to scan the posterior segment of an eye.

5.2.1 - Schematic and analytical description

To switch between each scan configuration, the designed optical beam scanner is able to independently select the direction (see section A) and the vergence of the output light beam (see section B) as a function of the system parameters of the double-pass configuration proposed. To better explain the working principle, various sets of components will be analyzed before combining them (see section C). Each of these sets as well as their combination are shown in Figure 5.2.

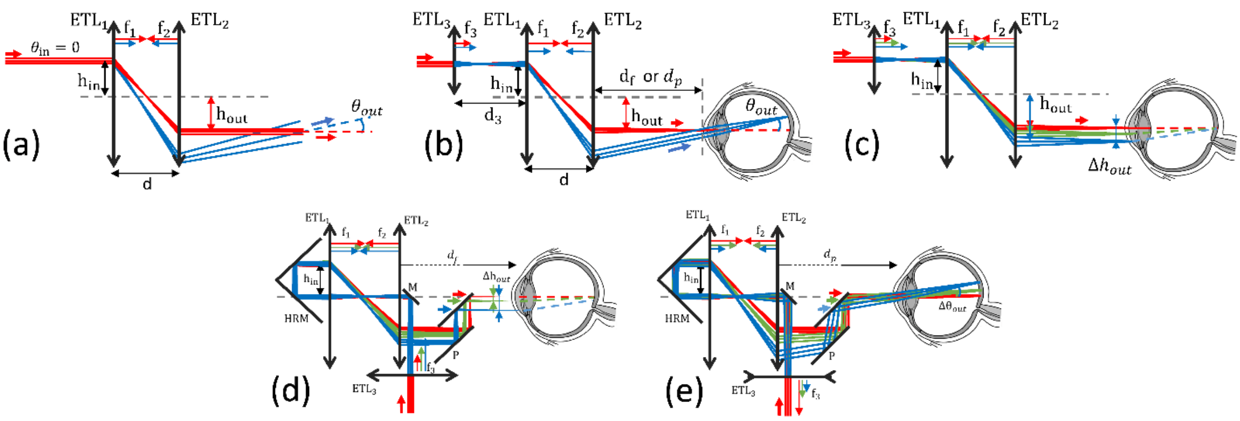

Figure 5.2 – *Optical schematic representation of the design of the proposed beam scanner using electro-tunable lenses (ETL). (a) Combinations of the focal lengths of ETL_1 and ETL_2, f_1 and f_2 respectively, separated a distance d allow the control of the output beam displacement, h_{out}, and deflection angle, θ_{out}, as a function of the input beam displacement, h_{in}, and angle, θ_{in}. (b) With an additional tunable lens, ETL_3 on axis with the input beam the vergence of the output beam can be controlled so that rays are focused at d_f or collimated when pivoting at d_p. (c) Example of a telecentric scan in a single pass configuration shifting the beam Δh_{out} evidencing the resolution variation through the scan. (d) Example of a telecentric scan in a double pass configuration using a hollow-roof-mirror HRM where the variation of the resolution is extensively reduced. M is a mirror, P is a periscope to shift the output beam to be colinear with the ETLs and d_f is the distance from ETL_2 to the plane where the beams are focused (e) Example of an angular scan in a double pass configuration where the output beam is collimated and pivots around the point d_p.*

A - Beam direction selection

For the selection of the displacement and deflection of the output light beam, only two ETLs are required. For the system to work is crucial to place the two ETLs (ETL_1 and ETL_2) on axis at a fixed distance *d* between them, as well as with an input offset h_{in} with respect to the input light beam form a collimator (see Figure 5.2(a)). Due to the offset incidence of the light beam on ETL_1, a lateral displacement is also induced into the output light beam which is dependent on the combination of the focal length of two ETLs. In such a way, different combination of the focal length of f_1 and f_2 allow to change the lateral displacement of the output beam. Using the paraxial ray transfer matrix analysis (ABCD matrix formalism) we obtained, the analytical equations for the desired transversal displacement h_{out} and output deflection angle θ_{out} as a function of the ETLs focal length (see Equations (12) and (13)) [183]. Both the transversal displacement h_{out} and the output deflection angle θ_{out} were calculated at the principal plane of ETL_2 with respect to the optical axis of the two ETLs.

$$h_{out} = h_{in}\left(1 - \frac{d}{f_1}\right) + d\theta_{in} \tag{12}$$

$$\theta_{out} \cong \theta_{in}\left(1 - \frac{d}{f_2}\right) - h_{in}\left(\frac{1}{f_2} + \frac{1}{f_1}\left(1 - \frac{d}{f_2}\right)\right) \tag{13}$$

From these formulae, we derived the combinations of f_1 and f_2 required to perform either a telecentric scan, as typically performed for anterior segment imaging; or an angular scan, as typically performed for imaging the posterior segment. For simplicity, we will only consider the case where $\theta_{in} = 0$.

The following Equations (14)-(16), show the previous Equations (12) and (13) rearranged to calculate the focal lengths of the tunable lenses, $f_1$and f_2, as a function of the parameters needed to perform a telecentric scan. The combination of f_1 and f_2 is obtained by changing the transversal displacement $h_{out}(t_i)$ linearly with time and keeping the output deflection angle $\theta_{out}(t_i)$ constant at zero. With these parameters, the equations show, as expected, that the sum of the focal lengths f_1 and f_2 is equal to the distance *d* between ETL_1 and ETL_2 , i.e., $f_1 + f_2 = d$. In such a way, the set form by ETL_1 and ETL_2 can be understood as a dynamic telescope and the output transversal displacement h_{out} is varied as a function of the telescope magnification (f_2/f_1), i.e., $h_{out} = -\frac{f_2}{f_1}h_{in}$.

$$f_1(t_i) = \frac{d\,h_{in}}{h_{in} - h_{out}(t_i)} \tag{14}$$

$$f_2(t_i) = d - f_1(t_i) \tag{15}$$

$$\theta_{out}(t_i) = 0 \tag{16}$$

The starting point of the telecentric displacement $h_{out}(t_o)$ was defined as the position were f_1 and f_2 have the same value, i.e., the case where the ETL_1-ETL_2 telescope have a x1 magnification factor and f_1 and f_2 are equal to the distance *d/2* between the two ETLs. The increment in transversal displacement Δh_{out} was defined with respect to the said starting point and the output light beam was assumed to be displaced through the clear aperture of ETL_2 towards the closest edge.

The following Equations (17) and (18), show the rearrangement of the previous Equations (12) and (13) to calculate the focal lengths of the tunable lenses, $f_1$and f_2, as a function of the parameters needed to perform an angular scan. In this case, the output transverse displacement $h_{out}(t_i)$ must vary accordingly, as dictated by trigonometry, to maintain constant the desired distance d_p of the pivoting point from the principal plane of ETL_2 ($\theta_{out} = atan\left((\Delta h_{out})/d_p\right)$). Moreover, it is also convenient to choose the same conditions as in the telecentric scan for the initial output transverse displacement $h_{out}(t_0)$ and for the initial output deflection angle $\theta_{out}(t_0)$, e.g., $h_{out}(t_0) = -h_{in}$ and $\theta_{out}(t_0) = 0$.

$$f_1(t_i) = \frac{d\ h_{in}}{h_{in} - h_{out}(t_i)} \tag{17}$$

$$f_2(t_i) = \frac{d\ h_{out}(t_i)}{h_{out}(t_i) - h_{in} + d\ \theta_{out}(t_i)} \tag{18}$$

$$h_{out}(t_i) = h_{out}(t_0) + d_p tan\big(\theta_{out}(t_i)\big) \tag{19}$$

B - Beam vergence selection

For the selection of the vergence of the output beam at each scanning configuration an additional lens ETL_3 is needed to be placed on axis with the input light beam before ETL_1 at a distance d_3 from it (see Figure 5.2 (b)) to allow for focus tuning and an independent control of the beam divergence from the control of the beam direction. Using the thin lens equation of the geometrical optics formalism under the paraxial approximation [183], we obtained the analytical equation of the focal length f_3 of ETL_3 required to focus the output beam at a desired distance d_f from the principal plane ETL_2 (see Equation (20)), as a function of the distance between the elements of the system (d, d_f and d_3) and the focal lengths f_1 and f_2. This way, the position of the beam waist of the output light beam can be modified as required at each scan configuration, generating a focused light beam to image the anterior segment of the eye (shown in Figure 5.2(b) with a red ray tracing) as well as a collimated output light beam during the scan of the posterior segment of the eye (shown in Figure 5.2(b) with a blue ray tracing).

$$f_3 = d_3 + \frac{df_1\big(f_2 - d_f\big) + f_1 f_2 d_f}{(f_1 - d)\big(f_2 - d_f\big) - f_2 d_f} \tag{20}$$

Figure 5.2(c) shows three transverse steps of an example of an anterior segment scan, where the focal lengths of the three ETLs are selected to generate a telecentric displacement Δh_{out} of the output beam while the focal distance d_f is maintained at the cornea. However, in this representation an increment in the beam numerical aperture for different scan positions can be observed when compared the red and blue ray traced beams. This effect would lead to an undesirable variation of the transverse resolution during the scan [184].

C - Double pass configuration

The variation in the numerical aperture of the beam can be reduced by converting the system from the single pass configuration shown in Figure 5.2(c) into a double-pass configuration, as shown in Figure 5.2(d) and (e). Firstly, the input light beam from a collimator was incident on axis on ETL_3 and propagated over a distance d_3 until ETL_2, to then propagate through the center of ETL_2 and ETL_1. Then, a hollow-roof mirror HRM, at a distance d_{HRM} from ETL_1, was used to induce the needed offset h_{in} and to redirect the light beam back towards ETL_1 and ETL_2 parallel to their optical axis to propagate through the ETL_1-ETL_2 sub-system a second time. Notice that each propagation through the ETL_1-ETL_2 sub-system is performed in the opposite directions. Thus, the magnification factor induced by the set ETL_1-ETL_2 sub-system to the beam numerical aperture is cancelled, reducing the overall transversal resolution variation.

Additionally, a mirror M allows the input light beam to be incident from a lateral side of the ETL_1-ETL_2 sub-system by folding the light beam when propagating through the distance d_3 between ETL_3 and ETL_2, avoiding the incident and output light beam to be parallel and at the sample plane facilitating the sample alignment. Lastly, a periscope P system can be used to compensate for the previously induced offset h_{in}, making the scan to start at a position on-axis with respect to the optical axis of ETL_1-ETL_2 sub-system.

There is still a residual variation of the beam numerical aperture throughout the scan as the input light beam (always assumed to be collimated) only propagates through ETL_3 once and f_3 needs to change to maintain the collimation or focused condition affecting the beam numerical aperture of the output beam. The previously presented Equation (20) for the focal length f_3 cannot be used in the double pass configuration as was obtained by only considering a single pass configuration through the ETL_1-ETL_2 sub-system. However, using again the thin lens equation under the paraxial approximation [183], the equation of the focal length f_3 for the double-pass configuration can be derived (see Equations 20(a)-(e)).

$$f_3 = d_3 - i_{22} \tag{21a}$$

$$with\, i_{22} = f_2(t) \cdot \frac{d - i_{12}}{d - i_{12} - f_2(t)}, \tag{21b}$$

$$i_{12} = f_1(t) \cdot \frac{2d_{HRM} + h_{in} - i_{11}}{2d_{HRM} + h_{in} - i_{11} - f_1(t)}, \tag{21c}$$

$$i_{11} = f_1(t) \cdot \frac{d - i_{21}}{d - i_{21} - f_1(t)}, \tag{21d}$$

$$i_{21} = f_2(t)\ \frac{d_f}{d_f - f_2(t)}, \tag{21e}$$

Where i_{21} is the conjugate distance to d_f from ETL_2, i_{11} is the conjugate distance to the intermediate focal plane at i_{21} from ETL_1 after a first pass, i_{12} is the conjugate distance to the intermediate focal plane at i_{11} from ETL_1 after a second pass, and i_{22} is the conjugate distance to the intermediate focal plane at i_{12} from ETL_2.

By setting the combination of the focal length of the three ETLs we can perform both a telecentric scan while focusing the output light beam at a constant working distance and an angular scan while maintaining a collimated output light beam pivoting at a specific point. This shall prove particularly useful for whole-eye imaging without the need to use mechanically switches to change between both scanning configurations.

5.2.2 - System parameters space: dependencies and limitation

An analysis of the system parameters, such as the fixed distances between the optical components of the system, was performed to optimize the design of the optical beam scanner in the double pass configuration. For this analysis we used the Equations (12)-(20), with the goal of maximizing the scanning range of the optical beam scanner in both scanning configurations, i.e., Δh_{out} and $\Delta\theta_{out}$ for the telecentric and angular scans, respectively.

During this analysis, the mechanical and optical specifications of low-cost off-the-shelf components were considered. The objective was to optimize the design of the experimental prototype of the beam scanner whose implementation will be discussed in the following sections. The optical elements considered and their most relevant specifications for the optimization analysis are listed in Table 5.1.

Table 5.1 *- List of off-the-shelf components selected for the whole-eye optical beam scanner system.*

Optical element	Commercial component	Specification
Collimator	F220APC-850 (Thorlabs)	$1/e^2$ beam diameter @λ=1060nm: 2.41 mm
ETL_1, ETL_2	EL-10-30-TC-NIR-12D (Optotune)	Clear aperture: 10mm Focal range: +50mm to +120mm
ETL_3	EL-3-10-NIR-26D (Optotune)	Clear aperture: 10mm Focal range: -∞ to -77mm and +77mm to +∞
HRM	HRS1015 (Thorlabs)	Dimensions: 25.4 x 25.4mm
M	#54-094 (Edmund)	45° Rod Mirror with a 3mm diameter
P	MRA05-P01 (Thorlabs)	Right-Angle Prism Mirror, L = 5.0 mm

A – Scan range analysis: ETL_1 and ETL_2 limitation factor

In the first place, we analyzed the optimization of the ETL_1-ETL_2 sub-system in the double-pass configuration shown in Figure 5.2(d) and (e). The mechanical distances analyzed in this case were the input offset h_{in} and the distance *d* between the two ETLs. The rest of the distances presented in the working principle d_3 and d_{HRM} do not affect the scanning range limitation because they only control the output beam vergence. During this analysis, we observed that the restricting parameters from Table 5.1 that limits the scan range of the optical beam scanner were the semi-clear aperture of ETL_2, as the output light beam was transversally displaced through its principal plane, and the minimum focal length available for ETL_1.

- Input offset h_{in} variation analysis:

The analysis of the variation of the input offset h_{in} was performed keeping the distance *d* constant at 150 mm (the optimum value of *d* after the analysis shown in the next sub-section) as the dependence of the scan range of the beam scanner with h_{in} is independent of the distance between the subset ETL_1-ETL_2.

Figure 5.3(a)-(c) show how the transverse scan range Δh_{out} varies as a function of the input offset h_{in}, while Figure 5.3(d)-(f) show how the angular scan range $\Delta\theta_{out}$ varies as a function of the input offset h_{in} and the ETL focal lengths. In Figure 5.3(a) and (d) the transverse and angular scan ranges are plotted as a function of the focal length f_1 of ETL_1 for different input offsets. The grayed-out area represents focal lengths that are too short and out of range for the selected ETL_1. Figure 5.3(c) and (f) show the transverse and angular scan ranges as a function of the transversal displacement h_{out} of the beam from the axis of ETL_2 for different input offsets. The grayed-out area represents the displacements that are larger than the clear semi-aperture of ETL_2 and therefore out of bounds for ETL_2. For each input offset h_{in}, the scan range determined by the most limiting factor was selected and plotted in Figure 5.3(b) and (e) showing the maximum permitted scan range Δh_{out} or $\Delta\theta_{out}$ as a function of the input offset h_{in}.

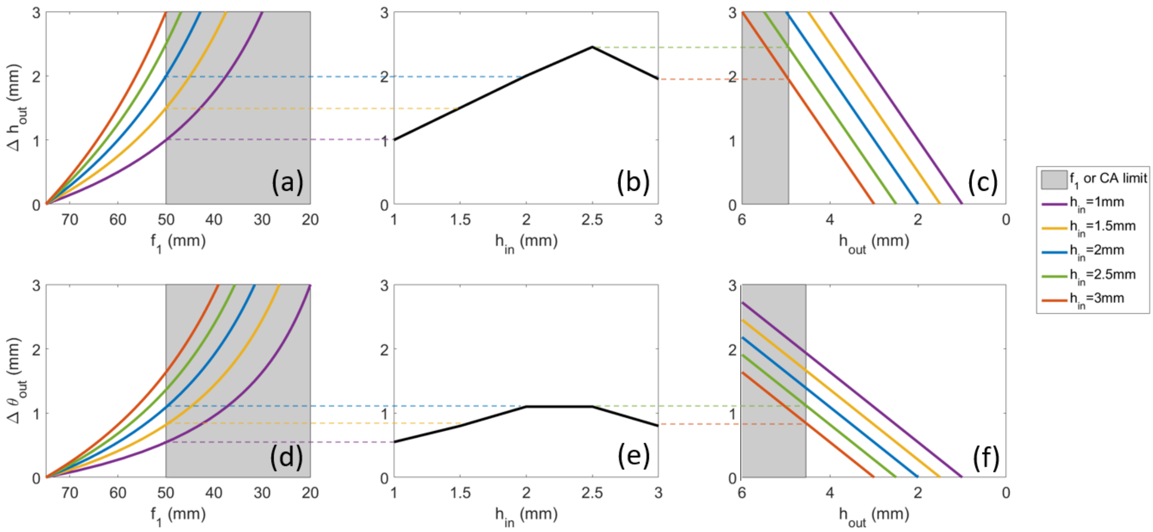

Figure 5.3 *- Scan range variation as a function of the input offset h_{in} for the proposed beam scanner, where the components and other distances are listed in Table 5.1. (a)-(c) The transverse scan range Δh_{out} variation as a function of the focal length f_1 of ETL_1, the input offset h_{in}, and the transversal displacement h_{out} of the beam from the axis of ETL_2, respectively. (d)-(f) The angular scan range $\Delta\theta_{out}$ variation as a function of same variables as in (a)-(c).*

Figure 5.3(a) and (d), show that the scan range increased when decreasing ETL_1 focal length and that larger input offsets generated a larger scan range for a given focal length, thus increasing the scan range when increasing the offset input h_{in}. On the contrary, Figure 5.3(c) and (f) show that smaller input offsets h_{in} allow to generate larger scan ranges. This was due to the starting point definition previously presented. Since the scan range always starts at the position were the transversal displacement of the output beam h_{out} equals the input offset h_{in} ($h_{in} = - h_{out}$), increasing h_{in} also implied increasing the transversal position h_{out} at the beginning of the scan thus reducing the range of displacement until the edge of ETL_2 semi-clear aperture. The resulting graphs of the maximum permitted transverse and angular scan range, Δh_{out} and $\Delta\theta_{out}$, as a function of the input offset h_{in} considering these competing trends have a peak at input offset

$h_{in} = 2.5$ mm (see Figure 5.3(b) and (e)), which in fact correspond to half of the semi-aperture of ETL_1. Therefore, this value was selected as the optimal input offset, and resulted in $\Delta h_{out} = 2.5$ mm and $\Delta\theta_{out} = 1.2$ deg.

- Distance *d* between ETL_1 and ETL_2 variation analysis:

The analysis of the variation of the distance *d* between the two ETLs of the ETL_1-ETL_2 sub-system was performed keeping the input offset h_{in} constant equal to 2.5mm, i.e., the optimum value to maximize the scan range as shown before.

Figure 5.4 shows how the transverse and angular scan range, Δh_{out} and $\Delta\theta_{out}$ vary as a function of the distance *d* between ETL_1 and ETL_2. In Figure 5.4(a) and (d) the transverse and angular scan range, respectively, are plotted as a function of the focal length f_1 of ETL_1 for different values of the distance *d*. Again, the grayed-out areas represent focal lengths that are too short and out of reach for ETL_1. On the other side, Figure 5.4(c) and (f) show the transverse and angular scan range, respectively, plotted as a function of the transversal displacement h_{out} of the beam from the optical axis of ETL_2 for different values of the distance *d*. Again, the grayed-out areas represent displacements that are over the clear semi-aperture of ETL_2 and therefore out of bounds for ETL_2.

Figure 5.4(a) and (d), show that the scan range increases when decreasing ETL_1 focal length and that larger values of the distance *d* between ETL_1 and ETL_2 generate a larger scan range for a given focal length. Figure 5.4(c) and (f) show that the scan range increases when increasing transversal displacement h_{out} irrespective of the distance between ETL_1 and ETL_2 due, as before, to the scan starting point considered. In this case, as the input offset h_{in} is maintained constant during the variation of the distance *d*, the scan always starts at the same transversal displacement h_{out} in the clear aperture of ETL_2 and thus the same scan range is always available. In Figure 5.4(b) and (e) the transverse and angular scan range, Δh_{out} and $\Delta\theta_{out}$ are plotted as a function of the distance d considering these competing trends, up to the limits imposed by the shortest focal length f_1 of ETL_1 and the clear semi-aperture of ETL_2. For each value of the distance d, the largest scan range determined by the most limiting factor was selected and plotted. The resulting curves reach a plateau at $d = 150$ mm. Therefore, for device footprint considerations, this value was selected as the smallest distance of 150 mm that, as before, resulted in $\Delta h_{out} = 2.5$ mm and $\Delta\theta_{out} = 1.2$ deg.

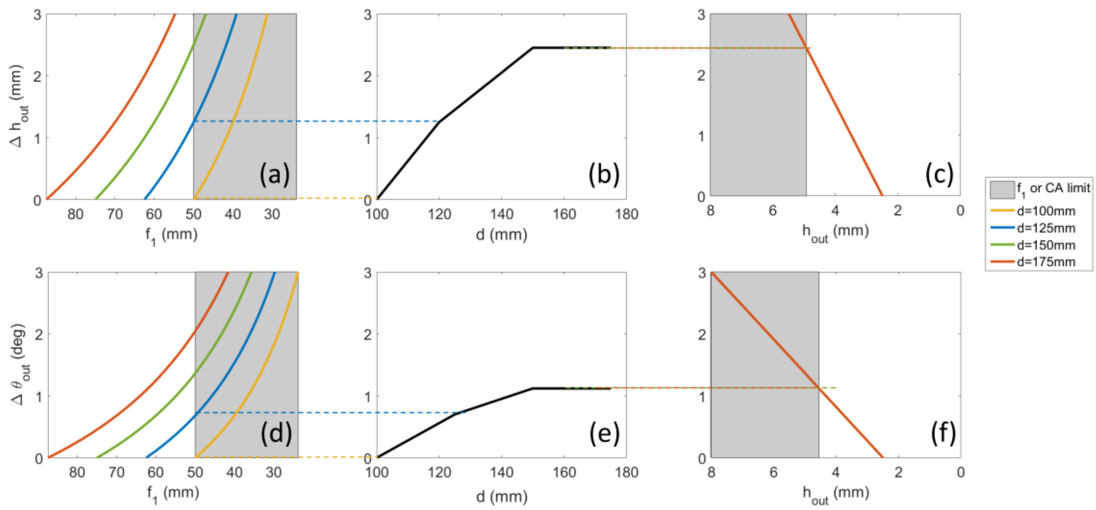

Figure 5.4 *- Scan range variation as a function of the distance d between ETL_1 and ETL_2, for the proposed beam scanner, where the components and other distances are listed in Table 5.1. (a)-(c) The transverse scan range Δh_{out} variation as a function of the focal length f_1 of ETL_1, the distance d, and the transversal displacement h_{out} of the beam from the axis of ETL_2, respectively. (d)-(f) The angular scan range $\Delta\theta_{out}$ variation as a function of same variables as in (a)-(c).*

B – Vergence control: ETL$_3$

Once the parameters of the ETL_1-ETL_2 sub-system were optimized, we analyzed how the distance d_3 between ETL_3 and the ETL_1-ETL_2 sub-system affected the range of working distance d_f and d_p for each scan configuration respectively. As before, the restricting parameters from Table 5.1 were considered. The parameters limiting the vergence control of the optical beam scanner were the minimum focal length f_3 available for ETL_3.The distance d_{HRM} between the HRM and ETL_1 was kept constant at 30 mm, the minimum available with the off-the-self components selected, and the input offset h_{in} and the distance *d* were kept at the optimum values found before: 2.5 mm and 150 mm respectively.

For this analysis the combination of f_1 and f_2 obtained from the previously optimized telecentric and angular scans was considered to be either focalized or to pivot at different working distances d_f and d_p respectively. In Figure 5.5(a) and (b), each working distance is represented with different line styles while each distance d_3 analyzed is shown with different colors (yellow and purple). The grayed-out area represents focal lengths that are out of range for the selected ETL_3. Figure 5.5(a) and (b) shows that, for both telecentric and angular scan configurations respectively, the range of working distance d_f and d_p respectively is reduced when the distance d_3 between ETL_3 and the ETL_1-ETL_2 sub-system is increased.

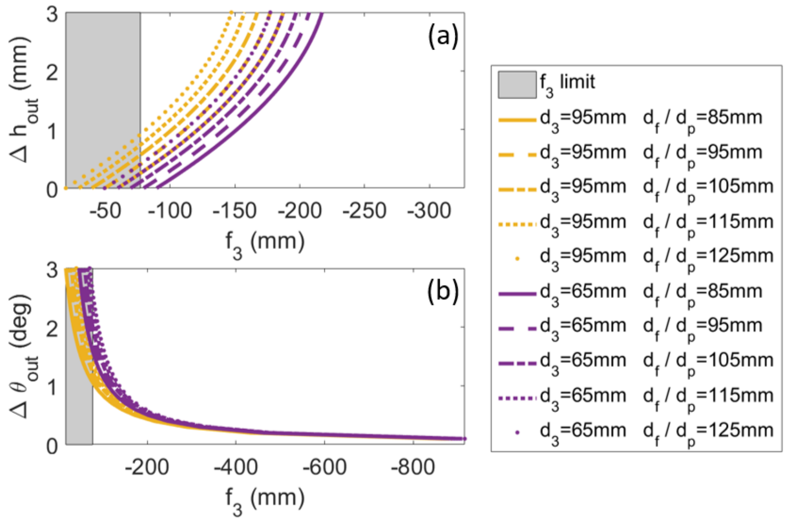

***Figure 5.5** - Analysis of the capability of vergence selection of the optical beam scanner for the telecentric scan mode (a-b) and the angular scan mode (c-d) as a function of: the focal plane distance and the distance d_3 between ETL_3 and the subset ETL_1-ETL_2 (shown in different colors), the focal plane distance or pivoting point (shown in different line styles), the distance d of the subset ETL_1-ETL_2 (shown at each column).*

5.3 – Simulation of the optimized designed optical beam scanner

In this section the expected specifications of the optimized optical beam scanner in the double pass configuration are presented, as well as its performance simulation considering both the analytical equation in MATLAB and OpticStudio software. The goal of this section is to show the expected performance of the optical beam scanner at the design configuration that will be experimentally implemented.

5.3.1 - System components and specifications

The optimal design parameters were based on the optical components listed in Table 5.1 and the analysis of the system variables presented in the previous section. The input offset h_{in} was 2.5 mm to allow the largest scan range in both scan configurations and the distance *d* between ETL_1 and ETL_2 was 150 mm. The working distance d_f and d_p was chosen to be equal to 105 mm in both scan configurations to allow a comfortable working distance to place the eye, similar to other ophthalmic scanners [120]. The distance d_3 between ETL_1-ETL_2 sub-system was set to be 72 mm and the distance d_{HRM} between the HRM and ETL_1 was set to be 30 mm. A summary of all mechanical distances is presented in Table 5.2.

***Table 5.2** – List of the optimized parameters for the optical design of the beam scanner when considering the commercial components in Table 5.1.*

System parameter	Value
d	150 mm
d_3	72 mm
d_{HRM}	30 mm
h_{in}	2.5 mm
ETL_1 focal range	From +75 mm to +50 mm
ETL_2 focal range	From +75 mm to +100 mm
ETL_3 focal range	From -∞ to -70 mm
d_f for the AS scan	105 mm
d_p for the PS scan	105 mm
Telecentric scan range	2.5 mm
Angular scan range	1.2 deg

5.3.2 - Optical performance simulation of the optimized beam scanner

Using the values in Table 5.2, we evaluated the focal lengths of ETL_1-ETL_3 required to image the anterior and posterior segment of an eye, according to the presented Equations (14)-(21a). We also validated the required focal lengths with a simulation of the designed beam scanner in OpticStudio.

Figure 5.6(a) and (b) show the combination of the focal length of ETL_1, ETL_2 and ETL_3 as a function of the desired displacement of the beam for both scanning configurations, telecentric and angular respectively, simulated to focus and pivot at the desired working distance d_f and d_p, respectively. The starting position of the angular scan, $\Delta\theta_{out} = 0$, is not shown in Figure 5.6(b) as the focal length of ETL_3 requires to be infinity. Under these conditions, and considering the limiting factors, including the clear aperture of the ETLs, the beam scanner was expected to have a telecentric scan range of 2.5 mm and an angular scan range of 1.2 deg.

The beam scanner was implemented in the optical design program OpticStudio and the combination of the focal length of six transverse and angular displacements obtained with the analytical equations were simulated. Figure 5.6(c) show the layout of the simulated model of the optimized beam scanner, at which the telecentric and angular scan were characterized by measuring the vertical displacement of the center of the output beam in the image plane at different axial positions. The transversal and angular displacement obtained from the OpticStudio model of the optical beam scanner are represented with red dots in Figure 5.6(a) and (b). In all cases the OpticStudio simulations were in good agreement with the results obtained from the analytical equations.

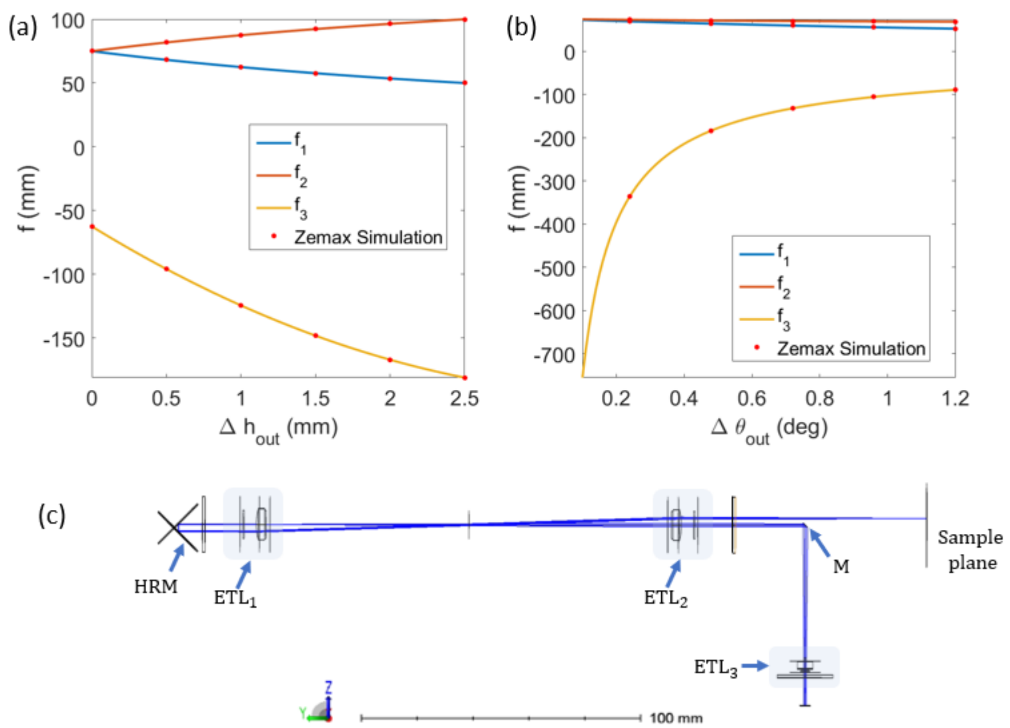

Figure 5.6 - *Calculation (solid lines) and simulation (red dots) focal length of ETL_1, ETL_2 and ETL_3 as a function of the (a) telecentric displacement for imaging the anterior segment, and (b) angular displacement for imaging the posterior segment; using the values of Table 5.2 and Equations (13)-(20) and OpticStudio models, respectively. (c) Layout of the simulated OpticStudio model of the beam scanner using the values of Table 5.2.*

We also analyzed the expected residual variation of the lateral resolution along the transverse and angular position. For this purpose, we analytically calculated the beam diameter along the beam axis (z) as the collimated Gaussian input beam was transmitted through the beam scanner components, using Equations (3.2.5)-(3.2.9a) of the book by Saleh et. al [183], that describe the waist properties of a Gaussian beam when imaged through an optical system. The variation of the output beam spot size, i.e., the beam diameter at the waist position, corresponding to the working distance d_f and d_p, is shown in Figure 5.7(a) and Figure 5.7(c) as a function of the transverse position for the anterior scan configuration and as a function of the angular position for the posterior scan configuration. Figure 5.7(c) shows a residual variation of the output beam spot size from 1.28 mm (at 0 deg) to 0.96 mm (at 1.2 deg) for the angular scan configuration at the pivoting point, ideally set on the eye pupil. To work out the beam spot size at the retina for the posterior scan, we used Equations 3.2-17 of [183] and we assumed a relaxed eye effective focal length of 22.2 mm [185]. Figure 5.7(b) shows the output beam diameter profile along the beam axis in the range of the working distance $d_f \pm 10$ mm for different transverse positions of the output beam for the anterior scan configuration.

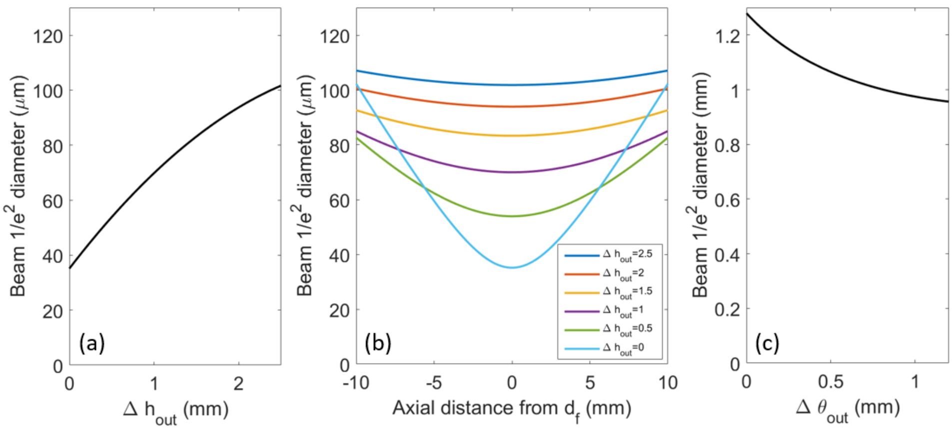

Figure 5.7 *- Theoretical transverse resolution of the beam scanner for the telecentric scan (a-b) and the angular scan (c). (a) The variation of the spot size at the working distance d_f for the telecentric scan. (b) The axial beam diameter profile for the telecentric scan at various transverse output positions with respect to the working distance d_f. (c) The variation of the spot size for the angular scan at the pupil plane.*

This analysis showed that the spot size, that determines the lateral resolution, varies from 35 μm (at 0 mm) to 102 μm (at 2.5 mm) on the focal plane at the cornea for the anterior imaging configuration, and from 23 μm (at 0 deg) to 31 μm (at 1.2 deg) on the retina for the posterior imaging configuration. A summary of the theoretical imaging specs is presented in Table 5.3. Thus, even though the double pass configuration of the beam scanner reduces the change in beam diameter considerably as can be roughly visualized in Figure 5.2(c) and (d), a remaining variation of the lateral resolution is still present. We observed that this variation is due to the need to vary the focal length of the third lens ETL_3 for each scan position.

Table 5.3 *- Theoretical imaging specification for the optical beam scanner the components listed in Table 5.1 arranged according to the parameters listed in Table 5.2.*

Theoretical Imaging Specifications	Value
Telecentric scan range	2.5 mm
Angular scan range	1.2 deg
Telecentric scan transverse resolution at focus (on anterior chamber)	35 – 102 μm
Angular scan transverse resolution at focus (on retina)	23 – 31 μm

5.4 – Experimental implementation of the optical beam scanner

This section describes the experimental implementation of the optical beam scanner described with the commercial components from Table 5.1 and the mechanical distances stated in Table 5.2. In this section, we present the experimental setup of the implemented beam scanner prototype and its characterization, for which each of the ETLs used was individually characterized in a high-speed focimeter achieving a starting point calibration before combining them in the beam scanner. The control system developed to drive the proposed optical beam scanner is also presented in this section, as is used for the full experimental characterization of the experimental beam scanner.

5.4.1 – Beam scanner control system

The structure of the electronic system developed to control the optical beam scanner prototype is shown in Figure 5.8. This system was designed to control the ETLs of the beam scanner with a customized communication protocol based on the firmware and software developed to control a combination of ETLs in the visual simulator SimVis Gekko [186].

For the control of the optical beam scanner, a low-cost Arduino Nano board microcontroller with 8-bit resolution was used to manage the components of the device when connected to a host PC through a USB connection. The USB connection of the Arduino was also used to deliver the power to the optical beam scanner, allowing it to be plugged into any compatible computer facilitating its use. The Arduino Nano board was programmed to be controlled from a MATLAB GUI interface developed to independently select the beam displacement, deflection and vergence of the different scan configurations. In such a way, though the GUI interface we defined the parameters of the scan configuration to be performed such as the scan type (telecentric or angular), the working distance and velocity of the scan. These parameters were communicated to the Arduino Nano board where a custom developed program was implemented to calculate the combination of focal lengths f_1, f_2 and f_3 using Equations (13) to (22) and to generate the corresponding electronic signal to drive ETL_1, ETL_2 and ETL_3.

The focal length or optical power of the ETLs was set by the duty cycle of a pulse width modulation (PWM) signal sent by the Arduino Nano board to the lenses through a lens driver (DRV8833, Texas Instruments). The duty cycle of the PWM signal was controlled with the 8-bit digital counts (DC) being 0 DC a duty cycle of 0% and 255 DC a duty cycle of 100%. Due to the high frequency of the PWM signal, the lenses are effectively subjected to a voltage between 0-5 V proportional to the PWM signal. To control the three ETLs, two lens drivers were required as the lens drivers are designed to control a bipolar stepper motor. Thus, each ETL was connected to the drivers as each of the stepper motor poles would be connected. Additionally, a custom switch interface was developed to generate the polarity switching with logic gates required for the control of ETL_3, allowing to change from a positive to a negative focal length f_3 as required due to the lenses specification to be able to place set the 0 D condition for the starting position of the angular scan. Lastly, the ETLs are connected to the driver through a flexible flat cable (FFC) with the help of a FPC/FFC adapter (not shown in Figure 5.8) to access their 2 driving pins with classical round cables.

The total cost of the three ELTs and their control electronics was ~900 USD.

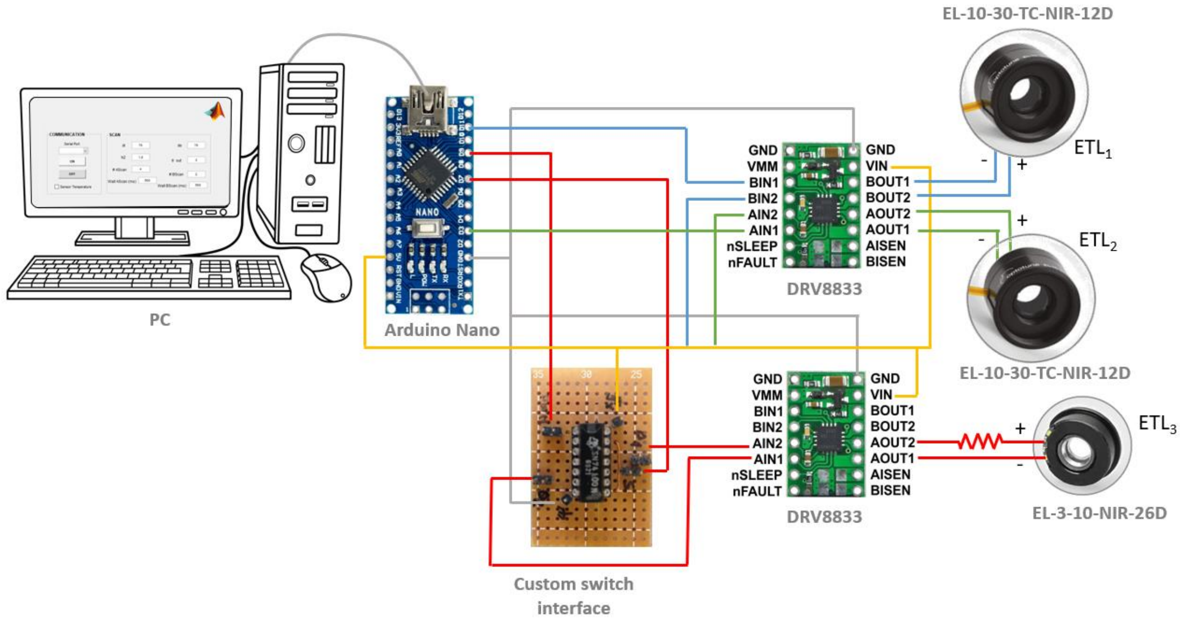

Figure 5.8 – Schematic representation of the electronic system developed for the control of the experimental prototype of the optical beam scanner.

5.4.2 – Calibration of the ETLs

The focal length variation with the input voltage of each ETL was characterized using a high-speed focimeter capable of performing a dynamic characterization of the ETLs as it can measure the optical power of the ETLs at high temporal sampling rates [122]. This calibration was used to establish a baseline of the optical power of the ETLs as a function of the applied voltage. When the ETLs were mounted on the optical beam scanner prototype this initial calibration was fine-tuned to achieve the desired performance. During this characterization of the ETLs the electronical system of the high-speed focimeter was used for the synchronization of the high-speed camera with the signal sent to the ETLs. This electronic system used a similar communication protocol to the one explained before but used a custom driver instead of a commercial one.

The calibration obtained with the high-speed focimeter of the optical power of ETL_1 as a function of the digital counts (DC) of the PWM electronic signal is shown in Figure 5.9(a). Since the optical power range variation that the high-speed focimeter was capable to measure was shorter than the total range required to be characterized, we divided the measurement range in three intervals to cover the full optical power range required for both scan configurations, anterior and posterior segment scan. Trial lenses conjugated with the ETL were used to change between the different intervals and to compensate for the ETL initial optical power. In Figure 5.9 each of the optical power range measured for ETL_1 with different trial lenses (TL) are shown with different dotted colors. The complete range was fitted to a quadratic curve and the equation was used as the base line for the calibration of the optical beam scanner. The calibration of ETL_2 was assumed to be equal to the calibration of ETL_1.

Similarly, Figure 5.9(b) shows the calibration of the optical power of ETL_3 as a function of the digital counts of the PWM signal obtained with the high-speed focimeter. As before, the negative and positive optical power range of ETL_3 were independently characterized using different trial lenses and are shown with red and blue spots. In both ranges, the data were well described with a linear fit ($R^2 > 0.99$ in both the positive and the negative diopter range).

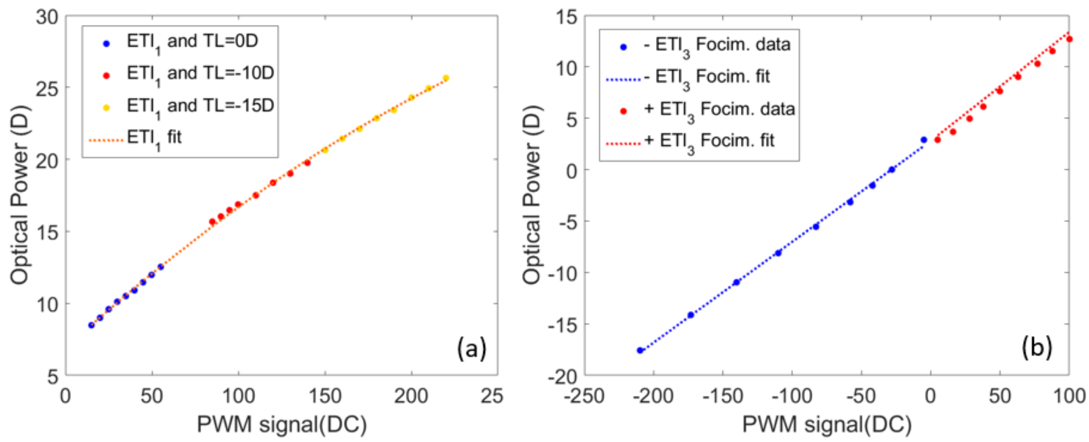

***Figure 5.9** – (a) Calibration of the whole range of ETL_1 obtained with the high-speed focimeter in three segments (blue, red and green) and it's fit to a quadratic polynomial (black). (b) Calibration of the positive (red) and negative (blue) range of optical power of ETL_3 obtained a high-speed focimeter.*

After the high-speed focimeter characterization, we also measured the potential deviation on the electronic signal generated for the control of the lenses by the electronic of the high-speed focimeter electronics and the one developed for the optical scanner (see Figure 5.8). To do this, we measured the voltage at the driving pins of the lenses when stimulated with both electronic systems. This characterization was only performed for ETL_3, as it was the one presenting the greatest difference in the electronic system due to the incorporation of the polarization switcher.

Figure 5.10 shows the comparison of the voltage measured at the driving pins of ETL_3 as a function of the digital counts of the PWM signal when stimulated with both electronical systems, i.e., the electronic setup of the high-speed focimeter and the optical beam scanner electronic control system. The results with the focimeter electronic are represented in blue and red and the results with the beam scanner electronic are represented in cyan and yellow. As can be observed, a notable difference (maximum difference 74 mV) was measured between both electronical systems. This difference could imply a difference of 0.035 D in power or 0.11 mm in focal length with respect to the calibration obtained with the high-speed focimeter.

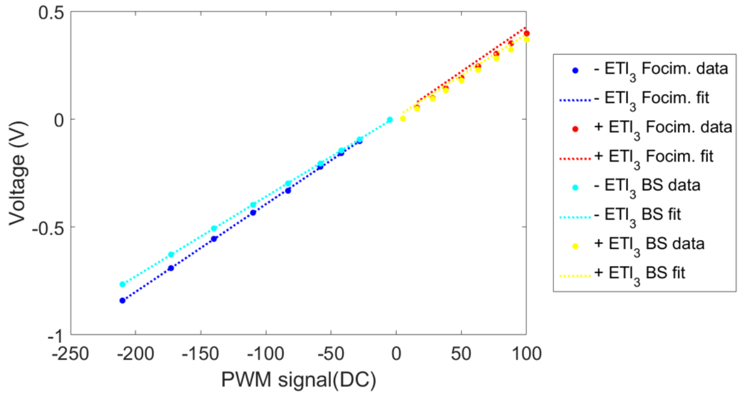

***Figure 5.10** - Comparison of the electronic signal to stimulate ETL_3 generated with the high-speed focimeter used for the calibration of the ETLs (blue and red) and the electronic system implemented for the control of the proposed beam scanner (cyan and yellow).*

Due to the difference shown in the electronical system performance and the segmented calibration of the ETLs performance, we were careful when transferring the obtained optical power calibration of the ETLs and adjusted the control signals accordingly when the ETLs were arranged in the optical beam scanner.

5.4.3 - Experimental setup and characterization

A prototype of the optical beam scanner was implemented in the laboratory with the off-the-shelf optical components from Table 5.1 and the optimized mechanical distances shown in Table 5.2. Figure 5.11 shows an overlay of the experimental prototype with a ray tracing of the beam at the starting point of the scan of the model eye.

***Figure 5.11** - Overlay of a picture of the experimental beam scanner prototype with the ray tracing of the beam through the beam scanner for the starting position of the beam scanner.*

<u>A- Optical performance experimental characterization</u>

The optical performance of the experimental beam scanner was characterized using a CCD camera (DCC1545M, Thorlabs) to profile the output beam around the working distance. This CCD was axially displaced over a range of 25 mm to profile the output beam at different axial positions. The analysis of the size and position of the beam at the CCD images allowed to characterize the two main features of the developed optical beam scanner: its capability to control the divergence and the direction of the output beam. This analysis was performed several times fine-tuning with minor modifications the initial calibrations obtained for the ETLs in the previous section 5.4.3 to iterative optimize the performance of the optical scanner in the two scan configurations of interest for ocular imaging: a telecentric displacement of a focused beam for imaging the anterior segment of the eye and an angular displacement of the collimated beam pivoting at the pupil plane of the eye to image the posterior segment of the eye.

Figure 5. 12 and Figure 5.13 show the beam displacement that was used to experimentally characterize the beam size and direction via beam profiling at several axial positions, for both the anterior and posterior segment scan configurations.

Figure 5. 12 shows a perspective view of the beam profile images acquired with the CCD at three axial positions, namely 12.5 mm before, at, and 12.5 mm after the working distance, d_f = 105 mm from ETL_2 and to the pivoting distance d_p. Figure 5. 12(a) shows the anterior segment scan configuration where the beam divergence and the focus at the working distance can be observed in the variation of the spot size between the central and the first and last axial positions shown. It is also evident that the beam axis is displaced laterally and parallel to the optical axis of the system throughout the scan. Figure 5. 12(b) depicts the posterior segment scan configuration at two angular positions. In this case, we can observe that the beam diameter is much larger than for the anterior scan configuration and rather constant in size for the three axial positions, denoting a collimated output beam. It is also clear that the beams overlap in the central axial position while they are laterally displaced in the two other positions, showing that the beam pivots around the central position.

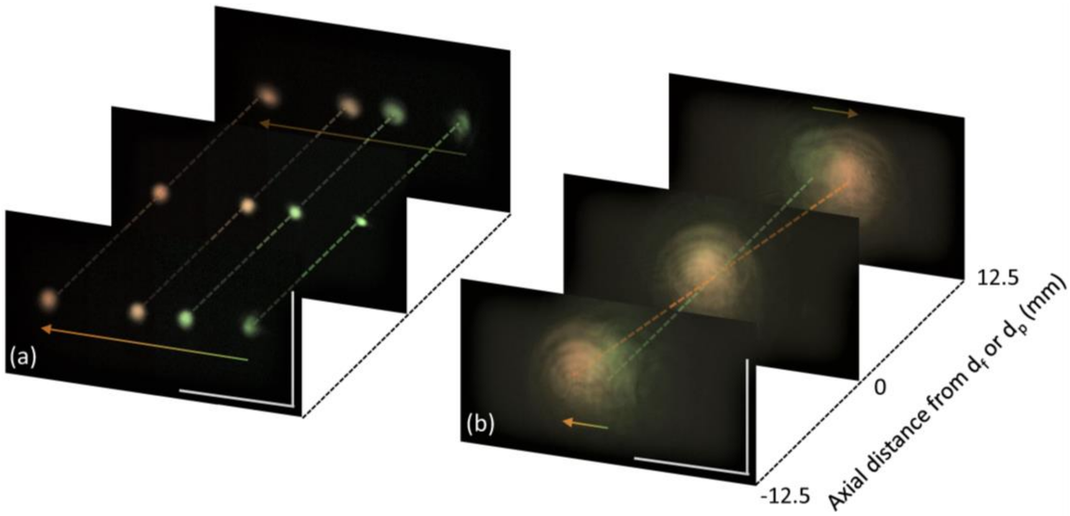

Figure 5. 12 *- A perspective view of the beam profile images at the three axial positions, namely 12.5 mm before, at, and 12.5 mm after the working or pivoting distance, d_f or d_p. (a) Anterior segment scan overlay of four transverse displacement profiles. (b) Posterior segment scan overlay of two angular displacement profiles. The arrows represent the scan direction with time. The scale bars represent 1 mm.*

The quantitative analysis of the beam spot diameter and direction from the beam profiles recorded at seven and five different axial positions for the anterior and posterior segment scan, respectively, is shown in Figure 5.13. The origin of the axial distance axis is set to the working distance, d_f and d_p. Figure 5.13(a) shows the experimental axial profile of the beam diameter (evaluated at the $1/e^2$ value of the peak intensity) for four transverse displacements in the anterior segment scan configuration (shown with dots). The experimental data was also fitted to the theoretical axial profile of a Gaussian beam with the minimum root-mean-square error from the experimental data points (shown with dashed lines). The focal planes for the four transverse displacements all lie within a range of 2.5 mm, confirming our ability to set a significantly constant working distance d_f throughout the scan. The beam diameter was also observed to increase when increasing the transversal displacement of the beam and, conversely, the transverse resolution decreased during the transverse scan, from 58 μm to 122 μm. This was expected as it was already observed in the simulation due to the variation in the focal length of ETL_3 that is required to maintain the focal plane at the set working distance. The spot size at each transversal position was in relatively good agreement with theory, as the measured spot size deviated less than 30 μm from the analytical results of Figure 5.7(a). The transverse resolution degradation by a factor of 2.1 was less severe than the 2.6 factor expected from the analytical results. A side effect of the reduction of transverse resolution is the increase in depth of field when increasing the transversal displacement, equal to twice the Rayleigh range of the associated beam.

Figure 5.13(b) shows the beam axis for the four beams at the increasing transverse displacements studied. This figure demonstrates the ability of the beam scanner to perform a telecentric scan as the deviation of the beam axis from a propagation direction parallel to the optical axis of the system was less than $\pm 0.1\,\text{deg}$ for every beam transversal displacement.

Similarly, Figure 5.13(c) shows the experimental axial profile of the beam diameter for four angular displacements in the posterior segment scan configuration. In this case, the experimental data was fitted to a line. The divergence of the beam was less than 0.3 deg for all the angular scan positions, demonstrating the ability of the implemented beam scanner to produce a highly collimated output beam throughout the angular scan. We also observed the expected reduction of the beam diameter during the scan, as predicted by the analytical analysis of section 5.3.2. The experimental spot size was smaller, by 0.46 mm on average, than the ones expected from the analytical results in Figure 5.7(c). Besides, the expected reduction of the beam diameter when increasing the angle of scan expected from the analytical results in Figure 5.7(c) was also observed.

Figure 5.13(d) shows the beam axis for the four beams at the increasing angular displacements considered in Figure 5.13(c). The pivoting point was measured at a distance of 103 mm from ETL_2, only 2 mm off from the expected position, and all measured beam axes crossed each other within a range of 1.5 mm. This demonstrates the ability of the beam scanner to perform an angular scan pivoting at a point.

These characterizations show experimentally the capability of the beam scanner to maintain a focal plane constant during a telecentric displacement of the light beam, as required for imaging the anterior segment of the eye; as well as performing an angular displacement of the beam while maintaining a collimated output beam, as required for imaging the posterior segment of the eye.

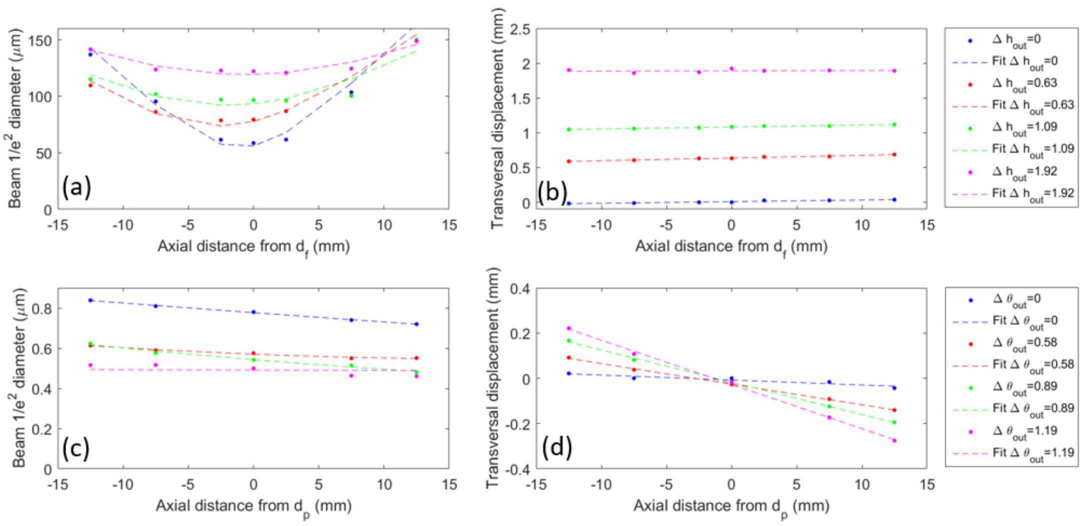

Figure 5.13 *- Experimental axial profiles of (a), (c) the beam diameter and (b), (d) the beam axis direction for four displacements in (a), (b) the anterior segment telecentric scan and (c), (d) the posterior segment angular scan, respectively.*

<u>B- Experimental calibration of the optical beam scanner</u>

Figure 5.14 shows the experimental calibration curves for the look-up table between the 8-bit digital counts (0-255) of the PWM signal (at a given polarity) and the corresponding optical power (reciprocal of the focal length in meters) for ETL_1 in blue, ETL_2 in red, and of ETL_3 in yellow. The experimental data is shown with dots and the polynomial functions fitted later used in the aforementioned Arduino Nano board code with dotted lines.

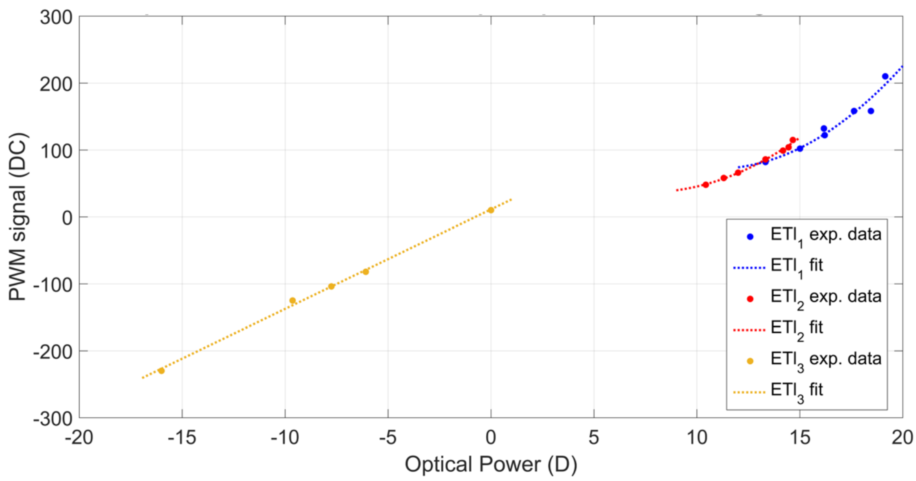

Figure 5.14 *– Experimental calibration for the look-up table between the 8-bit digital counts (DC: 0-255) of the PWM signal and the corresponding optical power in diopters (D) for ETL_1 in blue, ETL_2 in red, and of ETL_3 in yellow.*

5.5 - Whole-eye OCT scans

In this section the results obtained when integrating the beam scanner into an OCT system are shown. We present the experimental setup of the custom developed SS-OCT system in combination with the beam scanner prototype, and the cross-sectional OCT images obtained for several samples.

5.5.1 – SS-OCT experimental setup

The custom SS-OCT system was based on a fiber Mach-Zender interferometer configuration, similar to [120], as schematically shown in Figure 5. 15. The light source was a MEMS-based vertical-cavity surface-emitting laser (VCSEL) swept-source centered at 1060 nm with a sweep rate of 60 kHz over a spectral 10 dB bandwidth- of 100 nm (SL100060, Thorlabs), producing a theoretical axial resolution of 11 μm. The interferometric signal was acquired with a dual balance photodetector with a 3 dB-bandwidth from 3 kHz to 1 GHz (PDB481C-AC, Thorlabs) and digitized by a 12-bit 8-lane PCI Express digitizer (ATS 9360, Alazar Tech). The experimental axial depth range was ~33 mm, when sampling the interferogram at 1 GS/s. The experimental prototype of the new optical beam scanner was integrated into the sample arm of a custom developed SSOCT system to acquire whole-eye cross-sectional images of different ocular samples.

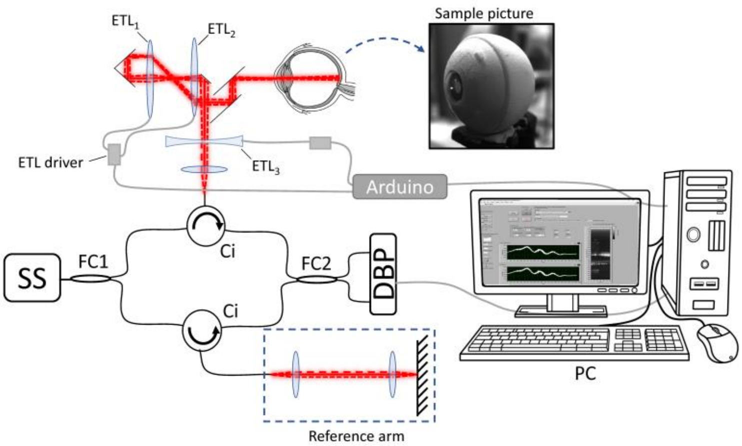

Figure 5. 15 *- Schematic of the custom SS-OCT system coupled with the proposed optical beam scanner, where SS: swept laser source, Ci: circulators, FC: fiber coupler, PC: computer, DBP: dual balanced photodetector. Sequential acquisition of the anterior and posterior segment scans is recorded in alternated B-scans.*

We compared the cross-sectional images acquired with the proposed optical beam scanner with those acquired with a standard telecentric scan system, i.e. the classical approach in anterior segment imaging, composed on two galvanometric scanning mirrors (Saturn 1B, ScannerMAX, Pangolin, USA) placed at the back focal distance of a 2" aperture f-theta telecentric scan lens (LSM05, Thorlabs, USA). The standard sample arm performed a telecentric scan over a transverse field of view of 8 mm; while with the proposed optical beam scanner, performed the two scan configurations that were sequentially alternated without any mechanical adjustment to obtain a whole-eye B-scan image over a field of view of 2 mm and 1.2 deg at each scan configuration. The two sample arms could be manually connected to the SS-OCT system and the path length matched reference arm was set up with a flip mirror. A custom LabView program was used to synchronize the OCT acquisition with the control of either scanner.

Table 5.4 reports the image acquisition specifications for either system. With the two optical beam scanners, 120 equidistant points every 2 ms, separated by 17 μm and 10 mdeg over a lateral range of 2 mm and an angular range of 1.2 deg in the telecentric and angular scans respectively were obtained. With the standard galvanometric scanner, a single scan method was used sampling 300 equidistant points separated 26 μm over a lateral range of 8 mm every 17 μs. With both scan mechanisms, 100 repetitions of the B-scans were averaged to improve the signal to noise ratio and image quality of the scan. The acquisition time of each measurement was 0.4 min and 0.5 s with the novel optical beam scanner and the standard galvanometric scanner respectively.

Table 5.4 *- Image acquisition specification for the proposed whole-eye beam scanner and a standard galvo-based anterior segment scanner used for comparison.*

Image acquisition specifications	Proposed whole-eye beam scanner	Standard Galvo-based anterior segment scanner
Telecentric scan range	2 mm	8 mm
Angular scan range	1.2 deg	NA
Number of A-scans in a B-scan	120	300
A-scan period	2 ms	17 μs
B-scan repetitions (for averaging)	100	100
AS scan transverse resolution at focus (on anterior chamber)	35 – 102 μm	$40\mu\text{mm}$
PS scan transverse resolution at focus (on retina)	23 – 31 μm	NA

5.5.2 – Ocular samples imaged

To compare the images with either scanner we used an OCT model eye (Modell-Augen Manufaktur, Germany) that mimics realistically the components of the human eye in both the anterior segment (the cornea and the crystalline lens) and the posterior segment (the main retinal layers as well as the macula and the optic nerve). We also acquired cross-sectional OCT images of an ex vivo rabbit eye, obtained from a local slaughterhouse, to demonstrate whole-eye imaging. Finally, we performed an *in vivo* test of the anterior segment with a volunteer subject.

<u>A - Human model eye</u>

Figure 5.16 shows an overlay of the OCT B-scans of the model eye obtained with the proposed beam scanner and the standard telecentric galvanometric scanner. The scans obtained with the experimental prototype of the optical beam scanner were overlapped with the larger B-scan obtained with the galvanometric scanner.

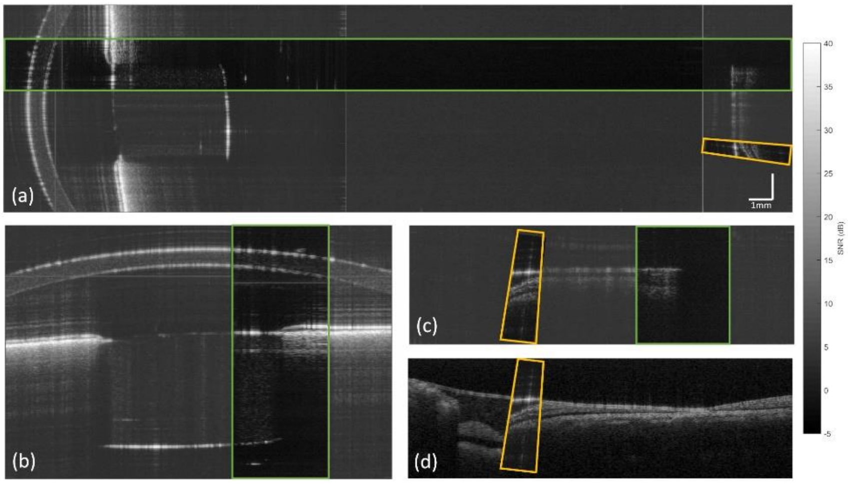

***Figure 5.16** - Overlay of the OCT B-scans of the model eye obtained with the proposed beam scanner and the standard telecentric galvanometric scanner for comparison. (a) B-scan of the entire eye. The boxed areas represent the whole-eye scans obtained with the proposed beam scanner, in green and yellow for the anterior and posterior segment scan configurations, respectively. (b) Close-up on the anterior segment. (c) Close up on the posterior segment, where only the image in the yellow box is artifact-free. (d) Co-location of image features in the posterior segment scan with model retina landmarks. The scanned area is at the edge of the model optic nerve.*

Figure 5.16(a) shows the comparison of the results obtained for the entire eye. The anterior segment of the model eye, including the cornea, iris and crystalline lens, can be observed in the partially transparent background image acquired with the standard scanner. The green square shows the corresponding anterior segment scan performed with the proposed optical beam scanner. A close-up view of the anterior segment scan is shown in Figure 5.16(b) to allow the comparison between all anatomical features and biometric dimensions obtained with the two scan systems. A good agreement between them is obtained regardless of the shorter field of view scanned by the proposed beam scanner.

It is in the posterior segment imaging that the value of the proposed scanner becomes evident when seamlessly reconfigured for a posterior segment scanning. Without the ability to switch to an angular scan, the standard telecentric scan rays get refracted towards a small area of the retina and the beam itself diverges, creating a defocused spot on the retina that does not scan laterally the retina. This leads to the artifactual image of a low-resolution, laterally unresolved, retinal depth profile, as seen in Figure 5.16(a). A close-up view is shown in Figure 5.16(c), where the same issue is observed in the image of the retina obtained with our proposed scanner set for anterior segment scanning (green square). However, when the scan configuration is switched in the proposed optical beam scanner to perform and angular displacement of a collimated beam (yellow box in Figure 5.16), different features of the model retina were clearly observed and thus the posterior segment of the model eye can be imaged. To verify and co-locate those features with a larger field of view on the retina, we also scanned the posterior segment of the model eye with the standard telecentric scanner by removing the anterior segment. This was possible, as the model eye was composed of two halves, comprising the anterior and posterior segments respectively, that can be unscrewed and separated. Figure 5.16 (d) shows that the area scanned by the proposed beam scanner perfectly matches the edge of the optic nerve of the model eye. This comparison exemplifies the ability of the proposed optical beam scanner to automatically switch to an optimized configuration to image the posterior segment of the model eye and observe the retina, which was not possible with the standard galvanometric scanner unless the optics of the sample arm was changed.

B - *Ex vivo* rabbit eye

We also imaged an *ex vivo* rabbit eye with the proposed beam scanner. Figure 5.17(a) shows the B-scan recorded with the telecentric scanning configuration. Figure 5.17(b) shows the subsequent B-scan recorded with the angular scanning configuration. Figure 5.17(c) shows a close-up view of the anterior segment shown in (a) where the cornea, the iris and the crystalline lens of the rabbit eye are clearly seen, and Figure 5.17 (d) shows a close-up view of the posterior segment shown in (b). As the posterior segment scan configuration pivots around the eye nodal point, the refractive optical components of the eye focus the light beam on the retina and the visibility of details of the inner and outer retina is increased when compared to Figure 5.17 (a) where the posterior segment image was hindered by the shadow cast by the iris and otherwise a repeated artifactual image of a retinal depth profile was caused by the eye refraction.

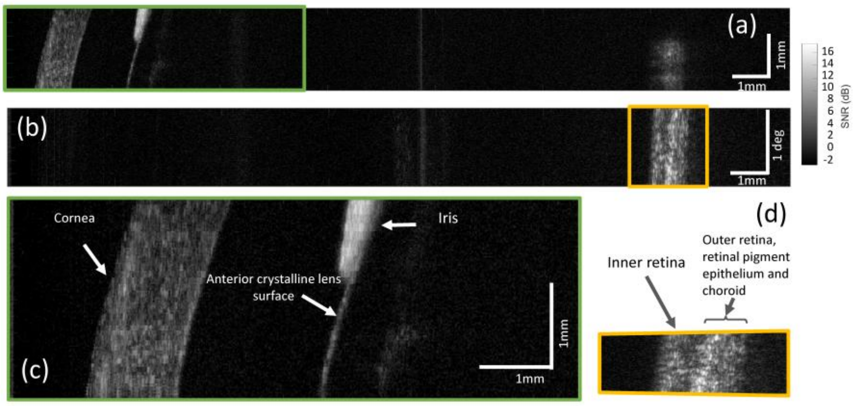

Figure 5.17 - *Whole-eye OCT B-scan of an ex vivo rabbit eye acquired with the proposed beam scanner. (a) B-scan acquired with the anterior segment scan configuration. (b) subsequent B-scan acquired with the posterior segment scan configuration; (c) close-up view of the anterior segment from (a). (d) close-up view of the posterior segment from (b).*

C – *In vivo* human eye

We also imaged an eye from a volunteer subject with the proposed beam scanner. Several experimental aspects such as the position of the working distance, the height of the beam and especially, the eye movements during acquisition, challenged the acquisition of images with the proposed beam scanner. The experimental sessions served to show the need to acquire data faster to achieve motion artifact-free in vivo images. Figure 5.18(a) shows the average B-scan of the anterior segment of the volunteer's eye recorded with the telecentric scan configuration where the cornea and the crystalline lens are seen. Figure 5.18(b) shows the iridocorneal angle of the same volunteer eye observed when the volunteer's eye was laterally displaced with respect to the field of view of the beam scanner.

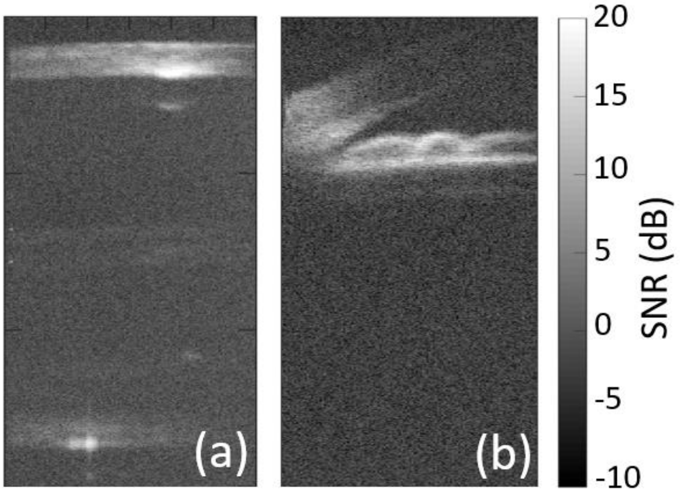

Figure 5.18 *– Anterior segment B-scans of a volunteer eye acquired with the telecentric scanning configuration. (a) Anterior segment close-up view. (b) Iridocorneal angle obtained by laterally displacing the volunteer's eye with respect to the field of view of the beam scanner.*

5.6 - Alternative implementations

To duplicate the scan range of the optical beam scanner developed we also proposed and patented the possibility of using a low-cost DC or stepper motor that synchronously rotates the HRM and the periscope P. Figure 5.19(a) shows a representative view of a 3-D simulation of the alternative proposed beam scanner. The components that rotate are indicated with a yellow shadow. The rotation of the HRM transmits the rotation to the input offset h_{in} of the light beam before the second pass through the ETL_1-ETL_2 sub-system performing a circle around the optical axis of the beam scanner. In this way, a symmetrical displacement of the output beam can be performed through both sides of the clear aperture of ETL_2. However, the rotation of the HRM would generate a cylindrical scan around the optical axis of the beam scanner, as the beam displacement was always defined to start at the same transversal position as the input offset h_{in} and to move towards the edge the clear aperture of ETL_2, thus preventing scanning at the center. To overcome this issue, a synchronized rotation of the periscope P is required, so that the starting point of the scan is aligned with the optical axis of the beam scanner. This implementation would unlock the potential of performing full 3-D scans by building radial sections or circular/spiral scan patterns through synchronization of the motor and the ETLs control. This scanner could also be understood as a polar coordinates scan where the angular coordinate is set by the rotation of the HRM-P set of components, and the radial coordinate is imposed with the ETL_1-ETL_2 set of components.

On the other hand, the synchronized rotation of the HRM and P at a significant large distance between them presents a challenge if a single motor is wanted to be used. A transmission system to connect the rotation of the two components would be needed to implement the scan considering all the cables and mounts of the rest of the opto-mechanical that are present between them. To avoid this issue an alternative implementation of the full 3-D scanner is shown in Figure 5.19(b), where the optical path between ETL_1 and $ETL_2$is folded over itself with 4 additional mirrors at 45 deg, in such a way that the HRM and the P end being side by side. As the axis of the rotation of both HRM and P is the same, a single dual shaft motor can be used to turn them both.

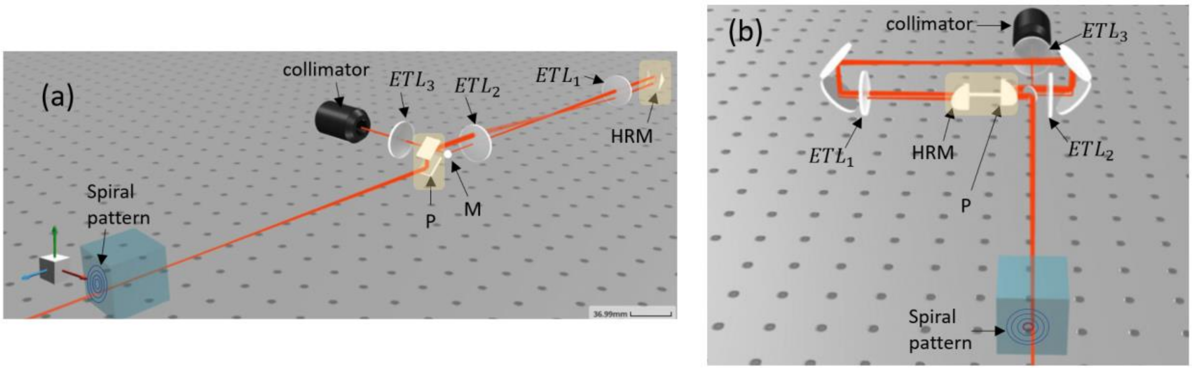

Figure 5.19 – *3-D simulations of the proposed beam scanner designed to perform full 3-D scans by building radial or circular scan patterns by performing a synchronized rotation of the HRM and the periscope P of the optical beam scanner design presented so far (a) and a folded design of the ETL_1-ETL_2 sub-system to allow an easier mechanical connection of the HRM and P to allow the use of a single motor.*

5.6 -Discussion

We presented an optical beam scanner with the ability to reconfigure the scanning and focusing configuration via low-cost non-mechanical components, and we employed it to provide quasi-simultaneous whole-eye imaging, albeit over a limited field of view. The device employs three ETLs, and several mirrors. We have presented its working principle and derived its analytical description, and we have characterized its dynamic scanning and focusing capabilities on an experimental proof-of-concept setup. We benchmarked whole-eye OCT images of a model eye against those produced with a standard galvanometric scanner, and then acquired whole-eye OCT images of an *ex vivo* rabbit eye, revealing details comparable to those seen in conventional anterior and posterior OCT scanners. Finally, an *in vivo* test was also performed.

We derived the analytical equations describing the relationship between the focal length of the three ETLs and the desired output beam displacement, deflection and divergence; and we have used them to optimize the mechanical distances between off-the-shelf components to maximize the transverse and angular scanning range of the proposed beam scanner. The optical characterization of the experimental prototype showed a good agreement between theoretical and measured beam profiles. However, the measured beam spot sizes in the anterior segment scan configuration were slightly larger than expected, especially for the smallest spot size, probably due to the presence of aberrations that prevent the formation of a diffraction limited spot size. This is not entirely unexpected, as the working principle requires the beam to be incident off axis from the ELT_1 optical axis, and the scan progresses toward the periphery of ETL_2, where the impact of aberration is higher. Larger ETL clear apertures would be beneficial in reducing this effect.

The implemented beam scanner prototype showed the expected undesirable variation of the transverse resolution along the scan direction in both scan configurations. Even though the double pass configuration through ETL_1 and ETL_2 partly compensate this effect, as the magnification in a single pass is inverted in the double pass, that is only valid for a collimated beam impinging on the ETL_1-ETL_2 telescope sub-system. Therefore, for both scanning configurations considered here, there is still some residual beam size variation due to the single propagation through ETL_3, and hence, a transverse resolution variation. One solution to prevent this variation would be the addition of a variable beam expander (i.e., a telescope made of two additional ETLs) to place between the collimator and ETL_3 in order to fully pre-compensate this residual variation. However, this solution adds to the device cost and footprint.

The minor experimental imprecisions found in the position of the focal spots or beam axes intersection with respect to the working and pivoting distance could be solved by employing a more precise control of the ETLs focal lengths by using a microcontroller with better digital resolution than the Arduino Nano board such as an ESP32 microcontroller with 16-bit resolution. Additionally, the implementation of a temperature control system of the electrotuneable lenses [187] would also allow a more precise control of the ETLs and thus of the position of the scanning beam.

A current limitation of the experimental implementation of the beam scanner is the switching frequency between adjacent scan positions or A-scans. Although the experimental data reported in this work was acquired at 500 Hz, the selected ETLs could respond at faster rates, up to 1 kHz and beyond that frequency for small diopter increments [188]. Future works could explore their use at greater speeds, achieving motion artifact-free in vivo images.

Another important limitation of the current experimental implementation is the limited transverse and angular scan range allowed, thus having a limited field of view. The characterization of each scan configuration led to a field of view of 2.5 mm and 1.2 deg for the telecentric (anterior segment) and angular (posterior segment) scan configurations, respectively. ETLs with larger apertures and wider focal ranges, especially towards shorter focal lengths, would enable larger transverse and angular scan ranges as the limiting factor obtained during the optimization process were the minimum focal length available for ETL_1 and the clear aperture diameter of ETL_2. An alternative could be the use of off-the-shelf ETLs with a clear aperture 6 mm larger than the one we used for ETL_2 in our prototype that could achieve a similar focal range to ETL_2, such as the EL-10-40-TC, that with the help of an offset lens could duplicate the scan range of the current system.

Another option to increase the field of view of the proposed beam scanner would be the addition of a magnifying two-lens telescope placed at the output of the beam scanner, such that the first lens of the added telescope would be placed a focal length away from the working distance (and pivoting point) of the proposed beam scanner. This telescope would increase by the magnification factor the transverse and angular scan range to image the anterior and posterior ocular segments respectively. However, it would also reduce the transverse resolution for the anterior segment scan and the posterior angular range as the beam spot sizes would also be magnified by the same factor. Therefore, the only effective solution for increasing both transverse and angular ranges, at the expense of transverse resolution, is the use of an adaptive telescope, where the second lens is another ETL, such that it creates a magnifying and demagnifying telescope for the anterior and posterior segment scan configurations, respectively.

It is also important to notice that in our experimental setup we only used half of the ETLs aperture. As presented in the alternative implementation of the beam scanner, by simultaneously rotating the hollow roof mirror HRM and the periscope P by 180 deg, we could double the scan range for both anterior and posterior segment configurations, as the full aperture of the ELTs would be exploited using the same combination of focal lengths sets to the scan on the first semi-aperture of the ETL_2. This would allow a field of view of 5 mm for the telecentric scan and 2.4 deg for the angular scan with the used ETLs, opening also the possibly of performing full 3 D-scans of the whole eye.

The comparison between the proposed beam scanner and a standard galvanometric mirror-based scanning method implemented in a custom SS-OCT system showed a good agreement between the anterior segment images of the human model eye acquired with both scan mechanism. The comparison also showed the benefits of the proposed beam scanner for the visualization of the retina of the model eye when non-mechanically switching to the angular scan configuration not possible with the standard galvanometric scanner that would require to exchange its optical components.

Nevertheless, the current implementation can already find good use in low-cost biometry by providing anterior segment 2-D central anatomy for the detection of the lens tilt and decentration, for example; and posterior segment anatomy, such as the foveal pit for fixation checks. In fact, commercial biometers, such as the Zeiss IOL Master 700 [163], already implement a small angular scan around the foveola, a central pit of the fovea, about 0.35 mm in diameter (or ~1.2 deg) [7], where only cone photoreceptors are present and which is specialized for maximum visual acuity [189]. By detecting a distorted image of the foveal pit, one can assume poor fixation, likely caused by patient’s eye motion, and therefore apply a quality check on the biometry reading. With the proposed beam scanner, fixation check and central 2-D anterior segment biometry will be readily available.

With all, the proposed beam scanner reduces the complexity and cost of other proposed whole-eye scanner based on mechanical switching or polarization multiplexing between the two segments scan configuration. Additionally, it provides the ability to reconfigure the scan configuration to best suit the specification application, i.e., it is not limited to using only pre-selected scan configurations. A summary of the scanning methods discussed in the introduction section is presented in Table 5.5. As the literature scanning methods are based on the use of galvanometric scanners, which duplicate the cost of the proposed ETL based optical beam scanner, we considered our proposed beam scanner as low-cost alternative. The galvo-based systems are also classified as medium if a single sample arm or detection method is used, and high-cost if dual detection systems or dual sample beams are implemented. Notice that multireference arm configurations have also been considered as medium cost as the optics involved in a reference arm are simpler than in the case of a multi-sample arm.

***Table 5.5** – List of scanning methods for whole-eye OCT imaging from the literature and the proposed optical beam scanner.*

Scanning method	Optical components	Estimated cost	Versatile scanning method	Versatile vergence beam	Sequential /Simultaneous
Single beam galvanometric scanner [120]	• Galvanometric scanner • Fixed objective lens	Medium	No	No	-
Single beam galvanometric scanner [74]	• Galvanometric scanner • Fixed objective lens • Multiple reference arm	Medium	No	No	Sequential Method: mechanical selection of reference arm
Single beam galvanometric scanner [178, 190]	• Galvanometric scanner • Adjustable objective lens	Medium	No	Yes	Sequential Method: programming
Single beam galvanometric scanner [173]	• Galvanometric scanner • Fixed objective lens with changeable sample path	Medium	Yes	Yes	Sequential Method: mechanical selection of sample beam path
Dual band galvanometric scanner [175]	• Galvanometric scanner • Dual objective lenses • Dual band detection	High	Yes	Yes	Simultaneous
Dual polarized beam galvanometric scanner [172, 176]	• Galvanometric scanner • Dual polarized sample arms • Dual detection	High	Yes	Yes	Simultaneous
Dual polarized beam galvanometric scanner [174]	• Galvanometric scanner • Dual polarized sample arms • Single detection	High	Yes	Yes	Sequential Method: optical switcher
ETL based beam scanner [191]	• Combination of 3 ETLs	Low	Yes	Yes	Sequential Method: programming

As Table 5.5 shows, no medium cost system is capable to fully exchange the scanning configuration and control the vergence of the output beam without involving the mechanical displacement of some optical component. Only at higher cost implementation, fully adjustable scanning configurations are obtained using optical switchers or simultaneous imaging systems.

The current system would already prove useful in low-cost biometry applications to provide 2-D anterior segment anatomy and fixation checks for improving the repeatability of biometry readings and leading to fewer refractive surprises. Sourcing larger aperture ETLs will enable to overcome the current limitations on the transverse and angular scan ranges and expand it use to diagnostic and scientific applications to glaucoma, myopia studies and beyond in several other fields.

5.7 - Conclusion

A novel optical beam scanner with reconfigurable non mechanical control of beam position, angle and focus using three low-cost ETLs was presented and whole-eye OCT imaging using the beam scanner was demonstrated. We derived the analytical equations for the focal lengths of ETL_1-ETL_3 to control the beam axis position, angle and focusing distance, and we set them for alternately providing a telecentric scan of a focused beam for anterior segment imaging and an angular scan of a collimated beam for posterior segment imaging. The expected scan range was 2.5 mm and 1.2 deg, and the expected transverse resolution was varying in the range 35 – 102 µm and 23 – 31 µm, for the anterior and posterior segment scans, respectively. We characterized the dynamic scanning and focusing capabilities of an experimental setup through beam profiling, after a thorough calibration procedure. The experimental measurements were in good agreement with the analytical expectations. We integrated the proposed beam scanner in a SS-OCT system and acquired whole-eye OCT images of a model eye and of an ex vivo rabbit eye, revealing details comparable to those seen in conventional anterior and posterior OCT scanners.

The proposed beam scanner reduces the complexity and cost of other proposed whole-eye scanners based on mechanical switching or polarization multiplexing between the two segment scan configurations. Additionally, it provides the ability to reconfigure the scan configuration to best suit the specific application, i.e., it is not limited to using only pre-selected scan configurations. The current system would already prove useful in low-cost biometry applications to provide 2-D anterior segment anatomy and fixation checks for improving the repeatability of biometry readings and leading to fewer refractive surprises. Sourcing larger aperture ETLs will enable to overcome the current limitations on the transverse and angular scan ranges and expand its use to diagnostic and scientific application to glaucoma, myopia studies and beyond, in several other fields.

Chapter 6
Ophthalmic progressive lens demonstrator

In this chapter, I present the working principle and proof-of-concept of a novel optical system that aims to allow presbyopic patients to test different progressive lenses before buying a progressive glass. The method is based on a wide field-of-view projection system that projects different progressive designs in the patient's pupil plane. We analyzed the theoretical optical performance of the designed systems, as well as an experimental implementation of a proof-of-concept.

The author of this thesis (1) performed the literature search, (2) developed the optical design of the system and its optical performance characterization, and (3) implemented and characterized the experimental prototype of the system (supervised by Dr. Enrique Gambra).

The principle of this work is protected by the patent [M2201P001EP] owned by 2EyesVision, in which I contributed to the manuscript preparation and I am the first co-inventor.

A video explaining the concept and use of the developed proof-of-concept system was presented at an event organized by SECPHO (Southern European Cluster in Photonics & Optics) in June 2022 with potential users to present the project and the device under use, in the context of the AEI project "Try First".

6.1 - Introduction

As mentioned in Chapter 1, presbyopia is associated with the aging of the eye, affects the entire population over the age of 40, and its prevalence is estimated to increase up to 1.8 billion people by 2050 [38]. Presbyopia is caused by the hardening of the crystalline lens in the eye, which makes it difficult to focus on nearby objects. This results in the need of a solution to correct this condition.

Nowadays, strategies to correct presbyopia include surgical procedures or the use of spectacles and contact lenses [37]. Although the correction through an IOL implantation in a refractive surgery procedure has become lately more popular [192], the use of ophthalmic lenses is still the most extended solution as it meets the main needs of the majority and is a non-invasive method [41]. The ophthalmic lenses used to restore near vision can be of three types: monofocal or single vision 'reading spectacles' to see only at near distance, bifocal or trifocal lenses to focus at two or three set distances, or progressive addition lenses (PAL) that allow to see through a wide range of distances from far to near through the same lens. Among them, progressive spectacles are the most common and advanced solution due to their comfort and functionality, although they also present disadvantages such as the need of an adaptation process or the selection of the proper lens design within a wide variety of options.

PAL offer a smooth variable optical power along the lens surface, allowing the viewer to have a good vision at different distances when looking through each region of the lens. Thus, PAL present a high added value on which manufacturers invest a significant amount of effort to improve their quality and properties. Figure 6.1 shows a schematic representation of the PAL. There are three main areas of interest in this ophthalmic lenses: the top zone, which is dedicated to far vision (FZ); the bottom zone, dedicated to near vision (NZ), and the intermediate region connecting the FZ and NZ, with a progressive variation of the optical power between both zones, called corridor (see Figure 6.1(a)). Due to this smooth vertical corridor on the lens surface, unavoidable aberrations are generated at the sides (mainly astigmatism), affecting the clarity of vision through the lateral parts of the lens. The aberration level increases from the center to the periphery of the lens.

There are two main categories of PAL optical designs: hard and soft designs. A schematic hard and a soft design are shown in the left and right representations of Figure 6.1(a) respectively, where the darkness degree of the shadowed areas represents the level of aberration being darker at the regions were the aberrations are higher. It can be observed that, despite the stronger aberrations profile, the hard designs provide wider clear vision areas for both far and near zones, whereas soft designs present lower aberration profiles but at the expense of narrower clear vision zone [192].

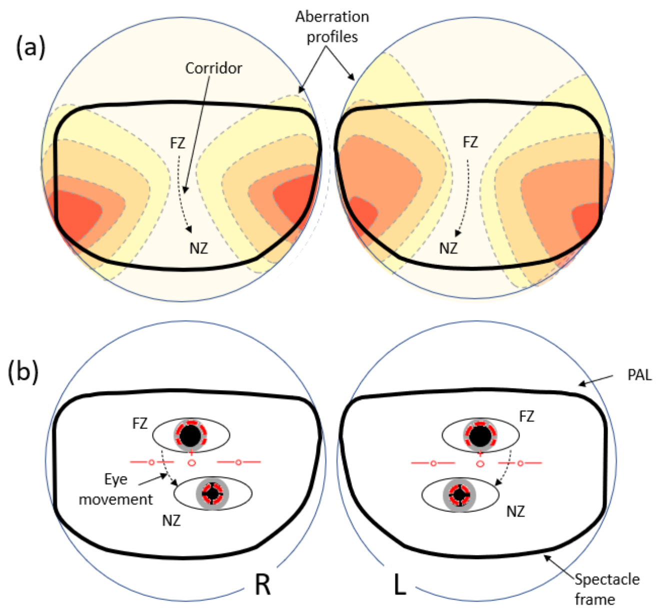

Figure 6.1 *– Schematic representation of the optical performance of a PAL. (a) Shows a hard (left) and a soft (right) design of a PAL with the vision zones labels. The shaded areas indicate the distribution of aberration, i.e., darker shade present higher amounts of aberrations. (b) Represents the line of vision movement required to clearly see distant and near objects by aligning the eye with each vision zone. The red marks indicate the usual indications of the PAL areas. (FZ: far zone, NZ: near zone and PAL: progressive addition lens).*

The spatial distribution of different vision zones across the spectacle surface implies a significant change in the use of ophthalmic lenses, as now the user needs to: 1) adequately rotate the eye to align the line of vision with each vision zone in order to focus objects at different distances and 2) to move the head to point towards the object, avoiding the lateral aberration at the sides of the corridor [193]. This rotation of the eye is also represented in Figure 6.1(b). The standard schematic marks that optometrists use to indicate each vision zone in the PALs are shown with red lines. A schematic eye is added centered at both vision zones together with the eye movement shown with a dashed black arrow. The position of the distance and near vision zones are determinant for the ergonomic use of the progressive lenses, being more comfortable when eye and head movements can be avoided. Ideally, the power design should be aligned with the user's needs and habits [194, 195]. This aspect is of high interest nowadays as the new techniques of progressive lens design and manufacturing allow a high level of personalization. Technological advances in the optical design and manufacturing of PALs such as freeform surfacing and computer design have allowed achieving a high level of customization for each individual patient [196, 197]. Additionally, with the purpose of acquiring the usual eye and head movements of a PAL user to optimize the personalized PAL, virtual reality systems such us Mimetika Mapper (INDO Optical) are already available [198].

Although, there has been a significant improvement in the selection of the PAL optical design regarding the spectacles frames and the consideration of user facial and vision features and head and eye movement [199, 200], the selection of the most adequate optical design with respect to the user's preferences is still nowadays a challenge. Many patients (ranging between 5% to 15%, based on internal surveys) face significant problems with their adaptation to PALs that leads to discarding the lenses and ordering new ones with a different design. This event affects all the value chain in the sale of progressive lenses, from the manufacturer that must produce new glasses, to the purchase experience of the user, the chair time of the optometrist, and even the environment, since the discarded glasses cannot be reused. Current methods for the selection of the PAL design consist in the use of questionaries and assumptions that do not lead to a straightforward adaptation to the selected optical design. To manage patient expectations as well as to help in the PAL prescription, all surveyed clinicians perceived that a system allowing to experience vision through different progressive lens design would be of significant benefit.

Recent technological developments have led to the appearance of visual simulators in the market. Desktop devices such as the VAO (VOptica, Murcia, Spain) [201] combine a wavefront sensor and a spatial light modulator (SLM) to manipulate the wavefront at the patient's pupil plane and thus allow to simulate vision through different profiles of lenses [202]. On the other hand, SimVis Gekko (2EyesVision, Tres Cantos, Spain) is a wearable see-through device based on the use of electro-tunable lenses (ETL) to project different IOL profiles into the patient's pupil plane using temporal multiplexing working principle [203, 204]. These systems have the potential of reducing chair time during the IOL selection procedure as well as a more satisfactory experience for patients due to a better management of expectations of the result after the surgery procedure [205]. However, the fact that the multifocal profile is generated in the pupil plane instead of on the spectacle plane (among other reasons) prevents the use of these systems for the simulation of PALs.

A different approach to attend this need is the use of 3-D virtual reality (VR) technology [206-208] based on a computer simulation of the addition and aberration profile of a PAL. In this case, the virtual scene shown to the user is affected by a computer-generated aberration profile of an ideal PAL. However, these systems present the disadvantage of having a reduced field of view as well as the fact that they show a computationally generated environment instead of allowing the observation of the natural surrounding environment with the real correction, requiring an extrapolation from what is being observed to what the final vision through the PAL would be (based on internal surveys to clinical users).

Another recent technique is augmented reality (AR) [209]. As in VR devices, AR is also based on a computer-generated profile of the PAL superimposed with a semi-transparent surface on the natural vision of the surrounding elements. The advantages of these systems with respect to VR are that they allow a wider field of view as well as the observation of the natural environment of the user [210]. Even so, they still do not represent a completely realistic representation of the progressive lenses as the progressive profile of the optics is simulated computationally and is superimposed to the natural scene.

To attend this need, the ideal solution would imply the possibility of testing a real progressive lens and being able to observe the real environment prior to the purchase. We disclose here a system capable of projecting any blank ophthalmic progressive lens into the patient's vision together with his/her refractive error. Thus, patients can directly observe their surrounding environment through a variety of real ophthalmic lenses without the need to mentally extrapolate their experience from the simulation to what they would see with their progressive lenses in the real world. The invention is a wide field see-through system with a constant magnification factor of x1 ensuring a natural observance of objects as well as able to project any ophthalmic lens design. In the following sections we present the working principle of the proposed device. We describe the main optical components, and we discuss its main requirements. Additionally, we present an experimental proof-of-concept based on commercial components, and finally, we introduce a custom optical design with the aim to fulfill the system requirements.

6.2 - Working principle description

In this section we aim to present the structure and working principle of an afocal projection system proposed for the projection of any PAL into the patients' vision. The developed demonstrator of PAL designs is based on an afocal projection system compound of two eyepieces (E) and a relay unit (RU) which, when combined with a physical blank PAL with 0 D power and trial lenses for the refractive error correction, allows to project any ophthalmic lens into a conjugated plane at a vertex distance in front of the patient's eye with no magnification and no image inversion (magnification factor M=+1).

The initial phase of the project was the definition of the working principle and the identification of the main requirements of the designed system. With the aim of providing a comprehensive understanding of how the various components of the system are combined, a block diagram of the main optical components is firstly presented, followed by the analysis of the requirements that are needed to be fulfilled to allow a clinical use of the system.

6.2.1 – Schematic description

The instrument is completely based on optical components with refractive and reflective surfaces, without any computation station, image processing unit or active optical elements. The aim of the optical system is to fit at a final head-mounted see-through device that comprises two observation channels, one for each eye, resulting in a binocular instrument with a magnification factor of x1. Figure 6.2 shows a schematic representation of a top view of the proposed system showing the arrangement of the following principal components:

- A projection system unit (PS), which consists of an optical system arranged in front of the optical axis of the patient's eye and comprises a conventional array of refractive lenses. It allows to project the user's pupil plane into a desired position in front of the PS and at a vertex distance *d* behind any blank PAL.
- A trial lens holder (TL), located at a conjugated plane of the user's pupil plane and in front of the PS, where a set of trial lenses can be placed to correct the user's refractive error if needed.

- A holder for a physical blank PAL, to place any blank PAL at a vertex distance *d* in front of the projected pupil plane to give the user a natural vision through all the vision zones of a real PAL.

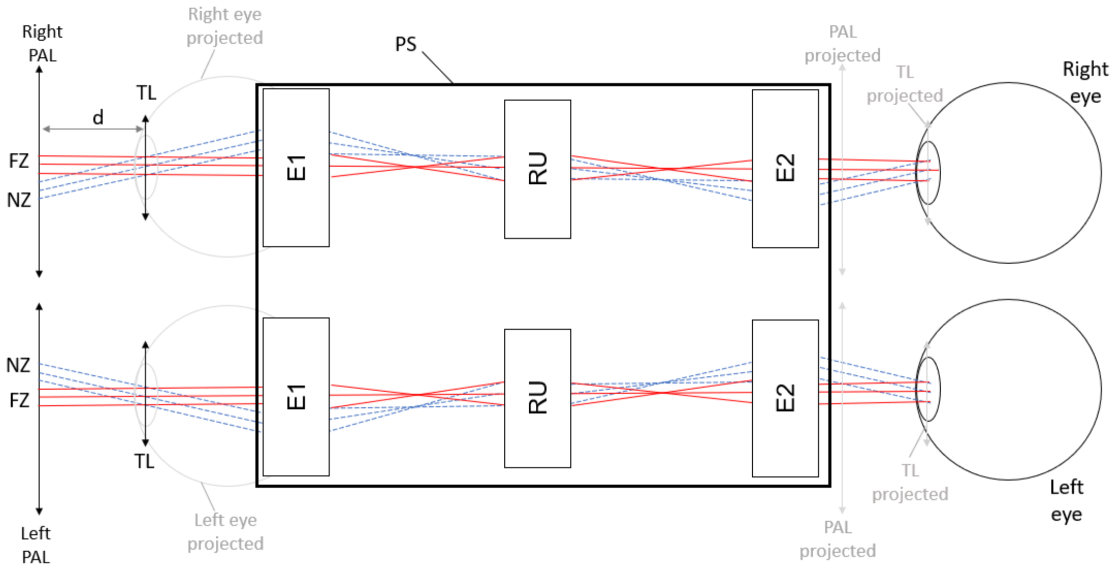

Figure 6.2 – *Schematic representation of the top view of the invention. The rays passing through the system for the far and near vision positions are shown with red and blue rays respectively. The eye is only shown at the position for far vision. Notice that for near vision the eye would need to be rotated in the nasal direction from the shown position. (FZ: far zone, NZ: near zone, PAL: progressive addition lens, TL: trial lens, PS: projection system, E: eyepiece and RU: relay unit).*

In such a way, while the user's eye is placed at the back of the PS, the blank PAL and the TL are placed at the front of it. The independent correction of the user's refractive error and the progressive addition allows the clinician to perform different combinations of refractive error and addition, as well as to use the same blank PAL with every patient. With the help of an easy axial and transversal manual displacement system, the PALs are properly aligned with the patient's pupil when seen through the PS unit. Thus, the user can comfortably move the eye through the corridor of the PAL from the FZ to the NZ and experience the influence of the different lateral aberration profiles of different PALs designs. With all, the proposed system can also be understood as a projector of the patient's pupil eye in front of the PS and behind the physical blank PAL, as well as a projection of the trial lens at the patient's pupil plane and the PAL design in front of the patient's eye at the vertex distance. All physical components of the demonstrator of PALs are shown in Figure 6.2 with black lines, while their projection through the PS have been drawn in grey.

The vision through the 2 vision zones, FZ and NZ, is also shown in Figure 6.2, with a red and blue beam respectively. As the scheme represents the top view of the invention, the horizontal beam passing through the center of the PAL corresponds to the far vision position while the tilted beam at the internal side of the PAL is the near vision. Notice that when looking through each vision zone the eye would need to rotate (not shown in the representation of Figure 6.2).

In Figure 6.2, the optical structure of the PS unit is also shown in blocks. The projection system PS is described as an optical system composed of 3 separated optical units: a first optical eyepiece (E1) that gathers light from a wide field of view, a relay unit (RU) to provide a finite conjugate image plane of the focal plane after E1 with a 1:1 imaging ratio (and inverted), and a second optical eyepiece (E2) to finally collimate the light at the pupil plane of the patient's eye. Thus, a non-inverted image with a magnification factor of x1 is achieved. The characteristics of the optical design of each of these optical components will be determined by the optical requirements of the device.

6.2.2 – System optical requirements

The optical requirements of the system were defined in order to ensure a comfortable and natural vision experience through the demonstrator with different progressive designs. They are classified in three categories presented in the following sections.

A-Image formation requirements:

To ensure a natural image projection of the observed scene in the patient's retina, the image projected by the system needs to be a non-inverted image with a x1 magnification factor.

To allow a x1 magnified image but also to reduce the cost of the device, it is convenient that the eyepieces E1 and E2 are equal, aligned on axis with respect to each other and placed facing each other in a mirror-like configuration, at a distance of 2f between them. In such a way, the second eyepiece E2 is placed at a distance equal to its back focal length from the back focal plane of the first eyepiece E1. However, this configuration would present a x(-1) magnification factor, and thus, although the entrance and exit pupil of the projection system PS will be equal and placed at a symmetrical position from the beginning and the end of the PS unit, the projected image would still be inverted.

To allow the formation of a non-inverted image while maintaining the x1 magnification requirement, a non-magnification relay unit RU needs to be used between the two eyepieces E1 and E2 to project the intermediate back focal plane of E1 inverted into the back focal plane of the second eyepiece E2, and thus undo the inversion that the two facing eyepieces would induce. In this work we propose the use of a triplet lens placed at a 4f configuration with respect to the intermediate focal planes of the eyepieces, i.e., at a distance equal to 2 times the focal length of the lens from the back focal plane of the eyepieces.

B-Visual comfort requirements:

To allow a comfortable visual experience when using the system, it is needed to avoid vignetting throughout the wide field of view that spectacles have. Thus, the field of view (FoV) and the entrance pupil (EP) of the projection system PS were defined considering the rotation that the eye performs when changing the gazing direction to see through the different areas of a spectacle lens [193].

The required field of view to allow the visualization of all the areas of interest of a blank PAL, FZ and NZ, was estimated as a function of the standard vertex distance of spectacles and the vertical separation between the FZ and NZ regions of a physical blank PAL provided by an ophthalmic lens manufacturer (Indo Optical, Spain) (see Figure 6.3). The measured vertical distance between the two vision zones of the PAL was 27.26 mm, and the vertex distance *d* between the center of the progressive lens and the center of rotation of the eye was 27 mm [211]. Thus, using simple trigonometry, the estimated FoV required to cover the whole range from the far to the near vision zones of a PAL was 53.5 deg.

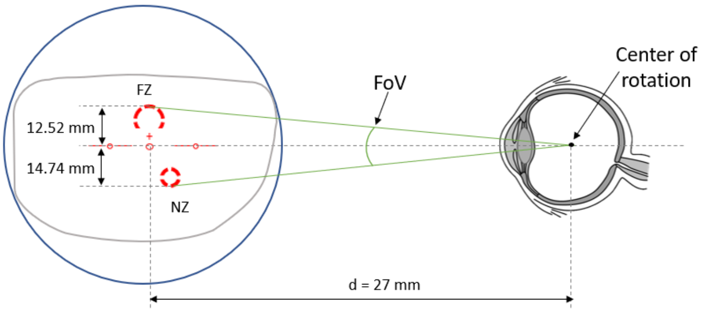

Figure 6.3 – *Estimation of the necessary field of view to evaluate progressive vision. The distance to the far zone and near zone from the center of the PAL lens were experimentally measured. The value of the vertex distance between the PAL and the center of rotation of the user's eye was based on the literature.*

With the estimation of the field of view, the exit pupil diameter of the projection system PS was calculated to allow to cover the vertical displacement of the eye pupil when the eye rotates to gaze through the whole field of view of the blank PAL (see Figure 6.4). The total exit pupil diameter was calculated considering the vertical displacement of the center of pupil Y as well as the vertical projection of the diameter of the pupil of the eye ΔY. Considering a distance from the pupil plane of the eye to the center of rotation of 12 mm [211], the vertical displacement Y of the center of the pupil when the gazing direction is rotated through the whole field of view is 10.8 mm. The vertical projection of the rotated pupil diameter ΔY was calculated assuming a pupil diameter of 4 mm (average size under light conditions) [6]. In such a way, the total exit pupil diameter requirement for the PS unit was 14.4 mm.

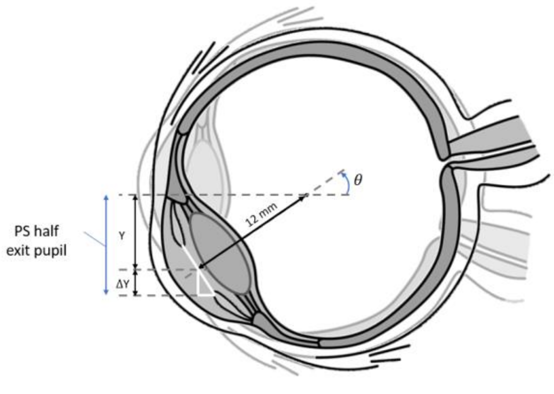

Figure 6.4 – *Schematic of an eye looking at the center of the field (background) and at the edge of the field of view (foreground). The center of the pupil moves a distance Y when the eye rotated by an angle θ.*

C-Ergonomic requirements:

Ergonomic requirements are the features of the system required to allow a comfortable posture of the patient when using the device. The two main ergonomic requirements considered are the eye relief and the apparent object distance.

The eye relief is defined as the distance between the closest surface of the PS unit and the patient's eye. To ensure enough space for the eyelash of the patient, an eye relief of at least 12 mm was defined.

Since the pupil plane of the eye of the patient is projected at a distance in front of the eye (as shown in Figure 6.2), objects will appear closer than they are when observed through the progressive lens demonstrator, thus having a different apparent object distance than in their natural vision. This would lead to an uncomfortable use of the device and could impair the natural viewing experience. To allow a natural use of the demonstrator of progressive lenses, the real and apparent object distances must be as similar as possible (and ideally the same), what would imply the addition of optical components such as mirrors to fold the optical path on the projection system and to place the projected pupil plane at a position where the natural object distance is still maintained.

With all, the requirements defined are summarized in the following Table 6.1.

Table 6.1 *- System requirements defined to allow a comfortable use of the progressive lens demonstrator system.*

System requirements		Parameter	Value
Image formation	1	Image inversion	None
	2	Magnification factor	x1
Visual comfort	3	Field of view	53.5 deg
	4	Exit pupil diameter	14.4 mm
Ergonomic	5	Reading/working distance	Natural
	6	Eye-relief	>12 mm

6.3 – Experimental proof-of-concept

In this section an experimental validation of the working principle of the progressive lens demonstrator is presented with a proof-of-concept system built using commercial components. The goal at this section is to verify the potential of the proposed approach to project a progressive lens into the patient's pupil plane, allowing the patient to observe the real environment through various progressive lens designs.

6.3.1 - Setup components

The optical components used to implement the proof-of-concept of the working principle of the progressive lens demonstrator are listed in Table 6.2. The eyepieces E1 and E2 were obtained from the commercial prismatic binoculars SPECTATOR (Bushnell) with a magnification factor of x4 and a nominal apparent field of view of 68 deg (FoV on the eyepiece side). The binoculars were unmounted, and the eyepieces were separated from the prismatic objective to be placed in the experimental system implemented. Two binoculars were used to implement the progressive lens demonstrator as 4 eyepieces are needed in total. The relay unit RU consisted of an afocal achromatic triplet TRS254-040-A (Thorlabs) with a focal length of 40 mm and an aperture of 25.4 mm. A set of three pairs of blank PAL with zero power were used during the experimental proof-of-concept, provided by an ophthalmic lens manufacturer (Indo Optical, Spain).

Table 6.2 – *List of commercial components used for the experimental validation of the PS system.*

Optical element	Commercial component	Specification
E1, E2	Eyepiece from Spectator sport binocular 4x 30 (Bushnell)	Apparent field of view: 68 deg Eye relief: 10 mm
RU	TRS254-040-A (Thorlabs)	Clear aperture: 25.4 mm Focal length: 40 mm
Blank PAL	Adapta, Eco and Balance (Indo Optical)	Base spherical power: 0D Addition: 2 D

A top view of the binocular system implemented using the pair of eyepieces from the binoculars and a triplet on each vision channel is shown in Figure 6.5(a). The eyepieces of the projection system were placed on axis and mirrored with respect to each other with the triplet located in between them, labeled as E1, E2 and RU respectively in Figure 6.2. The commercial eyepieces from the binoculars were compounded of three lenses and had an approximate focal length of 20 mm. The triplet RU was mounted at a distance 100 mm from both E1 and E2 on an axial translation system to allow its fine adjustment. Additionally, one of the vision channels was mounted on a transversal rail to allow its horizontal displacement and thus to adjust the interpupillary distance of the system.

For the alignment of the components of each vision channel, a red laser was first used. The laser was aligned parallel to the table to create a visual guide of the optical axis of the system. Then, each of the optical components was implemented on axis with the laser beam. Lastly, a camera was placed at the retina position of the projection system to adjust the distance between the optical components focusing the CCD image.

Figure 6.5(b) and (c) show a 3-D model of the mechanical frames designed to hold the trial lenses and the blank PAL respectively. The trial lenses holder is clamped to the eyepiece lens mount and contains two clips to place both spherical and cylindrical lenses, allowing to correct any patient refractive error (myopia or hyperopia and astigmatism). For the alignment of the blank progressive lenses a set of three micrometer displacers was used, one for the vertical displacement of the progressive lenses and two to independently displace each of them horizontally. We also designed custom frames to hold the blank PAL on top of the micrometers with magnets on the base to allow their easy removal and exchange. This way, an independent correction of the progressive addition and the refractive error was performed. Notice that due to the large diameter of the blank PALs used, we needed to cut the internal edge of the blank PAL to allow their centration with the patient's pupil.

Finally, a tripod was added to the base of the demonstrator system to allow staring at different parts of the room through different areas of the progressive glass, enabling the head movements required to avoid (or experience) the lateral aberrated areas of the PALs (see Figure 6.5(d)).

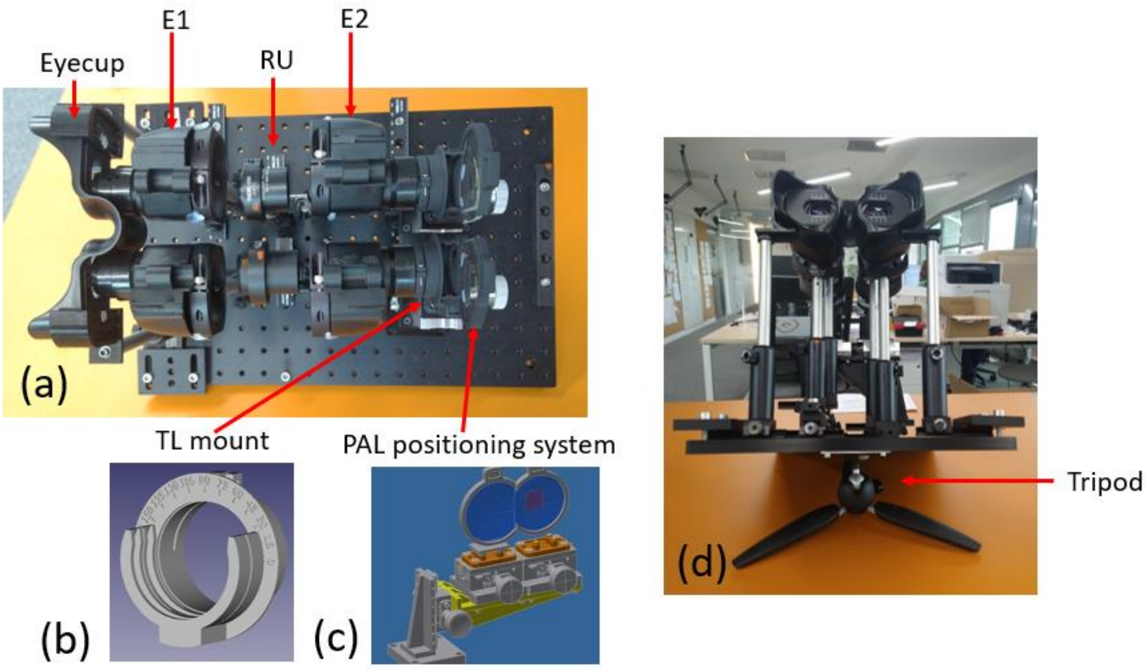

Figure 6.5 – *Images of the implemented proof-of-concept system showing: (a) top view of the binocular PALs demonstrator system, (b) 3-D modeling of the trial lenses clip mount for spherical/cylindrical lenses, (c) 3-D modeling of the micrometric system that allows for centration of PALs, fixed by a set of magnets and (d) front view of the binocular PAL demonstrator showing a tripod attached to the base to allow a smooth movement of the system to stare at different objects in the room. (PAL: progressive addition lens, TL: trial lens, PS: projection system, E: eyepiece and RU: relay unit).*

6.3.2 - Experimental validation

The optical performance of the experimental proof-of-concept was characterized by placing a camera at the exit pupil plane of the PS unit, substituting the patient's eye. Figure 6.6 shows images from the camera in two different scenarios. The first image, Figure 6.6(a), was taken without placing the camera behind the device, while the second and third, Figure 6.6(b) and (c), were taken with the camera placed in each of the vision channels of the binocular system. During this test no progressive lens was placed, so the optical quality of the projection system could be analyzed. As can be observed, the optical quality was similar of both vision channels, showing a significant reduction of the quality in the periphery. However, the insufficient optical quality was not totally unexpected as the optical components, despite being of good quality, had not been designed jointly for this purpose. A reduction in the illumination can also be observed, although it was concluded not to be limiting. Regardless of the low optical quality, the designed projection system was proven to work as an afocal projection system, allowing a non-inverted nor magnified visualization of the real world.

(a) (b) (c)

Figure 6.6 - *Optical quality of the experimental system: (a) reference image of the scene without passing through the projection system, (b) image of the same scene through the left vision channel of the system, (c) image of the same scene through the right vision channel of the system.*

The field of view covered by the experimental demonstrator when moving the eye laterally was 60 deg, while the gazing FoV observed at each position of the eye was below 50 deg due to the vignetting of the FoV generated by the pupil of the implemented projection system. Thus, the system did not allow for simultaneous vision of both near and far zones of the blank PALs. However, it did allow to encompass a portion of both simultaneously. This result is in line with the desired outcome although not optimum. The central area, dedicated to the intermediate working distance when PALs are on place, was clearly observed with the best optical quality rather than the rest areas, as it lies around the optical axis of the system, where the quality is best.

Figure 6.7 shows a case of use of the experimental implementation of the progressive lens demonstrator. Figure 6.7(a) and (b) show how to place the trial lenses needed to correct a myopic and astigmatic patient as well as the blank PAL to be tested respectively. In this phase, the yellow cross markers engraved by the ophthalmic lens manufacturer were substituted by UV ink mark, and the centration of the PALs was performed using lateral UV illumination. Figure 6.7(c) and (d) show the two main positions of use of the progressive lens demonstration, observing a far and a near distance object. The system is mounted on top of a tripod, so the user can hold it with the hands without effort and follow the clinician’s instructions to observe far distance objects at the screen (see Figure 6.7(c)) or close object at the piece of paper (see Figure 6.7(d)).

Despite the suboptimal optical quality of the implemented prototype, the device has been widely used to show the concept to various stakeholders (manufacturers, developers, optometrists… see private video ***here***), including the use of the device regarding the placement and centration of zero-base power progressive lenses (using UV light), placement of trial lenses for refractive correction and viewing through the device. With all, the concept was proved to work although the optical requirements were not fulfilled.

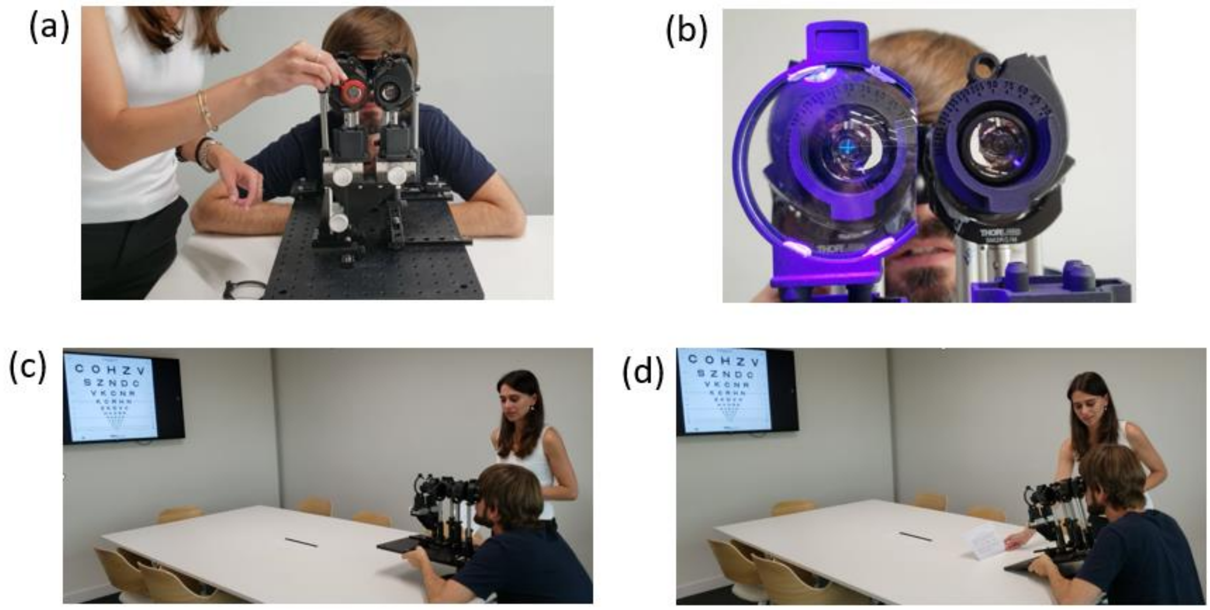

Figure 6.7 *– Experimental setup in use. (a) Shows how to place trial lenses to correct the patient's refractive error. (b) Shows the centration of the blank PAL with lateral UV illumination. (c) Shows a case of use where the patient is following the clinician's instructions to see a far distance object at the screen. (d) Shows a case of use where the patient follows the clinician instructions to observe a near object.*

6.4 – Projection system design

Due to the insufficient optical quality of the proof-of-concept, designing a new system based on custom optics was needed. Designing a wide-field optical system presents the following challenges:

- Obtaining good optical quality throughout the whole field of view and an undistorted image requires using a greater number of lenses to have more surfaces to solve the problem.
- Increasing the field of view also requires increasing the size of the exit pupil of the optical system, so that the user's pupil continues to fit within the system aperture when the eye moves laterally to observe the peripheral field, without causing vignetting or light loss.

In this section we present the optical design of the PS for our application, aiming to achieve good optical quality and to accomplish the requirements defined for the device. The optical performance of the system was analyzed at the retina plane of a model eye gazing both on-axis and off-axis with respect to the optical axis of the PS designed. Finally, an evaluation of the requirements is presented.

6.4.1 – Optical design description

The optical design of the afocal PS was performed using OpticStudio software. To maintain a reasonable cost for a final product, we tried to minimize the number of custom optical elements. Both eyepieces of the projection system, E1 and E2, were considered identical and were placed, as in the proof-of-concept, facing each other in a mirror configuration. The relay unit RU was also chosen identical to the one used in the proof-of-concept, an achromatic triplet (TRS254-040-A, Thorlabs) with a focal length of 40 mm and an aperture of 25.4 mm.

During the optical design process, the requirements imposed by the rotation of the eye to cover the far and near vision zone of a blank PAL were considered (53.5 deg of FoV and the 14.4 mm of diameter of the system's exit pupil). To reduce the complexity of achieving such a big exit pupil, an approximation to this requirement was performed. Instead of designing the projection system with a 14.4 mm diameter exit pupil to be placed at the pupil plane of the patient, the projection system was designed with a 4 mm diameter exit pupil placed at the center of rotation of the eye. The customized optical design was achieved by restricting the mechanical distances and optical requirements in a custom developed merit function.

Figure 6.8 shows the layout of the afocal projection system designed. The position of the elements of the patient's eye with respect to the PS are represented with yellow arrows. The center of rotation of the eye of the patient is placed at the exit pupil of the PS (in the right), and the same happens with its conjugated point at the entrance pupil of the PS (in the left). The pupil and retina planes of the eye of the patient, as well as their conjugated planes are similarly shown. The positions of the physical blank PAL and the trial lens, as well as the position of their conjugated projection, are indicated with red and blue arrows respectively. While the blank PAL is placed at 15 mm in front of the projected pupil -at the vertex distance considering the pupil plane at the ACD inside the eye- the trial lenses for the patients' refractive error correction are placed at the projected pupil plane.

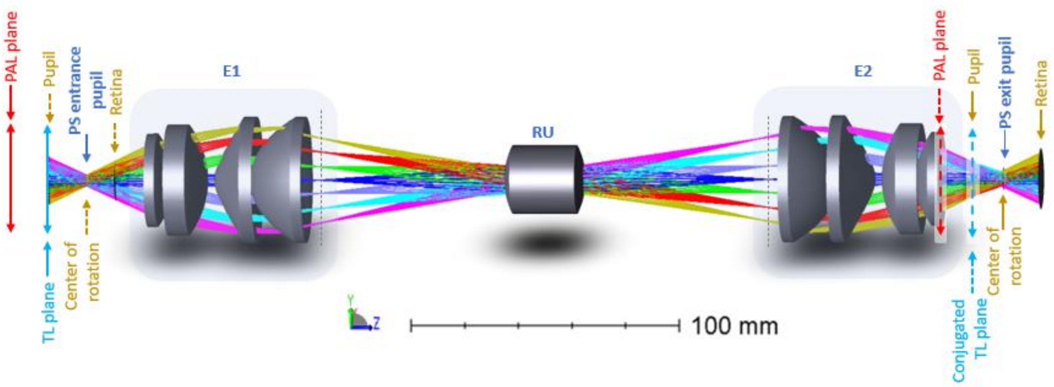

***Figure 6.8** – Layout of the optical design of the system based on symmetrical eyepieces. The position of the eye components, blank PAL and trial lens are shown in yellow, red and blue respectively. (PAL: progressive addition lens, TL: trial lens, PS: projection system, E: eyepiece and RU: relay unit).*

The data of the lenses designed for the eyepieces is presented in the following Table 6.3. The custom eyepieces are composed of four air-spaced plastic conical lenses with an effective focal length of 29.85 mm and a back focal length of 15.31 mm. The back focal plane of the eyepieces is also visible in Figure 6.8 (shown with dashed gray lines) at the position where the collimated incident light beams are focused. During the optical design process, the lenses of the eyepieces were defined as standard spherical lenses and their conic coefficients were sequentially added to improve the optical quality of the PS unit. In this case, the plastic materials used were: E48R, a polymer-based material used as a crown-like material, and OKP4 polystyrene-based material used a flint-like material. The reason to use plastic materials was to attempt a reduction of weight of the system as the device is intended to be head-mounted and the requirement of a wide field of view also imposes large lenses [212].

Table 6.3 *– Optical design of the custom eyepiece: four air-spaced plastic conical lenses were designed to gather a field of view of 54 deg.*

Surface	Radius (mm)	Conic	Semi-diameter(mm)	Thickness (mm)	Material
L1 – surface1	Infinity	0	17.35	10.26	E48R
L1 – surface2	-22.44	-1.37			
Air space				6.59	Air
L2 – surface1	-6.74	-3.25	20.59	5.61	OKP4
L2 – surface2	-33.03	-0.37			
Air space				2.45	Air
L3 – surface1	9.47	-3.64	23.58	11.79	E48R
L3 – surface2	64.56	0.65			
Air space				1.61	Air
L4 – surface1	18.10	-0.75	23.44	10.93	OKP4
L4 – surface2	18.83	-1.53			

The full field of view of the custom afocal PS reached 54 deg without vignetting. During the analysis of the optical performance of the afocal custom projection system alone before modeling a human eye, the RMS spot radius through the whole field of view of the afocal system was maintained below 0.8 mrad while the Airy disk radius was 0.17 mrad for the 4 mm entrance pupil diameter and a central wavelength of 0.588 μm. The sagittal and tangential field curvature were 0.64 D and 0.89 D respectively with a maximum distortion of 0.03%. The analysis of the optical quality of the system was also performed in a model human retina as shown in following section.

6.4.2 – Optical performance analysis on model retina

The model eye implemented for the optical quality analysis of the custom PS consisted of a paraxial lens with a focal length of 25 mm and a circular aperture of 4 mm of diameter acting as the refractive components of the eye with a 4 mm pupil size. The model lens was placed 12 mm before the exit pupil of the PS. This way, the exit pupil of the projection system was coincident with the center of rotation of the eye. The image surface was placed at 25 mm from the paraxial lens, simulating the retina. Additionally, the rotation of the whole model eye (lens and retina surfaces) with respect to the center of rotation was implemented with the use of coordinate break interfaces.

The optical performance was analyzed when the gazing direction of the model eye was both on-axis and off-axis with respect to the optical axis of the designed projection system. During the analysis, a collimated light beam with uniform apodization was always considered, and the average performance for the three main wavelengths of the visible range (0.486 μm, 0.588 μm and 0.656 μm) was analyzed. The optical performance at the model retina was evaluated with by analyzing the root mean square (RMS) spot radius, vignetting factor and fast Fourier transform of the modulation transfer function (FFT-MTF) performance. In all the gazing direction of the model eye, 7 different angular field of view from 0 deg up to 27 deg in the Y-axis- direction were analyzed, assuming rotational symmetry for the Y and X-axis of the system as all the optical components used had rotational symmetry.

A – On-axis at 0 deg gazing angle performance

Figure 6.9 shows the analysis of the optical quality of the system at the model retina for different fields of view up to 27 deg when the gazing direction of the model eye is on-axis with the optical axis of the custom projection system, thus looking at 0 deg though the PS.

Figure 6.9(a) shows the geometrical and RMS spot radius as well as the diffraction limited Airy disk. It can be observed that the RMS spot radius, shown with a yellow solid line, is maintained highly constant across the entire field of view of the PS with an average value of 14.35 $\pm$ 3.36 mm, 3.3 times larger than the Airy disk which is 4.36 mm for a 4 mm pupil diameter. The geometrical radius was reduced while the PS field of view increased, an opposite performance to the expected effect of a reduction of the optical quality in the periphery. This fact is related to the vignetting factor obtained thought the field of view, shown in Figure 6.9(b). The vignetting factor was observed to increase as the transmission factor decreased throughout the field of view of the designed projection system, due to the fact of having a 4 mm pupil placed in front of the exit pupil of the PS. Assuming a threshold of a 0.5 transmission, the gazing half field of view is obtained to be 8.23 deg and the full gazing field of view of a user 16.47 deg, smaller than the whole 54 deg of the PS.

Lastly, Figure 6.9(c) shows the MTF performance at the model retina also through the whole field of view of the PS. The sagittal and tangential performance are shown in solid and dashed lines respectively. The reference of the diffraction limited performance is also shown with a solid black line. In this case, the optical quality acceptance threshold of the PS in the model retina was defined as the MTF performance of an average 24-year-old person with a 4 mm pupil from the state of the art [213], shown with a red solid line. The comparison of the optical quality of the designed projection system PS with a young eye of high optical quality was aimed at ensuring a high system quality, even though when the system will be most commonly used with older eyes of lower optical quality. For fields below 10 deg, both sagittal and tangential fields have higher or similar optical quality to the defined threshold. However, for fields above 15 deg a clear difference between the sagittal and tangential analysis is observed: while the sagittal performance remains at the level of the threshold, the tangential analysis suffers a significant reduction showing the astigmatism presence on the PS system.

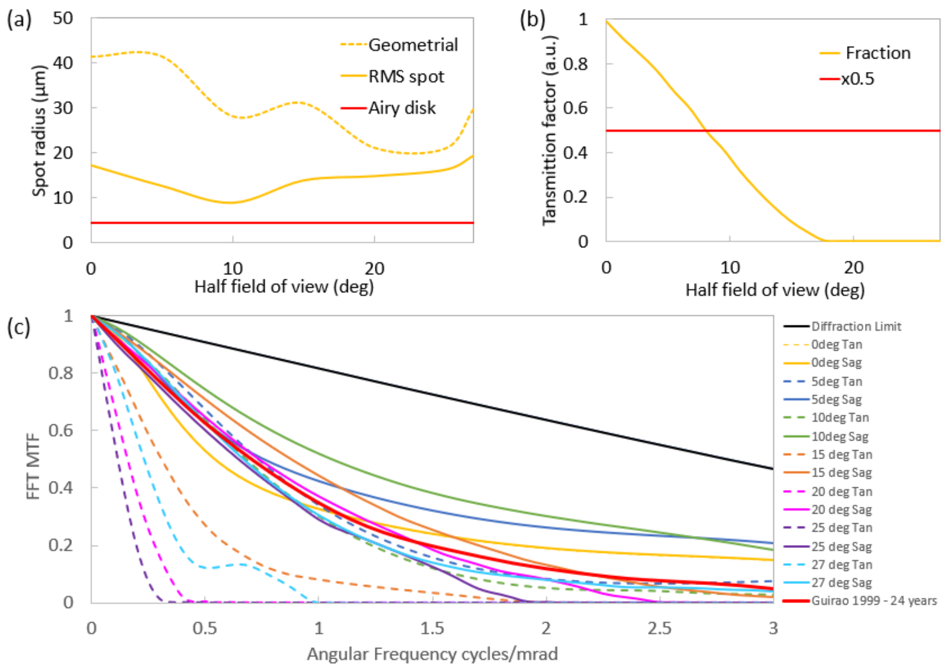

Figure 6.9 – *On-axis and peripheral optical performance of the designed projection system at the model retina with a gazing angle at 0 deg with respect to the optical axis of the projection system: (a) RMS spot radius (yellow solid line), geometrical spot radius (dashed yellow line) and reference Airy disk (red solid line); (b) transmission factor throughout the whole field of view of the projection system (yellow solid line) and threshold limit of 0.5 transmission (red solid line); and (c) fast Fourier transform of the modulation transfer function (FFTMTF) of the on-axis and periphery field of view at the sagittal (solid lines) and tangential direction (dashed lines).*

B – Rotated gazing angle performance

The off-axis optical performance was also analyzed by rotating, with respect to the defined center of rotation, the model eye with respect to the optical axis of the projection system. Thus, we changed the angle of the gazing direction to be on-axis with each of the angular positions of the field of view of the projection system analyzed before. Figure 6.10 shows the optical performance obtained when rotating the gazing position, following the same analysis performed for the on-axis gazing direction.

In Figure 6.10(a) the RMS spot radius obtained at the center of each gazing position is presented in spots with different colors, as well as the diffraction limited Airy disk as a reference shown with a solid red line. As can be observed, it is maintained considerable constant throughout all the gazing directions with a mean value of 14.07 μm and a standard deviation of 2.14 μm.

Figure 6.10(b) shows the gazing full field of view at each gazing direction as obtained from the vignetting analysis. At each gazing direction the maximum transmission always was at the angle of the field of view of the PS coincident with the gazing angle, and it decreased at both sides of the maximum peak as the FoV angle changes with respect to the gazing direction. By considering the x0.5 fraction threshold at both sides of the gazing direction, the patient's full field of view was calculated. As can be observed in Figure 6.10(b), the gazing full field of view is maintained highly constant with an average of 15.86 deg for gazing angles lower than 20 deg. For larger angles, the user's field of view is reduced due to the fact that the PS does not allow larger field than ± 27 deg.

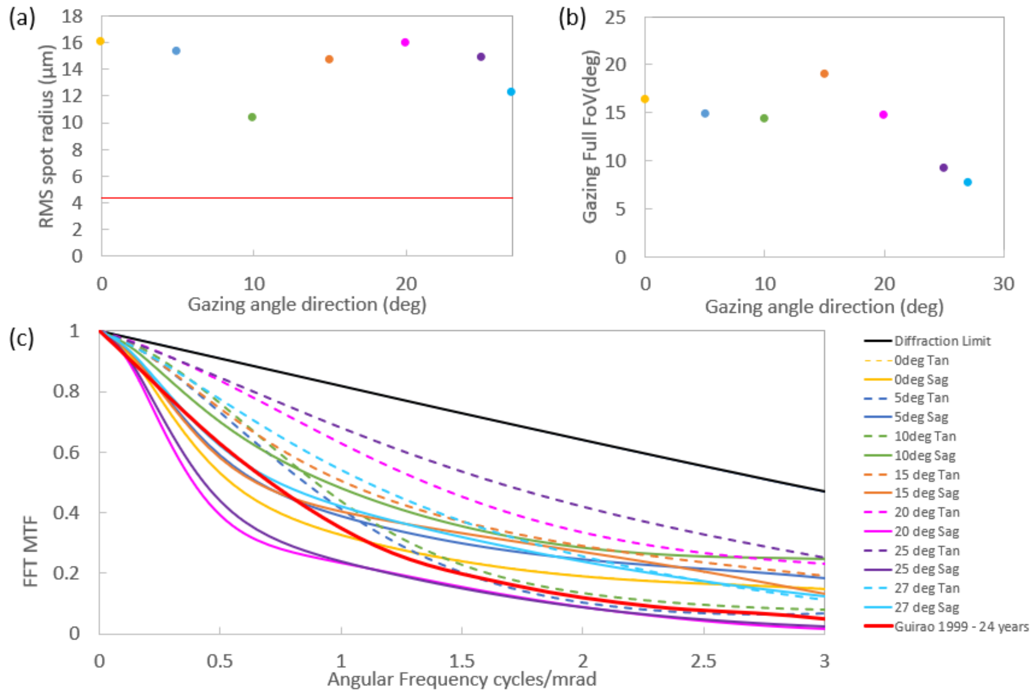

***Figure 6.10** – On-axis- optical performance at a model retina of the designed projection system when the gazing angle is changed throughout the whole field of view covered by the projection system:(a) RMS spot radius (in µm) for each gazing angle in color spots and the reference Airy disk in a solid red line, (b) gazing full field of view (deg) at each gazing position considering a threshold of x0.5 vignetting factor when analyzing the whole projection system field of view. (c) MTF performance of the on-axis- angle both in the sagittal and tangential direction in solid and dashed lines respectively.*

As in the previous analysis, Figure 6.10(c) shows the MTF performance for the angle FoV angle on-axis with each gazing position, showing again both the sagittal and tangential performance with solid and dashed lines respectively. The reference of the diffraction limited performance and the threshold of an average 24-year-old person with 4 mm pupil [213] are also maintained with black and red solid lines respectively. In this case, the on-axis field for all gazing angles up to 20 deg presented a good MTF performance in both sagittal and tangential directions, presenting an MTF performance above the threshold even for the case of gazing at 27 deg. Only the sagittal direction of the gazing angles of 20 deg and 25 deg were obtained to be slightly below the threshold of a 24 -year-old person optical quality.

6.4.3 – Requirements evaluation

Apart from the improved optical quality of the custom designed PS, the rest of the defined requirements were also evaluated. In the first place, the image formation requirement was validated with the angular magnification of x0.99 obtained at the merit function in the PS simulation. Thus, allowing the formation of a non-inverted nor magnified image.

Regarding the visual comfort requirements, as presented in the optical quality performance analysis, although the full field of view reached by the designed projection of 54 deg is enough to cover the vision of all the areas of a blank PAL, the gazing field of view is highly reduced to 15.86 deg due to the approach of having designed the PS with a 4 mm exit pupil to be placed at the center of rotation. This relationship between the required field of view -allowed by the projection system- and the gazing full field of view is schematically shown in the following Figure 6.11.

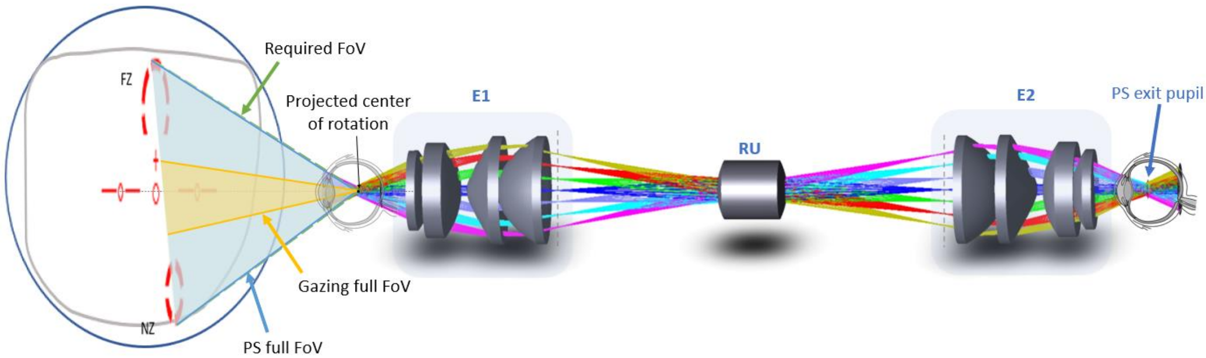

Figure 6.11 *– Schematic representation of the field of view required (green shadow), allowed by the custom designed projection system (blue shadow) and gazing (yellow shadow) to visualize the different areas of a blank PAL (note that the scale of the components drawn is not maintained). (FZ: far zone, NZ: near zone, PS: projection system, FoV: field of view, E: eyepiece and RU: relay unit).*

Regarding the ergonomic requirements, the eye relief was maintained at 12 mm by fixing the distance between the exit pupil and the first optical surface during the optimization of the optical design. As can be observed in the representations of the custom designed PS in Figure 6.8 and Figure 6.11, as well as in the experimental proof-of-concept in Figure 6.5 and Figure 6.7, the pupil plane of the patient is projected 34.38 cm forward from the real pupil position. This apparent object distance would imply that a patient will need to place any object 34.38 cm farther than usual to be able to observe it though the near vision zone. In order to solve it, the air space of the design PS was used to place folding mirrors to reduce the overall length of the system. However, due to the large size of the lenses, the shortest approximation reached (see Figure 6. 12) still resulted in a distance of 27.4 cm between the pupil plane and its conjugate plane, preventing from a natural and comfortable use of the device.

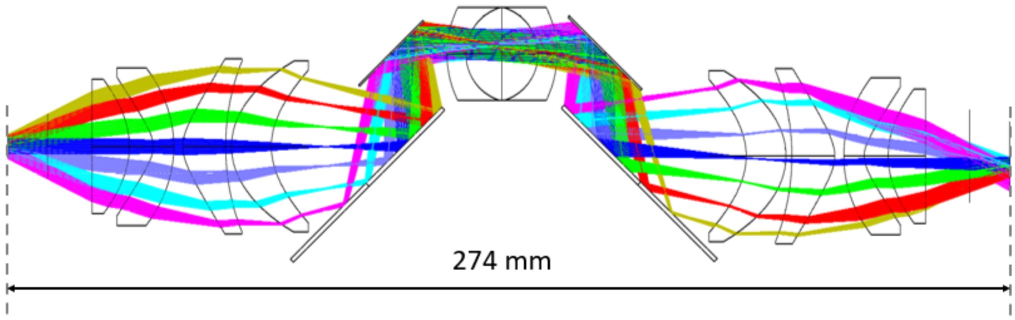

Figure 6. 12 – *Folded alternative implementation of the designed projection system incorporating 4 mirrors to reduce the overall length of the system from 343.8 mm to 274 mm.*

6.5 – Future work

After the initial steps of the project conceptualization, definition of requirements, experimental concept validation, and customized optical design to meet the requirements, the work in progress to advance the project is the optimization of the custom designed PS to achieve:

- A higher visual comfort by 1) correcting the position of the exit pupil of the PS with respect to the eye of the patient, moving it from the center of rotation to the pupil plane of the eye; 2) increasing the exit pupil to the calculated requirement of 14.4 mm. Thus, we aim to avoid the current limited gazing field of view.
- A more ergonomic apparent object distance by reducing the distance between the projected pupil plane and the real position of the pupil of the eye.

The current approach under study to achieve these goals is the modification of the designed eyepieces by considering the separation of the single block eyepiece into two different subunits, as introducing a folding mirror could help to reach a more natural apparent object distance. Adding at least one more lens is also being considered in order to maintain the optical quality performance when increasing the PS exit pupil diameter. Moreover, the possibility of reducing the footprint of the device to develop a compact system and convert it from an optical bench device to a head-mounted system is also under study, were the approximation of a free-form optical design of the system could be beneficial.

6.6 -Discussion

We have presented the concept of a progressive lens demonstrator with the capability of allowing to experience the vision through difference blank progressive lens designs without the need of manufacturing or buying a personalized spectacle for each patient. The proposed device is an afocal projection system that allows to simultaneously project a blank progressive lens with 0 D at a vertex distance from the pupil of the patient, and, at the same time, correcting the refractive error of the patient if needed. The projection system consists of two symmetric eyepieces placed on-axis in a mirror configuration with respect to each other, with a relay unit placed in between them at a 2f configuration conjugating the back focal plane of the eyepieces. We have implemented an experimental proof-of-concept based on commercial components and defined the main requirements of the device. We have also attempted a first custom design of the eyepieces to analyze the possibility of reaching the defined requirements.

The experimental implementation of the projection system based on commercial components allowed to prove its performance as an afocal projection system when combining two symmetric eyepieces with a triplet-based relay unit, showing its capability of projecting a noninverted image. However, the optical quality of the implemented system was observed to be insufficient to allow a proper validation of the experience through different aberration profiles of blank PALs. This could have been anticipated given that the optical components selected, especially the eyepieces from commercial prismatic binoculars, were not designed for the purpose for which they were being utilized in the developed device. Even so, the experimental proof-of-concept allowed to evaluate some of the requirements defined such as the need of a wide field of view to allow the visualization of all the areas of interest of a blank PAL, the far and near vision zones, as well as the aberrations outside the PAL's corridor. Moreover, it was also useful to validate the alignment methodology based on fluorescent ink and UV side illumination for the centration of the blank PAL to the center of the pupil of the patient, which is crucial for the proper use of the progressive blank lenses.

The experimental proof-of-concept also allowed to confirm the need of the projection system unit in the demonstrator of progressive lenses device. The conjugated pupil plane of the patient generated with the projection system opens the possibility of correcting the refractive error of the patient while still having the conjugated spectacle plane at the vertex distance from the pupil available for the addition correction. Thus, the clinician has the freedom to perform any combination of addition and refractive correction required with each patient using a reduced set of PALs.

The implemented system also showed an easy alignment of the blank PALs to the patient's pupil, as well as permitted to experience the need of vertically moving the head to change the view from far to near distance. Moreover, even though being a bulky limited implementation, the device has been widely used to show the concept to various stakeholders (manufacturers, developers, optometrists…) to initiate an evaluation of the needs and requirements of the clinicians. With all, the concept was proved to work although the optical requirements were not fulfilled.

The custom designed eyepieces for the wide field projection system showed the potential of reaching a good optical performance on the retina, allowing the implementation of a projection system with low optical aberrations (low enough for a young healthy person to reach a standard visual acuity), ensuring that the aberration profiles of the progressive lenses would be distinguished. The analyses of the optical performance of the projection system on a model retina when gazing on-axis with respect to the optical axis of the system gave a good retina optical quality through-out a range of 40 deg of the whole field of view of the projection system as the ray tracing simulation gave a highly constant RMS spot radius of 14.35 ± 3.36 mm, comparable to the 11 mm RMS spot radius obtained in the literature for the Liou and Brennan model eye [214]. However, when analyzing the MTF peripheral performance a reduced optical quality was observed, being significantly limited by astigmatism for fields of view larger than 15 deg. Different approaches can be considered to improve the periphery optical quality such as the addition of more lenses on the eyepiece looking after a smoother control of the ray tracing, the compensation of the astigmatism with a cylindrical lens and/or the modification of the lens surfaces type to a higher order aspherical coefficient surfaces. It is also important to notice that the peripheral performance of the designed projection system is being compared to the on-axis performance of a young eye, while it has been demonstrated that the optical performance on a normal eye presents a reduction of the optical quality due to the increment of aberrations such as astigmatism and coma towards the periphery [215, 216]. Thus, the reduction of optical quality towards the periphery is not considered as the mayor limiting factor of the system.

The main limitation of the current optical design is the limited gazing field of view obtained. Although the projection system designed has a full field of view of 54 deg to cover all the areas of interest of the blank PAL, due to the fact that the exit pupil of the projected system was wrongly designed to be on the center of rotation of the eye of the patient, the 4 mm pupil size of the model eye located in front of the exit pupil of the system highly reduced the gazing field of view to 15.86 deg due to vignetting. Due to the reduced gazing field of view obtained, the reduction of optical quality for fields larger than 15 deg was not considered as a highly limiting factor since the user's field of view for the on-axis gazing direction was obtained to be 16.47 deg, and therefore the user would not notice it due to the significant vignetting factor that these fields present.

One solution to prevent this limitation would be to consider the possibility of completing the uncovered range of the field of view by means of a vertical displacement of the PAL with respect to the optical axis of the PS or vice versa. However, the small field of view would still prevent the simultaneous visualization of the near and the far vision zones. The solution currently under development aims at changing the position of the exit pupil of the projection system to be placed at the pupil plane of the users, as well as to increase the diameter of the exit pupil to cover the displacement of the patient's pupil during the rotation of the eye when changing the gazing direction across the different areas of the blank PAL.

The on-axis performance of the custom designed projection system at different angular positions of the model eye also showed a similar trend. The on-axis RMS spot for each angular position of the model eye was maintained highly constant throughout the model eye rotation. The gazing field of view was also very constant around the central 40 deg. For angular positions above 40 deg, the field of view was significantly reduced, due to the combination of the vignetting of the model eye and the field of view of the projection system designed. The analysis of the on-axis MTF performance show good optical quality for most of the angular positions of the eye, being higher than the average performance of a young eye in both tangential and sagittal directions for all angular positions except for 20 deg and 25 deg, where only the sagittal field presented a slightly lower optical performance. Anyway, despite the reduced gazing field of view, the on-axis or foveal optical quality of the custom designed projection system is better than the average performance of a young eye. Thus, it can be assumed the optical performance would be enough to distinguish the aberration profiles of different blank PALs when looking at their different areas.

Another important limitation of the current design is the large apparent object distance obtained, that would require to locate an object at a distance of 67.4 cm when a close object distance of 40 cm wants to be actually tested [217]. To overcome this limitation, the current approach under analysis is the possibility of dividing the eyepiece into two air spaced blocks of lenses that would allow to introduce a folding mirror at a closer position with respect to the pupil and thus to reduce the difference between the real and the apparent object position.

Nevertheless, the current presented concept has shown the potential of projecting any ophthalmic progressive lens into patients' vision together with his/her refractive error. This patented invention could allow patients to experience the final vision through different real progressive lens designs, learning how progressive lenses perform and identifying the more comfortable option for them. The instrument will also benefit optometrists (reducing chair time and increasing progressive lens prescription) and manufacturers (reducing cost).

6.7 -Conclusions

We presented a new afocal projection system to project blank progressive addition lenses with 0 D base in front of the patient's eyes, correcting the patient's refractive error with standard trial lenses.

We described the main optical components needed to implement the projection system based on the combination of two equal eyepieces symmetrically placed in a mirror configuration facing each other with a relay unit at a 2f configuration between the eyepieces conjugating their corresponding back focal planes. We implemented a proof-of-concept system to validate the working principle of the proposed structure of optical components.

The progressive addition lenses alignment methodology was easily used for their centration to the patient's pupil using UV side illumination. We also proved to be able to independently correct the patient's refractive error from the progressive lens used. Although the optical quality of the implemented system was poor for the observation of the aberration profiles of the progressive lenses, it allowed to analyze the need of a large field of view of 54 deg to ensure the visualization of the areas of interest of the blank PAL.

We also performed a custom design of the projection system, and we analyzed its RMS and MTF optical performance at the retina of a model eye. Even though the limited gazing field of view of 15.68 deg, the on-axis optical performance of the custom system when the gazing direction of the model eye is rotated throughout the field of view of the projection system presented a comparable optical quality to a young human eye, concluding it would allow to distinguish the aberrations of blank PALs when looking at each area of the spectacle despite the limited gazing field of view. The off-axis peripheral analysis showed an expected reduction of optical quality towards the periphery.

In summary, the proposed structure of an afocal projection system is a good candidate for our demonstrator of progressive lenses, as we have proven its potential of fulfilling the device requirements with custom designed optical components. Sourcing an air-spaced optical design with a larger exit pupil plane and a folding mirror inside each eyepiece will potentially overcome the current limitation of the apparent object distance and the limited gazing field of view to allow a more natural vision experience through the system.

Chapter 7

Conclusions

This thesis was divided into three main sections: the first part described the development of a low-cost optical delay line to perform axial scans of an eye (Chapter 3-4), the second part described the development of a low-cost optical beam scanner to acquire whole-eye cross-sectional OCT images (Chapter 5), and the third part described the concept and first prototype of a new system to allow patients to experience vision through different progressive lens designs before manufacturing and purchasing custom spectacles for each patient (Chapter 6). The results of this thesis have an impact on the technology used during the evaluation and treatment of cataract and presbyopia patients.

The main accomplishments of this thesis are:

1. The development of a low-cost optical delay line capable of independently setting the scan frequency and the axial scan range based on a single diffraction grating implementation of a frequency-domain optical delay line with a stepper motor spinning a tilted mirror as actuator for axial scanning.

2. The combination of the proposed low-cost frequency domain optical delay line into a low-cost TD-biometer to measure the intraocular distances of an eye.

3. The development of a low-cost non-mechanical method to allow an independent selection of the output beam displacement, deflection, angle and focus, based on the combination of three electro-tunable lenses. This scanner can perform a sequential switch between different scanning configurations, without requiring any mechanical exchange in the optical system.

4. The combination of the proposed non-mechanical optical beam scanner into a SS-OCT system to acquire quasi-simultaneous whole-eye OCT images of different ocular samples.

5. The cost reduction of the implementation of the novel low-cost frequency domain optical delay line and beam scanner, which cost with of-the-shelf components is 750USD and 900USD respectively, with respect to the 2000USD cost of the standard galvanometric scanner used in both systems.

6. The design of an afocal projection system with a wide field of view to provide the experience of vision through different progressive addition lenses with different designs while correcting the patient’s refractive error.

The conclusions of this thesis are:

1. The implementation of a frequency-domain optical delay line based on a single diffraction grating outperforms a design based on two diffraction gratings, since a higher resolution, hence measurement accuracy, and scanning power are obtained.

2. A novel frequency domain rapid scanning optical delay line with a lower cost than the standard configuration is obtained by substituting the galvanometric scanner by a tilted mirror attached to the shaft of an inexpensive stepper motor with 3-D printed holders.

3. The proposed frequency domain optical delay line can be incorporated into a low-cost TD-biometer to measure the intraocular distances of a model eye with equivalent distances as a human adult eye.

4. A low-cost non-mechanical optical beam scanner capable of simultaneously adjusting the vergence and direction of the output beam has been designed. The proposed optical beam scanner allows to non-mechanically switch between the different scanning configurations, *e.g.*, the ones commonly used for anterior and posterior segment imaging.

5. The ability of controlling the displacement and divergence of a light beam has been described through the analytical equations governing the proposed beam scanner operation, validated via a simulation of its optical performance, and demonstrated by an experimental implementation with off-the-shelf components.

6. Quasi-simultaneous acquisition of whole-eye OCT images was achieved with the developed low-cost non-mechanical optical beam scanner since it proved capable of sequentially switching between the desired configurations to image the anterior and posterior segments of an eye. The proposed optical beam scanner revealed details of ocular samples -a model eye and an ex-vivo rabbit eye-, comparable to those observed in conventional anterior and posterior OCT scanners. Faster scanning speed will be required for in-vivo high-quality imaging.

7. The proposed beam scanner presents two main advantages with respect to standard scanners: 1) it reduces the complexity and cost of other whole-eye scanners, and 2) it is fully reconfigurable.

8. An afocal projection system has been designed to project blank progressive addition lenses with 0 D base in front of the patient's eye and to correct the patient's refractive error with standard trial lenses.

9. The main requirements of the projection system to allow vision through all the different areas of interest of the progressive lenses are a wide field of view and a large exit pupil diameter, what increases the complexity of the optical design.

10. A good optical quality at the central region of the field of view has been achieved with a custom optical design of the projection system. Redesigning of the optical system is needed to correct the presence of vignetting and non-natural apparent object distance.

List of scientific activities

1. Scientific publications

1. Urizar M. P., Gambra E., de Castro A., de la Peña A., Cetinkaya O., Marcos S., Curatolo A. Optical beam scanner with reconfigurable non-mechanical control of beam position, angle, and focus for low-cost whole-eye OCT imaging. Biomedical Optics Express, 2023. 14(9): p. 4468-4484 (2023) https://doi.org/10.1364/BOE.493917

2. Urizar M. P., de Castro A., Gambra E., de la Peña A., Pascual D., Cetinkaya O., Marcos S., Curatolo A. Long range frequency domain optical delay line based on a spinning tilted mirror for low-cost ocular biometry. *Submitted in Biomedical Optics Express.*

2. Patents

1.. M2201P007EP, Curatolo A., Urizar M. P., Gambra E. Optical delay line, interferometer and method for generating an optical delay based on a spinning tilted mirror. November 24th, 2022. Ownership: 2EyesVision SL.

2. M2201P001EP, Urizar M. P., Gambra E., Dorronsoro C. Apparatus and method for projecting a PAL lens in front of an eye. November 1st, 2022. Ownership: 2EyesVision SL.

3. M2201P006EP, Gambra E., Dorronsoro C., Barcala X., Sisó I., Alonso J.R., Urizar M. P., Esteban E., Rodríguez V., Marcos S. Binocular see-through vision device for far and near distances. June 8th, 2022. Ownership: 2EyesVision SL and CSIC.

4. P220787EP, Curatolo A., Urizar M. P., Marcos S., Gambra E. Apparatus and method for displacing and/or changing a direction of a light beam axis. March 15th, 2022. Ownership: CSIC and 2EyesVision SL.

3. Conferences

Personally presented

1. Urizar M. P., de la Peña A., Gambra E., de Castro A., Cetinkaya O., Marcos S., Curatolo A. Towards a low-cost optical biometer: development of a low-cost optical delay line for axial scans and a whole-eye beam scanner for fixation checks. Biophotonics for eye research summer school (Spain, 2023). *Poster contribution*

2. Urizar M. P., de Castro A., Gambra E., de la Peña A., Cetinkaya O., Marcos S., Curatolo A. Long-range frequency-domain optical delay line based on a spinning tilted mirror for low-cost ocular biometry. Photonic West (United States, 2023). *Poster contribution*

3. Urizar M. P., de Castro A., Gambra E., Cetinkaya O., Marcos S., Curatolo A. Development of a low-cost and versatile, ocular whole-eye scanner for optical coherence tomography. PhDay Física (Spain, 2022). *Poster contribution*

4. Urizar M. P., de Castro A., Gambra E., Cetinkaya O., Marcos S., Curatolo A. Design of a low-cost, versatile, whole-eye scanner for optical coherence tomography. Optica Biophotonics Congress: Biomedical Optics (United States, 2022). *Oral contribution*

5. Urizar M. P. Avances hacia el desarrollo de un biómetro ocular portátil y de bajo coste. Jornada de Doctorandos UCM (Spain, 2022). *Oral contribution*

6. Urizar M. P., de Castro A., Gambra E., Curatolo A. Design of a robust long-range optical delay line for low-cost ocular biometry. IONS (Ireland, 2021). *Oral contribution*

Presented by collaborators

1. Urizar M. P., de la Peña A., Gambra E., de Castro A., Marcos S., Curatolo A. A low-cost, non-mechanical optical beam scanner: experimental proof-of-concept for whole-eye OCT imaging. Optica Biophotonics Congress: Optics in the Life Sciences (Canada, 2023). *Oral contribution*

2. Villegas L., Urizar M. P., Zvietcovich F., Olalla P., de Castro A., Curatolo A., Revuelta L., Marcos S. Myopia control by Atropine and Latanoprost in a guinea pig model: impact on refraction, biometry and scleral mechanics. ARVO annual meeting (United States, 2023). *Poster contribution*

3. de Castro A., Martinez-Enriquez E., Urizar M. P., Marcos S. Modelling the effect of fixational eye movements on OCT corneal topography with raster and meridional scan patterns. Visual and Physiological Optics meeting (United Kingdom, 2022). *Oral contribution*

4. de Castro A., Martinez-Enriquez E., Urizar M. P., Curatolo A., Marcos S. Effect of axial and lateral fixational eye movements in corneal topography measurements with OCT. ARVO annual meeting (Virtual, 2021). *Poster contribution*

4. Invited talks

1. Urizar M. P., de Castro A., Gambra E., Curatolo A. Design of a robust long-range optical delay line for low-cost ocular biometry. Vision and Color Summer Data Blast (2022). *Oral contribution*

5. Grants

[2020-2023] Industrial PhD (IND2019/BMD-17262) fellowship of the Madrid Regional Government, to develop this thesis project. Advisors: Dr. Alberto de Castro and Dr. Andrea Curatolo from the Visual Optics and Biophotonics Lab, Spanish National Research Council (CSIC). Company advisor: Dr. Enrique Gambra. 2Eyes Vision.

6. Awards

1. BiOS Student 3-Minute Poster Presentation at Photonic West Conference, Sponsored by Neurophotonics and the Journal of Biomedical Optics. Second place. (30/01/2023)

2. Clinical and Translational Biophotonics innovation challenge: Endometriosis Challenge at the Optica Biophotonics Congress. Winner with the talk: Smart probe for guided laparoscopic biopsy to improve endometriosis diagnosis. (27/04/2022)

7. Other scientific activities

1. Co-direct 2 internships, one at VioBio laboratories and one at the company 2EyesVision.

2. Co-supervise a master thesis in the company 2EyesVision.

3. Member of the IO-CSIC Optica Student chapter, IOPTICA (formerly IOSA). Role of vice president in 2020 and 2021. We organized internal seminars, talk as well as invited talks, courses and participate in outreach activities in different Spanish cities collaborating with programs as Ciencia en el barrio, 11F, LGTBI+ in STEM, Scientifics seminars, Ciudad Ciencia, International Day of Light or Science Week.

Bibliography

1. Artal, P., *Optics of the eye and its impact in vision: a tutorial.* Advances in Optics and Photonics, 2014. 6(3): p. 340-367.
2. Kiely, P.M., G. Smith, and L.G. Carney, *The Mean Shape of the Human Cornea.* Optica Acta: International Journal of Optics, 1982. 29(8): p. 1027-1040.
3. Atchison, D. and G. Smith, *Optics of the Human Eye*. 2001: Oxford.
4. Ortiz, S., et al., *In vivo human crystalline lens topography.* Biomedical Optics Express, 2012. 3(10): p. 2471-2488.
5. Garner, L.F., *Calculation of the radii of curvature of the crystalline lens surfaces.* Ophthalmic and Physiological Optics, 1997. 17(1): p. 75-80.
6. Winn, B., et al., *Factors affecting light-adapted pupil size in normal human subjects.* Investigative Ophthalmology & Visual Science, 1994. 35(3): p. 1132-1137.
7. Sampson, D.M., et al., *Towards standardizing retinal optical coherence tomography angiography: a review.* Light: Science & Applications, 2022. 11(1): p. 63.
8. Puell Marín, M.C., *Óptica Fisiológica: El sistema óptico del ojo y la visión binocular.* Universidad Complutense de Madrid, 2006.
9. Rosales, P. and S. Marcos, *Phakometry and lens tilt and decentration using a custom-developed Purkinje imaging apparatus: validation and measurements.* Journal of the Optical Society of America A, 2006. 23(3): p. 509-520.
10. Sahin, A. and P. Hamrah, *Clinically relevant biometry.* Current Opinion in Ophthalmology, 2012. 23(1).
11. Augusteyn, R.C., et al., *Human ocular biometry.* Experimental Eye Research, 2012. 102: p. 70-75.
12. Scholtz, S. and A. Langenbucher, *(Un)avoidable errors in biometry - and some ideas how to overcome them*. 2020.
13. Schmid, G., *Axial and peripheral eye length measured with optical low coherence reflectometry.* Journal of Biomedical Optics, 2003. 8(4).
14. Hsiao, H., et al., *Telecentric design for digital-scanning-based HiLo optical sectioning endomicroscopy with an electrically tunable lens.* Journal of Biophotonics, 2021. 14(2): p. e202000335.
15. Roy, A., et al., *Variation of Axial Ocular Dimensions with Age, Sex, Height, BMI-and Their Relation to Refractive Status.* J Clin Diagn Res, 2015. 9(1): p. Ac01-4.
16. Hsiao, Y.-T., et al., *Axial length of cataract eyes: a comparison of two cohorts over a span of 10 years apart.* BMC Ophthalmology, 2021. 21(1): p. 111.
17. Schelenz, J. and J. Kammann, *Comparison of contact and immersion techniques for axial length measurement and implant power calculation.* Journal of Cataract & Refractive Surgery, 1989. 15(4): p. 425-428.
18. Schmid, G.F., et al., *Measurement of eye length and eye shape by optical low coherence reflectometry.* International Ophthalmology, 2001. 23(4): p. 317-320.
19. Faria-Ribeiro, M., et al., *Peripheral refraction and retinal contour in stable and progressive myopia.* Optom Vis Sci, 2013. 90(1): p. 9-15.
20. Brandt, J.D. and C.J. Roberts, *18 - The Impact of Central Corneal Thickness and Corneal Biomechanics on Tonometry*, in *Glaucoma (Second Edition)*, T.M. Shaarawy, et al., Editors. 2015, W.B. Saunders. p. 201-208.
21. Hoffmann, E.M., et al., *Distribution of central corneal thickness and its association with ocular parameters in a large central European cohort: the Gutenberg health study.* PLoS One, 2013. 8(8): p. e66158.
22. Navarro, R., *The Optical Design of the Human Eye: a Critical Review.* Journal of Optometry, 2009. 2(1): p. 3-18.

23. Dubbelman, M., G.L. Van der Heijde, and H.A. Weeber, *Change in shape of the aging human crystalline lens with accommodation.* Vision Research, 2005. 45(1): p. 117-132.
24. Martinez-Enriquez, E., et al., *OCT-based full crystalline lens shape change during accommodation in vivo.* Biomedical Optics Express, 2017. 8(2): p. 918-933.
25. Gaurisankar, Z.S., et al., *Correlations between ocular biometrics and refractive error: A systematic review and meta-analysis.* Acta Ophthalmologica, 2019. 97(8): p. 735-743.
26. Fard, A.M., et al., *Posterior pole retinal thickness distribution pattern in keratoconus.* International Ophthalmology, 2020. 40(11): p. 2807-2816.
27. Marcos, S., et al., *Simulating Outcomes of Cataract Surgery: Important Advances in Ophthalmology.* Annu Rev Biomed Eng, 2021. 23: p. 277-306.
28. Liu, Y.-C., et al., *Cataracts.* The Lancet, 2017. 390(10094): p. 600-612.
29. Gutmark, R. and D.L. Guyton, *Origins of the Keratometer and its Evolving Role in Ophthalmology.* Survey of Ophthalmology, 2010. 55(5): p. 481-497.
30. Sheard, R., *Optimising biometry for best outcomes in cataract surgery.* Eye, 2014. 28(2): p. 118-125.
31. Epitropoulos, A., *Axial length measurement acquisition rates of two optical biometers in cataractous eyes.* Clin Ophthalmol, 2014. 8: p. 1369-76.
32. Aristodemou, P., et al., *Improving refractive outcomes in cataract surgery: A global perspective.* World Journal of Ophthalmology, 2014. 4: p. 140-146.
33. Kim, S.Y., et al., *Accuracy of intraocular lens power calculation formulas using a swept-source optical biometer.* PLOS ONE, 2020. 15(1): p. e0227638.
34. Kane, J.X. and D.F. Chang, *Intraocular Lens Power Formulas, Biometry, and Intraoperative Aberrometry: A Review.* Ophthalmology, 2020.
35. Melles, R.B., J.T. Holladay, and W.J. Chang, *Accuracy of Intraocular Lens Calculation Formulas.* Ophthalmology, 2018. 125(2): p. 169-178.
36. Kasthurirangan, S. and A. Glasser, *Age related changes in accommodative dynamics in humans.* Vision Research, 2006. 46(8): p. 1507-1519.
37. Wolffsohn, J.S. and L.N. Davies, *Presbyopia: Effectiveness of correction strategies.* Progress in Retinal and Eye Research, 2019. 68: p. 124-143.
38. Holden, B.A., et al., *Global vision impairment due to uncorrected presbyopia.* Arch Ophthalmol, 2008. 126(12): p. 1731-9.
39. Evans, B.J.W., *Monovision: a review.* Ophthalmic and Physiological Optics, 2007. 27(5): p. 417-439.
40. Ambrósio, R. and S.E. Wilson, *LASIK vs LASEK vs PRK: Advantages and indications.* Seminars in Ophthalmology, 2003. 18(1): p. 2-10.
41. Charman, W.N., *Developments in the correction of presbyopia I: spectacle and contact lenses.* Ophthalmic and Physiological Optics, 2014. 34(1): p. 8-29.
42. Morgan, I.G., K. Ohno-Matsui, and S.-M. Saw, *Myopia.* The Lancet, 2012. 379(9827): p. 1739-1748.
43. Llorente, L., et al., *Myopic versus hyperopic eyes: axial length, corneal shape and optical aberrations.* Journal of Vision, 2004. 4(4): p. 5-5.
44. Scott, R. and T. Grosvenor, *Structural model for emmetropic and myopic eyes.* Ophthalmic and Physiological Optics, 1993. 13(1): p. 41-47.
45. Saw, S.-M., et al., *Myopia and associated pathological complications.* Ophthalmic and Physiological Optics, 2005. 25(5): p. 381-391.
46. Walline, J.J., *Myopia Control: A Review.* Eye & Contact Lens, 2016. 42(1): p. 3-8.
47. Faria-Ribeiro, M., et al., *Peripheral Refraction and Retinal Contour in Stable and Progressive Myopia.* Optometry and Vision Science, 2013. 90(1): p. 9-15.
48. Martínez-Plaza, E., et al., *Clinical Validation of a New Optical Biometer for Myopia Control in a Healthy Pediatric Population.* Children, 2022. 9(11): p. 1713.

49. Haigis, W., *Challenges and approaches in modern biometry and IOL calculation.* Saudi Journal of Ophthalmology, 2012. 26(1): p. 7-12.
50. Henry Mundt, G., Jr. and W.F. Hughes, Jr., *Ultrasonics in Ocular Diagnosis.* American Journal of Ophthalmology, 1956. 41(3): p. 488-498.
51. Olsen, T. and P.J. Nielsen, *Immersion versus contact technique in the measurement of axial length by ultrasound.* Acta Ophthalmol (Copenh), 1989. 67(1): p. 101-2.
52. Giers, U. and C. Epple, *Comparison of A-scan device accuracy.* Journal of Cataract & Refractive Surgery, 1990. 16(2): p. 235-242.
53. Fercher, A. and E. Roth, *Ophthalmic Laser Interferometry*. 1986 International Symposium/Innsbruck. Vol. 0658. 1986: SPIE.
54. Hitzenberger, C.K., et al., *Key Developments for Partial Coherence Biometry and Optical Coherence Tomography in the Human Eye Made in Vienna.* Investigative Ophthalmology & Visual Science, 2016. 57(9): p. OCT460-OCT474.
55. Shah, T.D., et al., *Update and understanding of optical biometer.* Global Journal of Cataract Surgery and Research in Ophthalmology, 2022. 1.
56. Santodomingo-Rubido, J., et al., *A new non-contact optical device for ocular biometry.* British Journal of Ophthalmology, 2002. 86(4): p. 458-462.
57. Fontes, B.M., B.M. Fontes, and E. Castro, *Intraocular lens power calculation by measuring axial length with partial optical coherence and ultrasonic biometry.* Arq Bras Oftalmol, 2011. 74(3): p. 166-70.
58. Bjeloš Rončević, M., et al., *Comparison of optical low-coherence reflectometry and applanation ultrasound biometry on intraocular lens power calculation.* Graefe's Archive for Clinical and Experimental Ophthalmology, 2011. 249(1): p. 69-75.
59. Lam, A.K.C., R. Chan, and P.C.K. Pang, *The repeatability and accuracy of axial length and anterior chamber depth measurements from the IOLMaster™*.* Ophthalmic and Physiological Optics, 2001. 21(6): p. 477-483.
60. Hitzenberger, C.K., *Low-coherence interferometry*, in *Handbook of Visual Optics*. 2017, CRC Press. p. 37-57.
61. Schmitt, J.M., *Optical coherence tomography (OCT): a review.* IEEE Journal of Selected Topics in Quantum Electronics, 1999. 5(4): p. 1205-1215.
62. BOETTNER, E.A. and J.R. WOLTER, *Transmission of the Ocular Media.* Investigative Ophthalmology & Visual Science, 1962. 1(6): p. 776-783.
63. Unterhuber, A., et al., *In vivo retinal optical coherence tomography at 1040 nm-enhanced penetration into the choroid.* Optics Express, 2005. 13(9): p. 3252-3258.
64. Artal, P., *Handbook of Visual Optics*, ed. P. Artal. Vol. I & II. 2017.
65. Delori, F.C., R.H. Webb, and D.H. Sliney, *Maximum permissible exposures for ocular safety (ANSI 2000), with emphasis on ophthalmic devices.* Journal of the Optical Society of America A, 2007. 24(5): p. 1250-1265.
66. Waelti, R., et al., *Rapid and precise in vivo measurement of human corneal thickness with optical low-coherence reflectometry in normal human eyes.* Journal of Biomedical Optics, 1998. 3(3).
67. Boehnke, M., et al., *Precision and reproducibility of measurements of human corneal thickness with rapid optical low-coherence reflectometry (OLCR).* Journal of Biomedical Optics, 1999. 4(1).
68. Hitzenberger, C.K., *Optical measurement of the axial eye length by laser Doppler interferometry.* Investigative Ophthalmology & Visual Science, 1991. 32(3): p. 616-624.
69. Hitzenberger, C., *Low-coherence interferometry in ophthalmology*. Europto Biomedical Optics '93. Vol. 2083. 1994: SPIE.
70. Drexler, W., et al., *Partial coherence interferometry: a novel approach to biometry in cataract surgery.* American Journal of Ophthalmology, 1998. 126(4): p. 524-534.

71. Masters, B., *Early development of optical low-coherence reflectometry and some recent biomedical applications.* Journal of Biomedical Optics, 1999. 4(2).
72. Bouma, B., *Handbook of Optical Coherence Tomography*. 2001: Taylor & Francis.
73. Hosseiny, H. and C. Rosa, *Design and optimization of a spectrometer for Spectral Domain Optical Coherence Tomography*. Vol. 9286. 2014. 92864Z.
74. Ruggeri, M., et al., *Imaging and full-length biometry of the eye during accommodation using spectral domain OCT with an optical switch.* Biomedical Optics Express, 2012. 3(7): p. 1506-1520.
75. Tao, A., et al., *Versatile optical coherence tomography for imaging the human eye.* Biomedical optics express, 2013. 4(7): p. 1031-1044.
76. Klein, T. and R. Huber, *High-speed OCT light sources and systems [Invited].* Biomedical Optics Express, 2017. 8(2): p. 828-859.
77. Song, G., et al., *First Clinical Application of Low-Cost OCT.* Translational Vision Science & Technology, 2019. 8(3): p. 61-61.
78. Kendrisic, M., et al., *Thermally tuned VCSEL at 850 nm as a low-cost alternative source for full-eye SS-OCT.* Optics Letters, 2023. 48(11): p. 3079-3082.
79. Dubbelman, M., et al., *Radius and asphericity of the posterior corneal surface determined by corrected Scheimpflug photography.* Acta Ophthalmologica Scandinavica, 2002. 80(4): p. 379-383.
80. Rosales, P. and S. Marcos, *Customized computer models of eyes with intraocular lenses.* Optics Express, 2007. 15(5): p. 2204-2218.
81. Sikorski, B.L. and P. Suchon, *OCT Biometry (B-OCT): A New Method for Measuring Ocular Axial Dimensions.* Journal of Ophthalmology, 2019. 2019: p. 9192456.
82. Dorsel, A., K.-H. Donnerhacke, and B. Moeller, *Interferometric arrangement with diffractive optical element for measuring intraocular distances*. 1997, Google Patents.
83. Wang, C., et al., *The measurement of ocular axial length in normal human eyes based on an improved Twyman-Green interferometer.* Journal of Biophotonics, 2021. 14(10): p. e202100021.
84. Chavanne, P. and R.P. Salathe, *Apparatus having a multiple angle transparent rotating element for measuring the thickness of transparent objects*. 2000, Google Patents.
85. Ballif, J., et al., *Rapid and scalable scans at 21 m/s in optical low-coherence reflectometry.* Optics Letters, 1997. 22(11): p. 757-759.
86. Huang, J., et al., *Meta-analysis of optical low-coherence reflectometry versus partial coherence interferometry biometry.* Scientific Reports, 2017. 7(1): p. 43414.
87. Suheimat, M., et al., *Refractive indices used by the Haag-Streit Lenstar to calculate axial biometric dimensions.* Ophthalmic and Physiological Optics, 2015. 35(1): p. 90-96.
88. Kanclerz, P., et al., *Repeatability and reproducibility of optical biometry implemented in a new optical coherence tomographer and comparison with a optical low-coherence reflectometer.* Journal of Cataract & Refractive Surgery, 2019. 45(11): p. 1619-1624.
89. Daniel, B., et al., *Eye motion compensation for accurate ocular biometry with a combined Purkinje mirror imaging (PMI) and optical low coherence reflectometry (OLCR) system.* Investigative Ophthalmology & Visual Science, 2015. 56(7): p. 1967-1967.
90. Akman, A., L. Asena, and S.G. Güngör, *Evaluation and comparison of the new swept source OCT-based IOLMaster 700 with the IOLMaster 500.* British Journal of Ophthalmology, 2016. 100(9): p. 1201-1205.
91. Khairallah, M., et al., *Number of People Blind or Visually Impaired by Cataract Worldwide and in World Regions, 1990 to 2010.* Investigative Ophthalmology & Visual Science, 2015. 56(11): p. 6762-6769.
92. Grimes, C.E., et al., *Systematic review of barriers to surgical care in low-income and middle-income countries.* World J Surg, 2011. 35(5): p. 941-50.

93. Lewallen, S. and P. Courtright, *Recognising and reducing barriers to cataract surgery.* Community Eye Health, 2000. 13(34): p. 20-1.
94. Ibrahim, M., et al., *Making Sight Affordable (Part I): Aurolab Pioneers Production of Low-Cost Technology for Cataract Surgery.* Innovations: Technology, Governance, Globalization, 2006. 1(3): p. 25-41.
95. Singh, K., et al., *Review of manual small-incision cataract surgery.* Indian J Ophthalmol, 2017. 65(12): p. 1281-1288.
96. Sharma, N. and C. Sharma, *Female gender: A significant barrier to access cataract surgery in rural Gurugram, Haryana, India.* British Journal of Visual Impairment, 2022. 0(0): p. 02646196221085848.
97. Mbwogge, M. and H.E. Nkumbe, *Exploring the Reasons for Low Cataract Surgery Uptake Among Patients Detected in a Community Outreach Program in Cameroon: Focused Ethnographic Mixed Methods Study.* JMIRx Med, 2022. 3(2): p. e35044.
98. Zhang, X.J., et al., *Barriers for Poor Cataract Surgery Uptake among Patients with Operable Cataract in a Program of Outreach Screening and Low-cost Surgery in Rural China.* Ophthalmic Epidemiology, 2014. 21(3): p. 153-160.
99. Wang, W., et al., *A Global View on Output and Outcomes of Cataract Surgery With National Indices of Socioeconomic Development.* Investigative Ophthalmology & Visual Science, 2017. 58(9): p. 3669-3676.
100. Lindfield, R., et al., *The challenges in improving outcome of cataract surgery in low and middle income countries.* Indian J Ophthalmol, 2012. 60(5): p. 464-9.
101. Kanclerz, P., *Optical biometry in a commercially available anterior and posterior segment optical coherence tomography device.* Clinical and Experimental Optometry, 2019. 102(5): p. 533-534.
102. Cherian, N., et al., *Comparison of a novel hyper-parallel optical coherence tomography biometer with a swept source OCT biometer in patients with cataracts.* Investigative Ophthalmology & Visual Science, 2022. 63(7): p. 3076 – F0548-3076 – F0548.
103. Chong, C., et al., *Large coherence length swept source for axial length measurement of the eye.* Applied Optics, 2009. 48(10): p. D144-D150.
104. Grulkowski, I., et al., *Retinal, anterior segment and full eye imaging using ultrahigh speed swept source OCT with vertical-cavity surface emitting lasers.* Biomedical Optics Express, 2012. 3(11): p. 2733-2751.
105. Borgia, A., et al., *Swept-Source Optical Coherence Tomography-Based Biometry: A Comprehensive Overview.* Photonics, 2022. 9(12): p. 951.
106. McGhee, C.N.J., J. Zhang, and D.V. Patel, *A perspective of contemporary cataract surgery: the most common surgical procedure in the world.* Journal of the Royal Society of New Zealand, 2020. 50(2): p. 245-262.
107. Chopra, R., S.K. Wagner, and P.A. Keane, *Optical coherence tomography in the 2020s-outside the eye clinic.* Eye (Lond), 2021. 35(1): p. 236-243.
108. Song, G., et al., *A review of low-cost and portable optical coherence tomography.* Progress in Biomedical Engineering, 2021. 3(3): p. 032002.
109. Kim, S., et al., *Design and implementation of a low-cost, portable OCT system.* Biomedical Optics Express, 2018. 9(3): p. 1232-1243.
110. Kim, J.E., et al., *Evaluation of a self-imaging SD-OCT system designed for remote home monitoring.* BMC Ophthalmol, 2022. 22(1): p. 261.
111. Jang, G.H., J. Kang, and J.-H. Chung, *Development of a portable ophthalmic OCT device and measurement of its performance*. SPIE Advanced Biophotonics Conference (SPIE ABC 2021). Vol. 12159. 2022: SPIE.
112. Roy, A., S.K. Patra, and T. Piwonski. *Low-cost semiconductor swept source laser for near-infrared Optical Coherence Tomography*. in *2020 IEEE Photonics Conference (IPC)*. 2020.

113. Moon, S. and E.S. Choi, *VCSEL-based swept source for low-cost optical coherence tomography.* Biomedical Optics Express, 2017. 8(2): p. 1110-1121.
114. Kendrisic, M., et al. *Thermally tuned VCSEL-based SS-OCT system*. in *Biophotonics Congress: Biomedical Optics 2022 (Translational, Microscopy, OCT, OTS, BRAIN)*. 2022. Fort Lauderdale, Florida: Optica Publishing Group.
115. DuBose, T., et al., *Handheld adaptive optics scanning laser ophthalmoscope.* Optica, 2018. 5(9): p. 1027-1036.
116. LaRocca, F., et al., *In vivo cellular-resolution retinal imaging in infants and children using an ultracompact handheld probe.* Nature Photonics, 2016. 10: p. 580.
117. Leahy, M., et al., *The how and why of a $10 optical coherence tomography system*. 2016. 96970T.
118. Subhash, H.M., et al. *Smartphone based Multiple Reference Optical coherence tomography (MRO™) system*. in *Biomedical Optics 2014*. 2014. Miami, Florida: Optica Publishing Group.
119. de la Hoz, A., et al., *Design and ex situ performance of a shape-changing accommodating intraocular lens.* Optica, 2019. 6(8): p. 1050-1057.
120. Curatolo, A., et al., *Multi-meridian corneal imaging of air-puff induced deformation for improved detection of biomechanical abnormalities.* Biomedical Optics Express, 2020. 11(11): p. 6337-6355.
121. McAuley, R., et al., *Co-axial acoustic-based optical coherence vibrometry probe for the quantification of resonance frequency modes in ocular tissue.* Scientific Reports, 2022. 12(1): p. 18834.
122. Dorronsoro, C., et al., *Tunable lenses: dynamic characterization and fine-tuned control for high-speed applications.* Optics Express, 2019. 27(3): p. 2085-2100.
123. Lankenau, D.E. *Modell-Augen Manufaktur (https://modell-augen-manufaktur.de/oct-model-eyes-with-air-chambers/)*. 2023.
124. Boss, D., et al., *Apparatus for modelling ocular structures*, USPO, Editor. 2019, Novartis AG: US.
125. Chavanne, P. and R. Paul Salathe, *Apparatus having a multiple angle transparent rotating element for measuring the thickness of transparent objects*, USPO, Editor. 1996: US.
126. Wälti, R. and G.F. Schmid, *Method and device for measuring the optical properties of at least two regions located at a distance from one another in a transparent and/or diffuse object*. 2004, Google Patents.
127. Waelti, R., U. Buri, and J. Breitenstein, *Method and apparatus for determination of geometric values on an object* USPO, Editor. 2004, Haag-Streit AG: US.
128. Cruysberg, L.P.J., et al., *Evaluation of the Lenstar LS 900 non-contact biometer.* British Journal of Ophthalmology, 2010. 94(1): p. 106-110.
129. Buckhurst, P.J., et al., *A new optical low coherence reflectometry device for ocular biometry in cataract patients.* British Journal of Ophthalmology, 2009. 93(7): p. 949-953.
130. Zhao, J., et al., *Evaluation of the repeatability of the Lenstar and comparison with two other non-contact biometric devices in myopes.* Clin Exp Optom, 2013. 96(1): p. 92-9.
131. Findl, O., *Comparison of Two Swept-Source OCT Biometry Devices.* Sponosred by Heidelberg Engineering, 2020: p. 24-25.
132. Chan, T.C.Y., et al., *Comparison of two novel swept-source optical coherence tomography devices to a partial coherence interferometry-based biometer.* Scientific Reports, 2021. 11(1): p. 14853.
133. Schiano-Lomoriello, D., et al., *Repeatability of automated measurements by a new anterior segment optical coherence tomographer and biometer and agreement with standard devices.* Scientific Reports, 2021. 11(1): p. 983.
134. Hsiung, P.-L., et al., *High-speed path-length scanning with a multiple-pass cavity delay line.* Applied Optics, 2003. 42(4): p. 640-648.

135. Dsouza, R., et al., *Voice coil based robust and miniature optical delay for multiple reference optical coherence tomography*. SPIE BiOS. Vol. 8942. 2014: SPIE.
136. Tearney, G.J., B.E. Bouma, and J.G. Fujimoto, *High-speed phase- and group-delay scanning with a grating-based phase control delay line.* Optics Letters, 1997. 22(23): p. 1811-1813.
137. Sampson, D. and T.R. Hillman, *Optical coherence tomography*, in *Lasers and Current Optical Techniques in Biology*, G. Palumbo, et al., Editors. 2004, The Royal Society of Chemistry. p. 481-572.
138. Smith, E.D.J., A.V. Zvyagin, and D.D. Sampson, *Real-time dispersion compensation in scanning interferometry.* Optics Letters, 2002. 27(22): p. 1998-2000.
139. Niblack, W.K., et al., *Dispersion in a grating-based optical delay line for optical coherence tomography.* Applied Optics, 2003. 42(19): p. 4115-4118.
140. Lee, K.-S., et al., *Dispersion control with a Fourier-domain optical delay line in a fiber-optic imaging interferometer.* Applied Optics, 2005. 44(19): p. 4009-4022.
141. Iftimia, N.V., et al., *Adaptive ranging for optical coherence tomography.* Optics Express, 2004. 12(17): p. 4025-4034.
142. Maguluri, G., et al., *Three dimensional tracking for volumetric spectral-domain optical coherence tomography.* Optics Express, 2007. 15(25): p. 16808-16817.
143. Pircher, M., et al., *In vivo investigation of human cone photoreceptors with SLO/OCT in combination with 3D motion correction on a cellular level.* Optics Express, 2010. 18(13): p. 13935-13944.
144. El-Haddad, M. and Y. Tao, *Real-time dynamic depth tracking for arbitrarily long range OCT imaging and surgical instrument tracking using a Fourier domain optical delay line.* Investigative Ophthalmology & Visual Science, 2015. 56(7): p. 4089-4089.
145. Zhang, J., J. Nelson, and Z. Chen, *Mirror image free Fourier domain optical coherence tomography*. SPIE BiOS. Vol. 5690. 2005: SPIE.
146. Dhalla, A.-H. and J.A. Izatt, *Complete complex conjugate resolved heterodyne swept-source optical coherence tomography using a dispersive optical delay line.* Biomedical Optics Express, 2011. 2(5): p. 1218-1232.
147. Meemon, P., K.S. Lee, and J. Rolland, *Phase-resolved Doppler imaging with dual-detection full-range frequency domain optical coherence tomography*. SPIE BiOS. Vol. 7891. 2011: SPIE.
148. Wu, T., et al. *Full-range swept source optical coherence tomography based on carrier frequency by transmissive dispersive optical delay line*. 2011. SPIE.
149. Lu, S.-H., S.-R. Huang, and C.-C. Chou, *Two-harmonic complex spectral-domain optical coherence tomography using achromatic sinusoidal phase modulation.* Optics Communications, 2018. 410: p. 222-227.
150. Kolokoltsev, Y., et al., *Rapid scanning optical delay line based on a diffraction grating pair for a low-coherence reflectometer.* Applied Optics, 2018. 57(16): p. 4542-4550.
151. Kolokoltsev, Y., et al., *Rapid scanning optical delay line based on a diffraction grating pair for a low-coherence reflectometer.* Applied Optics, 2018. 57.
152. Zvyagin, A.V., E.D.J. Smith, and D.D. Sampson, *Delay and dispersion characteristics of a frequency-domain optical delay line for scanning interferometry.* Journal of the Optical Society of America A, 2003. 20(2): p. 333-341.
153. Oldenburg, A.L., et al., *Fast-Fourier-domain delay line for in vivo optical coherence tomography with a polygonal scanner.* Applied Optics, 2003. 42(22): p. 4606-4611.
154. Liu, X., M.J. Cobb, and X. Li, *Rapid scanning all-reflective optical delay line for real-time optical coherence tomography.* Optics Letters, 2004. 29(1): p. 80-82.
155. Xu, L., et al., *Transmissive RSOD for balance-detection-based OCT*. Photonics and Optoelectronics Meetings 2009. Vol. 7519. 2009: SPIE.
156. Li, D. and Z. Ding, *Double grating based rapid scanning optical delay line for dispersion compensation in optical coherence tomography - art. no. 65340D.* Proceedings of SPIE - The International Society for Optical Engineering, 2007. 6534.

157. Silva, K.K.M.B.D., A.V. Zvyagin, and D.D. Sampson *Extended range, rapid scanning optical delay line for biomedical interferometric imaging*. Electronics Letters, 1999. 35, 1404-1406.
158. Armstrong, J.J., et al., *In vivo size and shape measurement of the human upper airway using endoscopic long-range optical coherence tomography.* Optics Express, 2003. 11(15): p. 1817-1826.
159. Williamson, J.P., et al., *Measuring airway dimensions during bronchoscopy using anatomical optical coherence tomography.* European Respiratory Journal, 2010. 35(1): p. 34-41.
160. Pande, P., et al., *Low-cost hand-held probe for depth-resolved low-coherence interferometry.* Biomedical Optics Express, 2017. 8(1): p. 338-348.
161. Rollins, A.M. and J.A. Izatt, *Optimal interferometer designs for optical coherence tomography.* Optics Letters, 1999. 24(21): p. 1484-1486.
162. Silva, D., *Optical coherence tomography: technology enhancements and novel applications*. 2003.
163. Sekundo, W., *The IOL Master 700*, in *Cataract and Refractive Surgery Today Europe*. 2015.
164. Ma, J., et al., *Utility of IOLMaster 700 Swept-Source Optical Coherence Tomography in Detecting Macular Disease for Preoperative Cataract Surgery Patients.* Clin Ophthalmol, 2021. 15: p. 3369-3378.
165. Rein, A.P., et al., *The Additive Value of Foveal OCT-Based Biometry to Fundus Biomicroscopy for Detecting Macular Pathology Prior to Cataract Surgery.* American Journal of Ophthalmology, 2021. 228: p. 8-15.
166. Koumbo Mekountchou, I.O., et al., *Peripheral eye length measurement techniques: a review.* Clinical and Experimental Optometry, 2020. 103(2): p. 138-147.
167. Porporato, N., M. Baskaran, and T. Aung, *Role of anterior segment optical coherence tomography in angle-closure disease: a review.* Clinical & Experimental Ophthalmology, 2018. 46(2): p. 147-157.
168. Romashchenko, D., et al., *Simultaneous measurements of foveal and peripheral aberrations with accommodation in myopic and emmetropic eyes.* Biomedical Optics Express, 2021. 12(12): p. 7422-7433.
169. Muralidharan, G., et al., *Morphological changes of human crystalline lens in myopia.* Biomedical Optics Express, 2019. 10(12): p. 6084-6095.
170. Ng, D.S.C., et al., *Advances of optical coherence tomography in myopia and pathologic myopia.* Eye, 2016. 30(7): p. 901-916.
171. Kuo, A.N., R.P. McNabb, and J.A. Izatt, *Advances in Whole-Eye Optical Coherence Tomography Imaging.* The Asia-Pacific Journal of Ophthalmology, 2019. 8(2): p. 99-104.
172. Nankivil, D., et al., *Handheld, rapidly switchable, anterior/posterior segment swept source optical coherence tomography probe.* Biomedical Optics Express, 2015. 6(11): p. 4516-4528.
173. Rodríguez-Aramendía, A., et al., *Whole anterior segment and retinal swept source OCT for comprehensive ocular screening.* Biomedical Optics Express, 2021. 12(3): p. 1263-1278.
174. Kim, H.-J., et al., *High-resolution, dual-depth spectral-domain optical coherence tomography with interlaced detection for whole-eye imaging.* Applied Optics, 2016. 55(26): p. 7212-7217.
175. Fan, S., et al., *Dual band dual focus optical coherence tomography for imaging the whole eye segment.* Biomedical optics express, 2015. 6(7): p. 2481-2493.
176. Kim, H.-J., et al., *Full ocular biometry through dual-depth whole-eye optical coherence tomography.* Biomedical Optics Express, 2018. 9(2): p. 360-372.
177. McNabb, R., et al., *Wide-field whole eye OCT system with demonstration of quantitative retinal curvature estimation.* Biomedical Optics Express, 2019. 10: p. 338.
178. Grulkowski, I., et al., *Swept source optical coherence tomography and tunable lens technology for comprehensive imaging and biometry of the whole eye.* Optica, 2018. 5(1): p. 52-59.
179. Benton, D., *Non-mechanical beam steering: ways and means*. SPIE Security + Defence. Vol. 10797. 2018: SPIE.

180. Savidis, N., et al., *Nonmechanical zoom system through pressure-controlled tunable fluidic lenses.* Applied Optics, 2013. 52(12): p. 2858-2865.
181. Zohrabi, M., R.H. Cormack, and J.T. Gopinath, *Wide-angle nonmechanical beam steering using liquid lenses.* Optics Express, 2016. 24(21): p. 23798-23809.
182. Urizar, M.P., et al. *Design of a low-cost, versatile, whole-eye scanner for optical coherence tomography*. in *Biophotonics Congress: Biomedical Optics 2022 (Translational, Microscopy, OCT, OTS, BRAIN)*. 2022. Fort Lauderdale, Florida: Optica Publishing Group.
183. Saleh, B.E.A. and M.C. Teich, *Fundamentals of photonics*. 2019.
184. Carrasco-Zevallos, O.M., et al., *Constant linear velocity spiral scanning for near video rate 4D OCT ophthalmic and surgical imaging with isotropic transverse sampling.* Biomedical Optics Express, 2018. 9(10): p. 5052-5070.
185. Atchison, D., *Schematic eyes*, in *Handbook of visual optics: Fundamentals and eye optics*, P. Artal, Editor. 2017. p. 235-248.
186. Chikri, Y.M., *Development of Electronics and Firmware for a Vision Simulation Device.* Universidad Carlos III de Madrid 2017.
187. Marrakchi, Y., et al., *Experimental characterization, modelling and compensation of temperature effects in optotunable lenses.* Scientific Reports, 2023. 13(1): p. 1575.
188. Chen, L., et al., *Electrically Tunable Lenses: A Review.* Frontiers in Robotics and AI, 2021. 8.
189. Dubis, A.M., et al., *Relationship between the Foveal Avascular Zone and Foveal Pit Morphology.* Investigative Ophthalmology & Visual Science, 2012. 53(3): p. 1628-1636.
190. An, L., et al., *Depth imaging through the anterior to posterior segment of the whole human eye based on optical coherence tomography in the spectral-domain.* OSA Continuum, 2021. 4(11): p. 2784-2795.
191. Urizar, M.P., et al., *Optical beam scanner with reconfigurable non-mechanical control of beam position, angle, and focus for low-cost whole-eye OCT imaging.* Biomedical Optics Express, 2023. 14(9): p. 4468-4484.
192. Charman, W.N., *Developments in the correction of presbyopia II: surgical approaches.* Ophthalmic and Physiological Optics, 2014. 34(4): p. 397-426.
193. Atchison, D.A., *Modern Optical Design Assessment and Spectacle Lenses.* Optica Acta: International Journal of Optics, 1985. 32(5): p. 607-634.
194. Meister, D.J. and S.W. Fisher, *Progress in the spectacle correction of presbyopia. Part 1: Design and development of progressive lenses.* Clinical and Experimental Optometry, 2008. 91(3): p. 240-250.
195. Rifai, K. and S. Wahl, *Specific eye–head coordination enhances vision in progressive lens wearers.* Journal of Vision, 2016. 16(11): p. 5-5.
196. Chamorro, E., et al., *Lens Design Techniques to Improve Satisfaction in Free-Form Progressive Addition Lens Users.* JOJ Ophthalmology, 2018. 6: p. 1-10.
197. Han, S.C., A.D. Graham, and M.C. Lin, *Clinical Assessment of a Customized Free-Form Progressive Add Lens Spectacle.* Optometry and Vision Science, 2011. 88(2): p. 234-243.
198. Mimetika Mapper, I.O. https://indo.es/es/optics/mimetika.
199. Alvarez, T.L., E.H. Kim, and B. Granger-Donetti, *Adaptation to Progressive Additive Lenses: Potential Factors to Consider.* Scientific Reports, 2017. 7(1): p. 2529.
200. Simonet, P., et al., *Eye and Head Movements for Changes in Gaze in a Presbyopic Population.* Investigative Ophthalmology & Visual Science, 2003. 44(13): p. 2779-2779.
201. Otero, C., et al., *Repeatability of Aberrometric Measurements With a New Instrument for Vision Analysis Based on Adaptive Optics.* Journal of Refractive Surgery, 2015. 31(3): p. 188-194.
202. Paniagua-Diaz, A.M. and P. Artal. *Adaptive Optics Visual Simulators: New tools for a complete and customized vision evaluation*. in *Imaging and Applied Optics Congress*. 2020. Washington, DC: Optica Publishing Group.

203. Akondi, V., et al., *Experimental validations of a tunable-lens-based visual demonstrator of multifocal corrections.* Biomedical Optics Express, 2018. 9(12): p. 6302-6317.
204. Vinas, M., et al., *Visual simulators replicate vision with multifocal lenses.* Scientific Reports, 2019. 9(1): p. 1539.
205. Zaytouny, A., et al., *Clinical validation of simulated multifocal intraocular lenses. SimVis GekkoTM simulations and reports on pseudophakic patients.* Investigative Ophthalmology & Visual Science, 2023. 64(8): p. 5421-5421.
206. Hoya-Vision-Simulator. https://www.hoyavision.com/.
207. Barbero, S. and J. Portilla, *Simulating real-world scenes viewed through ophthalmic lenses.* Journal of the Optical Society of America A, 2017. 34(8): p. 1301-1308.
208. Marin, G., E. Terrenoire, and M. Hernandez, *Compared distortion effects between real and virtual ophthalmic lenses with a simulator*, in *Proceedings of the 2008 ACM symposium on Virtual reality software and technology*. 2008, Association for Computing Machinery: Bordeaux, France. p. 271–272.
209. Kweon, H.J., *Method of simulating lens using augmented reality*, WIPO, Editor. 2013: Korea.
210. Aydındoğan, G., et al., *Applications of augmented reality in ophthalmology [Invited].* Biomedical Optics Express, 2021. 12(1): p. 511-538.
211. Atchison, D.A., *Spectacle lens design: a review.* Applied Optics, 1992. 31(19): p. 3579-3585.
212. Träger, F., *Handbook of Lasers and Optics*. 2007: Springer New York.
213. Guirao, A., et al., *Average optical performance of the human eye as a function of age in a normal population.* Invest Ophthalmol Vis Sci, 1999. 40(1): p. 203-13.
214. Almeida, M. and L. Carvalho, *Different Schematic Eyes and their Accuracy to the in vivo Eye: A Quantitative Comparison Study.* Brazilian Journal of Physics - BRAZ J PHYS, 2007. 37.
215. Lundström, L., J. Gustafsson, and P. Unsbo, *Population distribution of wavefront aberrations in the peripheral human eye.* Journal of the Optical Society of America A, 2009. 26(10): p. 2192-2198.
216. Gustafsson, J., et al., *Peripheral astigmatism in emmetropic eyes.* Ophthalmic and Physiological Optics, 2001. 21(5): p. 393-400.
217. Legge, G.E., et al., *Psychophysics of reading—I. Normal vision.* Vision Research, 1985. 25(2): p. 239-252.